Advanced characterization for the development of innovative non-volatile memories

Lucie Prazakova

Université Grenoble Alpes

THÈSE

Pour obtenir le grade de
DOCTEUR DE L'UNIVERSITE GRENOBLE ALPES
Spécialité : **Physique des matériaux**
Arrêté ministériel : 25 mai 2016

Présentée par
Lucie PRAZAKOVA

Thèse dirigée par **Eugénie MARTINEZ** et
Co-encadrée par **Emmanuel NOLOT** et **Gabriele NAVARRO**

préparée au sein du **CEA-LETI**
dans **l'École Doctorale de Physique de Grenoble**

Caractérisation Avancée pour le Développement des Nouvelles Mémoires Non-Volatiles

Thèse soutenue publiquement le **23 Mai 2022,**
devant le jury composé de :

M. Hubert RENEVIER
Professeur, Grenoble INP - Université Grenoble-Alpes (Président, Examinateur)
M. Lambert ALFF
Professeur, TU Darmstadt (Rapporteur)
Mme. Christine MARTINET
Ingénieur de recherche, iLM CNRS - Université Lyon (Rapporteure)
M. Olivier THOMAS
Professeur, IM2NP CNRS - Aix-Marseille Université (Examinateur)
Mme. Delphine LE CUNFF
Ingénieur, STMicroelectronics, Crolles (Examinatrice)
Mme. Yannick LE FRIEC
Ingénieur, STMicroelectronics, Crolles (Invitée)

Acknowledgements

I'd like to express my deepest thanks to my supervisors Emmanuel Nolot and Gabriele Navarro and my thesis director Eugenie Martinez. I greatly appreciate their guidance throughout the three years of my PhD experience, their patience, insightful feedbacks, and invaluable contributions to my professional development.

I would like to extend my sincere thanks to the colleagues from Service of Metrology and Characterization (SMCP), in particular from the Laboratory of Material Properties and Structure (LPMS), the colleagues from DCOS Department and the Platform of NanoCharacterization (PFNC), whom I had the opportunity to work with and to regularly meet in the hallways. I am grateful for their enthusiasm and willing collaboration, which resulted in many rewarding discussions. I also wish to thank for their kind help and assistance in the everyday laboratory life and for many professional and personal advice. I would like to especially thank to Denis Rouchon, Névine Rochat and Frédéric Fillot for their expertise in the field of material characterization within my PhD.

I would also like to acknowledge the Elettra Sincrotrone, Trieste, for providing me the unique beamline work experience and Hicham Khodja from CEA-IRAMIS for his collaboration concerning the Ion Beam Analysis.

Finally, I would like to thank to my parents for their lasting support over the distance and to my friends for the encouragement and optimism every time I needed. My special thanks belong to my friends Emiliano Martinez Vollbert for sharing the remarkable experiences over the three years of our PhD studies in Grenoble and Jana Válková with her family for their companionship, strong positive vibes, and creative advice.

Lucie Pražáková

Contents

Acknowledgements **3**
Contents **4**
Abstract – Résumé **7**
List of abbreviations **9**
Introduction **11**
1 Chapter 1 Phase-Change Memories: Principle and Technology **14**
1.1 Emerging Non-Volatile memories 15
1.2 Phase-Change Memories 16
1.2.1 PCRAM principle and structure 17
1.2.2 Threshold switching 18
1.2.3 Technological characteristics of PCRAM 19
1.2.4 PCRAM device engineering 21
1.2.5 Applications, trends on the market 23
1.3 Phase-change materials 25
1.3.1 Phase-Change Material structure 26
1.3.2 Ge-Sb-Te ternary system 33
1.3.3 Material engineering 37
1.4 Chapter summary 45
2 Chapter 2 Characterization of Phase-Change Materials **46**
2.1 Introduction to material characterization 47
2.1.1 Electrical properties 47
2.1.2 Vibrational spectroscopies 48
2.1.3 X-ray characterization 49
2.1.4 Transmission Electron Microscopy 51
2.2 Material characterization of GeSbTe alloys 52
2.2.1 Bonding arrangement in elemental alloys 53
2.2.2 Investigation of electrical and optical properties 56
2.2.3 Identification of structural units 58
2.2.4 N-bond formation and oxidation effects 59
2.2.5 Investigation of local environment 60
2.2.6 Microstructure analysis 61
2.3 Sample preparation and the experimental part of the thesis 63
2.4 Chapter summary 65

3 Chapter 3 Nitrogen-doped Ge, Sb and Te elemental compounds 66
3.1 GeN, SbN, TeN literature context 67
3.2 Quantification of N content 68
3.2.1 Quantification by IBA techniques 69
3.3 Spectroscopic studies of N-doped Ge, Sb and Te compounds 70
3.3.1 Ge and GeN layers 70
3.3.2 Sb and SbN layers 72
3.3.3 Te and TeN layers 73
3.4 Investigation of the local structure by XAS measurements 75
3.5 Simulations of the ideal nitride structures 77
3.6 Identification of nitrogen bonding in N-doped GeSbTe alloy 79
3.7 Structural evolution of the single-element layers 80
3.7.1 Structural evolution as a function of time 80
3.7.2 Structural evolution as a function of temperature 82
3.8 Chapter summary 85
4 Chapter 4 Ge-Sb-Te alloys 86
4.1 Ge-rich GST: Structural Evolution 87
4.1.1 $Ge_2Sb_2Te_5$ 87
4.1.2 Ge-rich GST 89
4.1.3 Summary of the section 93
4.2 Ge-rich GST: Effect of Ge content 95
4.2.1 As-deposited Ge-rich GST layers 95
4.2.2 Structural evolution of the Ge-rich GST layers as a function of temperature 97
4.2.3 Summary of the section 103
4.3 N-doped Ge-rich GST: Structural evolution 104
4.3.1 Structural evolution of N-doped Ge-rich GST as a function of temperature 104
4.3.2 Formation of Ge-N bonds in the structure 107
4.3.3 Summary of the section 109
4.4 N-doped Ge-rich GST: Effect of N content 110
4.4.1 As-deposited N-doped GGST 110
4.4.2 Annealed N-doped GGST 111
4.4.3 Summary of the section 114
4.5 Chapter summary 115
Conclusion and perspectives 116
References 121
List of publications 146
Résumé en français 147

Appendix 1 Theoretical background of characterization techniques 155
Appendix 2 N content quantification in GeN alloys..... 166
Appendix 3 IR and Raman spectra deconvolution of elemental systems..... 167
Appendix 4 "Ab initio" simulations of elemental nitrides..... 173
Appendix 5 Raman spectra deconvolutions of GST alloys..... 175

Abstract – Résumé

Title: Advanced Characterization for the Development of Innovative Non-Volatile Memories

Abstract

The development of innovative Non-Volatile Memory technologies (NVM) has become crucial as the amount of data required to be stored and processed is rapidly increasing. Among the several innovative NVM candidates, the Phase-Change Memory (PCRAM) demonstrated to be the most promising one, providing the solutions in the domain of stand-alone (e.g., Storage Class Memory) and embedded (e.g., microcontrollers) applications. PCRAM device structure is based on phase-change material integrated between two electrodes and undergoing the amorphous-to-crystalline phase change transition. The material engineering of such an integrated material plays the fundamental role in PCRAM device performances. In recent years, Ge-enriched or Nitrogen-doped GeSbTe (GST) alloys have demonstrated high thermal stability allowing the PCRAM device applications in the high-demanding automotive domain. Although the outstanding performances of PCRAM device with such integrated material have been reported, the deep investigation of material structure is still missing and the full understanding of crystallization mechanisms in such alloys represents a very active research topic.

This work aims at the thorough structural investigation of GST phase-change alloys targeting the high temperature stability. We study two main groups of materials: Ge, Sb and Te elemental systems and Ge-rich GST alloys. First, we focus on the characterization of the material structure and its evolution as a function of controlled thermal budget. Then, we report on the effect of Nitrogen (N) doping. We combine optical (Raman and Fourier transform infrared spectroscopy) and X-ray (X-ray diffraction, X-ray absorption spectroscopy) characterizations along with transmission electron microscopy and *"ab initio"* simulations in order to provide a complete and unique insight of the material structure. The investigation of Ge-rich GST alloys allows to describe several phenomena occurring during the crystallization process (i.e., Ge atoms diffusion, GST and Ge phases segregation, their nucleation and growth) and their dependence on Ge content in the alloy. The studies of elemental systems upon N doping present the effect of N incorporation on Ge, Sb and Te structure and describe the formation of N bonding. The results from N-doped elemental systems are applied to evaluate the N impact on the structure of complex Ge-rich GST alloys. The results of this work provide deeper understanding of GST alloys, highlighting the complementarity of used characterization techniques. Finally, future perspectives of GST alloys investigations are provided, suggesting further options of GST alloys engineering as well as the combination of characterizations, which can be employed.

Key Words: Phase-Change Memory, Ge-rich GST alloys, Nitrogen doping, FTIR spectroscopy, Raman spectroscopy, X-ray Diffraction.

Titre: Caractérisation Avancée pour le Développement des Nouvelles Mémoires Non-Volatiles

Résumé

L'accroissement significatif du volume des données numériques à stocker et à traiter conduit au développement de technologies innovantes de mémoires Non-Volatiles (NVM). En particulier, des Mémoires à Changement de Phase (PCRAM) semblent les plus prometteuses, adaptées aux applications autonomes (Storage Class Memory) et embarquées (micro-contrôleurs). Un dispositif PCRAM est organisé autour de l'élément clé qu'est le matériau à changement de phase, matériau dont le choix et les caractéristiques déterminent pour une large part les performances du dispositif. Ces dernières années, des matériaux GeSbTe (GST) enrichis en Ge et dopés par de l'azote (N) ont notamment démontré une stabilité thermique compatible avec les exigences des PCRAM embarquées pour le domaine automobile. Les performances des dispositifs PCRAM intégrant ces matériaux ont fait d'objet de publications, mais la compréhension fine de la structure et du mécanisme de cristallisation reste un sujet de recherche très actif.

L'objectif de ce travail est de contribuer à l'étude structurale approfondie des matériaux à changement de phase à base de GSTet caractérisés par une stabilité thermique compatible avec les applications embarquées. Nous avons particulièrement étudié deux groupes de matériaux : les systèmes élémentaires Ge, Sb et Te et les alliages GST enrichis en Ge. La combinaison des techniques d'analyse optiques (spectroscopies Raman et infrarouge), par rayons X (diffraction; spectroscopie d'absorption), par faisceau électronique (microscopie electronique en transmission) et des simulations *« ab initio »* nous a permis de caractériser finement la structure des matériaux et son évolution en fonction de la température, puis de révéler l'influence du dopage azote. L'étude de la cristallisation du GST enrichi en Ge a mis en évidence la coexistence et la compétition de plusieurs mécanismes dont l'influence relative dépend de la teneur en Ge dans les alliages. L'étude des systèmes élémentaires dopés par azote a permis de démontrer l'influence du dopage sur la structure et d'identifier la formation de liaisons élément-N. Ces résultats ont ensuite été étendus à l'étude de l'impact du dopage azote sur la structure de systèmes plus complexes de GST enrichis en Ge. Les résultats de cette thèse illustrent l'apport des différentes techniques analytiques et de leur combinaison à la compréhension fine de la structure et des mécanismes de cristallisation des matériaux à changement de phase.

Key Words : Mémoires à Changement de Phase, alliages GST enrichis en Ge, dopage Azote, Spectroscopie Infrarouge, Spectroscopie Raman, Diffraction des rayons X

List of abbreviations

AD	As-Deposited
ADF	Annular Dark-Field
AIMD	*Ab Initio* Molecular Dynamics
AIST	Ag-In-Sb-Te alloy
BEOL	Back-End-Of-Line
BJT	Bipolar Junction Transistors
CBRAM	Conducting Bridge Random Access Memory
DRAM	Dynamic Random Access Memory
DRF	Density Functional Theory
EDX	Energy-Dispersive X-ray analysis
EELS	Electron Energy Loss Spectroscopy
EXAFS	Extended X-ray Absorption Fine Structure
FCC	Face-Centered Cubic crystalline structure
FeRAM	Ferroelectric Random Access Memory
FET	Field Effect Transistor
FIB	Focused Ion Beam
FTIR	Fourier Transform Infrared Spectroscopy
FWHM	Full width in Half Maximum
GGST	Ge-rich GeSbTe
GGSTN	N-doped Ge-rich GeSbTe alloy
GST	GeSbTe alloy
HAADF	High-Angle Annular Dark-Field
HDD	Hard Disk Drive
HEX	Hexagonal crystalline stucture
IBA	Ion Beam Analysis
ICDD	International Centre for Diffraction Data
IR	Infrared
LA	Longitudinal Acoustic mode
LO	Longitudinal Optic mode
MD	Molecular Dynamics
MLC	Multilevel-Cell
MOSFET	Metal–Oxide–Semiconductor Field Effect Transistors
MP	Monkhorst-Pack mesh
MRAM	Magnetic Random Access Memory
NMR	Nuclear Magnetic Resonance
NRA	Nuclear Reaction Analysis
NVM	Non-Volatile Memory
OTS	Ovonic Threshold Switch
OxRAM	Oxide-based Random Access Memory
PBE	Perdew-Burke-Ernzerhof functional
PCRAM	Phase-Change Random Access Memory

PDF	Powder Diffraction File
PIXE	Particle Induced X-ray Emission
R vs T	Temperature-dependent Resistivity
RBS	Rutherford Back Scattering
ReRAM	Resistive Random Access Memory
RMC	Reverse Monte Carlo
SAED	Selected Area Electron Diffraction
SCM	Storage Class Memory
SGSTN	N-doped Sb-rich GeSbTe alloy
SLL	Superlattice-like
SSD	Solid State Drive
STAM	Static Random-Access Memory
STEM	Scanning Transmission Electron Microscopy
STT-RAM	Spin Torque Transfer Random Access Memory
TA	Transverse Acoustic mode
TEM	Transmission Electron Microscopy
TO	Transverse Optic mode
UV	Ultraviolet
VASP	Vienna *Ab initio* Simulation Package
VDOS	Vibrational Density of States
VIS	Visible
WDXRF	Wavelength Dispersive X-ray Fluorescence Spectroscopy
XANES	X-ray Absorption Near-Edge Structure
XAS	X-ray Absorption Spectroscopy
XPS	X-ray Photoelectron Spectroscopy
XRD	X-ray Diffraction
XRF	X-ray Fluorescence
XRR	X-ray Reflectivity

Introduction

In the digital era of the today's world, the rapid development and increasing number of electronic devices requires to handle huge amount of data. Indeed, the International Data Corporation predicts the amount of processed data to be to 175 zettabytes by 2025 [1]. The necessity to a store large amount of information in a limited space thus becomes increasingly crucial, leading to the development of innovative Non-Volatile Memory technologies (NVM) for both data storage and processing. Non-volatiliy of such technolgies provides the advantage that data storage does not need a constant power supply. The family of NVM significantly has expanded over the last years, using novel switching mechanisms, in order to achieve higher reliability, performance and scalability to the ultimate nanoscale level compared to the memory technologies present on the market. Among the innovative NVM candidates, the Phase-Change Memory (PCRAM) demonstrated to be the most promising one, fulfilling the increasing requirements in terms of higher densities and speed, lower power consumption and final device cost. Entering the market in the domain of stand-alone memories such as Storage Class Memory (SCM), PCRAM showed to be able to fill the gap between Non-Volatile storage (e.g., Flash and Hard-Disk Drives), while operating almost as fast as high performance Volatile Dynamic Random Access Memory (DRAM) devices. Recently, PCRAM has proved its maturity also for the embedded Non-Volatile Memory applications, demonstrating the potential for automotive grade applications or artificial intelligence systems.

The PCRAM device structure is relatively simple and consists of an active phase-change material sandwiched between two electrodes. The fundamental principle of PCRAM device is based on resistivity the change between an amorphous and a crystalline phase of the integrated phase-change material, allowing the non-volatile storage of the information in the device. The choice and engineering of the phase-change material plays a crucial role in tuning the PCRAM device performances. PCRAM device technology still faces technological challenges, in particular for embedded application demanding low power consumption and high temperature stability, such as the automotive industry. These challenges give rise to several objectives for material optimization. Among the main ones, we can name the improvement of the thermal stability of the phase-change material, thus the data retention and the reduction of the programming current of the PCRAM device. The most largely studied phase-change alloys comes from Ge-Sb-Te ternary system with $Ge_2Sb_2Te_5$ as the common reference alloy. While the material properties of $Ge_2Sb_2Te_5$ are not sufficient to achieve the requirements of embedded applications, the optimization of this alloy has shown excellent results in recent years. In particular, the most promising achievements concerning the improvement of the data retention were reported for Ge enrichment and for the Nitrogen (N) doping of $Ge_2Sb_2Te_5$ or other GeSbTe (GST) alloys. Although such optimized alloys enabled the introduction of phase-change materials in embedded PCRAM device demonstrating the outstanding performances reported in literature, the material structure and the crystallization mechanisms of such innovative phase-change materials still pose the questions, concerning:

- Structural arrangement of both amorphous and crystalline phases of Ge-rich GST alloys and the related structural changes upon applied thermal budget
- Crystallization mechanisms in Ge-rich GST alloys and their dynamics
- Effect of nitrogen doping on the structure and properties of Ge-rich GST alloys (e.g., formation of nitrogen bonding) and strucutral changes of the system upon applied thermal budget.

Some works have been reported recently on (N-doped) Ge-rich GST alloys, studying the Ge atomic diffusion and presenting the Ge and $Ge_2Sb_2Te_5$ phase segregation at higher temperatures (~400 °C) [2–4]. It was suggested that the system evolution is driven by primary nucleation and crystal growth of Ge phase in excess, followed by the crytallization of the GST cubic phase. The crystallized system was then described by large grains of GST in the matrix of small Ge nanocrystals. However, these structural investigations focus only on the analyses of the crystallization phase of Ge-rich GST alloys, provided by X-ray Diffraction and Transmission Electron Microscopy with Energy-Dispersive X-ray characterization techniques. Nevertheless, the structural changes may appear already in the amorphous phase of the material, far before the phase segregation and crystallization can be observed. Therefore, probing the amorphous phase along with the crystallization phase by various characterization techniques is required in order to complete the analyses of (N-doped) Ge-rich GST alloys.

This work focuses on the investigation of the structure and the crystallization mechanisms of innovative phase-change materials targeting high temperature stability. The thesis presents the characterization of two main groups of materials: a) Ge, Sb and Te elemental systems; b) Ge-rich GST alloys. Further, N doping effects are investigated in these materials, i.e, in both elemental and complex systems. The 100 nm-thick layers are characterized by combination of several characterization techniques, i.e., Raman and Fourier Transform Infrared Spectroscopy (FTIR), X-ray Diffraction (XRD) and Transmission Electron Microscopy with Energy-Dispersive X-ray Analysis (TEM-EDX), accompanied by Spectroscopic Ellipsometry, X-ray Absorption Spectroscopy (XAS) and by *"ab initio"* simulations. The understanding of material structure, bonding arrangements and phenomena during the amorphous-to-crystalline phase transition allows to highlight the key material characteristics responsible for higher thermal stability and thus for enhanced data retention of final PCRAM device. Also, it allows to identify the intrinsic material limits, opening new ways for material optimization for different PCRAM device applications.

Chapter 1 introduces the general principles of PCRAM technology. First, we present the technological characteristics and the desired performances of the PCRAM device. Further, we focus on the integrated phase-change material, describing the theoretical background related to different phases of the material, i.e., amorphous, crystalline and liquid phases, as well as the general physics of the crystallization mechanism. Ge-Sb-Te system is presented as the most common group of phase-change materials, introducing common reference alloys, i.e., binary GeTe and Sb_2Te_3 along with ternary $Ge_2Sb_2Te_5$. We further discuss the possible ways of GST alloys engineering either by changes in stoichiometry or by addition of other elements, allowing to enhance the material properties related to the final PCRAM device performances.

Chapter 2 presents the characterization of phase-change materials. It introduces the basic principles and the application of different characterization techniques, which are employed in this work, suitable for the investigation of both amorphous and crystalline phases of elemental systems and GST alloys. In this part, we present the advantages and the challenges of the different characterizations and we highlight the main structural information, which can be obtained by the material analysis. We demonstrate the practical application of these techniques on the known GST alloys. We present some results previously reported in literature, which provide the base of information for the investigation performed in the chapters 3 and 4 of this thesis.

Chapter 3 focuses on the Ge, Sb and Te elemental systems. We study undoped Ge, Sb and Te structures, analyzing the main structural features. We further follow their structural evolution upon N doping, highlighting the different effects of N in each elemental system. Moreover, the spectroscopic features related to the formation of X-N bonding (X = Ge, Sb or Te) are

identified. The experimental data are supported by *"ab initio"* simulations of related ideal nitride structures. The studies of the stability of both undoped and N-doped elemental systems as a function of temperature and time are performed, highlighting the remarkable stability of Ge-N bonds in N-doped Ge elemental system. This chapter provides the fundamental spectroscopic analyses of elemental systems doped with N, which can be further applied in the analysis of the effects of N doping in more complex systems, such as GST ternary alloys in PCRAM device technology, or generally inthe alloys based on Ge, Sb or Te elements.

Chapter 4 is dedicated to the investigation of undoped and N-doped Ge-rich GST alloys. First, the structure of undoped Ge-rich GST is described, using the comparison with reference $Ge_2Sb_2Te_5$. The structural evolution of both alloys is observed as a function of temperature, allowing the identification of main stable structural units in Ge-rich GST. The results provide a description of the overall crystallization mechanism in Ge-rich GST alloys. Further studies are performed on Ge-rich GST with large range of Ge enrichment in order to investigate the effect of Ge content. These studies highlight the enhanced or reduced effects of different competing phenomena, which occur during the structural evolution and following crystallization of the system, and their dependences on Ge content. Second, the investigation of N-doped Ge-rich GST alloys as a function of temperature and N content demonstrates the effect of N doping on the described structural evolution and crystallization mechanism and highlights the formation and the role of Ge-N bonds in the alloy. This chapter contributes to the description of the structure and bonding arrangements in GST alloys and provides better understanding of bonding reorganization and crystallization mechanism, which gave rise to long debates until today.

Finally, chapter 5 provides the general conclusions, highlighting the main results of this work and suggesting some perspectives for further material investigation and characterization of GST alloys.

Chapter 1

Phase-Change Memories: Principle and Technology

Phase-Change Memory (PCRAM) employs an innovative functional concept relying on the reversible transition between amorphous and crystalline phase of an integrated chalcogenide phase-change material sandwiched between two electrodes. This reversible phase transition is achieved by Joule heating and it is accompanied by large contrast in electrical resistivity. Owing to this simple concept and the oustanding performances, the PCRAM technology have been attracting a lot of attention, becoming the most promising candidate for the next generation of Non-Volatile Memory technology.

In this chapter, we provide an overview on PCRAM technology and integrated phase-change materials. We first first introduce the current NVM technologies and we highlight the outstanding qualities of PCRAM. After, we describe the principles and functionality of PCRAM device, its technological characteristics, applications and major challenges. In the second part, we focus on the phase-change material integrated in the PCRAM device. We introduce the general concepts of the phases as well as the transition mechanisms involved in the phase-change phenomena. We introduce the most common materials from Ge-Sb-Te system (i.e, binary GeTe and Sb_2Te_3 and ternary $Ge_2Sb_2Te_5$ alloys) and we describe the possibilities of material engineering by stoichiometric variations and elemental doping, allowing to overcome the technological challenges of PCRAM device.

1.1 Emerging Non-Volatile memories

Semiconductor memory has always been an indispensable component of modern electronic systems enabling to store the data either in volatile or non-volatile way. Volatile memories need the constant power supply to hold the stored information. On the contrary, Non-Volatile Memories (NVM) retains the stored information even when the power supply is turned off. The main representatives of Volatile Memories are Dynamic Random-Access Memory (DRAM) and Static Random-Access Memory (SRAM), while Flash Memories (NOR and NAND) belong to the NVM group, both representing the dominant solid-state memory technologies over the last decades.

The family of NVM significantly expanded over the time in an effort to fulfill the changing trends of the market and the increasing requirements in terms of higher densities and speed, lower power consumption and final device cost [5]. Intensive material research allowed the development of several candidates for new emerging NVM technologies (Fig. 1.1) using innovative concepts for the data storage, such as the direction of the magnetic orientation (magnetic memories MRAM, spin torque transfer memories STT-RAM), the electric polarization of a ferroelectric material (ferroelectric memories FeRAM) or the resistance changes (resistive memories ReRAM: conducting bridge memories CBRAM, oxide-based memories OxRAM, phase-change memories PCRAM) [6,7]. While some candidates are mature enough to be already present on the market, others are still in development or exploration phase. Nevertheless, the emerging NVM technologies are considered as the possible replacement for the dominant solid-state Flash memories. Emerging NVM takes the advantage of higher operation speed, lower programming voltages, higher scalability and back-end-of-line (BEOL) integration [6,8–11]. Today, two domains are mainly focused for emerging NVM applications:

- Stand-alone applications, in particular the Storage Class Memory (SCM), filling the performance gap between volatile DRAM and non-volatile NAND in memory hierarchy;
- Embedded applications, in which the memory device is directly integrated on the chip during the manufacting process.

Along with the development of new NVM technologies, the market for the memory devices also expanded from computing to wider range of applications, such as automotive micrcontrollers, artifitial intelligence, neuromorphic computing, photonics or information technology in health care [8,11–14]. Moreover, new memory devices based on organic and polymer materials are investigated, providing the new class of NVM technologies with large flexibility, suitable for applications in different kinds of flexible electronics [7,8].

PCRAM, in particular, has demonstrated to be the most promising among the emerging NVM technology. STTRAM features high switching speed (<10 ns) and high endurance (>10^{12} cycles) however, suffers from lower scalability, worse data retention and problems with thermal budget for BEOL integration. ReRAM provides good scaling ability; however it demonstrates lower endurance (10^6 cycles), high read current noise and poor reliability (low data retention due to programming current). In comparison, PCRAM demonstrated relatively high endurance ($10^9 – 10^{12}$) when still maintaining high switching speed (<10 ns). PCRAM features much higher resistance change between the two memory states than MRAM, while providing lower resistance noise than ReRAM [7,8,10]. Moreover, PCRAM takes advantage from good scalability owing to both 3D integration and multilevel cell storage and high temperature data retention achieved by material optimization, which is decribed more in detail in the section 1.3.3. The maturity of PCRAM is demonstrated by their successful introduction on the market in both SCM and embedded application, discussed in the section 1.2.5.

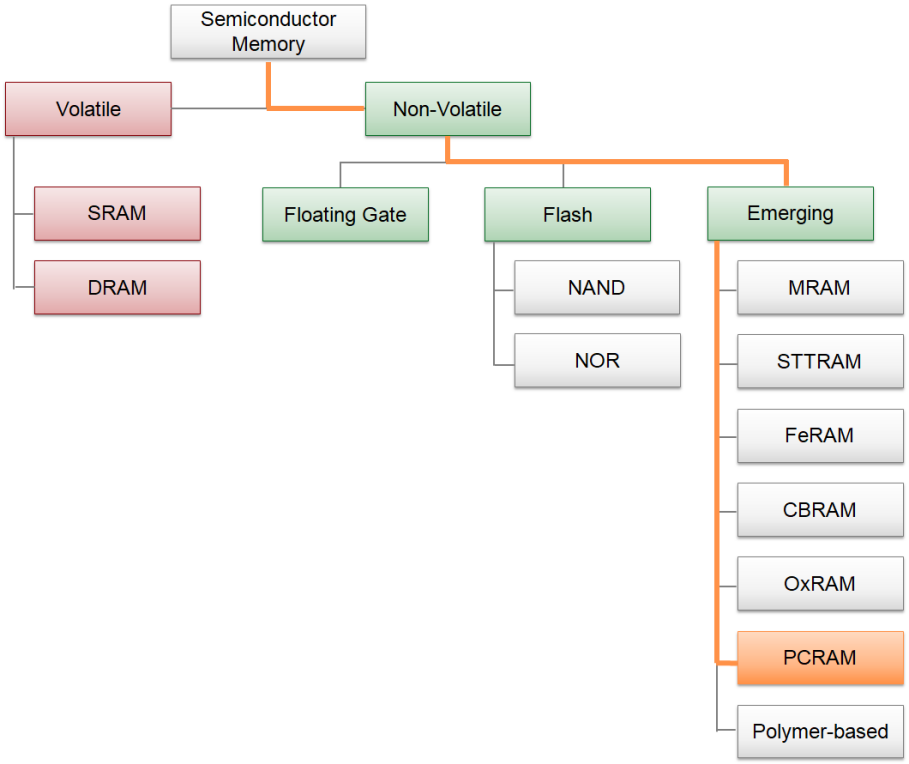

Fig. 1.1: Flow chart of the semiconductor memory classification, highlighting the PCRAM between emerging Non-Volatile Memory technologies.

1.2 Phase-change Memories

Phase-Change Memories (PCRAM) are considered today as the most promising among the emerging NVM technologies. Their origin dates back to late 1960s to the research on the electronic properties on amorphous Te-As-Si-Ge chalcogenides made by Ovshinski [15]. He demonstrated the significant contrast in optical and electronic properties between the amorphous and crystalline phases of the alloys and suggested to exploit such properties for possible data storage. The first attempts to develop the PCRAM device continued in early 1970s, owing to the rapid expansion of computer applications. However, these first PCRAM devices showed slow transition speed and high programming currents resulting in huge power consumption during the programming operations. For these reasons, they were never commercialized. The interest in PCRAM device development was renewed from 1990s with the development of Ge-Sb-Te (GST) alloys, in that time exploited in phase-change technology for rewritable optical disks applications (CD's, DVD's, Blu-Ray disks). Ge-Sb-Te alloys showed the ability to switch between the amorphous and crystalline phase in tens of nanoseconds, several orders of magnitude faster than former PCRAM device prototypes from 1970s. The renewed approach for the development of PCRAM device was based on electrically induced phase change in the integrated GST alloy and the association of the stored information to the resistance values of the amorphous and the crystalline phase. In order to exploit the PCRAM in solid-state memory devices, the memory element (PCRAM device) must be coupled with a selecting device, which allows to select the individual memory element for reading and writing. Metal–Oxide–Semiconductor Field Effect Transistors (MOSFETs), Bipolar Junction Transistors (BJTs), Diodes, and recently also Ovonic Threshold Switch (OTS) have been proposed as suitable selectors [5,16,17].

1.2.1 PCRAM principle and structure

The structure of the PCRAM device is based on a thin layer of a phase-change material, which is sandwiched between two electrodes (Fig. 1.2). The fundamental principle of the PCRAM device is the reversible transition between amorphous and crystalline phase of the phase-change material. The application of electrical pulses on the bottom electrode produces the Joule effect, providing a precisely controlled amount of heat and reaching local temperature increase in the integrated material, thus inducing the phase change.

Starting from the amorphous phase, an applied electrical pulse increases the temperature in the active region of the material above the crystallization temperature (T_x), therefore, the crystallization process occurs (i.e., SET operation). The applied pulse shall be long enough to achieve the crystallization of the entire amorphous material (Fig. 1.3). Melt-quenching process is employed for material amorphization (i.e., RESET operation). First, a high and sharp electrical pulse induces the melting of the phase change material, i.e., the temperature within the PCRAM device reaches above the melting temperature (T_m) of the integrated material (usually at about 600 °C for common phase-change materials). Once the phase-change material is molten, it must be rapidly quenched below glass transition (T_g) temperature in order to reduce the atomic mobility and preserve the disordered amorphous phase. Both amorphous and crystalline phases are stable and thus they are used to store the binary information, i.e., logical states 0 and 1, corresponding to amorphous phase and crystalline phase, respectively. The amorphization process is usually very fast (few tens of picoseconds). On the contrary, the crystallization takes typically much longer (tens to hundreds of nanoseconds) and therefore becomes a crucial step of the writing process.

The phase transformation is accompanied by large electrical and optical contrast. While the optical contrast (i.e., change of the reflectivity) is widely employed in the optical data storage, the electrical contrast (i.e., change of resistivity) is used to store the information in case of the PCRAM device (Fig. 1.2). The amorphous phase is high-resistive, reaching the resistivity values of three or four order of magnitude higher than low-resistive crystalline phase [17–19]. The resistance state of the PCRAM device is read with a sufficiently small current pulse (i.e., READ operation), which does not modify the programmed state.

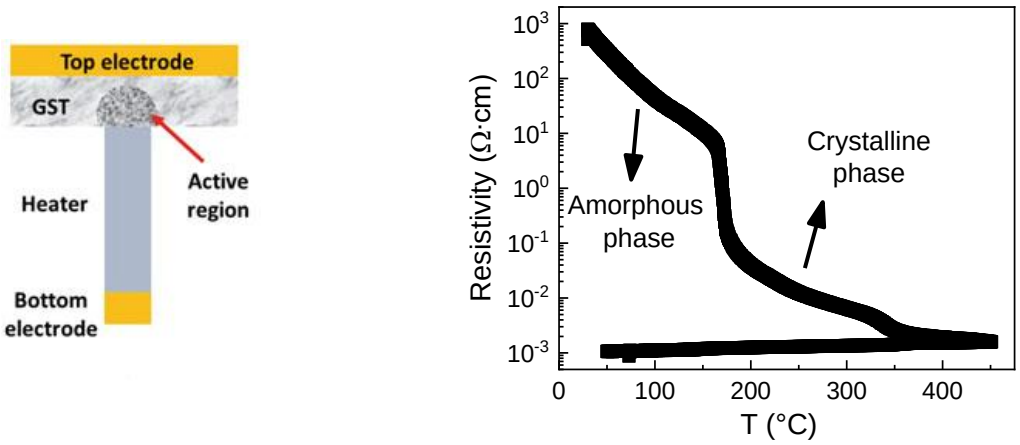

Fig. 1.2: (left) The cross-section schematic of the PCRAM device with a phase-change material (GST) sandwiched between top and bottom electrode, highlighting the active region in the GST material above the heater; (right) Resistivity vs Temperature measurements demonstrating the phase transition from high-resistive amorphous phase to low-resistive crystalline phase of GST material [5].

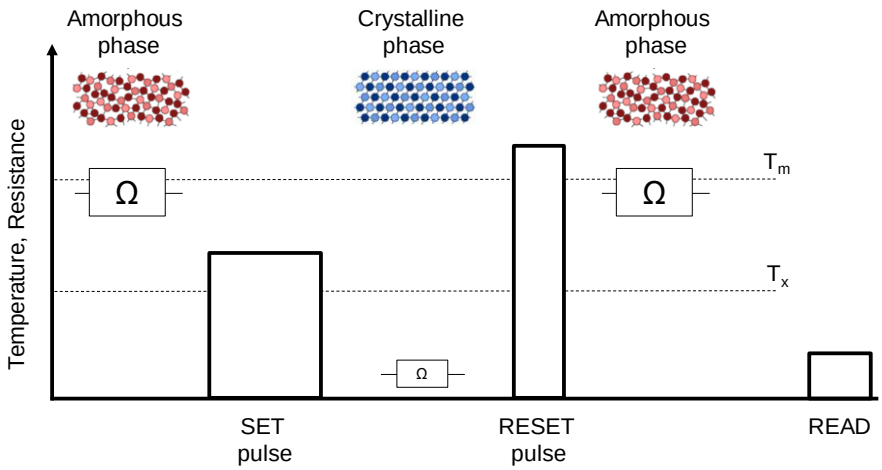

Fig. 1.3: Illustration of PCRAM device operational principle: Crystallization requires a long current (SET) pulse reaching the temperature in the phase-change material above its temperature of crystallization (T_x). Amorphization is achieved by a short intense (RESET) pulse melting the material, (i.e., increasing the material temperature above the melting point T_m) followed by fast cooling. Low current pulse is applied to perform READ operation [9].

1.2.2 Threshold switching

The threshold switching represents a key phenomenon in electrical characteristics of amorphous chalcogenide materials. Current-Voltage curve (Fig. 1.4) illustrates the response of a PCRAM device in its amorphous phase to an applied voltage. For small voltages (i.e., subthreshold region), only a marginal current flows through the PCRAM device. High resistivity of the amorphous state in this region leads to low heat dissipation in the device, which makes material crystallization at such small voltages practically impossible. At a specific voltage, called Threshold Voltage (V_{th}), the amorphous phase undergoes an abrupt change of conductivity, i.e., the electronic threshold switching. Longer pulse application then produces enough Joule heating to crystallize the phase-change material. The threshold switching phenomenon leads to abrupt change of conductivity in the amorphous material, enabling much larger current flowing in the PCRAM device, which allows the SET and RESET programming of the PCRAM device at reasonably low voltages [6].

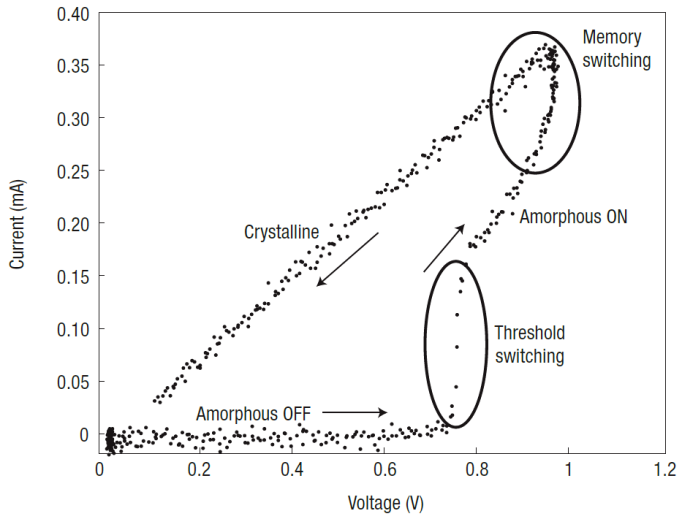

Fig. 1.4: Current-voltage curve of a phase-change material initially in the amorphous phase. Only a marginal current flows at small voltages (amorphous OFF). Abrupt change in conductivity is achieved at the threshold switching, allowing much larger current flow in the material (amorphous ON). Longer voltage application leads to the material crystallization (Memory switching) [20].

1.2.3 Technological characteristics of PCRAM

As described in the section 1.1, the PCRAM device features promising performances among the emerging NVM technologies. In particular, the PCRAM provides:

- high contrast between RESET and SET states
- high switching speed
- high data retention
- high endurance
- low programming current

High resistivity contrast (usually three or four orders of magnitude) between the RESET and SET states is required in order to distinguish the recorded information during the read operation. Data retention performance is driven by the stability of the amorphous phase and the T_x of the phase-change material. The materials with low T_x (i.e., low stability) may undergo a spontaneous crystallization and therefore would not be able to guarantee the code integrity. Resistance drift represents another issue concerning the amorphous phase stability. This phenomenon is assigned to the structural relaxation of the amorphous phase upon ageing in time (i.e., the reduction of local structural defects, described in the section 1.3.1), which leads to changes in electrical properties and causes the increase of the amorphous phase resistance [21,22]. Although the resistance drift is likely related to structural relaxation, the physical mechanisms are not clear and structural studies or *ab initio* simulations are lacking. The reliability and the endurance of the PCRAM device is expressed by number of performed write/read cycles (cyclability). Repeated cycling induces structural changes in the integrated phase-change material, such as the elemental segregation, the formation of element-rich / -poor regions near one of the electrodes and the void formation over the bottom electrode. These changes represent the failure mechanisms in PCRAM, when the device can no longer be switched between the resistive states, thus leading to poor endurance.
PCRAM can be relatively demanding in terms of energy consumption. Reset programming current should reliably achieve the melting of the active region of the device. The reset current is determined by various material properties (e.g., melting temperature, thermal conductivity) as well as by the PCRAM device structure. However, high programming current values impose stringent requirements on integrated selector device and its size (i.e., larger selector area). The reduction of the programming current is therefore necessary in order to achieve both high memory array density and low power consumption in PCRAM device, and it represents one of the key challenges for large adoption of the PCRAM technology [5,23].

The PCRAM device performances demonstrate to be closely linked with the properties of the integrated integrated phase-change material. The PCRAM device performances associated with the specific material specific material properties are summarized in
Table 1-I. However, the requirements on PCRAM device performances are sometimes conflicting. The relationship between the thermal stability and the switching speed represents a typical example. The increase of the crystallization temperature of the phase-change material and hence the stability of the amorphous (RESET) phase can be achieved by the optimization of the material composition (changes in stoichiometry, doping). However, this change is accompanied by an increase of the crystallization time, i.e., SET speed, which needs to be taken into account. The optimization of material properties and hence PCRAM device performances thus needs to find a necessary compromise.
The PCRAM performances and their challenges also depend on particular PCRAM application requirements. Indeed, the requirements in stand-alone applications are more oriented to endurance and switching speed, while the embedded applications are much more stringent in terms of the data retention at high temperatures, as listed listed in
Table 1-II.

Table 1-I: Relation between the performance of PCRAM device and the properties of integrated phase-change material.

PCRAM performance	Phase-change material property
High data retention	- High T_x and thermal stability of the amorphous phase
High switching speed	- Fast crystallization
High cyclability	- Equvalent material density of amorphous and crystalline phase - Material stability (reduced elemental migration and material segregation)
Low power consumption	- Moderate T_m - Low thermal conductivity

Table 1-II: PCRAM device performance requirements for stand-alone data storage and embedded memory applications [19,24,25].

	Stand-alone data storage	Embedded memory
Applications	Storage Class Memory (SCM)	Automotive industry (microcontrollers)
Requirements	- Operation temperature: 80 °C - Endurance: 10^9 cycles - Switching speed: orders of ns	- Temperature budget of 400 °C for 60 min (BEOL integration) - Preservation of programmed information during the soldering step at 260 °C for 2 min - Data retention: 10 years at 150 °C

1.1.1.1 PCRAM device scaling

Scaling of the device dimensions is an important step to increase the storage density. PCRAM technology showed to be a good candidate featuring such high scalability, allowing the device scaling down to nm size. However, the device scaling implies various technological challenges for both the device cell architecture and the integrated phase-change material. From the device point of view, carefulel ectrical and thermal engineering is necessary. Concerning the integrated phase-change material, it is important to evaluate the corresponding changes in material properties as a function of film dimensions: crystallization speed, thermal stability of amorphous phase and related crystallization temperature, melting temperature, thermal conductivity, electrical resistivity of both phases and threshold voltage [5,17].
Indeed, the increase of the crystallization temperature and hence the improved stability of amorphous phase was observed in some phase-change alloys for the films thinner than 10-15 nm. The choice of substrate and encapsulation materials starts to play an important role, as the influence of surfaces and interfaces on the crystallization behavior increases along with the importance of heterogeneous nucleation. For example, some metal encapsulation layers were found to reduce the crystallization temperature likely due to metal-induced

crystallization [17]. The reduction of melting temperature was demonstrated in GeTe thin layers, highlighting lower melting temperature of more than 100 °C for layer thicknesses of <10 nm, when compared to bulk. The decrease of the melting temperature was also reported for $Sb_{70}Te_{30}$ layers with the film thickness reduced from 70 to 10 nm [5]. The reduction of melting temperatures (while maintaining high crystallization temperatures) is technologically favorable, leading to reduced power requirements for the PCRAM device. The thermal conductivity values were also found to decrease with material thickness, owing to which the heating losses in the devices are reduced [17].
The ultimate scaling limit is reached for the layer thickness at which the phase change in the material does not occur anymore. Films as thin as 1-2 nm were demonstrated to be still success fully crystallized, highlighting the capability of phase-change materials to scale down to such small dimensions. Moreover, phase-change material nanowires and nanoparticles are investigated, likely providing further scaling possibilities [5,19,26–28].

1.2.4 PCRAM device engineering

Although the PCRAM demonstrates the promising performances to be competitive on the market, their optimization is further necessary in order tofulfill the requirements of the as largest applications range as possible. Both the PCRAM device design and the integrated phase-change material can be engineered in order to provide the best final performances and to exploit the device scalability. Various cell design structures are suggested, balancing the thermal efficiency and the electrical characteristics. The reduction of the RESET programming current represents, in particular, one of the main challenges in PCRAM technology, as discussed in the section 1.2.3. The continual material research focuses on improving the phase-change material properties in terms of fast crystallization, high thermal stability and reduced material segregation. In the following, we briefly present these two key approaches of the PCRAM device engineering.

1.2.4.1 Cell design optimization

The PCRAM cell design requires the engineering of each element involved, i.e., top electrode, bottom electrode and/or heater, dielectric and phase change material in terms of material composition, thickness and the interaction and contact area at the interfaces.
In general, the cell architectures are divided in two main groups: built-in heater and self-heating PCRAM. In the built-in heater structure, the contact area between the bottom electrode and phase-change material is reduced by using a heater element generating the heating necessary for the phase transition. Fine material engineering of the heater element is required as its material needs to be compatible with both bottom electrode and phase-change material. The self-heating architecture relies on the Joule heating generated directly inside the phase-change material. Its advantage is simpler structure and the absence of mechanisms related to the heater element; however, self-heating structures may require higher current densities. Some examples of different PCRAM device structures are shown in Fig. 1.5 and the thorough description of their mechanism can be found in [5,26,29–31].

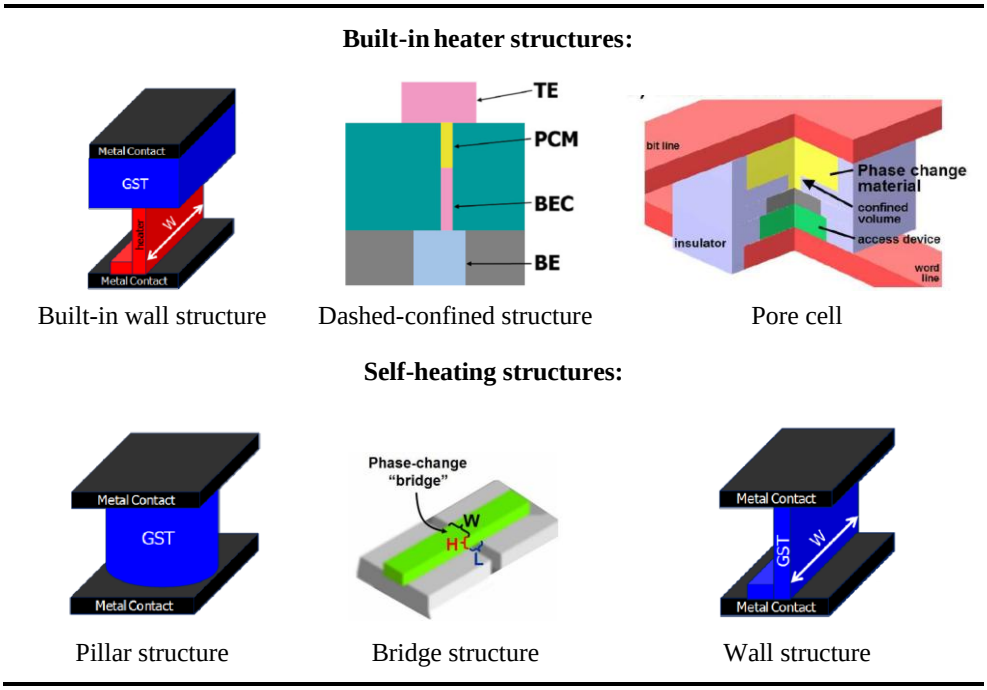

Fig. 1.5: Schematic representation of different PCRAM device architectures: (top row) built-in heater structures and (bottom row) self-heating structures [19,32–34].

The heating efficiency can be improved by varying the cell geometry and by the development of new device structures. As an example, Fig. 1.6 shows the basic PCRAM device structure, varying the heater length (L_h) and the phase-change material thickness (L_c), highlighting the calculated temperature map within the PCRAM device. Keeping the diameter of the heater constant, the optimal geometry was found for well-balanced L_h and L_c values, where the peak temperature is maximized at the interface between the heater and phase-change material. On the contrary, short and long L_h result in excess heating either of the phase-change material or of the heater, respectively [23].

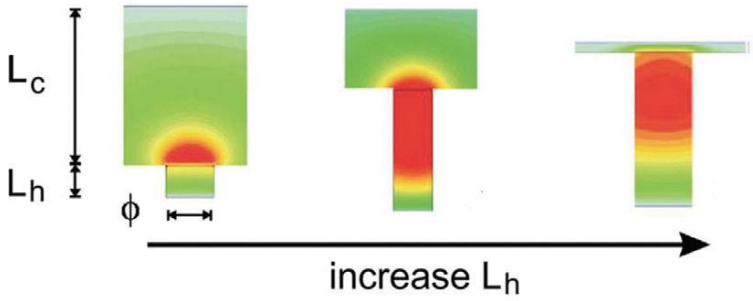

Fig. 1.6: Temperature maps in basic PCRAM cells varying the bottom electrode length (L_h) and phase-change material thickness (L_c). The sum L_h+L_c remains constant [23].

Considering the PCRAM device architecture, the interfaces between the electrodes and the phase-change material represent one of the crucial points. Good adhesion between the electrodes and integrated phase-change material needs to be achieved. On the contrary, the interaction between the electrodes and phase-change material, in particular the interdiffusion, must be avoided. Careful engineering of the interface between the bottom electrode (or heater) and the integrated phase-change material is particularly necessary, as it is the region where the phase-change material is repeatedly melted and hence experiences the highest thermal stress during PCRAM device programming. Void formation and elemental

segregation resulting in element-rich/-poor regions near electrodes are the common failures of the PCRAM device upon cycling. The importance of careful interface engineering even increases with the device scaling and thus the decreased thickness of the integrated phase-change material, as described in the section 1.1.1.1.

1.2.4.2 Phase-change material engineering

The PCRAM device performances are closely linked with the key properties of the integrated phase-change material, as presented in the section 1.2.3. For an identical PCRAM cell design and size, the optimization of the phase-change memory material is the first option to improve the device performances. The variation of the material stoichiometric composition, substitution by other elements or doping by additional elements are the possible ways to achieve the modifications of both thermal (e.g., T_x, T_m) and electrical (e.g., resistivity) properties of the integrated material and hence of the PCRAM device performances. The phase-change material engineering is described more in detail in the section 1.3.3.

1.2.5 Applications, trends on the market

In the last decade, the PCRAM technology has demonstrated its high industrial potential. Owing to the unique programming mechanism, PCRAM provides a wide set of interesting performances, such as fast programming speed, high endurance and excellent scalability [8,10,35], described in the sections 1.1 and 1.2. 3D integration of PCRAM can further increase its performance in terms of storage density. Indeed, owing to the two-terminal device structure, PCRAM can be implemented in crossbar architectures including the direct integration of OTS selecting device [7,23,36,37] (Fig. 1.7). Another prominent feature of PCRAM technology is the capability of multilevel-cell (MLC) storage [38]. The large resistivity contrast between the crystalline and amorphous phases of the integrated phase-change material allows the introduction of intermediate resistance states between the SET and RESET states. The intermediate resistance levels can be programmed by carefully controlling programming pulses, i.e., by varying the volume of the amorphized part of the phase-change material. Although the MLC storage in PCRAM device is still challenging, a reliable MLC storage of 4-level data has been successfully demonstrated [39].

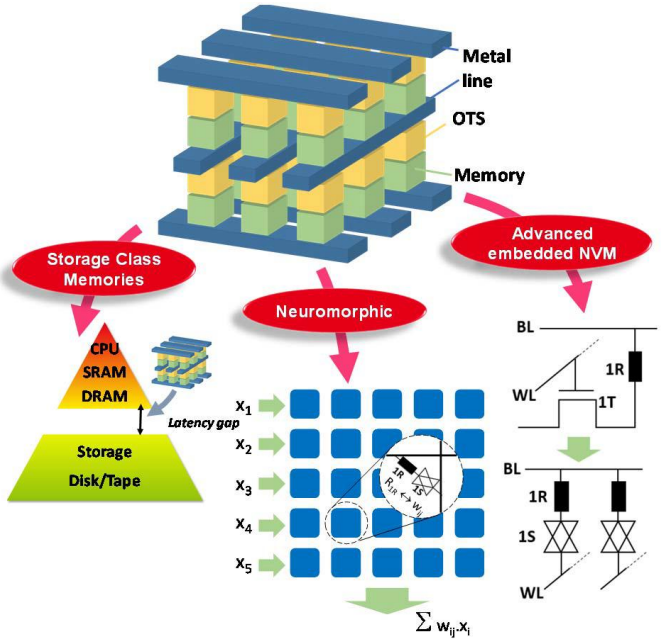

Fig. 1.7: 3D crossbar array architecture of the PCRAM cell with the OTS selector and possible application for Storage Class Memories, Embedded applications and Neuromorphic systems [37].

The maturity of PCRAM technology has been proven by its commercialization in the field of stand-alone SCM filling the performance/cost gap between memory and storage technologies (Fig. 1.8). Indeed, the memory technology, represented by volatile SRAM and DRAM, features high access speed but also high cost. On the other side, the storage class elements include Flash memories with hard disks (Solid State Drive (SSD) or Hard Disk Drive (HDD)), which are non-volatile with lower cost and slower access speed. In 2015, Intel and Micron developed 3D XPoint Memory technology, integrating the PCRAM (based on GST alloys) and OTS in crossbar arrays. This technology was later commercialized under the brand name Optane™ (Fig. 1.9) [40]. It demonstrated to be up to 1000 times faster and to have up to 1000 times greater endurance than NAND, while being ten times denser than DRAM [41]. Recently, the 2nd gen. XPoint Memory has been released [40,42].

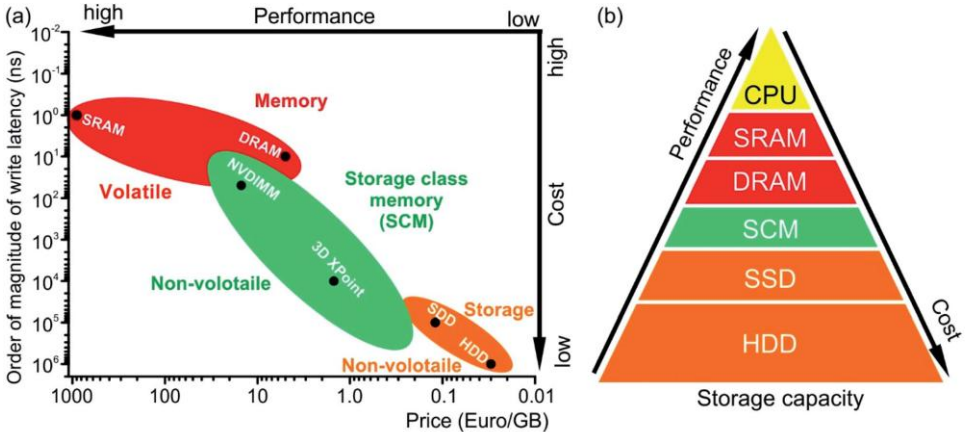

Fig. 1.8: (left) Write latency as a function of the cost for different volatile and non-volatile memories; (right) Memory hierarchy highlighting the relationship between performance, cost and storage capacity. The PCRAM as a Storage Class Memory (SCM) can fill the gap between memory and storage elements [43].

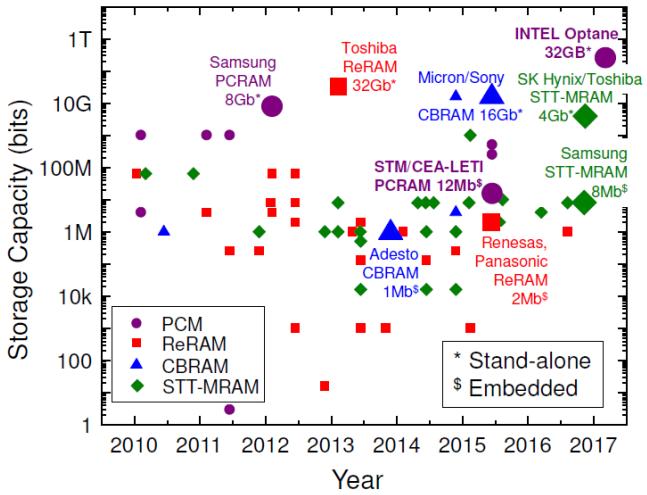

Fig. 1.9: The evolution of the storage capacity over the last decade for different types of NVM used in stand-alone and embedded applications. Intel Optane with storage capacity of 32 GB represents the stand-alone PCRAM. The 12 Mb PCRAM illustrates the development of the field of embedded PCRAM, achieved by STM/CEA-Leti [35].

Embedded applications become another domain, in which the PCRAM has already demonstrated its potential. PCRAM shows the advantage compared with the conventional Flash memory in terms of scalability and the possibility of BEOL integration. On the contrary, high-temperature data retention represents a major challenge for the PCRAM in embedded applications. Indeed, in addition to 10 years data retention at 85 °C, embedded

memory application requires the compatibility with the soldering step of the memory chip on the printed circuit board (thermal budget of 260 °C for 2 min). The automotive applications have even more stringent specifications, requiring several years of data retention at 150 °C. An optimization of GST phase-change alloys by increasing the Ge content brought promising results in matching the target data retention temperature for the PCRAM device. Although some challenges still need to be overcome (e.g., programming current, crystallization speed, resistance drift) [10], the first successful integration of PCRAM in 28nm FD-SOI technology for an automotive microcontroller chips has been recently demonstrated by STMicroelectronics (Fig. 1.9) [44,45].
A quite novel field for PCRAM application can be found in neuromorphic computing systems [12,14,46,47]. In a conventional von Neumann computing system architecture, the processor is separated from the main memory (by von Neumann bottleneck), limiting the system in time and energy as the data are moved back and forth between the two units (Fig. 1.10). By contrast, novel non-von Neumann architecture in computing systems is proposed, inspired by the neural network of human brain. In the non-von Neumann scheme, the computing is done at the location of the data, i.e., the synaptic weights can be stored and adjusted directly in memory. The PCRAM device can provide the desirable characteristics, such as rapid, low-power programming of multiple levels, adequate data retention and high endurance. Moreover, the good scalability and the PCRAM device integration in dense crossbar arrays provide a possible path implementing highly efficient neuromorphic computing systems.

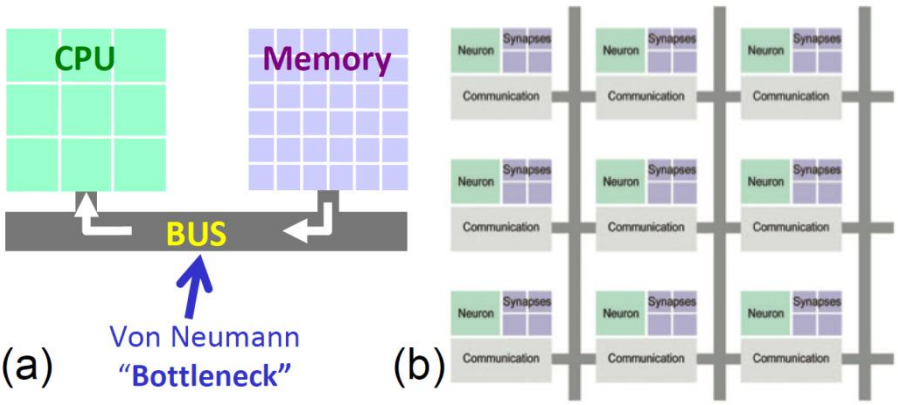

Fig. 1.10: a) Von Neumann architecture of the computing system with a processor (CPU) and memory separated by Von Neumann bottleneck; b) Non-Von Neumann architecture, where the computing is done directly in data location, inspired by human neural network [46].

1.3 Phase-change materials

Phase-change materials are mostly amorphous chalcogenides, usually Te-based alloys, which can undergo reversible structural changes accompanied by large optical and electrical contrast. These contrasts upon phase transition along with the threshold switching mechanism (described in the section 1.2.2) were first observed in the As-Te-In and As-Te-Se alloys in 1960s and such materials were suggested for use in memory devices [17]. A major breakthrough was reached in early 1990s by the exploration of alloys from Ge-Sb-Te ternary system, in particular the alloys lying on the pseudo-binary line between GeTe and Sb_2Te_3. These alloys showed large optical and electrical contrast and relatively fast phase transition in comparison with the previously studied alloys, leading to the rebirth of PCRAM technology. Another family of phase-change materials was based on compositions around the eutectic Sb_2Te. A particular attention was paid to Ag/In-doped Sb_2Te alloys (AIST) which found a wide use in optical data storage systems (DVD and Blu-Ray disks) [20,48–52]. Moreover,

non-chalcogenide materials based on Ge-Sb [53,54] and Ga-Sb [55–57] alloys were also found to exhibit the phase-change behavior.
The development of new phase-change materials suitable for memory applications is still ongoing. Stoichiometry deviation and element substitution/doping have proven to be effective methods to modify the material properties of GST alloys. Partial or complete substitution of Ge and Sb by other elements from the same groups (In, Bi, Si, Sn) was investigated [58–63]. Light elements (C, N or O) [64–67] showed to be promising candidates for doping the GST alloys. Diverse transition metals (e.g., Mo, Ni, Zn, Cd, Cu, Ag) [68–75] were also studied as possible doping elements. Moreover, new promising ternary materials were suggested. For example, a particular interest has been recently paid to CrGeTe alloys that feature an inverse resistance change upon crystallization (i.e., low resistance of amorphous phase and high resistance of the crystalline phase) compared to the common GST alloys [76,77].
A particular attention is paid especially to Ge enrichment and nitrogen doping of GST alloys, which demonstrated to greatly increase the temperature of crystallization and thus to improve the thermal stability of these alloys. These improvements are particularly interesting for PCRAM device in embedded applications and their stringent requirement on data retention over the extended temperature range. Both Ge enrichment and N doping are discussed more in detail in the section 1.3.3.
Although the phase-change materials are mostly employed in promising PCRAM, their applications are much wider. Taking advantage of the high optical contrast upon phase transition, the phase-change materials were found to be suitable for multiple applications in optical and photonic devices, such as optical modulators, reconfigurable metasurfaces or tunable absorbers [13,78–82].

1.3.1 Phase-Change Material structure

The PCRAM device functionality is based on phase transitions of the integrated phase-change material, as presented in the section 1.2.1. Therefore, the general concepts of the involved phases, i.e., liquid, amorphous and crystalline phase, as well as the transition mechanisms need to be introduced.
The phase-change process in the alloys can be described on the basis of glass formation concept (Fig. 1.11). When a melt (i.e., liquid phase) is quenched, it can solidify to form either a crystal or a glass, depending on the cooling rate. At a low cooling rate, the liquid solidifies creating the crystalline phase at the T_m, which is characterized by sharp discontinuity of the thermodynamics variables such as Enthalpy (H), Entropy (S) and molar Volume (V) of the system. On the contrary, a sufficiently fast cooling rate allows to avoid the crystallization and to transform the melt into a supercooled liquid below the T_m. The rapid temperature decrease is accompanied by large viscosity increase until the critical point called glass transition temperature (T_g), at which the supercooled liquid transforms into a glass. The atomic mobility becomes too small to allow the structural rearrangements required to reach the equilibrium and the material remains in frozen disordered state. T_g is commonly defined as the temperature, at which the viscosity equals $1 \cdot 10^{12}$ Pa·s and in general, T_g is roughly reached at ~2/3 T_m.
The obtained glass is out of its thermal equilibrium and subject to ageing effects, i.e., the glass structure undergoes relaxation processes as a function of time, reducing the local defective structures produced by the particular quenching history and moving the system towards the equilibrium conditions (lower entropy values and more efficient use of space) [16]. These structural relaxation processes affect the stability of the amorphous phase of the material in the PCRAM device, causing the resistance drift, discussed in the section 1.2.3.

The glass formation is strongly connected with the temperature-dependence of the viscosity η of a material. A glass-forming liquid is called as strong when following an Arrhenius-like behavior:

$$\eta = \eta_0 \, e^{\frac{\Delta E_A}{k_B T}} \tag{1.1}$$

where ΔE_A represents the activation energy for viscosity, k_B is the Boltzmann constant and η_0 is the high temperature limit of η. Glass-forming liquids possessing softer interatomic interactions (i.e., ionic, van der Waals) are called as fragile and display more complex behavior represented by bowed T-variation of viscosity leading to a high activation energy near T_g (Vogel-Tamman-Hesse-Fulcher behavior) [16]. The fragility index m is introduced as a measure of the deviation from the Arrhenius-like behavior. Several studies correlated the fragility index with crystallization behavior, showing that the rate of structural ordering accelerates near T_g for fragile liquids [83–86]. From this point of view, phase-change materials with rather a fragile-liquids behavior may appear favorable.

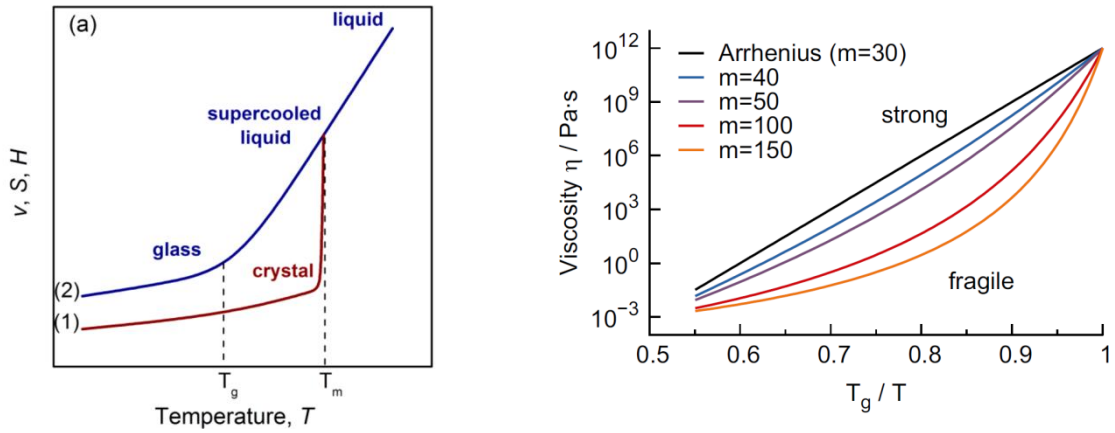

Fig. 1.11: (left) Temperature dependence for the molar Volume (V), Entropy (S) and Enthalpy (H) of glasses and crystals. Starting from the liquid phase, an abrupt decrease of the values is observed at melting temperature (T_m) in case of crystal formation, while gradual decrease of the values continues until the point of glass transition temperature (T_g) in case of glass formation; (right) The temperature dependence of viscosity highlighting the Arrhenius-like behavior for strong liquids. Steeper dependence at T_g is characteristic for fragile liquids, the deviation from Arrhenius-like behavior is indicated by fragility (m) [84,87].

1.3.1.1 Glass forming tendency

The attempts to search for the optimal glass forming compositions and to predict the properties of glass networks led to the development of the bond constraint theory, which was introduced in late 1970s [88]. This theory describes the rigidity of an amorphous covalent network based on its mean atomic coordination. Considering the liquids constrained only by bond-bending and bond-stretching interactions, the number of mechanical constraints per atom n_c can be computed. If n_c~3, corresponding to the degrees of freedom per atom in 3D space, the glass is optimally constrained and glass formation with minimal enthalpic changes can be expected. Based on the number of constraints n_c, three distinct types of glasses are distinguished: flexible (floppy) (n_c<3), intermediate (n_c~3) and stress rigid (n_c>3) [16,84,89].
The relation between the number of contraints n_c and the coordination number r [84] follows the equation:

$$r = \frac{2}{5}(n_c + 3) \tag{1.2}$$

For the ideal glass with n_c~3, the average coordination number r equals 2.4. The average coordination r is characteristic for an atomic species. Changes in the glass stoichiometry therefore lead to the modification of r and consequently also of the glass rigidity.
The investigation of the relationship between the glass rigidity and the temperature-dependence of the viscosity (strong-fragile behavior) of the glass forming liquids was presented in [89]. It shows that optimally constrained glasses (i.e., intermediate) give rise to strong glass-forming liquids, for which an easy glass formation is expected. On the contrary, both floppy and stressed rigid glasses are fragile glass-forming liquids.
The bond constraint theory was employed to interpret the XAS data from GST alloys in [90,91], demonstrating that the common stoichiometric GST alloys belong to intermediate region, i.e., they are perfect glasses. However, constraints algorithms based on molecular dynamics (MD) simulations were later developped and applied to GST alloys, highlighting only two regimes in Ge-Sb-Te ternary diagram without an intermediate region. While the small region of Te-rich alloys is described as flexible, the vast majority of GST compositions belong to stress-rigid regime. The commonly used GST phase-change alloys lying on the GeTe-Sb_2Te_3 tie-line belong to this second category (Fig. 1.12) [92].

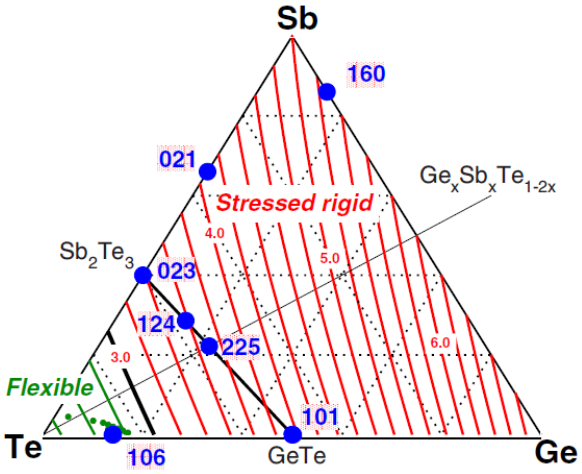

Fig. 1.12: Ternary diagram of Ge-Sb-Te phase-change alloys highlighting the regions of flexible and stress-rigid regime of glasses along with the determined number of constraints n_c [92].

Discussing the average coordination of the atoms in glass, the so-called 8-N rule also needs to be mentioned. Considering an ideal glass, the valence requirements of the present atoms are satisfied, thus equal to 8-N, where N is the number of valence electrons (s and p electrons) of an atom. As an example, germanium is expected to be fourfold coordinated, antimony threefold coordinated and tellurium should adopt a twofold coordination. The 8-N rule is generally obeyed for N>4 (i.e., V, VI and VII group of elements), whilst the rule deviation can be observed for the elements of IV group as well as for the heavier and less ionic Te. Indeed, the presence of both tetrahedral and octahedral coordination species was demonstrated in GeTe and GST phase-change alloys [93–96].
The average coordination number r can be applied for the prediction of the T_g of a glass, based on the proportional relation between r and T_g, considering that T_g is related to glass rigidity. However, further studies showed that not only the number of bonds but also the bond strength must be taken into account. An improved model proposed in [97] relates the T_g to the enthalpy of atomization calculated from bond enthalpies of the homonuclear and heteronuclear bonds present in the system.

1.3.1.2 Liquid and Amorphous phase

Understanding the nature of the glass structure presents one of the most challenging problems of solid-state physics. Glass structure is classically described on the basis of the random network model, a concept introduced in [98]. However, several other models have been suggested over the years. In particular, three models were presented for chalcogenide glasses: the chain-crossing model [99], the random covalent network model [100] and the chemical bond approach [101].

Liquid and amorphous phases are similar in terms of structure, both characterized by the lack of long-range order and translational periodicity. Despite the lack of the long-range order, a sort of local structure on the atomic scale is still present. This short-range order is rather similar to that of the corresponding crystal. The liquid and amorphous phases, however, possess broader distribution of bond lengths and bond angles compared to the crystalline phase, representing disorder in the structure.

The short-range order of the amorphous phase occurs in the 2 – 4 Å length scale and involves the nearest-neighbor and the next-nearest-neighbor atomic correlations. The investigation of such a local structure demands the implementation of advanced experimental methods, such as neutron diffraction or X-ray Absorption Spectroscopy (XAS), namely EXAFS (Extended X-ray Absorption Fine Structure) and XANES (X-ray Absorption Near-Edge Structure). Recently, structural modelling such as reverse Monte Carlo (RMC) and (*ab initio*) molecular dynamics (MD, AIMD) simulations have started to be employed along with these experimental techniques in order to study both amorphous and liquid phases of a wide range of elements and alloys [16]. Moreover, besides the detailed analyses of the local structure, these methods allow to determine the relationship between the structural and the electronic properties (e.g., calculations of electronic density of states and band gap) [95,102,103].

Two main processes are usually employed to obtain the amorphous phase: melt-quenching and vapor-phase deposition. The amorphous phase obtained via melt-quenching is expected to inherit the structural features of the liquid, including well-ordered structural motifs such as rings or clusters. Vapor-phase deposition, on the contrary, leads to more structurally disordered amorphous phase due to much higher cooling rates involved. More structural defects, such as dangling bonds or wrong bonds, can also be expected. So-called wrong bonds refer to homopolar bonds in stoichiometric glasses as a result of a deviation from stoichiometry (e.g., As-As and S-S homopolar bonds present in stoichiometric As_2S_3 glass, instead of containing As-S bonds only).

In case of phase-change materials and their use in PCRAM technology, the fabrication steps and their effects on the atomic structure of the resulting amorphous phase must be taken into account. While the PCRAM device fabrication initially involves an as-deposited amorphous film (usually by sputtering), the melt-quenching process is important from the PCRAM device functionality point of view as it effectuates the RESET operation, i.e., the transition from crystalline to amorphous phase.

1.3.1.3 Crystalline phase

The atomic arrangement and the electronic structure of the crystalline phase have been identified as key points to understand the contrast between the amorphous and crystalline phase. Contrary to the amorphous and liquid phases, the crystalline phase features long-range order with atoms occupying specific places in the lattice (Fig. 1.13). The crystalline phase of the phase change materials was demonstrated to feature the octahedral-like atomic arrangement. Moreover, high intrinsic vacancy concentration can be found in many phase-change alloys [20].

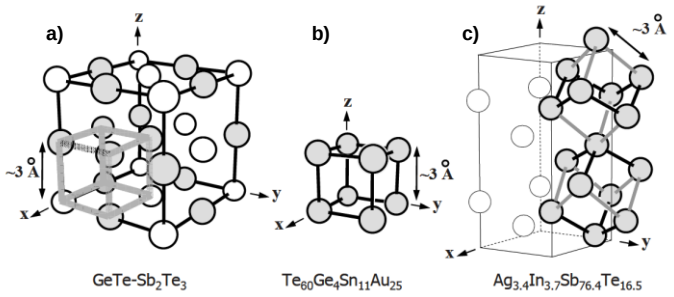

Fig. 1.13: Examples of different crystallographic systems with correpsonding alloys: a) metastable cubic crystalline structure of typical GST alloy. Te atoms occupy one sublattice, while Ge and Sb atoms and vacancies randomly occupy the second sublattice. b) Simple cubic crystalline structure, in which all the atoms statistically occupy the lattice sites. c) Distorted simple cubic crystalline structure (rhombohedral structure), typical for example for AIST alloys [16].

Considering the 8-N rule, the crystalline systems possessing on average four valence electrons per atoms (e.g., Si, Ge, GaAs) will adopt the fourfold tetrahedral coordination owing the favorable sp^3 hybridization. However, phase-change alloys have on average more than four valence electrons per atom and thus the tetrahedral configuration is rather unfavorable since the occupation of antibonding sp^3 states would be necessary. An approach based on resonant bonding mechanism [104] was proposed in order to explain the bonding arrangement and the changes upon the crystallization in phase-change materials. This approach shows that p-electrons are employed into unsaturated covalent bonding (i.e., more bonds are formed than which can be saturated with the number of valence electrons) to obtain the octahedral-like atomic arrangement (Fig. 1.14). The resonant bonding thus gives rise to electron delocalization leading to increased electronic polarizability, which is described upon phase-change material crystallization.

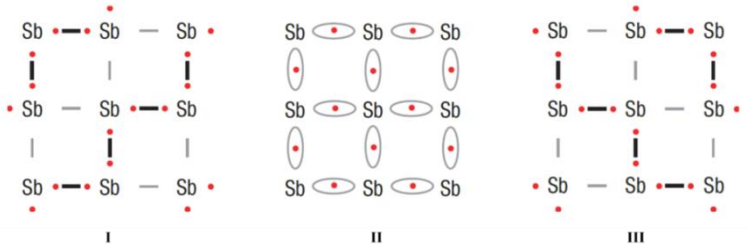

Fig. 1.14: Schematic diagram of the resonance bonding represented on the structure of Sb. Schemes I and III represent the limit case for bonding in undistorted Sb, while the resonant bonding with the pronounced electron delocalization is shown in scheme II [104].

However, new explorations suggest the concept of metavalent bonding, in order to clarify the nature of resonant bonding mechanisms for different material classes (i.e., organic compounds and inorganic solids) [105]. The metavalent bonding mechanism is based on unique combination of material parameters (e.g., optical and vibrational properties, atomic coordination, electron and charge distributions) arising from the particular bonding nature. Indeed, the simulations performed for a large set of materials allowed to identify the new material class between metals and covalently-bonded solids. The metavalent bonding mechanism provides a new perspective on phase transition and functional principle of phase-change materials. While the amorphous phase of the phase-change alloys was shown to demonstrate rather covalent bonding, crystalline phase can be characterized by metavalent bonding, featuring the combination of characteristics between covalency and metallicity.
The identification of the bonding mechanisms of the crystalline phase of phase change materials has demonstrated to be essential to understand the phase transition and the material properties. Moreover, it allows to draw the structure-properties maps useful for the

identification of new material candidates (Fig. 1.15). The first attempts to design such a map was proposed in [106], classifying the candidates for phase-change materials. Recently, new 2D and even 3D material maps were demonstrated, providing the material classification along with the quantified bonding properties [105,107].

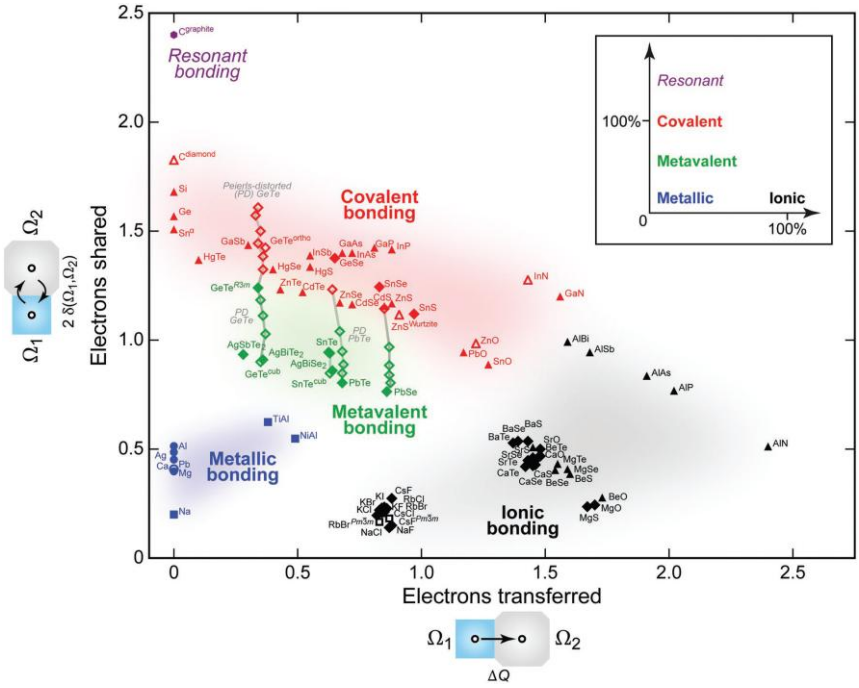

Fig. 1.15: Material map of electronic interactions and bonding in materials, highlighting the new class of materials featuring the metavalent bonding. The metavalent bonding is positioned between (metallic and covalent bonding mechanisms [107].

1.3.1.4 Crystallization mechanism

The crystallization mechanism and its kinetics is one of the limiting processes in technological applications, characterizing the amorphous phase stability and affecting the programming speed of the PCRAM device. Two processes are involved in the crystallization mechanism, namely nucleation and growth. Nucleation is the process of forming the crystallite clusters within the amorphous matrix, while growth refers to the increase of the crystallites size. The driving force for crystallization is the free energy gain between the amorphous and crystalline phase.

To describe the nucleation process, the classical nucleation theory first provided by Gibbs in 1878 is usually used [16]. The difference in free energy $\Delta G(r)$, also called as reversible work for a crystal, is determined by two contributions. First, the energy gained by forming the crystal phase and second, the energy required to form the interface between the crystalline cluster and the amorphous phase:

$$\Delta G(r) = -\Delta G_{ac} \cdot V(r) + \sigma_{ac} \cdot A(r) \tag{1.3}$$

Where $-\Delta G_{ac}$ is the (Gibbs) free energy difference between amorphous and crystalline phase (per unit volume), σ_{ac} is the specific interface free energy of the crystal-amorphous interface. V and A represent the volume and the external surface of the cluster, respectively. For the sake of simplicity, the clusters are assumed spherical with radius r. The evolution of $\Delta G(r)$ as a function of r is displayed in Fig. 1.16 and the curve passes through a maximum at:

$$r_c = 2\sigma_{ac} \,/\, \Delta G(r) \tag{1.4}$$

where r_c is the critical radius (in order of nanometers). Small cluster radii ($r<r_c$) are not energetically favorable and hence spontaneously decay. Above the critical cluster size ($r>r_c$), the first term in the equation (1.3) dominates, thus the energy is gained when the cluster is formed and the cluster grows. ΔG_c is called as critical work for cluster formation and can be considered as an activation barrier of nucleation.

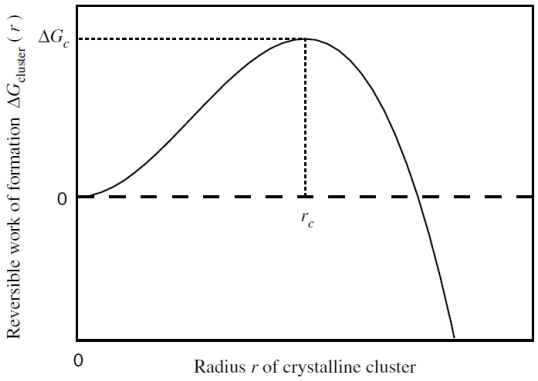

Fig. 1.16: Reversible work for a crystal ($\Delta G(r)$) as a function of crystal radius. r_c denotes the critical radius for which $\Delta G(r)$ reaches the maximum value and is considered as the activation barrier for the nucleation [16].

The classical nucleation theory by Gibbs is purely thermodynamic and assumes that clusters evolve by the addition or removal of atoms to/from the cluster. Later, additional assumptions, including the probability of critical and post-critical cluster to grow or shrink, lead to the introduction of kinetic models. These models define the steady-state homogeneous volume nucleation rate I^{SS} and introduce a time period (i.e., incubation period), necessary to establish a steady state distribution of the clusters in the system [16].

In general, two types of nucleation process can be distinguished: the homogeneous nucleation, when the nucleation occurs inside the amorphous phase; and the heterogeneous nucleation, using impurities or interfaces as nucleation sites. In practical cases, both types coexist. The above-described nucleation theory for homogeneous nucleation also applies for heterogeneous nucleation. However, in such case, lower work for critical cluster formation and reduced number of atoms in the amorphous phase contributing to the nucleation are employed (i.e, only a fraction of atoms is in contact with the impurity or interface). The heterogeneous nucleation rates are orders of magnitude higher than homogeneous nucleation rates, thus dominating the nucleation process of the system.

Once a critical cluster has been transformed into a stable crystalline nucleus, more atoms can diffuse, growing the crystallite to a macroscopic size. The crystal growth is thus driven by the reorganization of the atoms along the crystal-amorphous interface, lowering the overall energy of the system. The crystal growth velocity reaches its maximum close to T_m (i.e., at higher temperature than the maximum of the nucleation rate), while falling to zero after passing T_m. A detailed discussion on the crystallization kinetics can be found in [16,17,84].

Depending on the process dominating the crystallization, the mechanism can be categorized either as nucleation-dominated or growth-dominated. The nucleation-dominated crystallization features relatively short incubation times, high nucleation rates and slow growth velocities. The time to crystallize does not depend on the volume of the amorphous phase. The growth-dominated crystallization, on the contrary, is characterized by low nucleation rates and high growth velocities. It exhibits the volume dependence, i.e., the smaller the volume of the amorphous phase, the faster the crystallization is completed. Both crystallization mechanisms are observed in phase-change materials. While $Ge_2Sb_2Te_5$ alloy exhibits the nucleation-dominated crystallization, AIST alloys are considered as growth-dominated (much lower nucleation rate and longer incubation time were observed) [17,108,109].

1.3.2 Ge-Sb-Te ternary system

The exploration of GeSbTe (GST) ternary alloys (Fig. 1.17) started the new era of optical data storage and PCRAM technology. In particular, the stoichiometric compositions along the pseudo-binary line between Sb_2Te_3 and GeTe of the phase diagram, such as $Ge_1Sb_4Te_7$, $Ge_1Sb_2Te_4$ and $Ge_2Sb_2Te_5$, were found to be very promising. Multiple studies and first-principle calculations were performed to understand the atomic structure of these alloys and to identify the mechanisms leading to the formation of stable structures with the lowest energies [110,111].

Some common features of GST alloys along the GeTe-Sb_2Te_3 pseudo-binary line can be observed. The most widely used GST alloys mentioned above crystallize into two crystalline structures: a metastable cubic phase at lower temperatures (T_x ~100-160 °C) and a stable hexagonal phase at higher temperatures (T_x >200 °C) [112]. Based on the similarities between parental GeTe and Sb_2Te_3, the hexagonal structure of stoichiometric GST alloys can be seen as superlattice of these binary alloys with a stacking sequence dictated by Sb_2Te_3 structure. Moreover, large number of vacancies is present in both metastable cubic and stable hexagonal crystalline phase, lowering the energy of the crystalline phases. In the cubic crystalline phase, the vacancies randomly occupy the cation sites, while in the hexagonal phase the vacancies form ordered planes separating the GST building blocks. The systematic investigation of $(GeTe)_n(Sb_2Te_3)_m$ homologous series, their structure and properties can be found in [111,113–115]. The T_m of these alloys is observed at 590 – 630 °C, depending on the composition [110].

Moving along the GeTe-Sb_2Te_3 pseudo-binary line, several tendencies in the alloys' properties can be observed, depending on the ratio between GeTe and Sb_2Te_3. The increasing Sb_2Te_3 fraction in a GST alloy reduces T_x and increases the crystallization speed, as demonstrated by resistivity measurements in [116]. These effects result from the presence of higher number of weaker Sb-Te bonds (277.5 kJ/mol) compared to stronger Ge-Te bonds (402 kJ/mol) [116]. Among the stoichiometric GST alloys, the $Ge_2Sb_2Te_5$ is taken as the most common reference compound. The referential binary GeTe and Sb_2Te_3 systems as well as $Ge_2Sb_2Te_5$ are presented more in detail in following sections.

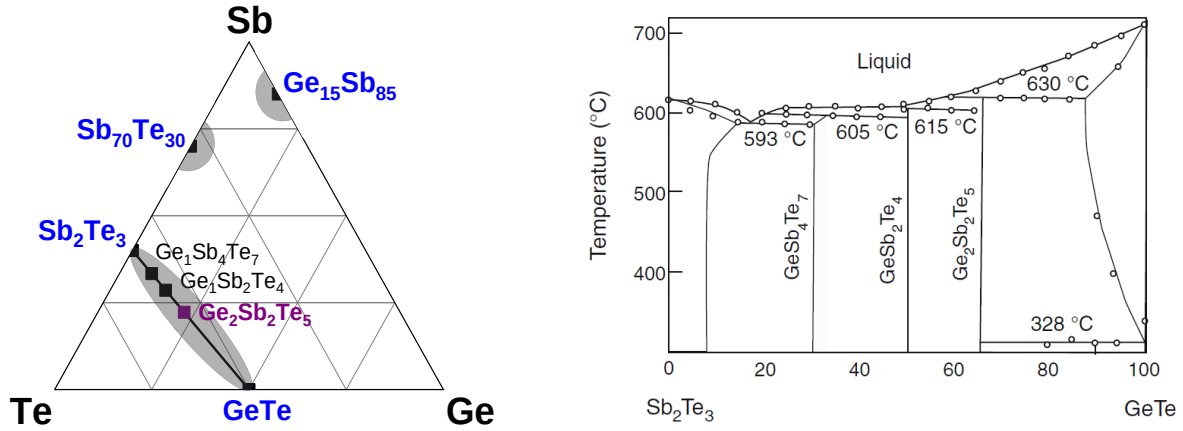

Fig. 1.17: (left) Ternary Ge-Sb-Te diagram, highlighting the principal stoichiometric alloys on the GeTe-Sb_2Te_3 tie-line and other regions of common phase-change alloys (grey zones); (right) Phase diagram of the GeTe-Sb_2Te_3 system [117].

1.3.2.1 GeTe

The stoichiometric GeTe alloy ($Ge_{50}Te_{50}$) has been investigated from both fundamental and technological point of view. GeTe represents one of the first examples of Te-based

chalcogenide alloys in the field of phase-change memory technology due to its fast crystallization rate and a high temperature stability [118–120]. Besides the use in memory technology, GeTe alloys are also implementated in thermoelectric, ferroelectric and even spintronic fields of applications [121]. Despite its relatively simple chemical composition as a binary alloy, GeTe still poses fundamental questions, in particular concerning the bonding arrangement and mechanisms associated with amorphous-to-crystalline phase transition.

The crystalline GeTe (T_x ~180 °C) possesses distorted rhombohedral structure (R3m), in which both Ge and Te atoms use the p shell electrons to create sixfold coordinated octahedral resonant bonding in the network (Fig. 1.18). The Peierls-like distortion of the rhombohedral structure leads to the splitting of the six Ge-Te bonds into 3 shorter (stronger) and 3 longer (weaker) bonds, reducing the energy of the occupied states. In the ideal GeTe crystalline structure, each site is occupied either by Te or by Ge atoms; however, several studies have revealed the presence of intrinsic vacancies in Ge sublattice (up to 10 %) [121,122]. At higher temperatures (>350 °C) the rhombohedral GeTe transforms into cubic phase with a rocksalt structure.

In the amorphous phase of GeTe, the average coordination number of Ge inferred from EXAFS decreases from sixfold to fourfold, hence Ge atoms adopting a tetrahedral coordination [93,122]. Further EXAFS investigations along with RMC and MD simulations and XRD data revealed the coexistence of both octahedral and tetrahedral coordination of Ge atoms in the amorphous phase. Indeed, Ge atoms were shown to be mostly fourfold coordinated, but only approximately one third is present in tetrahedral environment, while the majority remains in defective octahedral environment [95,96,123–125].

1.3.2.2 Sb_2Te_3

Sb_2Te_3 represents the second parent composition of the GST phase-change alloys. This binary alloy features high crystallization speed. However, low crystallization and melting temperatures represent the major challenges of Sb_2Te_3, leading to poor thermal stability of the amorphous phase for PCRAM applications. Besides the PCRAM technology, Sb_2Te_3 has been widely studied for its excellent near room temperature thermoelectric properties and hence for possible applications in thermoelectric devices [126]. Furthermore, Sb_2Te_3 and its related compounds (Bi_2Se_3 and Bi_2Te_3) have been recently demonstrated as suitable materials for topological insulator device applications [127,128].

Sb_2Te_3 crystallizes in a rhombohedral layered structure, which can be viewed as a series of Sb, Te and intrinsic vacancies ordered in planes along the c axis of the unit cell (Fig. 1.18). The building blocks consist of repeated quintuple Te-Sb-Te-Sb-Te layers of atoms, each quintuple layers being terminated by Te atoms plane due to the excess of tellurium. The separation between the blocks is described as a layer of ordered vacancies. The bonding between the Te atoms of the adjacent planes can be explained in terms of van der Waals interaction. The Sb and Te atoms in the center of the building block are sixfold coordinated, whereas the Te atoms at the edge of the blocks are only threefold coordinated to the neighbor Sb atoms within the block.

The amorphous and liquid structures of Sb_2Te_3 were studied in particular by AIMD simulations, showing that Sb atoms are mostly fourfold coordinated and Te atoms mostly threefold coordinated, forming the four-membered ABAB rings (A = Sb, B = Te). A large fraction of homopolar Sb-Sb bonds (up to ~35 %) and six-membered Sb chains were evidenced as well as homopolar Te-Te bonds, though arranged only into dimers and trimers [96].

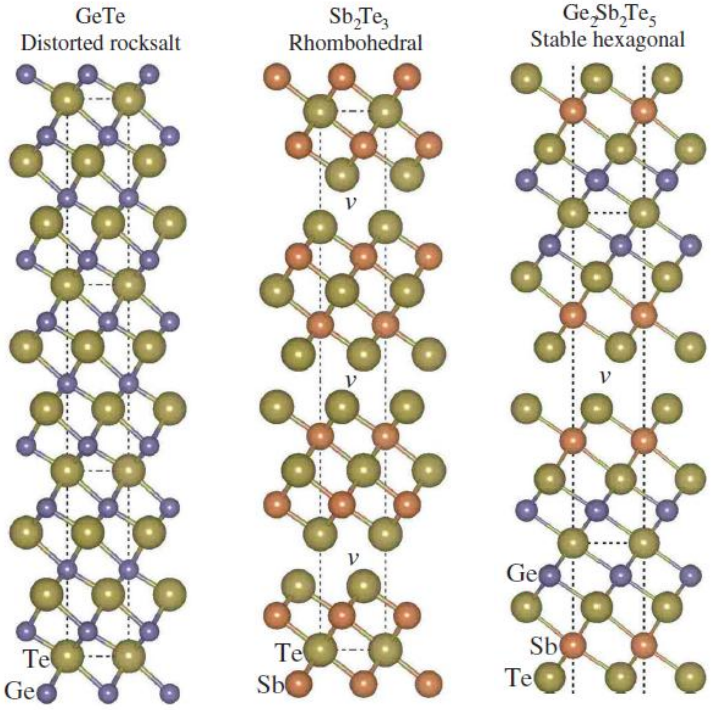

Fig. 1.18: Crystal structures of bulk GeTe, Sb_2Te_3 and $Ge_2Sb_2Te_5$ alloys. Ge (blue), Sb (orange), Te (green) and intrinsic vacancies (v) are indicated [111].

1.3.2.3 $Ge_2Sb_2Te_5$

$Ge_2Sb_2Te_5$ alloy became a prototype material for PCRAM device. Amorphous $Ge_2Sb_2Te_5$ first crystallizes into cubic (rocksalt type; fcc) metastable structure at ~160 °C and further transforms irreversibly into the stable hexagonal (hex) phase at temperatures above 300 °C (Fig. 1.19) [129]. In the cubic crystalline phase, the tellurium atoms occupy the anion sublattice, while germanium, antimony and intrinsic vacancies randomly occupy the cation sublattice. The intrinsic vacancies compose up to 20 % of the cation sublattice, reducing the average number of valence electrons and thus lowering the energy of the fcc crystalline phase [20,113]. The hexagonal phase adopts the structure of the parenting Sb_2Te_3 alloy with the building blocks consisting of 9 planes, where a plane fully occupied by Te atoms alternates with a plane occupied by Ge or Sb atoms or their random mixture (Fig. 1.18). Though the stacking sequence of the hexagonal crystalline phase appears well defined, the occupation of the cation sites remains a source of debate, giving rise to various models described in [111,130–132].

The structure of amorphous and fcc crystalline phase of $Ge_2Sb_2Te_5$ has been widely studied in order to understand the origin of the reversible phase-change mechanism. Based on experimental and theoretical studies, the amorphous phase is characterized by the presence of fourfold coordinated Ge atoms in tetrahedral environment, while the atoms in fcc crystalline phase exhibit the octahedral environment. An umbrella-flip model (Fig. 1.20) was suggested based on EXAFS data describing the transition of Ge atoms from tetrahedral to octahedral sites upon crystallization without the rupture of strong covalent bonds [133]. Subsequent studies confirmed the tetrahedral coordination of germanium [134,135], however other studies also suggested the formation of even-numbered rings, analogous to the crystal phase [125]. Later, MD simulations revealed that a fraction of Ge atoms are indeed in tetrahedral coordination, however favored by Ge-Ge and Ge-Sb bonds (i.e., “wrong bonds”) rather than Ge-Te bonds, as stated by the umbrella-flip model. The majority of Ge atoms along with all Te and Sb atoms in amorphous phase were found in a defective octahedral-like geometry,

i.e., with octahedral bonding angles but with atom coordination lower than six (Fig. 1.20). Finally, the presence of few dimers and trimers of Te atoms in the amorphous phase was reported [96].
Though a simple local structural scheme like the umbrella-flip model is attractive, it cannot explain the existence of several features, such as the presence of homopolar bonds or the difference in optical reflectivity, which accompanies the phase transition mechanism. A new approach to understand the phase transition are suggested based on metavalent bonding mechanism recently described in crystalline phase of phase-change materials (section 1.3.1.3). This approach highlights the change of the nature of bonding mechanism from covalent to metavalent upon crystallization and allows to associate the changes in material properties (e.g., octahedral-like coordination, increase of chemical and electrical polarizability and changes in vibrational porperties) [105].

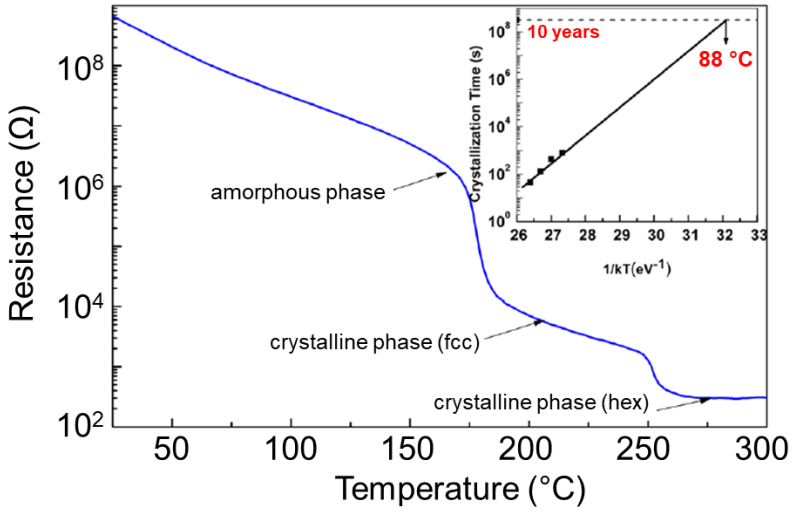

Fig. 1.19: The temperature dependence of resistance of as-deposited $Ge_2Sb_2Te_5$. The inset graph shows Arrhenius extrapolation highlighting the corresponding 10 years data retention value [136].

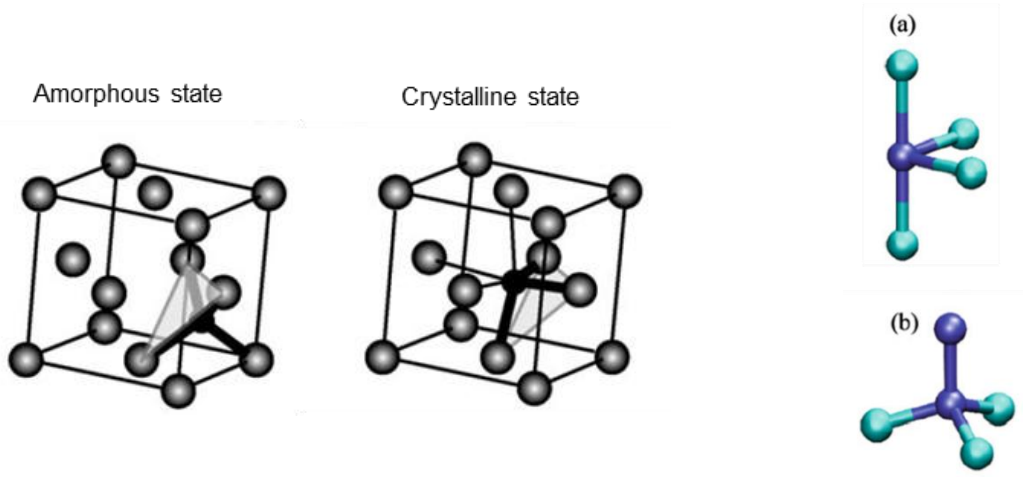

Fig. 1.20: (left) Schematic representation of the local structure in the amorphous and crystalline phases upon umbrella-flip model; (right) A scheme of the GeTe structural units (Ge - dark blue, Te – light blue): a) Ge in defective octahedral coordination, b) Ge in tetrahedral coordination [21,137].

1.3.3 Material engineering

Although $Ge_2Sb_2Te_5$ appears to be a promising alloy, some of its properties, such as the crystallization temperature ($T_x \sim 150$ °C), showed to be limiting for the use in embedded PCRAM applications, which require high temperature data retention (section 1.2.3). The technological challenges posed by PCRAM led to the material engineering of the stoichiometric alloys, optimizing the material properties and thus the PCRAM device performances. The current main goals for modifying the stoichiometric compounds aim to:

- interfere with the crystallization process and increase the crystallization temperature, thus improving the thermal stability of the amorphous phase (RESET state) and the data retention of the PCRAM device;
- increase the electrical and thermal resistivity of the phase-change material to reduce the programming (RESET) current.

The search for material optimization of the GST alloys adopted two main directions, which will be discussed in the following sections: changing the stoichiometric ratio of the GST alloys and doping the GST alloys by additional elements.

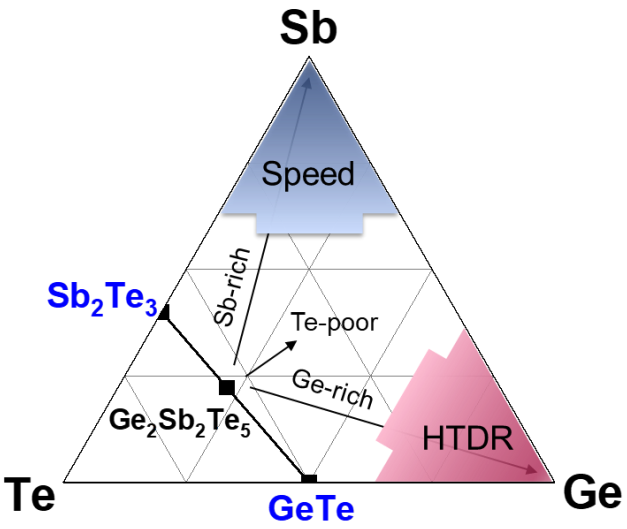

Fig. 1.21: Ge-Sb-Te ternary diagram highlighting the directions of GST material engineering for targeting the PCRAM device performances: fast speed and high temperature data retention (HTDR).

1.3.3.1 Nonstoichiometric GST alloys

Starting from the $Ge_2Sb_2Te_5$, the search for non-stoichiometric compositions in Ge-Sb-Te ternary system can follow one of three directions: Te-poor, Ge-rich and Sb-rich alloys (Fig. 1.21). The exploration of Te-poor region was motivated by increasing the average coordination number, assumed to play a fundamental role in crystallization process. Decreasing the Te content leads to higher rigidity of the alloy and activation energy of crystallization, thus enhancing the stability of the amorphous phase over time. However, engineering of GST composition towards Te-poor region shows to affect both electrical and thermal performances of PCRAM device. The amorphous resistance and threshold voltage decrease with decreasing Te content. Despite lower melting temperature of Te-poor GST, the material features worse thermal confinement during the phase change, resulting in higher programming current and thus higher power consumption [138,139].

Ge-rich GST

The first attempt to investigate the Ge-enrichment in GST alloys was reported in [140]. The investigation of $Ge_2Sb_1Te_2$ alloy and the Ge-enriched compositions along a tie-line between Ge and Sb_2Te_3 highlighted the so-called "golden composition". This Ge-rich composition demonstrated higher T_x compared to $Ge_2Sb_2Te_5$ and hence enhanced thermal stability of RESET state, while maintaining the fast switching speed of the PCRAM cell. Further studies focused on Ge-rich composition along the tie-line between $Ge_2Sb_2Te_5$ and Ge. It was shown that T_x is progressively increases with the Ge content up to 350 °C, whereas the crystalline phase becomes more resistive (Fig. 1.22) [24]. However, the XRD patterns of Ge-rich GST alloys annealed at high temperatures show the presence of two cubic crystalline phases corresponding to $Ge_2Sb_2Te_5$ and Ge crystalline phases, which indicates the system segregation (Fig. 1.23). Recent studies by TEM-EDX analyses confirmed the formation of Ge-rich and Sb-/Te-rich regions in the Ge-rich GST thin films and suggested that the phase segregation begins with the nucleation and appearance of Ge nanocrystals followed by the crystallization of $Ge_2Sb_2Te_5$ phase (discussed in the section 2.2.6) [3].

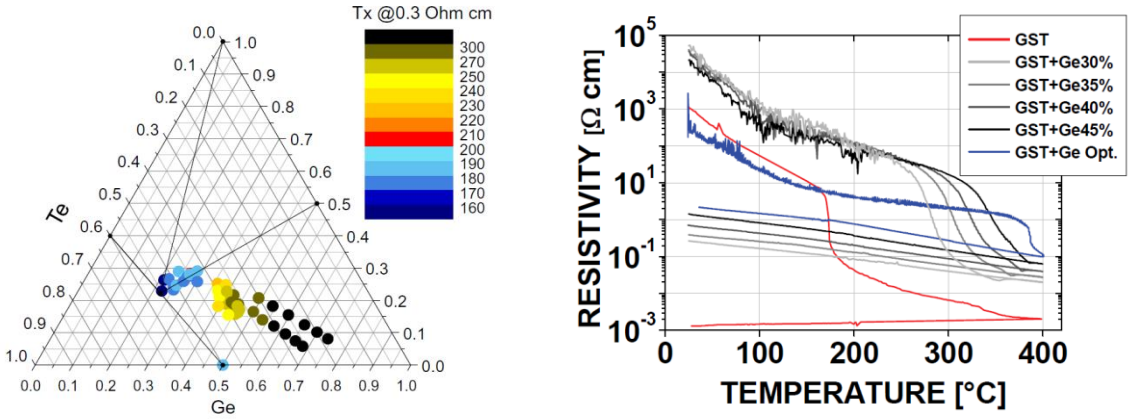

Fig. 1.22: (left) Evolution of the crystallization temperature as a function of Ge-enrichment in GST alloys; (right) Optimization of Ge-rich GST alloy highlighting the delayed amorphous-to-crystalline phase transition and increased resistivity of the crystalline phase with increasing Ge enrichment [24,141].

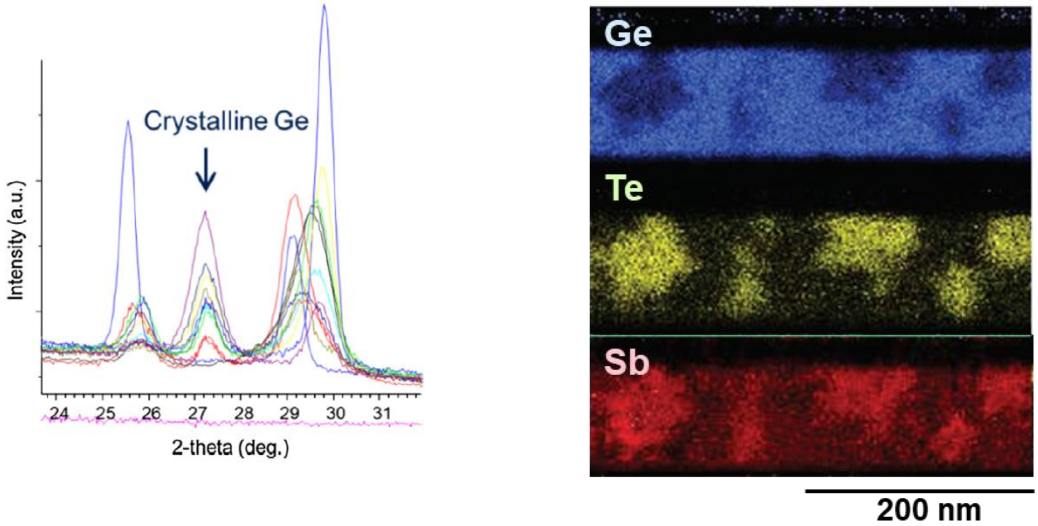

Fig. 1.23: (left) X-ray diffraction of Ge-rich GST alloys after annealing at ~450 °C demonstrating the Ge crystalline phase, i.e., Ge segregation; (right) STEM-EDX maps of Ge, Sb and Te of Ge-rich GST alloy annealed at 450 °C highlighting the formation of Ge-rich and Sb-rich/Te-rich regions [3,24].

Despite the phase segregation observed in thin films, the PCRAM device based on Ge-rich GST alloys exhibits functional electrical characteristics. Higher thermal stability of the amorphous phase allows better data retention of the PCRAM devices programmed in the RESET state. For instance, the $Ge_2Sb_2Te_5$ alloys enriched by 45 at.% of Ge demonstrated the stability of the RESET state for at least 10 years at temperatures up to 200 °C, which is well above the required specifications for automotive applications [141]. On the other hand, Ge content has a strong impact on the crystallization speed, hence a trade-off between the high data retention of the RESET state and the reduced programming speed is necessary. However, even with the reduced crystallization speed, the programming time is still orders of magnitudes shorter than that of Flash memories currently used for embedded applications (milliseconds for RESET operation). Concerning the stability of the programmed SET state, the resistance drift was observed in Ge-rich GST alloys, while no drift was reported for $Ge_2Sb_2Te_5$ [142].

The analyses of elemental distribution showed strong composition inhomogeneity in the active region of the PCRAM cell, demonstrating highly Sb-rich core of the active zone (above the heater element), whereas the surrounding side areas become Ge-rich (Fig. 1.24). Further investigations attributed the phenomenon to Ge segregation during the cell programming operation [143,144]. Indeed, the applied RESET pulse forms a conductive path between the heater and the upper electrode, melting the integrated Ge-rich GST material in the active zone. Ge atoms are driven from the liquid to the solid phase at the liquid/solid interface. The liquid/solid interface moves closer to the heater with the ramp-down of the applied pulse, hence more Ge atoms are segregated, creating the Ge-rich crystalline zone and leaving the molten region Ge impoverished. Sb atoms show exactly the opposite trend, i.e., they concentrate near the heater element, as they tend to stay in the liquid phase. It was shown that this segregation phenomenon within the cell is the result of the first programming operation of the PCRAM cell [145]. The integrated memory device is in high-resistive state after the manufacturing and needs an electrical activation (i.e., forming operation) as the final part of the PCRAM cell fabrication. Moreover, it was demonstrated programming the device with low current density can minimize the SET resistance drift [145].

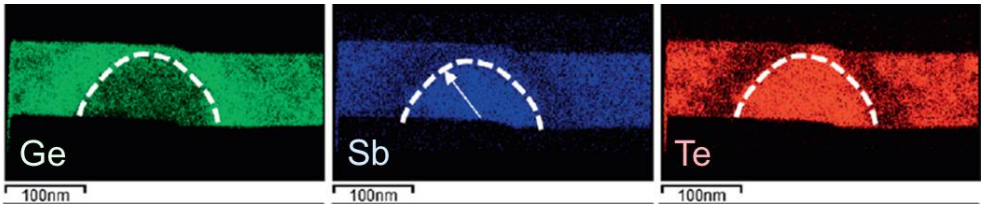

Fig. 1.24: Ge, Sb and Te maps of the PCRAM cell programmed to RESET showing the composition inhomogeneity and Ge segregation at the outer boundaries of the active region [145].

Despite the segregation phenomenon described above, the thermal stability of both RESET and SET states can be ensured by optimizing the Ge enrichment of the alloy, as shown on the example of GST + Ge 45 at.% [141]. TEM and STEM/EELS studies showed that after the first RESET operation and consequent segregation effect, an equivalent of GST + Ge 25 at.% was retained at the active region, still ensuring the thermal stability up to 240 °C (T_x of GST + Ge 25 at.%) (Fig. 1.25).

Another optimized Ge-rich GST alloy, so-called T alloy, was presented in [143], demonstrating the ability to retain data in extended temperature range and to guarantee code integrity after soldering thermal profile, hence validating this type of material also for embedded applications. Further engineering of GST alloys by Ge-enrichment highlighted the possibility to tailor the PCRAM device electrical performances and the data retention properties according to application requirements. While the reported T-alloy fits with the most

challenging requirement of data retention, other presented Ge-rich GST, called as D-alloy, showed better performance of the SET state, thus offering more flexible solution, if not extremely challenging retention properties are requested [24].

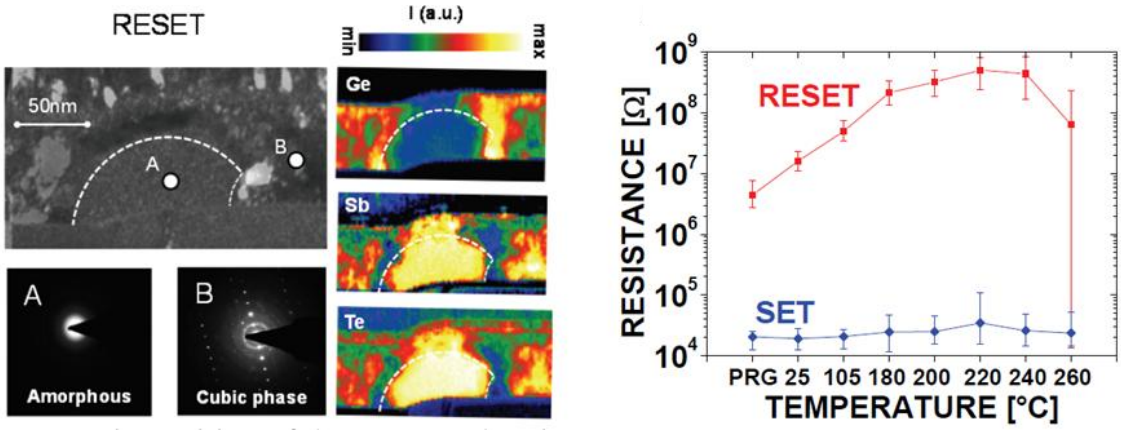

Fig. 1.25: (left) Superimposed TEM BF/DF images and STEM/EELS signal for GST + Ge 45 at.% device in RESET state, showing the amorphous dome with GST + Ge 25 at.% alloy in the active volume; (right) SET and RESET resistance of the corresponding PCRAM device showing the stability up to 240 °C [141].

Sb-Rich GST

Opposite to Ge-rich GST compositions, Sb-rich GST alloys attract the attention due to high crystallization speed, caused by the growth-dominated crystallization mechanism. The main challenge of Sb-rich GST alloys is the relatively low thermal stability of the amorphous phase. Systematic studies on different Sb-enriched / Sb-doped systems were performed, showing large dependencies of the final material properties on the deposition process parameters. The systematic studies performed on $GeSb_xTe$ alloys based on Ge-doped Sb_2Te and Sb-doped GeTe [140,146,147] highlighted higher crystallization temperature and lower resistance of the crystalline phase compared to $Ge_2Sb_2Te_5$ (Fig. 1.26). Very fast crystallization times for Sb-doped alloys were observed, but the systems also suffered from Ge or Sb segregation. Further studies performed on the Sb-enriched $Ge_2Sb_2Te_5$ [148,149] demonstrated the gradual disappearance of the transition to the cubic crystalline phase, reaching only one phase transition to rhombohedral crystalline structure for highly Sb enriched compositions. Contrary to above mentioned Sb-rich systems, highly Sb-enriched GST alloys (>35 at.% of Sb enrichment) do not show the elemental segregation [148]. The integration of Sb-rich GST material in PCRAM device demonstrated high speed (20 ns), high endurance (10^{15} cycles) and data retention (4.5 years at 85 °C), revealing the high potential of these materials and possible envisaging DRAM-type applications [148,150].

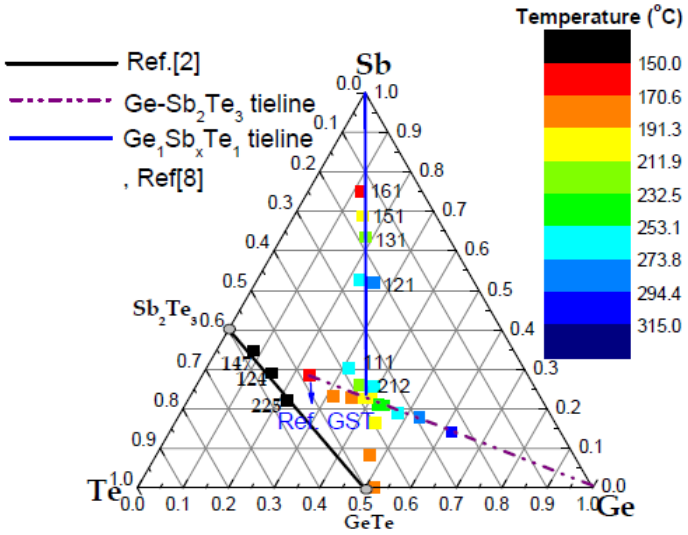

Fig. 1.26: Ge-Sb-Te ternary diagram highlighting the material optimization by Sb enrichment along the GeTe-Sb tie-line [140].

1.3.3.2 Doping by light dopant elements

Tuning the properties of the GST alloys by light elements (N, C and O) has been explored since the use of these alloys in optical data storage [151,152]. Following these achievements, N, C, and O doping were expected to improve the performance of PCRAM devices. Indeed, these dopants showed positive effects on data retention, power consumption and endurance [153–155]. An intensive effort is hence devoted to understand the role of these dopants on the GST structure, the crystallization mechanisms and their kinetics. In general, N, C and O elements act like interstitials in the GST alloy structure, reducing the free active volume necessary for fast crystallization and thus increasing T_x [67,156]. However, each dopant exhibits a distinct effect on the GST alloy structure and its properties. The detailed understanding of the dopants impact on both amorphous and crystalline phases is thus required.

Oxygen doping

PCRAM devices based on oxygen-doped $Ge_2Sb_2Te_5$ were successfully experimented, allowing to decrease the RESET current, while maintaining a 10-year data lifetime at 100 °C [5,157]. These achievements are attributed to increased electrical and thermal resistances of the material. Indeed, the investigations performed on O-doped GST thin layers demonstrated increasing T_x, crystal grain size and lattice parameters with oxygen concentration up to 10 %, which is attributed to the formation of Ge-O bonds in the system. Above this value, T_x conversely decreases as a result of suppressed GST phase crystallization and system segregation to Ge-O, Sb-O and Sb_2Te_3 (Fig. 1.27) [67,158–160].
The stability of GST alloys upon O incorporation does not involve only the O doping during the deposition process, but possible uncontrolled oxidation processes of the alloys under air exposure also needs to be considered. TEM studies reported in [161] showed that a 10 nm-thick $Ge_2Sb_2Te_5$ film kept in ambient condition for 2 weeks required only 35 °C for complete transformation from amorphous to crystalline phase whereas the film kept in vacuum required 130 °C. Effective capping strategies avoiding the material degradation are therefore necessary to be engineered.

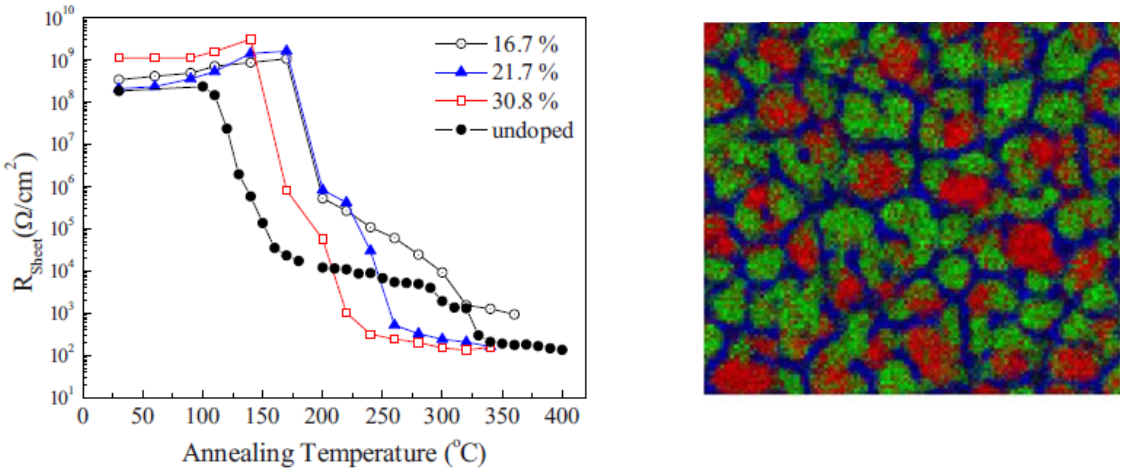

Fig. 1.27: (left) Resistance as a function of temperature of the undoped and O-doped GST225 alloys; (right) STEM-HAADF mapping of O-doped GST225 alloy after heating at 200 °C showing the islands rich in Sb (green) and Te (red), while Ge (blue) migrated into the gaps between the islands, forming the Ge-O bonds. The image view field is 125 nm [158,160].

Carbon doping

Carbon doping showed to be an effective strategy to improve the material properties and the PCRAM device performances. Carbon incorporation in the GST alloys leads to preferential formation of Ge-C bonds leading to improved thermal stability of the amorphous phase and to the increase of T_x above 300 °C [64,162]. Upon crystallization, the Ge-C bonds break giving rise to the formation of nanometer-scale carbon clusters in crystalline phase (Fig. 1.28). The carbon chains cause much more severe lattice distortions than one carbon atom, inducing electron and phonon scattering and resulting in resistance increase and thermal conductivity decrease. At the device level, these effects lead to the reduction of programming current. It was reported that PCRAM device based C-doped GST alloy (C ~5 at.%) yields more than 50 % of current reduction compared to the device with undoped GST [163]. The formation of the carbon clusters at the grain boundaries inhibits the crystallization process and restrains the grain growth, being responsible for slower operation speed. On the other hand, stable carbon clusters featuring low diffusion coefficient significantly reduce the long-range migration of Ge, Sb and Te atoms, avoiding the system segregation and enhancing the endurance performance (up to 10^8 cycles) of the PCRAM devices [162–164].

Although further research is necessary, relatively high thermal stability and high endurance of C-doped GST-based devices show high potential of these materials in PCRAM technology [165–167]. Moreover, 12-state multi-level cell storage implemented in a 128 Mb PCRAM chip has been recently demonstrated using a C-doped GST alloy, opening a promising path towards large-scale and energy-efficient neuromorphic computing systems [164].

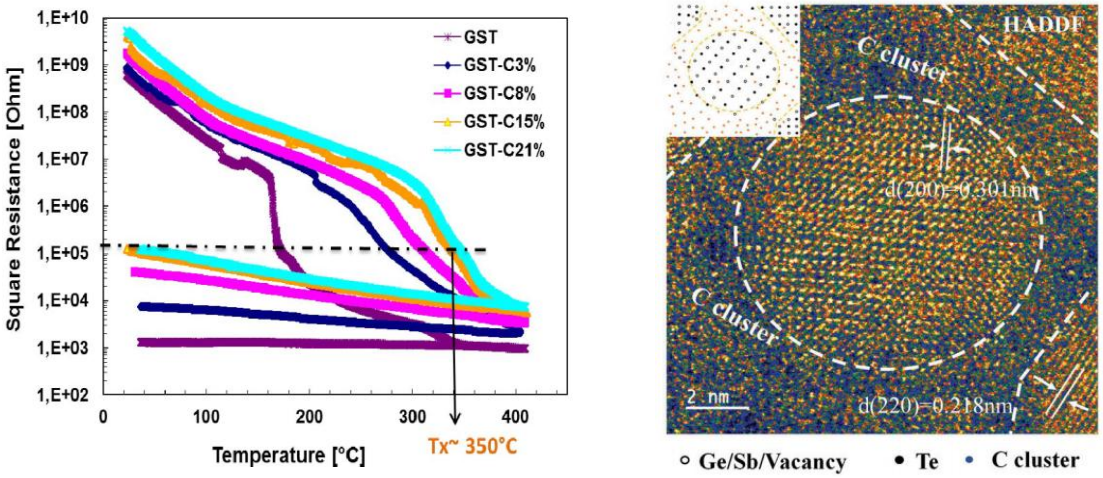

Fig. 1.28: (left) Resistance as a function of the temperature of the C-doped GST225 alloys; (right) STEM-HAADF image of crystalline grain and surrounding amorphous carbon cluster regions [164,166].

Nitrogen doping

N-doped alloys are in particular investigated due to highly enhanced thermal-retention properties of the amorphous phase. Hence, these alloys may present a suitable solution for the targeted high-temperature data retention of embedded PCRAM device applications.
Indeed, N incorporation in GST increases T_x, the incubation time for crystal nucleation and growth and the resistivity of the crystalline phase. From the microstructural point of view, it was shown that nitrogen preferentially forms strong covalent bonds with Ge atoms [168]. Nevertheless, possible presence of molecular N_2 in N-doped GST alloys was also reported [169]. The molecular N_2 is believed to exist at interstitial and vacancy sites and it is assumed to easily diffuse out upon annealing [59]. On the contrary, the formation of Ge-N bonds may reduce the atomic diffusivity, leading to an increase of the crystallization temperature. The precipitation of the Ge-N bonds at grain boundaries upon crystallization results in the reduction of the grain size. From the PCRAM device point of view, N doping effects result in improved cyclability and in enhanced efficiency of Joule heating during RESET operation, hence in the reduction of programming current [59,67,154].
The material optimization by N doping, however, needs to be considered carefully. The N incorporation delays the amorphous-to-fcc crystalline phase transition to higher temperatures. However, excessive N incorporation was shown to completely suppress this transition, allowing the direct crystallization to the stable hexagonal phase, which can lead to PCRAM device degradation [152,170].
Further promising achievements are obtained by N doping of Ge-enriched GST alloys. The combination of Ge enrichment and N doping results in enhanced effects of both material optimization, i.e., the increase of T_x and the resistivity of fcc crystalline phase along with the reduction of the grain size (Fig. 1.29 and Fig. 1.30). Concerning the microstructure, Ge-enrichment increases the stability of both amorphous and cubic crystalline phase. The formation of Ge-N bonds in the system due to N doping could likely delay the Ge and GST phase segregation, leading these alloys to meet outstanding thermal stability and endurance of embedded PCRAM device, compatible with automotive requirements [171]. The microstructure of N-doped Ge-rich GST and its changes upon the amorphous-to-fcc phase transition are being currently largely investigated.

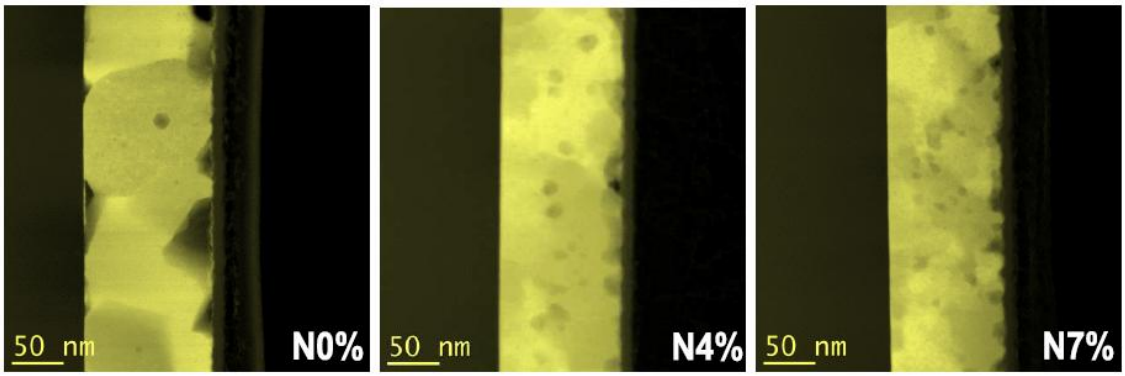

Fig. 1.29: STEM-HAADF images on undoped and N-doped Ge-rich GST alloy annealed at 450 °C showing finer crystalline structure of the alloy with increasing N content [171].

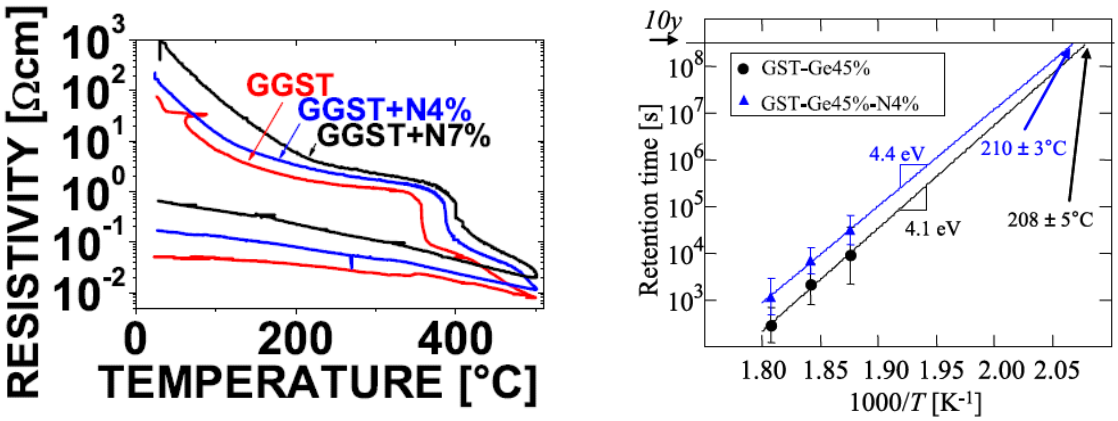

Fig. 1.30: (left) Temperature dependence of resistivity of N-doped Ge-rich alloys; (right) Arrhenius plot of data retention time for undoped and N-doped GST+Ge45%, highlighting the improved 10 years data retention, compatible with automotive requirements (i.e., at least 2 years at 150 °C) [171,172].

1.4 Chapter summary

The PCRAM technology demonstrates to be the most promising and mature among the emerging NVM technologies. It shows high potential in stand-alone Storage Class Memory applications, filling the gap between volatile memories and non-volatile data storage owing to the balanced combination of high performance and acceptable cost. PCRAM device engineering further enables this technology to target embedded memory applications, achieving stringent requirements on high temperature data retention for automotive industry.

The PCRAM device performances are closely linked with the properties of integrated phase-change material and thus the device performance can be tuned by the phase-change material engineering. The most largely studied phase-change alloys come from Ge-Sb-Te ternary system. $Ge_2Sb_2Te_5$ alloy, commonly used as a reference, lies on the pseudo-binary line of the parental GeTe and Sb_2Te_3 binary alloys. $Ge_2Sb_2Te_5$ features reversible amorphous-to-fcc crystalline phase transition at 150 °C, which is not high enough for high-temperature data retention applications. Nonetheless, two main directions are applied for the material optimization: the exploration of nonstoichiometric GST alloys and the alloy doping with light elements. Investigation of Sb-rich and Ge-rich alloys showed promising results in increasing the PCRAM device speed and data retention, respectively. However, these alloys often suffer from phase segregation. Upon doping, light elements (nitrogen, in particular), are incorporated in interstitial sites and form preferably bonds with Ge atoms of the alloy. The presence of Ge-N bonds was reported to increase the crystallization temperature and thus to provide higher stability of the amorphous phase. Moreover Ge-N bonds contribute to hinder the grain growth, reducing the material segregation.

The combination of both material optimizations (i.e., Ge enrichment and N doping) can bring promising achievements in terms of high-temperature data retention of the PCRAM device for the embedded applications. The optimized N-doped Ge-rich GST alloys need to be investigated in order to provide the deep insight into the material structure. Indeed, the clear understanding of the effects of both Ge-enrichment and N doping on the GST alloy structure and the crystallization mechanisms is still lacking. Therefore, this thesis provides a thorough material investigation employing various characterization techniques, which are presented in the chapter 2. The presented material studies first focus on N doping effect on elemental systems (chapter 3) and further on the effect of both Ge enrichment and N doping in GST alloys (chapter 4).

Chapter 2

Characterization of Phase-Change Materials

The performances of PCRAM device relies on the unique properties of phase-change materials, in particular on their amorphous and crystalline structure, as reported in chapter 1. Therefore, deep understanding of the structure of both amorphous and crystalline phase, their atomic arrangements and bonding are thus fundamental. The comprehension of atomic arrangement and bonding along with their evolution during the crystallization mechanisms enable to determine the origin of the material properties. Moreover, it allows to identify the intrinsic material limits and to optimize the materials in order to meet the requirements of different PCRAM device applications. The material characterisation is an ever-growing field in science including large variety of characterization techniques, which can be used in order to probe the material structure on the nanoscale and microscale level and to provide the complementary information.

In this chapter, we briefly present the main electrical, optical and X-ray characterization techniques, later used in this work for the structural investigation of elemental systems and phase-change alloys. We describe their potential contribution to structural analyses and possible challenges (e.g., material, instrumental, data analysis), which needs to be taken into account. Further, we illustrate the practical application of these techniques on elementary (Ge, Sb, Te), binary (GeTe, Sb_2Te_3) and ternary alloys (GST) alloys. We highlight the previously reported results obtained in the different domains of material analyses, e.g., atomic arrangement, local structure and microstructure analyses or studies of nitrogen bonding in the GST alloys and oxidation effects. Finally, we complete the chapter by presenting the samples preparation of the studied elemental systems and Ge-rich GST alloys along with the experimental parameters of the measurements techniques used in this work.

2.1 Introduction to material characterization

Various characterization techniques are employed nowadays in material analysis, based on the different interactions of photons, electrons or ions with a studied material. Advanced material characterization can provide a deep insight in the material structure and determine the electronic, optical, thermal and mechanical properties of materials [173]. Table 2-I summarizes different domains of material characterizations along with the characterization techniques applied in this work. The basic principles, interests and challenges in employing these techniques for phase-change material investigation, notably for GST alloys, are briefly discussed in the following sections. The theoretical background of the characterization techniques the most widely applied in this work (i.e., FTIR spectroscopy, Raman spectroscopy and XRD) is described in the Appendix 1.

Table 2-I: Different categories of material characterization according to the field of study and the characterization techniques used in this work.

Material characterization categories	Characterization techniques
Electrical properties	Resistivity measurements
Optical characterization	FTIR spectroscopy, Raman spectroscopy, spectroscopic ellipsometry
X-Ray characterization	XRD, XPS, WDXRF, XAS
Microscopy	TEM-EDX

2.1.1 Electrical properties

The *in-situ* resistivity measurements during the sample annealing (R vs T) are generally performed using a specific annealing ramp and the amorphous-to-crystalline phase transition of the material is observed. As the high resistive amorphous material begins to crystallize, the resistivity sharply decreases reaching low values for the formed crystalline phase. The resistivity values remains low upon sample cooling back to the room temperature. The material resistivity is usually characterized by 4-point probe technique applying the passing current through the outer probes and measuring the voltage through the inner probes. As a result, sheet resistance of the material is determined.

The R vs T curve (Fig. 2.1) can provide plenty of information. The slope angle of the resistivity drop can indicate the nature of the crystallization process, i.e., rapid growth-dominated crystallization (sharp resistivity drop) or slower nucleation-dominated crystallization (more gradual resistivity drop). The resistivity value of the crystalline state brings additional information concerning the reading window and efficient programming current (and hence the power consumption) of the final PCRAM device [24]. R vs T measurements performed with different annealing ramps are used in Kissinger analysis, calculating the value of activation energy of the crystallization (E_A) [174,175]. Using the data from the samples annealed at different temperatures, the retention properties of RESET state can be evaluated based on the Arrhenius plot [17,24]. This equation allows to extrapolate the maximum temperature (fail temperature) to evaluate the system stability (i.e., 10 years of data retention).

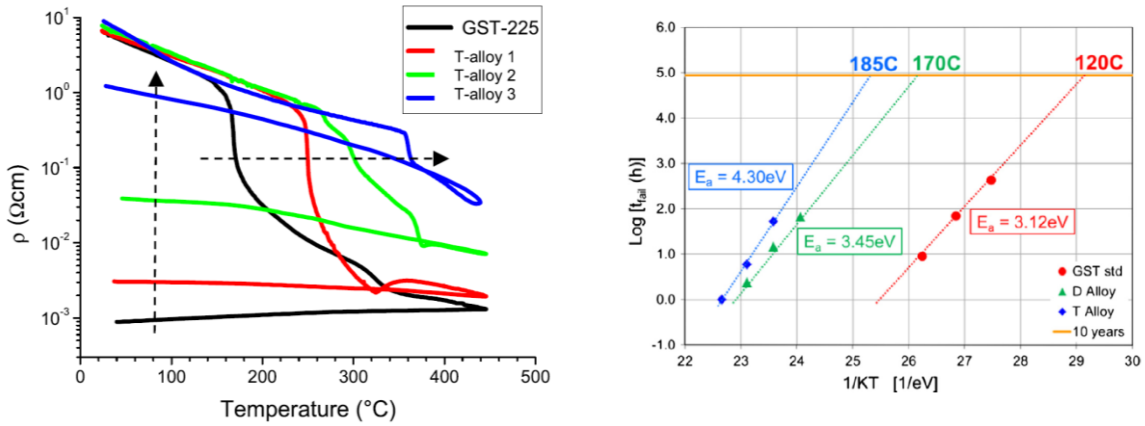

Fig. 2.1: (left) R vs T curves of $Ge_2Sb_2Te_5$ (GST225) and three different Ge-enriched GST alloys referred as T-alloys; (right) Arrhenius plot extrapolation for 10 years of RESET data retention of GST225, D-alloy and one specific T-alloy [24,143].

2.1.2 Vibrational spectroscopies

Raman and Fourier Transform Infrared (FTIR) spectroscopies belong to the group of vibrational spectroscopies. They provide the identification of vibrational modes related to specific bonds or structural units. Depending on the specific selection rules based on the different principles of these techniques, the vibrational modes can be IR-active, Raman-active or both. FTIR spectroscopy is based on the absorption process of the IR radiation. The interaction of the IR radiation with the molecules is described in terms of a resonance condition, where the specific IR radiation frequency matches the frequency of a normal vibrational mode of the molecule. The energy of the IR radiation is absorbed only under the condition that the molecular vibration changes the dipole moment of the molecule, derived from partial charges on the atoms. For the approximation, the partial charges can be estimated from the electronegativity values. On the contrary, Raman spectroscopy is based on scattering mechanism, involving the polarizability of the molecule and induced dipole moment. It is a two-photon inelastic event, in which the incident photon interacts with the molecule and loses part of its energy to the molecular vibration, while the remaining energy is scattered as a photon with changed frequency, giving rise to two possible energy shifts (i.e., Stokes and anti-Stokes scattering). In general, IR spectroscopy is a suitable technique for the observation of polar groups and the asymmetric vibrations of the molecules [173,176,177], while symmetric and in-phase vibrations of non-polar bonds or groups are more easily studied by Raman spectroscopy.

The symmetry elements, such as planes, axes or center of symmetry are applied in order to classify the molecules and to describe their vibrations. Group Theory provides useful analysis, determining the number of normal vibrations in each symmetry species and giving the approximate idea of the vibrational spectra patterns. The Mulliken symbols (e.g., A_{1g}, E_u) are then widely used to describe the symmetry of a vibration [178]. The vibrational bands in IR and Raman spectra are characterized by frequency, intensity and band shape. Since the vibrational energies are unique to each molecule and depend on the masses of the atoms, geometric arrangement and chemical bonds, the IR and Raman spectroscopy techniques provide unique information about a molecule, such as its structure and chemical environment.

FTIR and Raman spectroscopies find their application for the investigation of undoped and N-doped GST alloys, as these techniques can provide useful information about both amorphous and crystalline structure. As the ternary Ge-Sb-Te system is quite complex, GST alloys provide various vibrational modes. The identification of vibrational modes in such alloys can be then based on structural analysis of elemental (Ge, Sb and Te) and binary

(GeTe, Sb_2Te_3) systems. For example, the investigation of GeTe alloys by Raman spectroscopy performed in [179] provides the description of GeTe vibrational modes related to various $GeTe_{4-n}Ge_n$ (n = 0, 1, 2, 3, 4) structural units. FTIR spectroscopy, on the contrary, seems to be effective for the identification of bonding with nitrogen. GeN alloys studied in [180–182] can be shown as a good example, discussed more in detail later in the section 2.2.1. The investigation of GST alloys by FTIR and Raman spectroscopy, however, can also meet several challenges. For the FTIR spectroscopy, the thickness of the layer can be limiting. Thin layers (tens of nm) cannot possibly give the signal strong enough when employing the classical transmittance mode of measurements, resulting in highly noisy IR spectra and therefore more difficult or imprecise analysis. The application of oblique angles of incidence or measurements in reflectance mode could overcome this problem of low sensitivity in such layers. Moreover, IR measurements can be affected by substrate and encapsulation layer choice, their thickness and transparency in the investigated IR region. For example, SiO_2 and TiN as encapsulation layers are not suitable due to their absorption.

In Raman spectroscopy measurements, the choice of laser excitation source is particularly crucial. Laser wavelength, power, density and duration of the laser exposure need to be considered. Raman scattering intensity is proportional to the fourth power of the excitation frequency ν^4, thus stronger signal is expected for shorter excitation wavelengths. On the other hand, for non-transparent samples, longer excitation wavelengths allow deeper light penetration. This variation of the optical density of a material as a function of laser wavelength allows performing the depth profiling of some materials, notably the semiconductors [183]. Strong phenomena, such as fluorescence and absorbance, can also occur as side effects, causing strong interference in the Raman spectra. Moreover, high laser energy or intensity can lead to destructive effects in a material, such as sample heating, photodecomposition or laser ablation [184]. The examples of application of FTIR and Raman spectroscopies in the investigation of GST alloys are shown in the sections 2.2.3 and 2.2.4.

2.1.3 X-ray characterization

X-ray characterization employs electromagnetic radiation with energy between 125 eV and 125 keV and wavelength λ between 0.01 nm and 10 nm and includes a large range of techniques. The interaction of X-rays with a material results in two main processes: scattering and photoelectric absorption.

The elastic scattering is used by X-ray Diffraction (XRD) studying the diffraction process and therefore the microscopic structure in crystalline materials. XRD measurements performed in classical Bragg-Brentano configuration with θ-2θ scan mode result in XRD patterns with diffraction peaks, whose positions and intensities allow the identification of the crystalline phase by the comparison with Powder Diffraction File (PDF) cards in a database. Moreover, the relative intensities of the peaks in XRD pattern can provide information about preferred orientation of the crystalline grains. The diffraction angles and the calculated d-spacing are used to determine the lattice constants. The peak width, in particular the value of full width in half maximum (FWHM) can be used to calculate the average crystallites size (L) by the Scherrer's equation:

$$L = \frac{K\lambda}{\beta cos\theta} \tag{2.1}$$

Where, K is the shape factor, λ is the wavelength and β is the diffraction peak broadening at FWHM after subtracting the instrumental broadening. The use of Scherrer's equation assumes that the crystallites size is the only contribution of the line broadening and neglects possible microstrain and defects contributions to the peak width. However, the strain and stress in the material as well as preferred grain orientation can be further investigated employing different

measuring configurations, i.e., changing the angle between the incident beam and the sample or using the sample rotation. The examples of XRD analyses on GST alloys are given in the section 2.2.6.

In the process of the photoelectric absorption, the X-rays are absorbed by an atom and the energy is transferred to an inner-shell electron. This photoelectron is ejected, keeping the excess of the energy from the incident X-rays and leaving the atom in an excited state with an empty inner electronic shell. X-ray Photoelectron Spectroscopy (XPS) uses this effect and measures the kinetic energy of the ejected photoelectron, which allows to analyze the original binding energy of the electron, particular to each element, following the formula:

$$E_K = h\nu - E_B \tag{2.2}$$

Where E_K and E_B are the kinetic and binding energy of the electron, respectively, and $h\nu$ is the energy of incident X-ray.

The created hole is filled by an electron from outer shells (higher energy levels), emitting photons with the energy corresponding to the difference of energies between the involved electronic levels (Fig. 2.2). This photon energy is used in X-ray Fluorescence (XRF) analysis. Another related process of electronic recombination can occur, when the energy between the involved electronic levels is transferred to another electron from outer shells, which is consequently ejected from the atom (Auger electron).

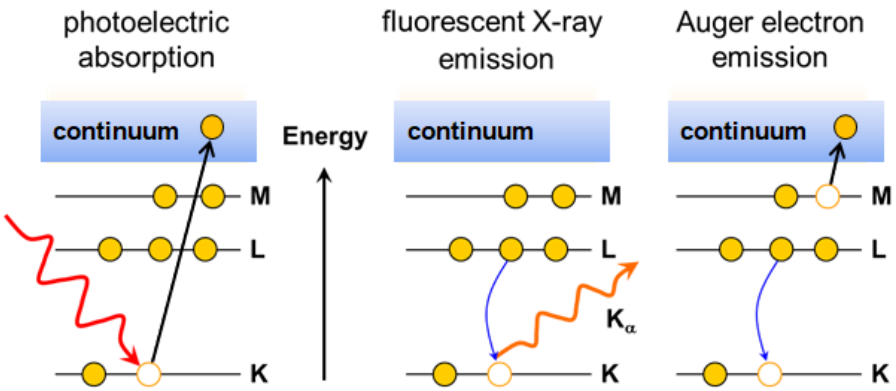

Fig. 2.2: Schematic representation of photoelectric absorption, and electron recombination filling the hole in inner electron shell by resulting in fluorescent X-ray emission and Auger electron emission.

Moreover, X-ray absorption spectroscopy (XAS) techniques can be employed. The spherical wave function of a photoelectron ejected during the photoelectric absorption process interferes with the waves backscattered from neighboring atoms, resulting in oscillations above the absorption edge in the spectrum (Fig. 2.3), i.e., changes in X-ray absorption coefficient $\mu(E)$. XAS techniques measure the energy dependence of the $\mu(E)$, providing a unique information about local atomic structure of a selected element. Two regions can be discerned in X-ray absorption spectra: XANES (X-ray Absorption Near-Edge Structure) and EXAFS (Extended X-ray Absorption Fine Structure).

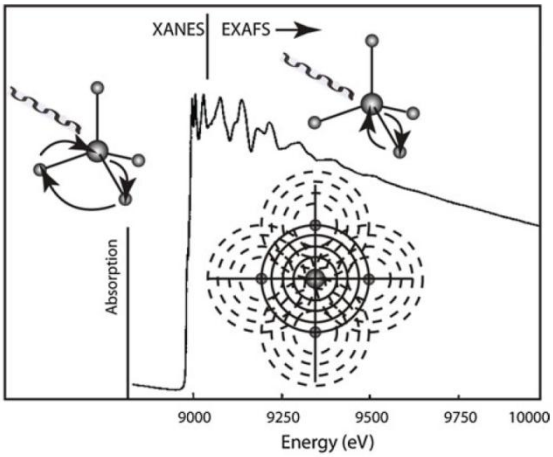

Fig. 2.3: Absorption spectra showing the absorption edge and the oscillation above the absorption edge. Pre-edge, edge and near-edge regions are studied by XANES, the oscillations above the absorption edge are studied by EXAFS. The upper insets show multiple scattering and single scattering processes responsible for XANES and EXAFS features, respectively. The lower inset illustrates the scattering interference between the onward and back-scattered waves [117].

XRF and XPS techniques allow the qualitative analysis of the material, providing elemental information. Moreover, XPS provides uselful information of the chemical state and the electronic structure of a material. These techniques can also provide quantitative analysis of the chemical composition, which can be employed as non-destructive metrology in process control. Precise calibration protocols are, however, necessary for XRF quantitative analysis, using standard samples for the calibration or establishing the calibration curve by means of other techniques probing the composition and elemental depth profiles, such as for example Ion Beam Analysis (IBA).

In contrast to XRD studying the microstructure of the crystalline phase, XAS analyses provide information about local atomic arrangement around the selected element. In particular, XANES provides the information about the electronic structure, covalency, oxidation states and site symmetry, while the analysis of the EXAFS signal can determine the type of the neighboring atoms, bond distances and average coordination number. These techniques and their analyses are, however, time-consuming and highly demanding on the equipment, requiring the synchrotron source for incident X-ray radiation. The examples of GST characterization by X-ray techniques are provided in the sections 2.2.4 and 2.2.5.

2.1.4 Transmission Electron Microscopy

Transmission electron microscopy (TEM) utilizes high energy electrons to characterize a material. It can provide morphologic, compositional and crystallographic information from a sample, depending on the employed measurement mode [173]. For example, scanning mode of an electron beam across a sample (STEM) makes these microscopes suitable for analytical techniques, such as mapping by energy dispersive X-ray spectroscopy (EDX), electron energy loss spectroscopy (EELS) or annular dark-field imaging (ADF). These signals can be obtained simultaneously, allowing direct correlation of image and spectroscopic data. Using a high-angle annular dark-field (HAADF) detector, it is also possible to obtain atomic resolution images where the contrast is directly related to the atomic number (sometimes called Z-contrast image) [173]. On the other hand, sample preparation can present major difficulties for TEM analysis, as it is usually time consuming requiring the application of special preparation techniques, e.g., focused-ion beam, mechanical polishing or chemical etching.

The application of TEM analysis for phase-change materials can contribute to the investigation of microstructure at nanoscale level, providing complementary information to XRD analysis probing larger sample volumes. TEM-EDX mappings allow to directly observe the phase segregations and the formation of enriched zones in the studied material. Moreover, it can provide the insight into the degradation mechanisms of a material during PCRAM cells operation (Fig. 2.4) [5].

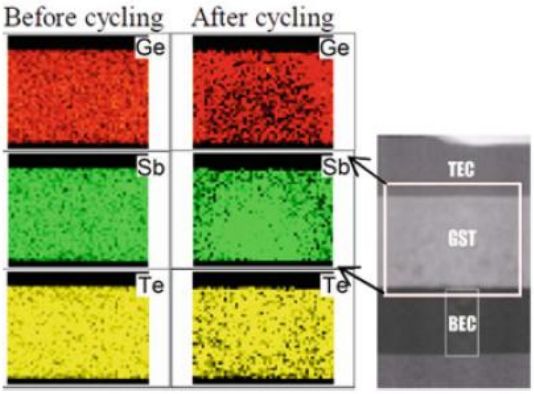

Fig. 2.4: TEM-EDX analysis showing the behavior of a GST alloy before and after PCRAM device cycling. The images after cycling highlight the formation of Ge-poor and Sb-rich region in the GST alloy [5].

2.2 Material characterization of GeSbTe alloys

Employing a wide range of characterization techniques enables to probe the structure of phase-change material and give some insights into both amorphous and crystalline phases. Depending on the chosen characterization method, different information can be obtained, as illustrated in Fig. 2.5. The application of several techniques provides complementary information, thus enabling to demonstrate the overall picture of material structure and crystallization mechanism. For example, while Raman and FTIR spectroscopies refer to bonding arrangement in the alloys, probed in both amorphous and crystalline phases, complementary information can be provided by XRD studying the developed crystalline phases of a material, identifying the lattice parameters, crystal orientation and size or internal strain and stress. Besides, the experimental characterization techniques can be accompanied by *"ab initio"* simulations, being largely applied in recent years. The application of various characterization techniques in the investigation of several issues related to GST alloys are presented in the following sections.

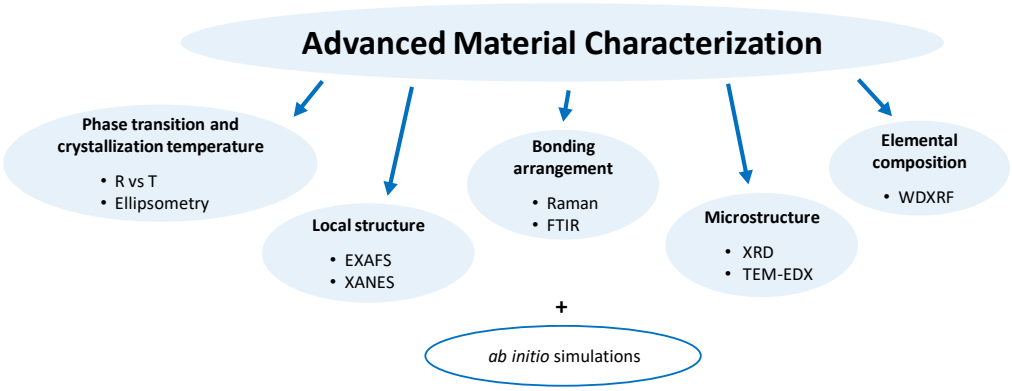

Fig. 2.5: Schematic representation of the different fields of study, allowing to obtain information about the material structure, bonding and atomic arrangement. The characterization techniques, applied in this work, are shown to illustrate how to provide such kind of information. Ab initio simulations can complete the experimental techniques, providing unique insight into the material structure.

2.2.1 Bonding arrangement in elemental alloys

Raman spectrum of amorphous Ge (a-Ge) shows a broad band in the range from 30 cm^{-1} to 300 cm^{-1}, consisting of four contributions, which are labeled as transverse/longitudinal optic (TO, LO, respectively) and acoustic (TA, LA, respectively)–like modes (Fig. 2.6), the terms derived from density of states. These modes need to be understood as symmetric bending and stretching vibrational modes of Ge-Ge bonds in amorphous structure [185,186]. The crystalline Ge (c-Ge), on the contrary, features only one sharp peak in Raman spectra at 300 cm^{-1}. The observation of vibrational modes in elemental Ge allows the identification of related bonds in more complex systems, such as Ge-rich GST alloys, as shown later in Chapter 4.

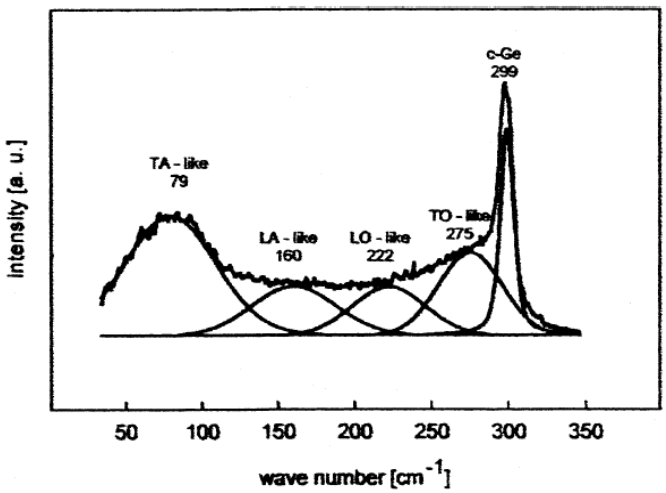

Fig. 2.6: Raman spectrum of Ge layer, showing the amorphous (TO-, LO-, LA- and TA-like) modes in the range from 30 – 300 cm^{-1} along with the intense sharp peak at 300 cm^{-1} of the Ge crystalline phase (c-Ge) [187].

Undoped Ge layers were studied particularly by Raman spectroscopy, while FTIR spectroscopy demonstrated to be useful for the investigation of N-doping effect in amorphous Ge network. A band with maximum at about 700 cm^{-1} (Fig. 2.7) was observed in GeN alloys studied in [180]. The band integrated intensity was reported to increase with the N content in the alloy (up to 36 at.% of N). This band is assigned to the vibrations of in-plane asymmetric stretching vibration of Ge_3N group, formed by planar bonded N atom with three Ge neighbors [180,188]. For low N content in Ge, only one contribution to the absorption band is evidenced. However, for higher N content, an asymmetric form of the band is observed, indicating the presence of additional contributions. These contributions are reported to result from Ge-N vibrations of the same Ge_3N group in different environments. Indeed, nitrogen is more electronegative than germanium and its increasing content in the alloy gives rise to modifications in the electronic charge distribution around the germanium atoms, changes in Ge-N interatomic distance and thus to the frequency shift of the vibrations to higher wavenumbers. Some of the configurations of the additional absorption bands are depicted in Fig. 2.7; however, other configuration possibilities are not excluded. Indeed, any change in stoichiometry by addition of N may result in multiple configurations, slightly modifying the vibrational frequency. The illustration of discrete modes resulting from different atom coordinations around Ge_3N group is beneficial, but only one broad additional contribution can be also suggested, including large variety of configurations. Moreover, the presence Ge dangling bonds was suggested, associated with coordination defects in the structure (due to fluctuation in the bond angles and lengths), inducing a broad absorption band at about 1100 cm^{-1}. However, the indicated frequencies of these additional bands may slightly vary as a function of subtracted background in the IR spectrum and the performed baseline correction.

The results presented in [180] and shown in Fig. 2.8 consider higher slope for the IR spectra of GeN alloys with high N content including its intensity to IR band contributions, as the baseline was determined at zero value of the absorption coefficient. Different choice of baseline subtraction in order to avoid the background effects would reduce the slope of IR spectra, hence slightly changing the values of position and integrated intensity of presented contributions.

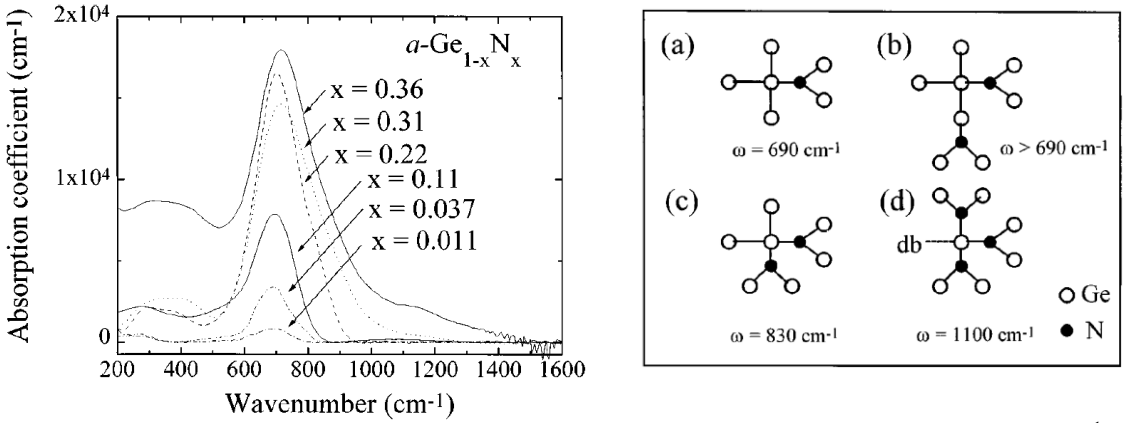

Fig. 2.7: (left) IR spectra of GeN alloys, highlighting the band of Ge_3N vibrational modes at 700 cm^{-1} and its intensity increase with N content in the alloy; (right) Schematic representation of different chemical environments of Ge_3N structural unit, suggested to induce the frequency shift of the Ge-N vibration [188].

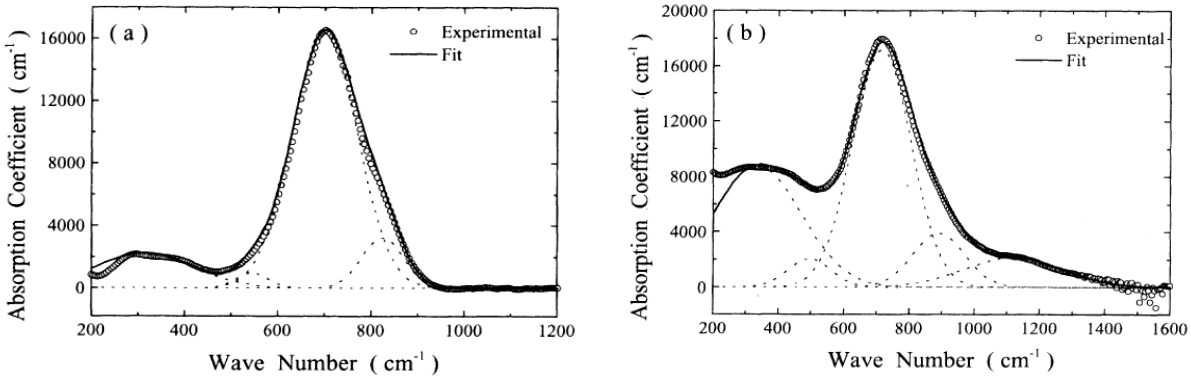

Fig. 2.8: IR spectra of GeN alloys with the band of Ge_3N vibrational modes at 700 cm^{-1} showing several band contributions and their evolution as a function of N content, while the baseline is kept at zero value of absorption coefficient for (left) N content of 22 at.%; (right) N content of 36 at.%. The IR spectra of GeN with N ~36 at.% highlights the increased intenisty of contribution at 300 cm^{-1} (disorder-induced breathing mode) and additional contribution at 1100 cm^{-1} (dangling bonds contribution) [180].

Antimony crystalline structure does not feature any IR-active vibrational modes. Raman spectrum (Fig. 2.9) shows two sharp peaks at ~110 cm^{-1} and ~145 cm^{-1}, corresponding to E_g and A_{1g} modes, i.e., in-plane vibrational mode and out-of-plane vibrational mode, respectively [189–191]. Furthermore, low intense second-order Raman scattering can be observed at 240-300 cm^{-1}. The investigation of amorphous Sb (a-Sb) layers has been limited, due to rapid crystallization at room temperature, which poses several challenges to a-Sb layers preparation. The Raman spectrum of a-Sb layer deposited at low temperature (100K) was acquired, showing relatively structureless higher-frequency band in the Raman spectrum with maximum at 150 cm^{-1} [192]. Recently, the hindered crystallization of Sb was observed in ultrathin films (3-10 nm-thick) encapsulated by capping layers [193]. Such ultrathin layers could provide new possibilities for material characterization; however, their thickness could also present several challenges for different characterization techniques. Nevertheless, the Sb

confinement at nanoscale already brings some promising results, such as reduction of structural relaxations responsible for aging or the drift in time of the electrical conductivity in the amorphous phase. These properties of ultrathin Sb layers are also suggested to be further exploited for precise Neuromorphic computing and for Photonic applications [191,193].

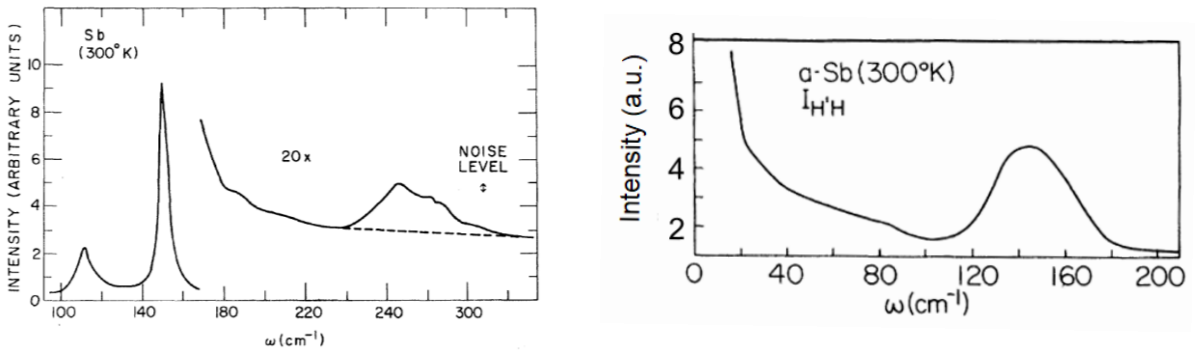

Fig. 2.9: (left) Raman spectrum of crystalline Sb, highlighting two sharp peaks at 110 cm^{-1} and 145 cm^{-1} corresponding to E_g and A_{1g} vibrational modes, respectively. The inset shows the second-order scattering at 240-300 cm^{-1}; (right) Raman spectrum of amorphous Sb (a-Sb) highlighting only one broad band related to a-Sb vibrational modes at 150 cm^{-1} [189,192].

Concerning the crystalline structure of Te, several works have been reported [194–197]. The crystal lattice of trigonal Te can be seen as built up of helical chains located at the corners and center of hexagonal array. The helical chains along the c axis are completed every third atom (Fig. 2.10). The bonding between the atoms in the chains has a covalent character, whereas the bonding between atoms in adjacent chains is weaker (van der Waals type) [194,198]. The IR and Raman vibrational modes were reported in [194]. Four optic modes, corresponding to two non-degenerate (A_1, A_2) and two doubly degenerate modes (2 E) were identified (Table 2-II). In an idealized crystal, the frequencies of the A_1 mode and the 2 E modes are determined by covalently bonded atoms in the chains, whereas the frequency of the A_2 mode is solely due to weak inter-chain interactions. Comparisons of the A_1 and A_2 modes frequencies can give an idea of the relative strength of the inter- and intra-chain forces. On the other hand, the comparison of the frequencies of the two E modes can give information about the intra-chain forces [194].

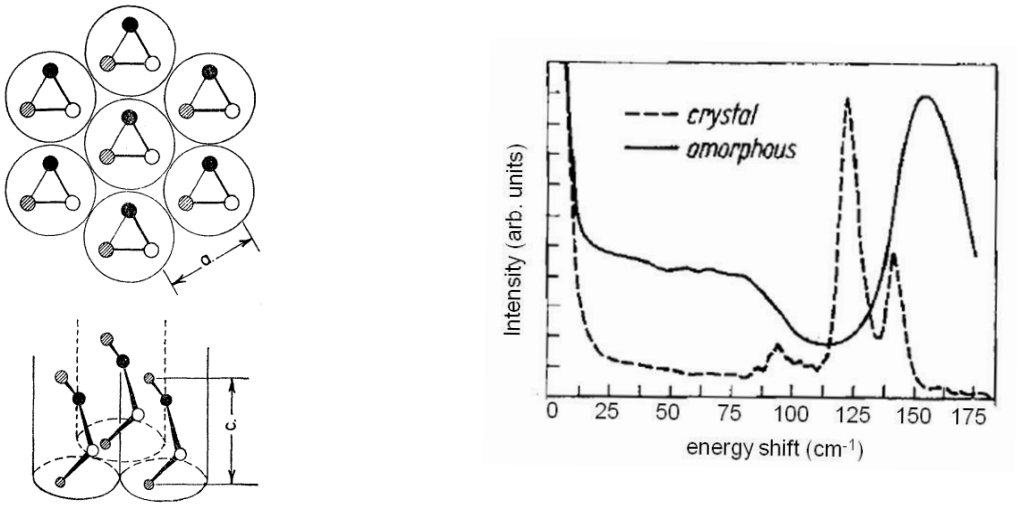

Fig. 2.10: (left) Schematic representation of Te crystalline structure along the a (top) and c (bottom) axis. Similarly shaded atoms are at the same level in neighboring chains and above each other in the same chain; (right) Raman spectra of crystalline and amorphous Te, highlighting the sharp peaks of crystalline Te modes at ~90 cm^{-1}, ~120 cm^{-1} and at ~140 cm^{-1} and broad band of amorphous Te at ~150 cm^{-1}[195,199].

Table 2-II: Vibrational modes of crystalline Te structure and their phonon frequencies, along with the notation if they are IR- or Raman-active [194].

mode		Phonon frequencies (cm^{-1})	spectrum
A_1	Symmetric breathing	122	Raman
A_2	Rigid chain rotation	88	IR
E	Symmetric stretching / intra-chain rotations	93	IR / Raman
E		142	IR / Raman

Amorphous Te (a-Te) is reported to crystallize at 10 °C and is unstable at room temperature [199]. The Raman spectrum of a-Te acquired at low temperature (77K) is dominated by broad band at ~150 cm^{-1} accompanied by low intense shoulder at 90 cm^{-1} (Fig. 2.10). It was suggested that this vibrational frequency is proper to Te chains, which is, in Te crystal structure, depressed to be in the range of ~90-140 cm^{-1} due to ordered structure and long range interactions [199]. Contrary to Sb, the investigations of a-Te brought some interpretations about the bonding arrangement in the amorphous structure. It was proposed that a-Te consists of short chains with less than 10 Te atoms. It was also shown that the intra-chain bond length is decreased relative to c-Te, while the inter-chain distance is increased [199–201]. These interpretations were recently confirmed by density functional studies on calculated a-Te structures [202].

2.2.2 Investigation of electrical and optical properties

The R vs T plot of different phase-change materials is shown in Fig. 2.11. A large contrast between amorphous and crystalline phases can be observed, reaching up to five orders of magnitude for N-doped GST alloy. The sharp drop of resistivity indicates the different crystallization temperature T_x, related to the stability of the amorphous phase. Alloys with higher crystallization temperature are preferred as they can meet the material stability requirements for embedded and automotive applications. Sharp resistivity drop can be observed in the case Sb_2Te, GeSb and AIST alloys corresponding more likely to the growth-dominated crystallization, whilst more gradual resistivity drop in GST and N-doped GST rather indicates the nucleation-dominated crystallization.

Complementary to R vs T dependencies, the measurements of optical reflectivity as a function of temperature can be performed using the *in-situ* ellipsometry. The phase transition in phase-change alloys is accompanied by a large contrast in optical reflectivity, demonstrating low values for amorphous phase and high values for crystalline phase (Fig. 2.11). The sharp transition of the reflectivity can also serve for the determination of T_x. A shift of the T_x to higher temperatures can be observed with increasing N content in GST alloy, as well as changes in the transition dynamics. Indeed, *in-situ* ellipsometry analysis confirmed the effects of N doping on transition kinetics, i.e., the reduction of both nucleation and growth rates along with the increase activation energy for crystallization [174,203].

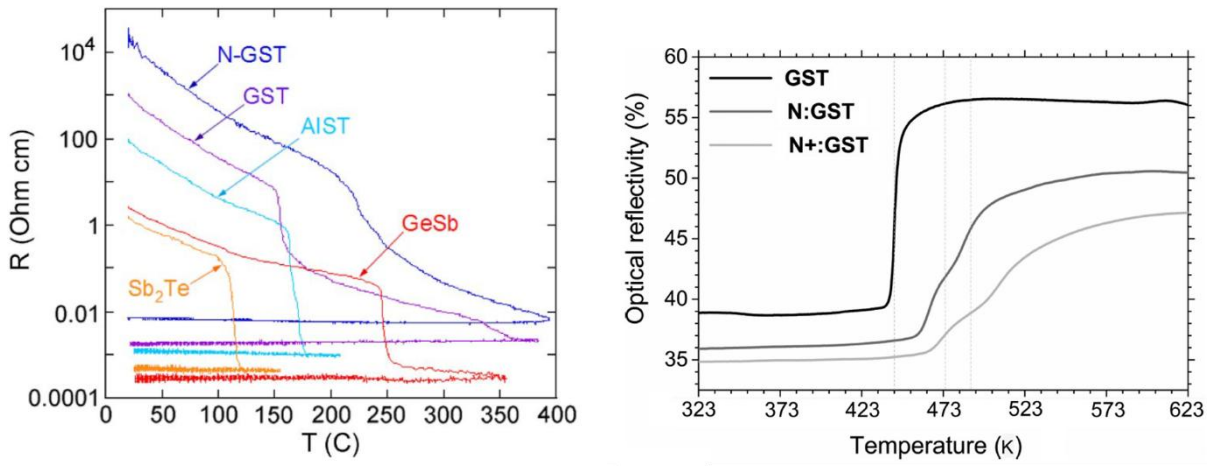

Fig. 2.11: (left) R vs T curves of different phase-change alloys; (right) Optical reflectivity as a function of temperature for GST and two N-doped GST alloys [26,203].

The R vs T curve can be affected by several factors, such as such as film thickness, heating rate, deposition method and parameters. The R vs T plots of $Ge_2Sb_2Te_5$ films with reduced thicknesses (Fig. 2.12) showed the significant increase of crystallization temperature (from about 150 °C to 250 °C). The phenomenon is likely related to the reduced amount of material available for the nuclei formation and thus the initiation of crystallization. Also, reduced crystallization speed was observed when the film thickness was reduced under a certain value (<10 nm) due to the grain growth stopped along the direction of layer thickness [204,205]. Concerning the impact of heating rate on R vs T curves of $Ge_2Sb_2Te_5$, the amorphous-to-crystalline phase transformation shifts towards higher temperatures with increasing heating rate. Simultaneously, the calculated overall activation energy of crystallization E_A was significantly reduced, resulting likely from the reduced activation energies for both nucleation and growth due to enhanced atomic diffusion at higher temperatures [175].

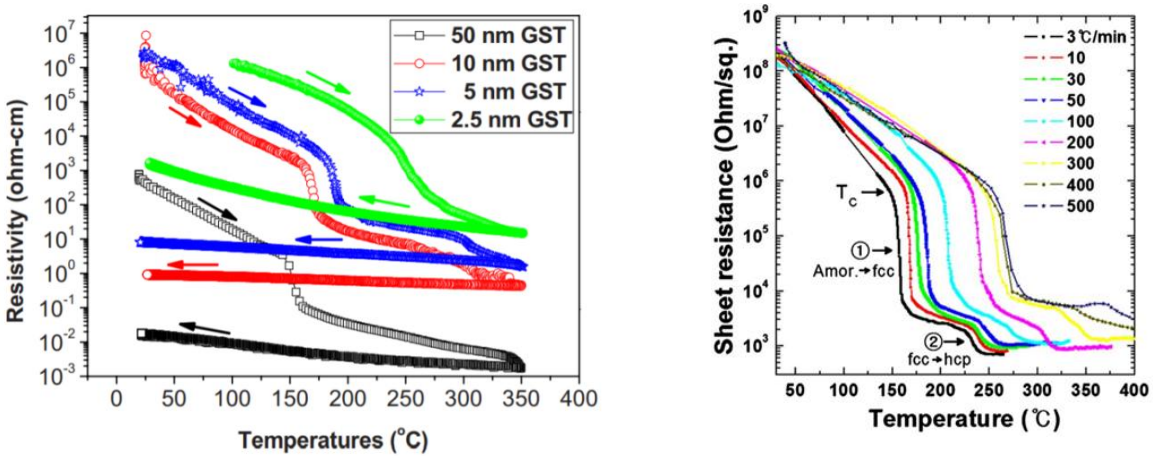

Fig. 2.12: (left) R vs T curves of the $Ge_2Sb_2Te_5$ films with various thickness highlighting the shift of the phase transition to higher temperatures with reduced layer thickness; (right) R vs T curves of the $Ge_2Sb_2Te_5$ films annealed with different heating rates [175,204].

2.2.3 Identification of structural units

Raman spectroscopy has demonstrated to be a suitable method for the identification of structural units present in chalcogenide alloys, either in the amorphous or the crystalline phases. Moreover, the spectral analysis of parental binary alloys can contribute to better understanding of the structural arrangement of more complex systems, such as ternary GST (Fig. 2.13). The Raman spectrum of as-deposited crystalline GeTe alloy shows two sharp peaks at 122 cm^{-1} and 141 cm^{-1} assigned to E_{2g} and A_{1u} vibrational modes of Ge-Te bonds, respectively [206,207]. The spectra of as-deposited crystalline Sb_2Te_3 alloy shows three peaks at 68 cm^{-1}, 112 cm^{-1} and 166 cm^{-1}, assigned to the A_{1g} and E_{2g} vibrational modes of Sb-Te bonds [127,208–210]. The Raman spectrum of as-deposited amorphous $Ge_2Sb_2Te_5$ alloy features a broad band between 100 cm^{-1} and 200 cm^{-1} indicating several contributions. The dominant contribution at ~150 cm^{-1} can be related to various vibrational modes, likely rising from both Sb_2Te_3 component and/or GeTe component. Moreover, Te-Te characteristic vibrational modes are known to also appear at the corresponding wavenumber [211]. However, Te-Te contribution can be excluded as it is very unlikely that Te-Te bonds exist in $Ge_2Sb_2Te_5$. EXAFS studies and *ab initio* calculations later confirmed their absence, showing the presence only of few dimers or trimers in disordered structure, which could not give rise such intense Raman band [96]. Taking into account the analogy with amorphous GeTe alloy, the band could be assigned to edge-sharing GeTe tetrahedra [179,212]. However, the most probable assignment refers to the stretching modes of $SbTe_3$ pyramids, supported by large spectra similarities with amorphous Sb_2Te_3, scaling analogy with the isomorphous Sb_2S_3 system and higher polarizability of the Sb_2Te_3 component in comparison with the GeTe [211,212]. The second contribution forming a broad shoulder at ~120 cm^{-1} is assigned to the vibrations of $GeTe_{4-n}Ge_n$ (n = 0, 1, 2) mixed units [179]. The Raman spectrum of $Ge_2Sb_2Te_5$ undergoes significant changes upon annealing. After annealing at 400 °C, $Ge_2Sb_2Te_5$ is known to be in the ordered hexagonal crystalline phase as confirmed by XRD [213,214]. The position of strong sharp peak at ~160 cm^{-1} corresponds to the A_{1g} mode of Sb_2Te_3 binary alloy, thus demonstrating that the Sb-Te units form the dominant structural order. On the contrary, the relative intensity of mixed GeTe modes decreases likely due to structure ordering, while the position of this contribution is maintained.

Besides the identification of the main structural units, Raman spectra can provide valuable information about the structural changes as a function of composition (Fig. 2.13). Broad Raman band between 100 – 200 cm^{-1} is shown to be common to different amorphous GST alloys along the GeTe-Sb_2Te_3 pseudo-binary line. As the Ge content in the alloys increases, slight shift of the main contribution to higher wavenumbers can be noticed as well as more pronounced contribution of GeTe modes at 120 cm^{-1} [215].

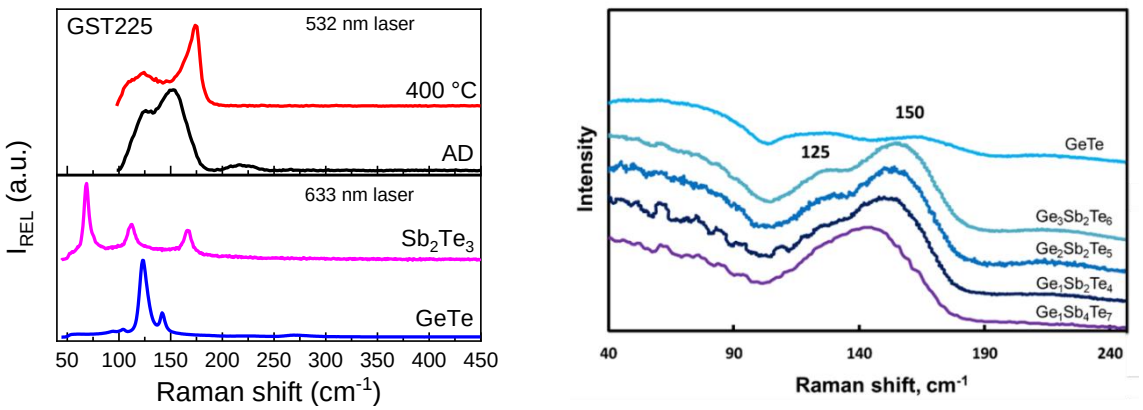

Fig. 2.13: (left) Raman spectra of as-deposited binary GeTe and Sb_2Te_3 alloys (633 nm laser), as-deposited (AD) and annealed $Ge_2Sb_2Te_5$ alloy (532 nm laser); (right) Raman spectra evolution as a function of GST alloys composition along the GeTe-Sb_2Te_3 pseudo-binary line [215].

2.2.4 N-bond formation and oxidation effects

Understanding the effect of light dopant elements when introduced into the structure of GST alloy becomes one of the key points for optimization of material properties. Either as a substituent or as an interstitial, the light dopant element will interact with GST alloy, possibly forming bonds with its elements. XPS has shown to be an effective technique to probe the binding states to display the formation of element-N bonding in the alloys (Fig. 2.14). Moreover, this technique can highlight the possible presence of molecular nitrogen in highly N-doped alloys. As a surface technique, XPS is particularly suitable to observe surface effects, such as layer oxidation by identifying the binding of the elements with oxygen [216–218].

Besides XPS, FTIR spectroscopy has also proven to be suitable for the observation of N bonds in GST phase-change alloys, as already shown in the section 2.2.1. While Ge or Sb elements are IR inactive in mid-IR range, doping the alloys by nitrogen leads to enhanced disorder, inducing a considerable charge transfer between these atoms and N atom and thus producing strong IR absorption bands. Indeed, this effect has been observed for N-doped Ge alloys (Fig. 2.7). Whereas XPS is a surface technique, FTIR spectroscopy considers the bulk structure of the studied material. Moreover, not only the type of bonding, but also the entire structural units can be identified. FTIR spectroscopy can also serve to examine the layer degradation. An example is shown on Fig. 2.15, where several bands appear in the IR spectrum after air exposure due to interaction of the layer with the atmosphere.

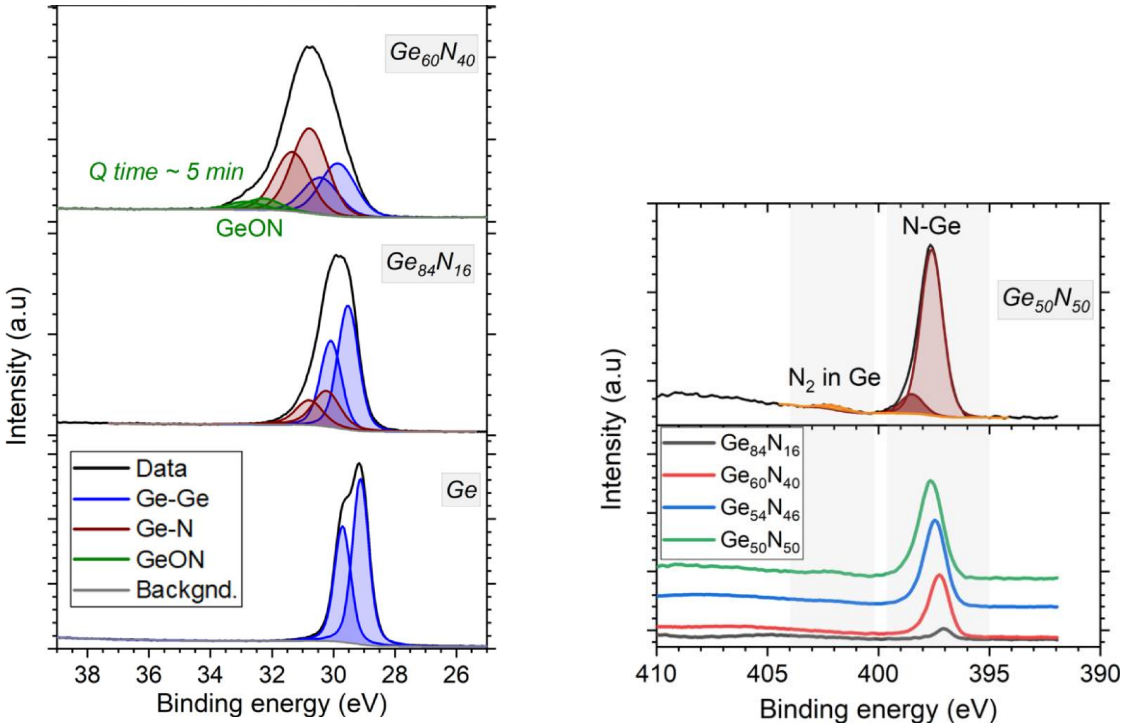

Fig. 2.14: XPS spectra of undoped and N-doped Ge compouds, demonstrating the different binding states and the formation of Ge-N bonding. (left) XPS Ge3d spectra highlighting the contribution of Ge-Ge, Ge-N and GeON binding states; (right) N1s spectra, highlighting Ge-N binding states and the presence of molecular N_2 in highly N-doped Ge [218].

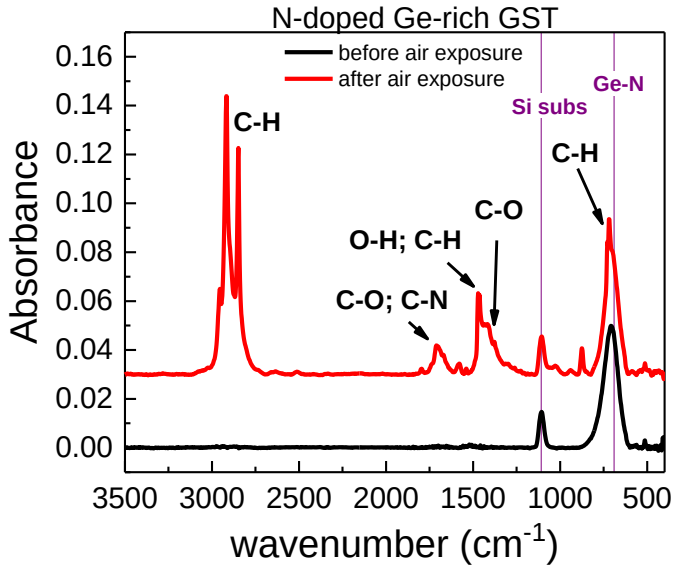

Fig. 2.15: IR spectra of annealed N-doped Ge-rich GST alloy before and after air exposure showing the layer oxidation.

2.2.5 Investigation of local environment

Employing the XAS technique to investigate the local environment of the GST alloy allowed revealing the presence of shorter and longer Ge-Te bonds in the GST structure and identifying the octahedral and tetrahedral coordination of Ge atoms in the amorphous and crystalline phases, discussed already in Chapter 1. These results provided the development of the umbrella-flip model describing the phase-transition. Recently, XAS studies were performed on crystalline GST alloys with innovative superlattice-like structure ($GeTe/Sb_2Te_3$) to investigate the structure at the layer interfaces and to observe the lattice distortion and atoms intermixing [219].

The experimental XAS studies started to be supported by density functional theory (DFT) calculations with AIMD simulations, in particular for the liquid or the amorphous phase. AIMD simulations allow to obtain a detailed picture of the structure and chemical bonding, while the calculations are employed to compute the electronic properties and their correlation with the material structure (Fig. 2.16). Owing to the simulations along with the experimental XAS data, the coexistence of tetrahedral and defective octahedral coordination of Ge atoms in amorphous phase was demonstrated [96] as well as the conflict between DFT and XAS interpretation of the presented umbrella-flip model [96,124]. The insight on the local structure and its geometry is obtained from the angle distribution function and the average coordination number, calculated from partial pair correlation functions. An important information can be further obtained by calculation of the vibrational density of states (VDOS), providing the distributions of vibration frequencies, which can be further compared to experimental data from Raman or FTIR spectroscopy [90,96,102,220,221].

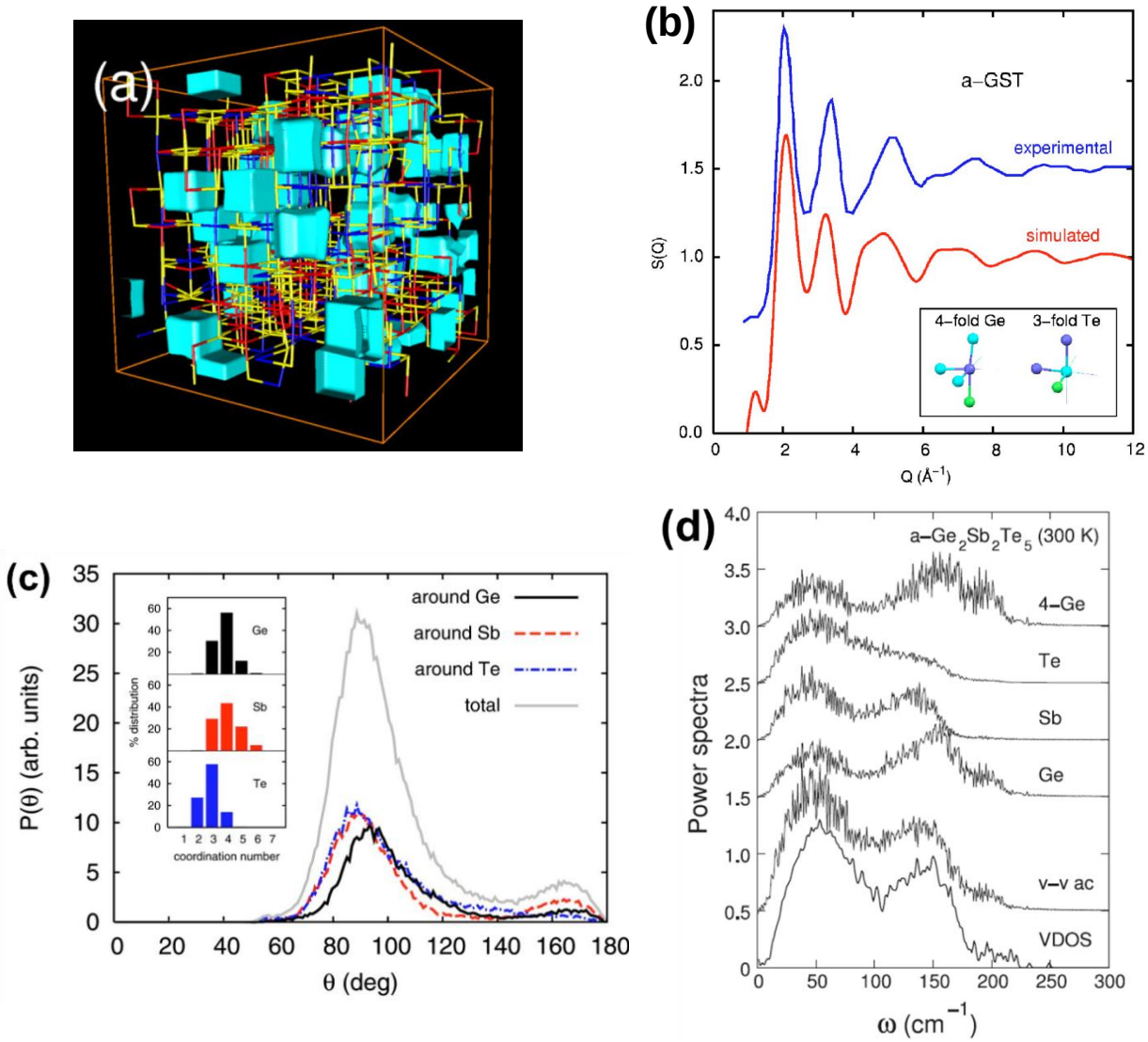

Fig. 2.16: a) Simulation of c-$Ge_2Sb_2Te_5$ system: Ge (red), Sb (blue), Te (yellow), vacancies (light blue); b) calculated and experimental x-ray scattering function S(Q). The inset shows the illustration of defective octahedral sites for 4-fold coordinated Ge and 3-fold coordinated Te atoms. c) Angle distribution function for Ge, Sb and Te atoms. The inset highlights the distribution of coordination numbers. d) Calculated vibrational densities of states for amorphous $Ge_2Sb_2Te_5$ using two different methods (VDOS and v-v- ac spectra) and partial vibrational densities of states for Ge, Sb, Te elements and 4-fold coordinated Ge [96,102].

2.2.6 Microstructure analysis

Complementary to invetigations presented in the sections 2.2.1 - 2.2.5, which focus on the local bonding arrangement and the structural units in the material, the microstructure of the crystalline phase can be effectively probed by XRD. The XRD patterns can give the information about crystalline phases, internal stress and strain, texture and crystallites size. As an example, the effect of N doping on $Ge_2Sb_2Te_5$ cubic crystalline structure is shown in Fig. 2.17. The increasing N content results in peaks broadening in the XRD pattern due to less developed cubic crystalline phase (reduced crystallites size). Higher N contents result in complete disappearance of the peaks related to cubic crystalline phase, followed by the appearance of new set of peaks related to the formation of $Ge_2Sb_2Te_5$ hexagonal crystalline phase.

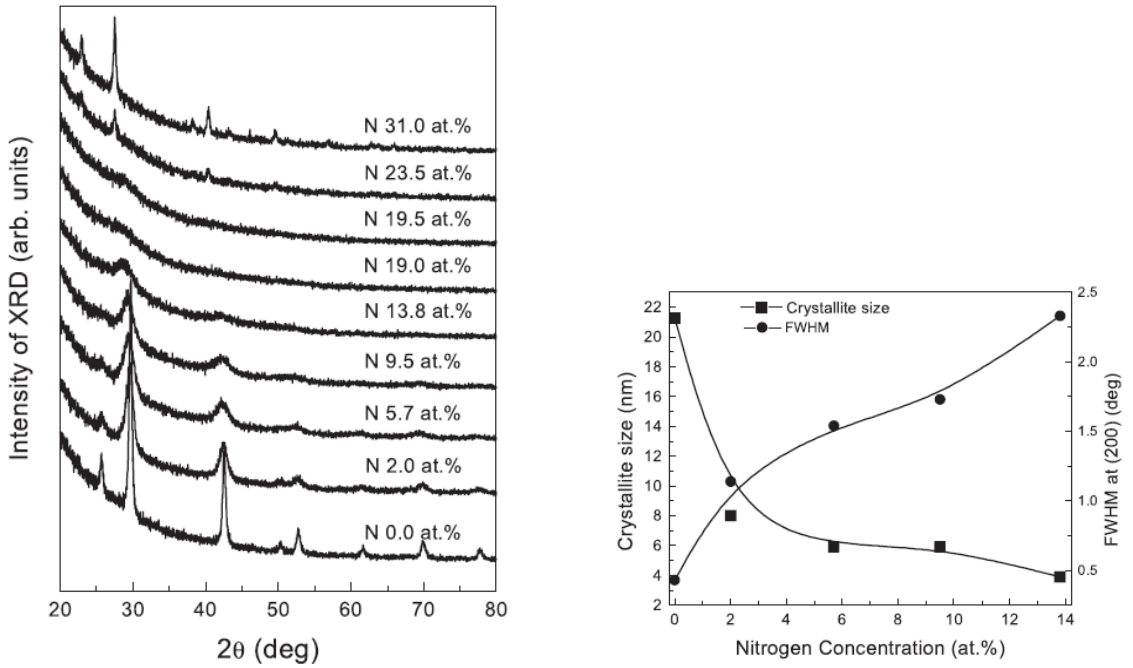

Fig. 2.17: (left) the impact of increasing N content on XRD patterns of crystalline $Ge_2Sb_2Te_5$ showing well-formed cubic crystalline phase for undoped alloy and hexagonal crystalline phase for N = 31 at.%; (right) The evolution of crystallites size and FWHM of the [200] peak as a function of increasing N content [152].

Recently, XRD studies characterizing structural and mechanical properties in undoped and N-doped $Ge_2Sb_2Te_5$ alloys were reported in [203,222]. The combination of *in-situ* XRD with X-ray reflectivity (XRR) was used to observe the volume shrinkage and to evaluate the strain and stress during alloy crystallization and upon N doping. The results demonstrated a considerable stress upon crystallization accompanied by density increase (1 - 4 %) and thickness reduction (1 - 10 %) depending on N content [203]. Subsequently, out-of-plane stress relaxation was observed, favored by the grain growth of the crystalline phase.

XRD results can be notably supported by TEM images with corresponding selected area electron diffraction (SAED) patterns (Fig. 2.18). TEM images can highlight the crystallization phases and the atomic order of the studied material, as well as possible voids formation or material segregation to element-rich/-poor zones. Indeed, Energy Dispersive X-ray Spectroscopy (EDX) combined with TEM can provide elemental mappings of studied alloys. Such studies, combining XRD and *in-situ* TEM analyses, were recently performed to investigate the crystallization process in undoped and N-doped Ge-rich GST alloys and the layer oxidation (Fig. 2.19) [3,4,223]. These studies demonstrated the coexistence of two crystalline phases, resulting from Ge and GST phase segregation upon alloy crystallization. It was concluded that the crystallization is activated through primary formation and crystallization of pure Ge regions, followed by crystallization of stoichiometric GST phase. These observations further suggest the nucleation-dominated phase change process with Ge homogeneous nucleation taking place randomly in Ge-rich GST layer. Although the studied layers were protected by thin TiN capping layer, oxygen diffusion was observed followed by oxygen accumulation in the Ge-rich regions of the layer.

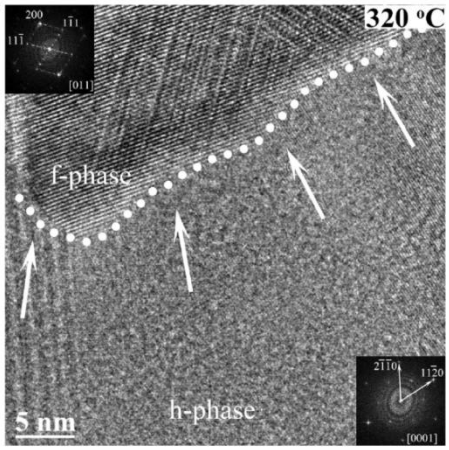

Fig. 2.18: HRTEM image of grain boundary at the transition between cubic crystalline phase (f-phase) and hexagonal phase (h-phase) [224].

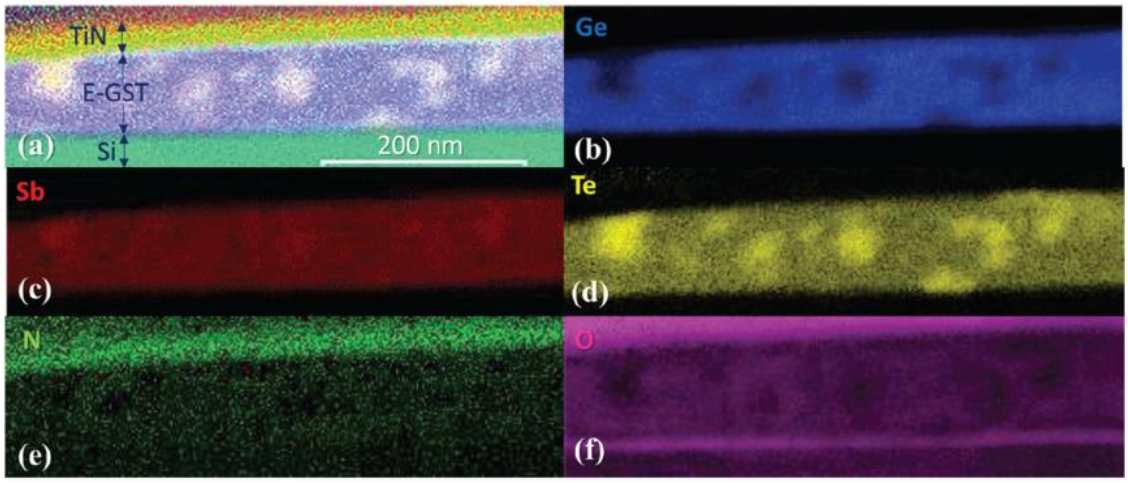

Fig. 2.19: TEM-EDX mapping of a Ge-rich GST alloy: (a) Superposition of the STEM EDX maps of (b) Ge, (c) Sb, (d) Te, (e) N and (f) O of the layer annealed at 400 °C for 30 minutes [3].

2.3 Sample preparation and the experimental part of the thesis

In this work, the undoped and N-doped alloys of two main groups of materials were investigated: a) Ge, Sb and Te elemental systems; b) Ge-rich GST alloys. The layers were deposited on 200 nm Si substrate wafers, if not specified otherwise in the text. The deposition by magnetron sputtering (for Ge, Sb and Te layers) and co-sputtering from Ge and $Ge_2Sb_2Te_5$ targets (for Ge-rich GST alloys) was performed (EVATEC CLN 200). The layer deposition was kept at room temperature. The undoped layers were deposited under Ar atmosphere. The N-doped layers were prepared by reactive sputtering from the same targets and with Ar/N_2 gas mixture in the deposition chamber. The different N contents in the layers were obtained by varying the ratio between Ar and N_2 gas flow during the film deposition. The layers were protected by *in-situ* deposited encapsulation layers to prevent surface oxidation. The summary of the deposited layers is listed in Table 2-III. The composition of the as-deposited layers was measured by Wavelength Dispersive X-ray Fluorescence Spectroscopy (WDXRF Rigaku AZX 400) using the methodology described in [225].

Table 2-III: Summary of deposited thin layers along with their parameters. The thickness of the layers was targeted to 100 nm. The layers were protected by thin carbon capping layer to prevent oxidation.

Thin layers	Doping	Atmosphere in deposition chamber	Layer thickness	Encapsulation
- Ge, Sb, Te - Ge-rich GST	Undoped	Ar	100 nm	Carbon layer ~3.5 nm
- Ge, Sb Te - Ge-rich GST	N-doped	Ar/N_2 mixture		

The *ex-situ* annealing was performed with a ramp-up of 10 °C/min. The samples of the layers were annealed for the duration of 5 minutes at the target temperature under inert N_2 atmosphere. The layers were characterized by the combination of several characterization techniques:

- RvsT measurements: the layers of $Ge_2Sb_2Te_5$, undoped and N-doped Ge-rich GST were deposited with similar process parameters on SiO_2 substrates and protected by a 10 nm-thick SiN capping layer for the purpose of RvsT measurements. The measurements were performed with four-point probe technique with a fixed heating rate of 10 °C/min.
- FTIR spectroscopy: The IR transmittance spectra converted to absorbance were acquired in the range from 4000 cm^{-1} to 30 cm^{-1} (Bruker Vertex 70VA) with the resolution of 4 cm^{-1}, accumulating 64 scans.
- Raman spectroscopy: Raman spectra were measured at room temperature (Renishaw InVia) using the 532 nm laser diode excitation source and the focusing lens with the magnitude 100x and numerical aperture 0.85. The measurements were performed in the Raman shift range from 100 cm^{-1} to 1000 cm^{-1}. The laser power was kept at low level (<0.6 mW) to avoid the heating and hence the induced modification of the layer morphology.
- Spectroscopic Ellipsometry: The *in-situ* ellipsometry (Woollam M2000) measurements of as-deposited Ge-rich GST samples were performed using the incident light in the visible range. The same ramp as in *ex-situ* annealing (10 °C/min) was used for the measurements.
- XRD: The data were obtained at room temperature with a two-circle diffractometer (PANanalytical Empyrean) using the Cu Kα radiation (λ = 1.5406 Å) as X-ray source. The measurements were performed in Bragg-Brentano geometry within the 2θ range 22°-56° (with a step size of 0.01°).
- TEM-EDX: The samples were prepared by Ga^+ Focused Ion Beam (FIB) milling (FEI Helios 450). Silicon oxide and tungsten protection layers were deposited to protect the regions of interest from the tails of the ion beam. The samples were observed at 200 kV using a probe corrected Titan Themis FEI microscope equipped with the Super-X detector system for EDX. The EDX mappings were obtained with the resolution of 320x900 pixels using a dwell time of 50 µs. The quantification was performed using the k factors implemented in the Bruker Esprit software.
- XAS: EXAFS and XANES measurements were performed at the XRF beamline at Elettra Sincrotrone Trieste, Italy. The Ge-K EXAFS measurements, Sb-L_3 and Te-L_3 XANES measurements were performed in fluorescence mode for the undoped and N-doped Ge, Sb and Te samples, respectively. Theoretical EXAFS functions for Ge-Ge, and Ge-N pairs were generated using the FEFF program package [226].

2.4 Chapter summary

The unique properties of phase-change materials are determined by their structure, which makes the structural investigation an important part of the material engineering. Both the amorphous and crystalline phase structures need to be investigated in order to understand the bonding arrangement, structural evolution, phase transition dynamics and kinetics. Probing the short- and long-range order of the phase-change alloys can be performed by appropriate combination of characterization techniques. Electrical, optical, X-ray characterizations along with Transmission electron microscopy were briefly presented in the first part of this chapter, describing their potential contribution and possible challenges concerning the structural analysis of phase-change alloys.

Employing various characterization techniques and/or their combination can provide essential information, as highlighted in the second part of this chapter. Resistivity measurements do not only provide the information about electrical properties but can also indicate the possible nature of the crystallization mechanism (nucleation-dominated, growth-dominated). Raman and FTIR spectroscopies introduce the analysis of the bonding arrangement and highlight the structural units forming both amorphous and crystalline phase of the material. FTIR spectroscopy together with XPS has proven to be effective in analyzing the bonding in doped elemental systems and GST alloys as well as the layer degradation by oxidation process. XAS analyses provide deep information about the local structure concerning the closest neighbors of selected element of a studied material. XRD analysis is a powerful technique to analyze the crystalline structure, identifying the crystalline phases, determining the crystallites size and the stress and strain in the alloy upon crystallization. TEM can complete the microstructural analysis at the nanoscale level. The TEM-EDX elemental mapping allows to observe phase segregations, elemental migration and voids formation in studied alloys.

The characterization techniques demonstrated in this chapter are employed in the following investigation of undoped and N-doped elemental Ge, Sb and Te systems and Ge-rich GST alloys presented in the chapters 3 and 4. The combination of the employed techniques allows to obtain complementary information on both the bonding arrangement and the miscrostructure, thus to provide the overall picture of structural evolution and phase transition dynamics. The results of the material characterization already reported in literature and demonstrated in the second part of this chapter provide the important base of information for this following investigation.

Chapter 3

Nitrogen-doped Ge, Sb and Te elemental compounds

Ternary GeSbTe (GST) alloys have demonstrated to be key phase-change materials for PCRAM technology, as shown in the chapters 1 and 2. Moreover, the material engineering of GST alloys has been extensively investigated over the past years as a possible approach to improve the phase-change material properties. In particular, the nitrogen doping has shown the promising improvements concerning the thermal stability of the alloys. Although such promising achievements, the impact of nitrogen incorporation on the material structure and its bonding arrangement is not fully understood. The characterization of the nitrogen doping effect in a complex structure such as in ternary GST alloys requires the primarily investigation of the nitrogen impact and bonding in elemental systems.

In this chapter, we provide deep spectroscopic investigation of as-deposited undoped and N-doped Ge, Sb and Te elemental layers, carried out principally by FTIR and Raman spectroscopy, in order to identify the vibrational features characteristic of N bonding in the structure. The experimental spectroscopic results are supported by *"ab initio"* simulations of the related ideal nitride structures. Further, the study of structural evolution as a function of the temperature is provided in order to investigate the stability of as-deposited layers. The main results obtained from the investigation of N-doped elemental Ge, Sb and Te layers are further applied to ternary alloys to provide first approach structural analysis of N-doped GST.

3.1 GeN, SbN, TeN literature context

Germanium, Antimony and Tellurium are metalloids considered as "Technology critical elements" [227,228], used for a wide range of applications in optics, photonics, microelectronics and solar cells industry [229–236]. In particular, oxides, nitrides or even oxynitrides of these elements have drawn attention over the past years. Germanium and germanium nitride (GeN) alloys are systematically studied in the field of microelectronics owing to their structural similarities with conventional Si and SiN alloys [237–242] and high carrier mobility. Germanium nitrides and oxynitrides are investigated as potential gate insulators or passivation layers for Ge-based field effect transistors (FETs) and radiation detectors [243–246]. High-pressure antimony nitrides and antimony azides were prepared, seen as potential candidates for high-energy density materials [247–249]. Potentially stable antimony oxynitrides were also recently presented in [250]. Moreover, the SbN alloys along with GeN and other metal nitrides are considered as an attractive class of anode material for rechargeable lithium batteries [251–253]. Tellurium chemistry has reached a significant development in the field of Te-rich tellurides and tellurium coordination chemistry, in which the Te-N bond is stabilized by organic ligands or by adopting the heterocyclic structure [197,254–258]. Indeed, highly N-enriched cyclic compounds based on TeN_6 prepared under high pressure were proposed in [259], potentially facilitating the application of such alloys in high-energy density materials. On the contrary, only few inorganic tellurium nitride compounds are identified. TeN, Te_3N_4 and Te_4N_4 binary nitrides were reported in literature, although described as highly unstable [260]. Considering the analogy with other elements of the same group, i.e., S and Se, the sulfur and selenium nitrides E_2N_2 and E_4N_4 (E = S, Se) compounds are known, adopting ring and cage-like structures, respectively [197,255,261]. Tellurium nitrides, however, demonstrate different nature. Te_3N_4 is commonly referred as empirical composition, but its structure is unknown so far. Recently, stable 2D chalcogenide nitrides 1T-XN_2 (X = S, Se, and Te) were designed via first-principles simulations, opening the potential way for applications in optoelectronic devices working under blue or UV light, and in mechanical sensors [262].

A map of inorganic nitrides was suggested in [263], predicting the formation of binary nitrides and calculating their formation enthalpies. While the formation enthalpy of GeN system is about -0.25 eV/at (Ge_3N_4 structure), the calculated value for SbN system increases to 0.18 eV/at (SbN structure) and for TeN system to 0.68 eV/at (Te_3N_4 structure; 1.09 eV/at for TeN_2 structure) [263,264]. These values indicate the high stability of GeN system, while the formation of SbN and TeN is much less favorable. The binding states in GeN, SbN, TeN and their N-doped binary and ternary alloys were investigated by XPS in [265]. Ge-N, Sb-N and Te-N binding states were identified in prepared thin films as well as the apparition of molecular N_2 state in highly N-doped elemental alloys.

The benefit of N doping of binary (GeTe, SbTe) and ternary (GST) chalcogenide alloys is largely investigated in the field of PCRAM technology. It has been suggested that N doping in these alloys leads to the preferential formation of Ge-N bonds, which are responsible for the increase of crystallization temperature and the reduction of the grain size of the formed GST crystalline phase [171,266,267]. However, the effect of N incorporation in GeSbTe alloys raises also several questions related to the bonding configuration, concerning in particular possible nitrogen bond formation with Sb and Te elements.

The deep investigation of bonding arrangement in GeN, SbN and TeN elemental alloys by using various optical and X-ray characterization techniques can greatly contribute to the understanding not only of the structure of N-doped GST alloys used in the field of PCRAM, but also of other complex systems based on these elements used in different technological fields, such as for example N-doped GaSb alloys used in optoelectronics and high-power electronics [268–272].

3.2 Quantification of N content

The GeN, SbN and TeN layers with different N contents were prepared varying the N_2 flow during the film deposition from 0.5 sccm up to 40 sccm. The N content in the layers discussed in this chapter refers to the N_2 flow used during deposition. The composition of the layers was measured by WDXRF. The values obtained for GeN layers were corrected based on the quantification performed by IBA, as described in the section 3.2.1.

Fig. 3.1 presents the WDXRF quantification of the N content in the studied layers as a function of N_2 flow. Ge layers feature the highest N incorporation, reaching more than 50 at.% of N content for N_2 flow from 20 sccm. On the contrary, Te showed to be the least prone to incorporate the N. The comparison of the N content for the N_2 flow of 2 sccm, 10 sccm and 20 sccm is shown in Table 3-I. The tendency of the systems to incorporate the nitrogen is related to the possibility to form the corresponding X-N bonds (X = Ge, Sb or Te). The formation enthalpies of known nitride structures presented in the section 3.1 can be used in order to approximate the tendency of Ge, Sb and Te to form the related nitride, i.e., to bond with nitrogen. The reported values demonstrate that germanium nitride presents the most stable nitride structure among the studied systems.

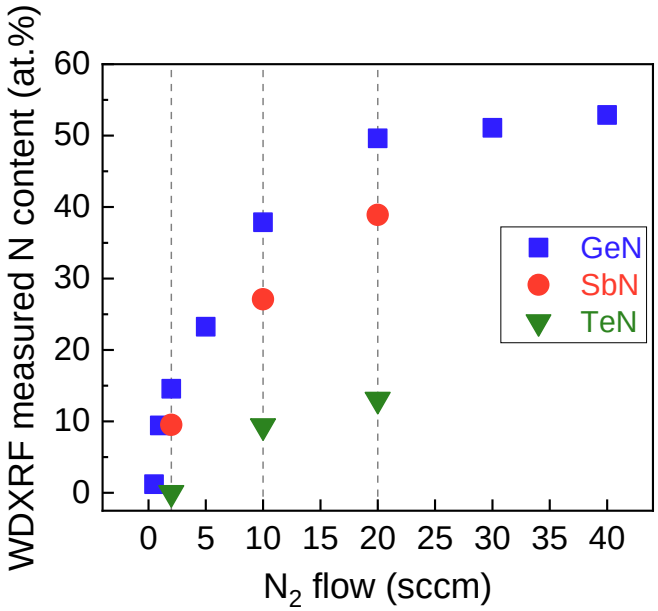

Fig. 3.1: N content in N-doped Ge, Sb and Te layers measured by WDXRF as a function of N_2 flow during the deposition. Dashed lines indicate the N_2 flow of 2 sccm, 10 sccm and 20 sccm. The highest incorporated N content is observed for GeN layers.

Table 3-I: Comparison of the N content in Ge, Sb and Te for the N_2 flow of 2 sccm, 10 sccm and 20 sccm.

N_2 flow	**N content (at. %)**		
	GeN	**SbN**	**TeN**
2 sccm	14.5	9.5	0
10 sccm	37.9	27.0	9.3
20 sccm	49.6	38.9	13.1

3.2.1 Quantification by IBA techniques

WDXRF is a useful non-destructive in-line process control method, which enables to obtain precise sample stoichiometry. Fundamental parameter methods combined with pure elemental samples have shown good accuracy for the XRF quantification of heavy elements. On the contrary, the quantification of low-Z elements, such as nitrogen, brings some complex issues, as described in [225], which makes this method inappropriate for N-doped complex alloys, such as GeSbTe. IBA (Ion Beam Analysis) techniques have shown to be suitable and independent methods to quantify the nitrogen standards for such alloys and thus allowing to establish the calibration curves for in-line WDXRF measurements. Nuclear Reaction Analysis (NRA) can be adopted for N quantification, accompanied by Rutherford Back Scattering (RBS) and Particle Induced X-ray Emission (PIXE) for determining Ge and Sb and Te contents. The collaboration with CEA-IRAMIS was established in order to adopt the IBA as a reference technique for WDXRF quantification of N-doped elemental alloys and further for N-doped GeSbTe alloys.

The experimental approach of N quantification is based on the $^{14}N(d,p0)^{15}N$ nuclear reaction. At first, the cross-section control was performed on 200 nm-thick SiN_x films, due to large discrepancy between the referenced and simulated cross-section data (Fig. 3.2). The measurements of $^{14}N(d,p0)^{15}N$ nuclear reaction were performed in the range from 1775 keV to 1975 keV in order to precisely determine the cross-section maximum. The Si-N ratio was measured by proton RBS, performed at 1490 keV (i.e., the energy at which the cross-section for Si and N are well referenced and shows the minimal discrepancy). The number of counts as a function of energy for the used nuclear reaction shows a good match between the experimental data and simulated data based on the available data base (Kokkoris&SigmaCalc; Fig. 3.2). Based on these results, the cross-section by Kokkoris are adopted for the data simulation of following sample measurements, performed at maximum energy of 1925 keV and using the corrective factor of 1.083.

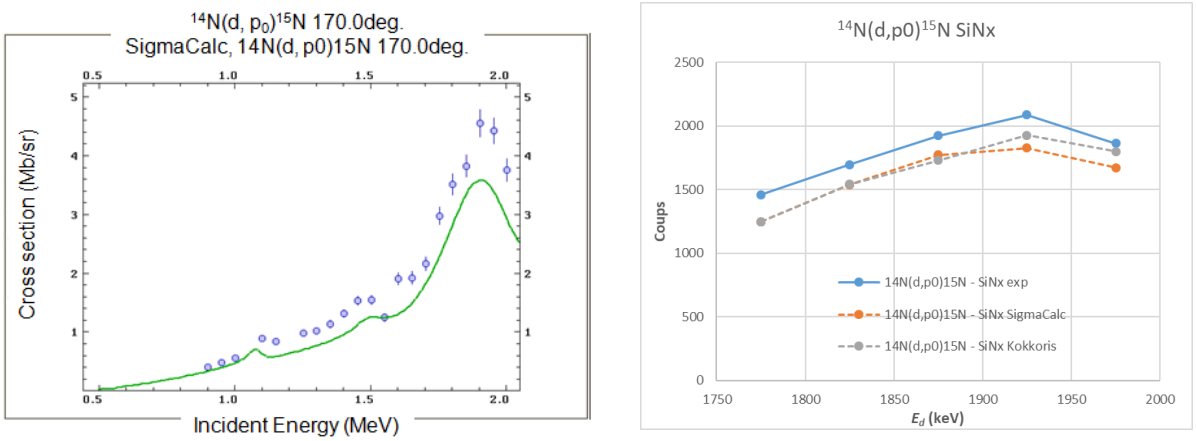

Fig. 3.2: (left) Illustration of simulated and bibliographic data of the cross-section for $^{14}N(d,p0)^{15}N$ reaction; (right) Comparison of the intensity (counts) as a function of the incident energy of the experimental and simulated data of the cross-section control performed on SiNx samples.

A set of N-doped Ge layers with a nominal thickness of 100 nm was deposited on 300 mm Si wafers by reactive sputtering (Applied Materials Endura300) in Ar/N_2 gas mixture in the deposition chamber. The layers with different N incorporation were prepared by varying the ratio between Ar and N_2 gas flows during the film deposition, increasing the N_2 flow from 0 to 50 sccm. The layers were protected by an *in-situ* deposited carbon capping layer (~5 nm). The quantification of N content in prepared GeN layers was performed by WDXRF, after which the samples were sent to CEA-IRAMIS in order to perform IBA measurements. The quantification of N content was performed based on the protocol established by SiN

cross-section control described above. The Ge content was verified by NRA and PIXE. The comparison of the samples compositions determined by both WDXRF and IBA techniques is presented in the Appendix 2. The IBA data for N quantification were used to adjust the calibration curve for N quantification in Ge layers by WDXRF. The values of N content for the GeN layers presented above in this section were obtained using the corrected calibration curve.

3.3 Spectroscopic studies of N-doped Ge, Sb and Te compounds

FTIR and Raman spectroscopy were used as characterization techniques to investigate the structure of both undoped and N-doped elemental alloys. The IR and Raman spectra decomposition and fit parameters for all three N-doped systems are reported in Appendix 3.

3.3.1 Ge and GeN layers

The undoped Ge layer does not show any absorption features in the IR spectrum in the investigated wavenumber range. On the contrary, N doping of Ge produces a strong IR absorption band with the maximum at about 690 cm^{-1} and a second broad band at about 300 cm^{-1} (Fig. 3.3). Based on the investigation of GeN and GeN:H alloys [181,182,188,239], these bands are related to in-plane asymmetric stretching and disorder-induced breathing vibrational modes of Ge_3N skeletal group, respectively. The asymmetric form of both bands in the IR spectra becomes more evident with increasing N content and indicates the presence of more than one contribution. Indeed, main contributions at 680 cm^{-1} (ν_s) and at 280 cm^{-1} (ν_b) and additional contributions with maxima at 750 cm^{-1} (ν_s') and at 390 cm^{-1} (ν_b') were identified in our IR spectra. The demonstrated additional contributions present one of the possible approches for GeN band deconvolution, as described in the section 2.2.1. Only one additional contribution was added in the case of our studied GeN layers. However, more than one additional contribution at fixed positions and FWHM could be also employed. The integrated intensity of the GeN bands ($\nu_s + \nu_s$') increases with N content, reaching the maximum value for GeN 20 sccm (Fig. 3.4). The same trend was observed in previous investigations [180,188], described in the section 2.2.1. However, contrary to those previously reported results, we further observe the intensity decrease for highly doped GeN compositions (N content about 50 at.% and more), while the band broadening still continues. Furthermore, we did not observe any other band at higher wavenumbers (>900 cm^{-1}), reported in previous studies [180] and assigned to dangling bonds due to disordered structure (also described in the section 2.2.1).

The Raman spectrum of the undoped Ge layer (Fig. 3.3) shows a characteristic band in the range from 100 cm^{-1} to 300 cm^{-1}. This band is assigned to amorphous Ge (a-Ge) and composed by the contributions of main TO-like mode (275 cm^{-1}), LO-like mode (220 cm^{-1}) and LA-like mode (160 cm^{-1}) [187,188,273], thus indicating the amorphous character of the deposited alloys. The TA-like mode is not observed here as it appears at wavenumbers (~80 cm^{-1}) below the edge of the used notch filter. Significant broadening of the a-Ge band is observed with increasing N content. Moreover, a new broad band with the maximum at about 700 cm^{-1} appears in the spectra. This band is assigned to the vibrations of the Ge_3N group, observed also in IR spectra [188]. More than one contribution to this broad band can be distinguished, in particular in spectra of GeN with high N content (about 50 at.% and more, i.e., from GeN 20 sccm), which can be correlated with the main band observed in IR spectra. The contributions of vibrational modes originating from the Si substrate also become evident in the GeN spectra as the N content increases: the main peak at 521 cm^{-1}, second order scattering modes at 950 cm^{-1} and at 300 cm^{-1} (in GeN 40 sccm) [274,275]. Their intensity increases with the N content due to progressive transparency of the GeN layers related to the changes in optical properties (i.e., optical absorption) [188].

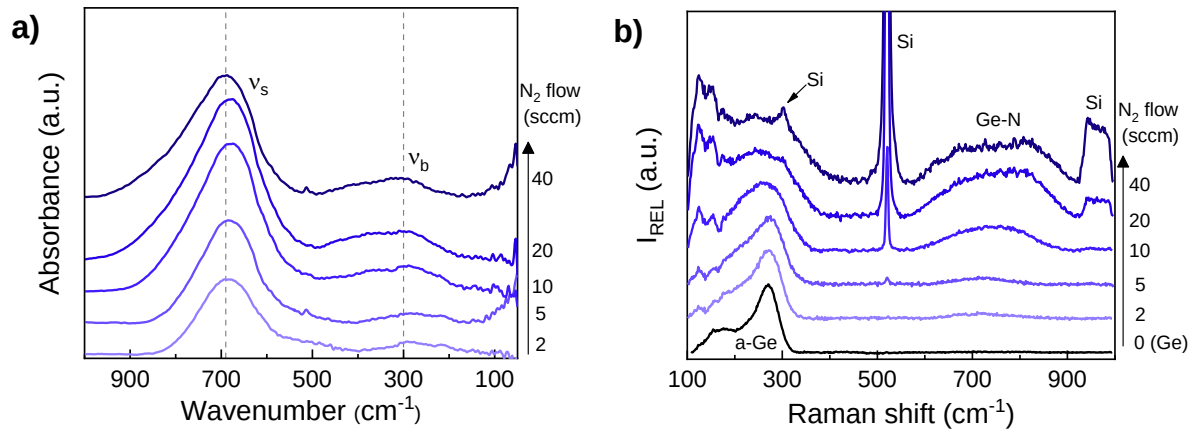

Fig. 3.3: IR (a) and Raman (b) spectra of undoped and N-doped Ge. The IR spectra shows the main broad band at ~680 cm^{-1} (ν_s) and second band at 300 cm^{-1} (ν_b), corresponding to stretching and breathing modes of Ge_3N units, respectively. Raman spectra highlight the boradening of a-Ge modes (100 – 300 cm^{-1}) and the appearance of the band related to Ge-N modes (600 – 800 cm^{-1}) with increasing N content.

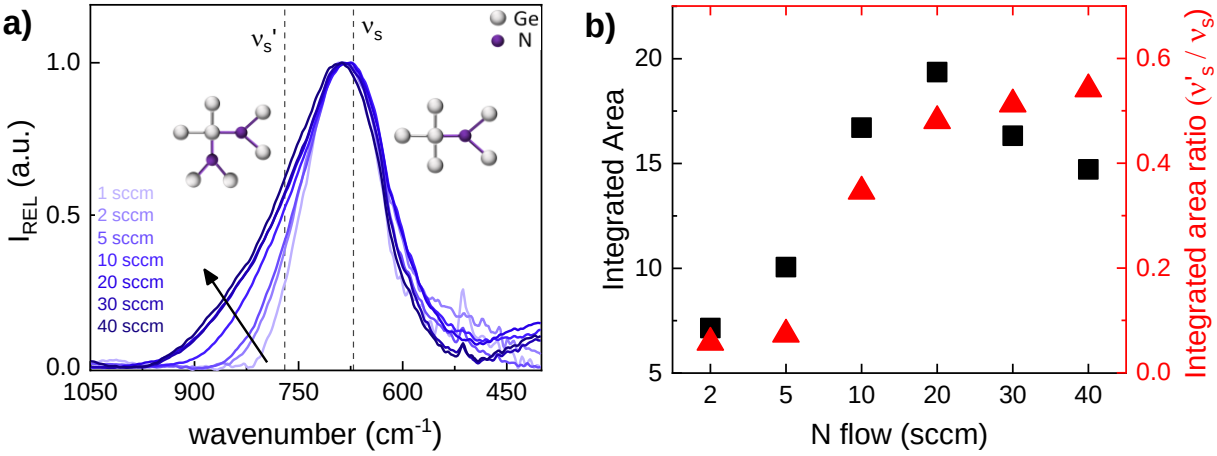

Fig. 3.4: a) normalized IR band, highlighting the shoulder broadening with increasing N content. The dashed lines indicate the positions of main and additional contributions. The inset illustrations represent the bonding arrangement between Ge and N atoms in the structure; b) Integrated area of IR band at ~690 cm^{-1} assigned to the Ge-N bond vibration (black points) and the ratio of integrated areas of its contributions (main contribution at ~680 cm^{-1}, additional contribution at ~750 cm^{-1}, red points).

The presence of additional contributions (ν_s') in the main band of the IR spectra (at 690 cm^{-1}) was described in [180,188]. The N incorporation leads to changes in local environment, in which more Ge neighboring atoms around the Ge_3N group are bonded to nitrogen. This leads to inductive effects resulting in the shift in the main vibrational energy to higher wavenumbers and to the consequent appearance of an additional contribution ν_s'.

As the layers feature a high degree of disorder, which further increases with N incorporation, this additional contribution ν_s' represents the sum of possible different Ge-N bonds configurations, adding their shifted vibrational modes to the main band. Therefore, the integrated intensity of the main band at about 690 cm^{-1} increases with the formation of new Ge-N bonds. However, the formation of new Ge-N bonds leads to the saturation of the system, resulting in a maximum for GeN 20 sccm (N content about 50 at.%). The vibration of the Ge_3N group becomes highly affected by the presence of neighboring Ge-N bonds, thus causing the reduction of its vibrational mode ν_s at 680 cm^{-1}. This results in the reduction of the band integrated intensity in the layers with higher N content, even though the broad additional contribution ν_s' at 750 cm^{-1} continues to slightly grow (Fig. 3.4), leading to the

preponderance of configurations richer in N atoms. These observations correspond to the increasing intensity of the Ge-N band in Raman spectra. At the same time, the broadening of modes assigned to a-Ge (i.e., vibration of Ge-Ge bonds) suggests reduction of Ge-Ge bonds contribution in the layer structure and preferential formation of Ge-N bonds in the alloy.

3.3.2 Sb and SbN layers

Undoped antimony is known to be IR-inactive in the explored wavenumbers range. IR spectra of N-doped Sb layers (Fig. 3.5) feature a broad band at 600 cm^{-1}, whose intensity increases with the N content in the layer. The asymmetric form of the band suggests the presence of more than one contribution. In particular, the main contribution ν_1 can be found at ~560 cm^{-1}, accompanied by an additional band ν_2 at ~630 cm^{-1}. Other bands can be observed at about 300 cm^{-1} (ν_3) and 145 cm^{-1} (ν_4). The intensity of the band at 300 cm^{-1} also increases with N content, whilst the band at 145 cm^{-1} reduces.

The Raman spectrum of Sb layer (Fig. 3.5) shows two sharp peaks at 115 cm^{-1} and 150 cm^{-1} corresponding respectively to E_g and A_{1g} modes of crystalline Sb [189,276] along with second order scattering mode at about 270 cm^{-1} [189]. This indicates that the undoped as-deposited antimony layer is already crystalline. Indeed, fast spontaneous crystallization of Sb at room temperature is reported as well as Sb crystallization dependance on deposited layer thickness (the crystalline structure is observed for the layer thickness more than few nm) [189,192,277–280]. N doping in Sb layers results in significant changes in Raman spectra. The spectra of N-doped Sb feature a broad band in the range between 100-200 cm^{-1} instead of the sharp peaks observed for crystalline Sb. This may indicate the amorphous nature of the structure of N-doped Sb layers. Indeed, a similar band has been observed in the Raman spectra of undoped amorphous Sb (a-Sb) [192]. Furthermore, a shift of this broad band towards higher wavenumbers can be observed with increasing N content (inset of Fig. 3.5b), resulting from the increasing intensity of the band contribution originating likely from Sb-N bonds vibrational mode (spectra deconvolution in Appendix 1). N doping also affects the Sb second-order scattering mode (at about 270 cm^{-1}), causing its broadening. A new broad band with a maximum at 600 cm^{-1} can be observed (in particular for SbN 20 sccm), corresponding to the wavenumber of the main band in IR spectra. The small sharp peak at 520 cm^{-1} in the spectrum of SbN 20 sccm is assigned to the Si mode of the substrate.

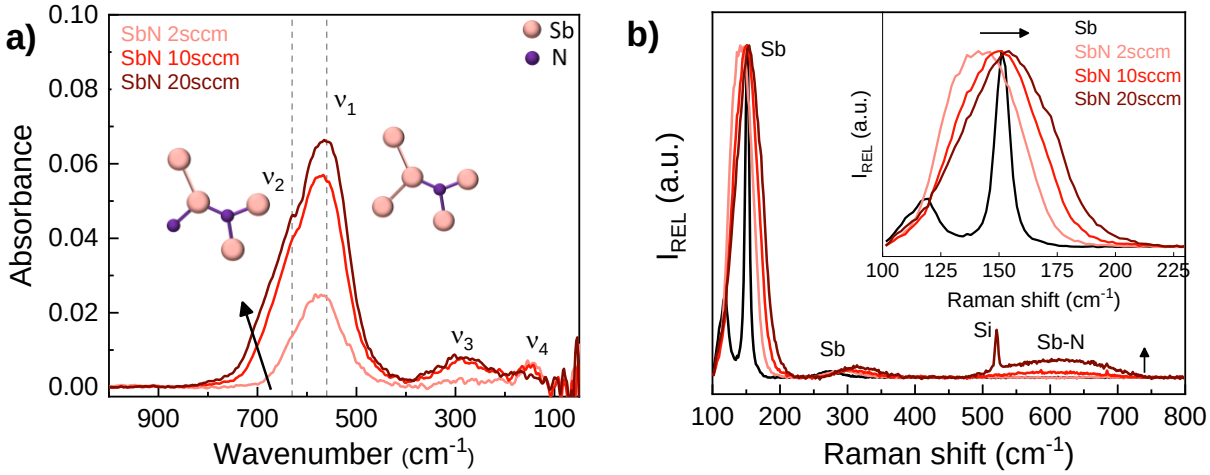

Fig. 3.5: IR (a) and Raman (b) spectra of undoped and N-doped Sb. IR spectra show the absorption band at 600 cm^{-1}, assigned to Sb-N vibrational modes. The inset illustrations represent the bonding arrangement between Sb and N atoms in the structure. Raman spectra highlight two sharp peaks of crystalline Sb, broadened into one band upon N doping.

Crystalline Sb has a rhombohedral structure with a three-fold coordination symmetry [281]. Sb and N elements belong to the same group of periodic table; hence they have the same valence electrons number and coordination. The same coordination of Sb and N likely facilitates the Sb atoms substitution by N atoms, leading to the formation of Sb-N bonds. This can also explain the high N incorporation into Sb layers, as shown in Fig. 3.1. The substitution of Sb by N atoms was also observed in N-doped GaSb alloys [282]. The Sb substitution by N atoms and the Sb-N bonds formation cause the Sb atoms displacement from their original lattice position as the N atoms have smaller atomic radius compared to Sb. This will lead to disorder increase in the layer, breaking the long-range order of the Sb crystalline structure. This is evidenced in Raman spectra, where the Sb crystalline peaks enlarge into one broad amorphous band.

The formation of Sb-N bonds is evidenced by the broad absorption band in IR spectra. Similar IR band assigned to the vibrational mode of Sb-N bonds was also observed in [283]. An analogy with GeN can be used to identify the IR bands of SbN alloys. The IR spectra of both undoped elements feature no active vibrational modes, while N doping results in a strong IR absorption band in the range from 400 cm^{-1} to 800 cm^{-1}, composed of two contributions (ν_1 and ν_2). The IR band of SbN is shifted towards lower wavenumbers with regard to the GeN one, since Sb atoms are heavier. Considering the same coordination of Sb and N atoms, the formation of Sb_3N structural units might be suggested, similarly to Ge_3N identified in GeN layers. The two identified contributions of the main IR band (ν_1 and ν_2) then likely represent the Sb-N vibration of Sb_3N structural units and disorder-induced vibration of the same units impacted by the neighboring N atoms arranged in different configurations as the N content increases. The IR band ν_3 at 300 cm^{-1}, also, likely results from Sb-N vibration, as its intensity increases with N content. The IR band ν_4, on the contrary, can be likely related to the Sb (A_{1g}) vibrational mode observed in Raman spectra, which becomes IR-active due to increased disorder induced by N doping.

3.3.3 Te and TeN layers

Undoped tellurium is highly transparent in IR, hence no contribution should be expected until far IR. Indeed, the IR spectrum of Te (Fig. 3.6) features a sharp peak at 90 cm^{-1} corresponding to the A_2/E_1 vibrational modes in trigonal Te (c-Te) [196,284,285], indicating that the as-deposited Te layer is crystalline. Another broad and less intense band, however, is observed in the range 850 - 550 cm^{-1}. This band is assigned to the Te-O vibrations [286,287], thus indicating that undoped Te layer is oxidized even when protected by an encapsulation layer. The oxidation of similar Te layers was observed by XPS studies [218]. The Raman spectrum of undoped Te (Fig. 3.6) shows two sharp peaks at 122 cm^{-1} and 142 cm^{-1}, assigned to the A_1 and E_2 modes of trigonal Te, respectively [196,284,285,288,289], thus confirming the crystalline structure of the as-deposited Te layer. No contributions attributed to Te-O vibrations were found in the Raman spectrum.

Introduction of nitrogen into Te results in the intensity reduction of the Te mode at 90 cm^{-1} in the IR spectra. This mode disappears completely in TeN 10 sccm and TeN 20 sccm. On the contrary, a broad band composed by several contributions is observed in the IR range between 850 cm^{-1} and 250 cm^{-1} and increases in intensity with the incorporation of N. Moreover, weak broad bands in the range from 4000 cm^{-1} to 1000 cm^{-1} were observed in TeN 20 sccm, corresponding to O-H, N-H and N-O characteristic vibrations [290] (Appendix 3). This range, however, is not further considered in our analysis. Raman spectra of TeN layers show a progressive broadening of the peak at 142 cm^{-1}, resulting from an arising additional contribution with maximum at about 150 cm^{-1}. This peak has been previously attributed to amorphous Te (a-Te) [289]. No further bands are observed at higher wavenumbers.

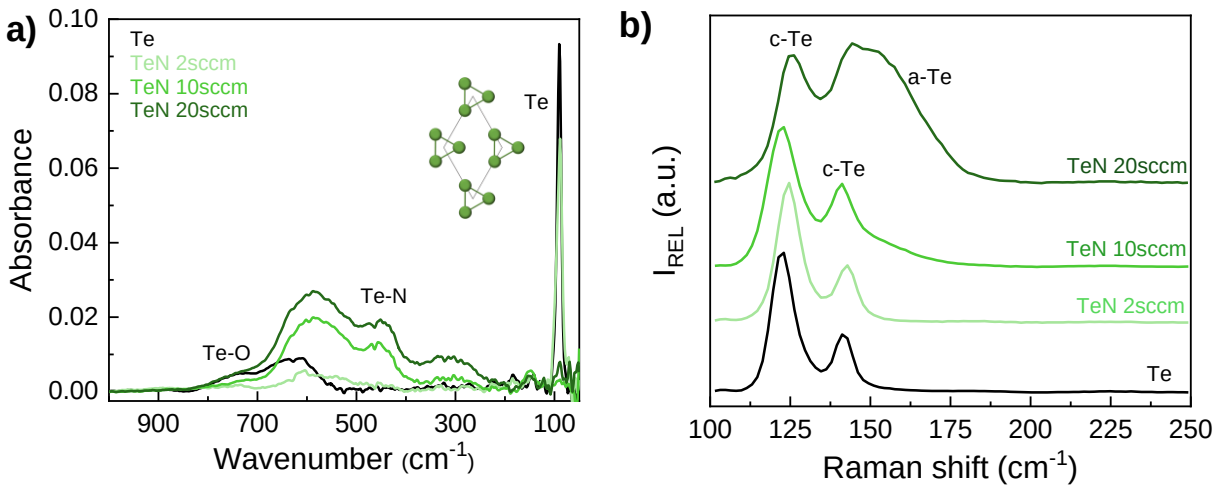

Fig. 3.6: IR (a) and Raman (b) spectra of undoped and N-doped Te. IR spectra demonstrate Te-O contribution in undoped Te layer, broad band assigned to Te-N in N-doped Te and the reduction of sharp peak at 90 cm^{-1} upon N doping. The inset illustration represents the Te crystalline structure with Te chains. Raman spectra highlight two sharp peaks of crystalline Te (c-Te) and the appearance amorphous contribution (a-Te) upon N doping.

The trigonal crystalline structure of Te is composed by helical chains of Te atoms at the corners of a hexagonal array, when seen from the c-axis of the crystal [194,195,197]. The bonding between the atoms in the chains is covalent adopting the angle near 90° in order to minimize the repulsion of the np lone pairs of the adjacent atoms. The second lone pair of a Te atom (in ns orbital) is reported to have no stereochemical effect [197]. The Te atoms between the adjacent chains are bonded by weaker secondary interactions formed by overlapping electronic orbitals between the Te np lone pair and antibonding orbitals in adjacent Te chains [197,285,291]. It is important to note, that these interactions are, however, stronger compared to those of selenium and sulfur, since the polarizability increases down in the column of the periodic table towards heavier elements [197]. This would also explain lower reactivity of Te and thus a reduced tendency to form different compounds with regard to its S and Se analogues. Te crystalline structure with intra-chain and inter-chain bonding can therefore likely impede the N incorporation, as it is evidenced by WDXRF measurements (Fig. 3.1).

The results of IR and Raman spectroscopy show that N atoms, when incorporated, have major impact on weaker inter-chain bonds (i.e., reduction of A_2 mode at 90 cm^{-1} in IR spectra), whilst stronger covalent intra-chain bonds are much less affected (A_1 and E_2 modes at 122 cm^{-1} and 142 cm^{-1}, respectively, in Raman spectra are maintained). These observations indicate that N atoms likely occupy the interstitial space between the covalent chains of the Te structure. Indeed, owing to the helical form of Te chains, the crystalline unit can be seen as cage constituted of eight Te atoms from four adjacent Te chains. Similar cage structure was already described in molybden chalcogenides Mo_6E_8 (E = S, Se, Te), known as Chevrel phases, incorporating the atoms of an element M (usually a metal) into its cavities [292]. In the case of Te structure, such cage could incorporate N atoms placed between two planes of Te atoms as N atoms prefer to adopt the tetrahedral geometry.

The incorporated N atoms can likely form three Te-N bonds to the three closest Te atoms, while maintaining its lone pair. The formation of Te-N bonds requires using the electrons from np lone pair of the affected Te atoms, which would lead to breaking the inter-chain interactions, as observed in IR spectra. The incorporation of two N atoms in one Te crystalline unit cell is highly preferable as the np lone pair of the affected Te atoms provides two electrons. These electrons need to be bonded in order to maintain the neutrality of the structure, i.e., one affected Te atom would form two Te-N bonds. In such configuration,

the N atom would be likely incorporated only in one of a-axis directions of the crystalline structure (Fig. 3.7), which also correlates with low N content quantified in Te compounds. The formation of Te-N bonds gives rise to broad band in IR spectra, resulting from induced dipole moment owing to partial charge transfer as nitrogen is more electronegative than tellurium. In particular, three band contributions can be distinguished (see Appendix 3) likely corresponding to three Te-N bonds between N and different Te chains. The formation of Te-N bonds was also observed in similar TeN layers by XPS [218].
Besides the formation of Te-N bonds in the structure, changes in the distances between the Te chains can be expected as the atomic radius of N atoms is much smaller with regard to that one of Te. Moreover, as a reaction to the presence of N atoms in the structure, the np lone pair from Te atoms, which are not bonded to N, could adopt different direction in space with regard to their original position, thus guiding the spatial arrangement of the Te structure. These effects would lead to disorder increase in the structure, having an impact on vibrational modes of Te-Te in the chains, represented by slight broadening of the c-Te peaks and the appearance of the a-Te band in Raman spectra.

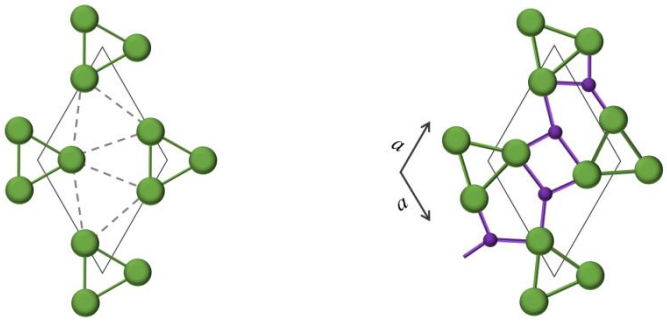

Fig. 3.7: Schematic representation of a) crystalline Te structure highlighting weaker inter-chain bonds (dashed lines) and b) N-doped Te structure with broken inter-chain bonds, highlighting the Te-N bonding and N-incorporation in the interstitial positions, in the direction of only one of the a-axis of the Te structure.

3.4 Investigation of the local structure by XAS measurements

The local atomic structure of the presented layers has been studied by EXAFS and XANES techniques. The Ge-K EXAFS measurements, Sb-L_3 and Te-L_3 XANES measurements were performed in fluorescence mode for the undoped and N-doped Ge, Sb and Te samples, respectively.
The Fourier transform of EXAFS signal for the undoped Ge layer (Fig. 3.8) features only one contribution corresponding to Ge-Ge distance [240,293]. A second additional contribution is observed in the GeN layers at shorter distance, corresponding to Ge-N pair [240,293]. The relative importance of these contributions varying upon N content in the Ge layer can be observed. The intensity of the Ge-Ge contribution reduces, while the intensity of the Ge-N contribution increases. In GeN 40 sccm layer, only the Ge-N contribution is present, while the Ge-Ge contribution completely disappeared, suggesting that the bonding arrangement in this layer is determined mostly by Ge-N interactions. This corresponds with the presence of strong Ge-N vibrational modes observed in IR and Raman spectra and would explain the extensive broadening (and gradual disappearance) of a-Ge modes in Raman spectra of GeN alloys (Fig. 3.3).
XANES measurements were performed on undoped and N-doped Sb and Te compounds (Fig. 3.9) deposited with the lowest N_2 flow of 2 sccm for both types of alloys. The spectra of both undoped Sb and Te layers feature oscillatory absorption structures in the near edge region, while no pre-edge transitions are observed. Upon N doping, SbN layer features no shift of the edge position, but shows the diminution of absorption features indicating

significant changes in the local atomic environment of the Sb atoms. Similar disappearance of absorption features was reported in [294], where the Sb structure was studied as a function of temperature and where this diminution of the absorption structures is related to increased disorder in the Sb structure. This result is thus consistent with the IR and Raman spectra (section 3.3.2) referring to an amorphous-like disordered Sb structure upon N doping. Contrary to SbN, N doping in Te layers does not cause any changes in the absorption edge and near-edge absorption structures (for the used low N_2 flow), which further supports the results presented in section 3.3.3.

Though these results well correspond with the findings from the IR and Raman spectroscopy, further investigation of the local structure of N-doped elemental layers with higher N content would be a great asset. Besides the L_3 edge for Sb and Te alloys, the K edge with higher core-electron binding energy could be probed, contributing with additional information. Moreover, the analyses of XANES spectra using reverse Monte Carlo simulations can be suggested, supporting the experimental results with models of possible atomic configurations (not explored in the frame of this work).

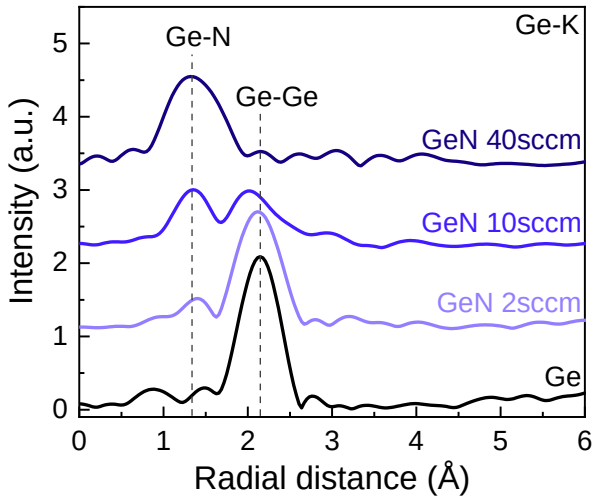

Fig. 3.8: Fourier transform of EXAFS signal of undoped and N-doped Ge, demonstrating the Ge-Ge and Ge-N contribution. Ge-N contribution becomes dominant, while Ge-Ge contribution disappears with increasing N content.

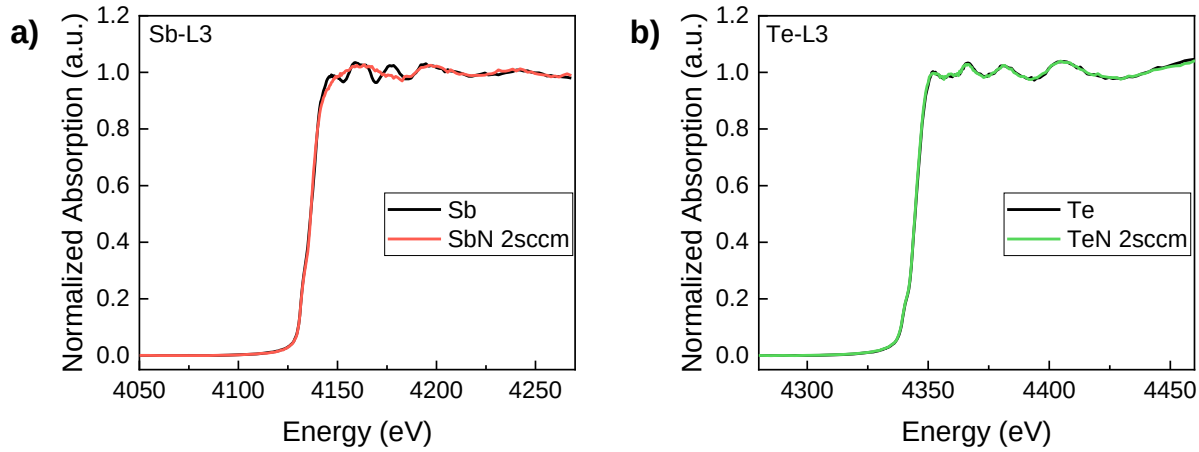

Fig. 3.9: Xanes spectra of a) Sb and SbN layers and b) Te and TeN layers. SbN layer shows the reduction of absorption features compared to the spectrum of Sb, while TeN spectra do not show any significant changes.

3.5 Simulations of the ideal nitride structures

The results of spectroscopic analyses presented in the section 3.3 are further supported by *"ab initio"* simulations of IR and Raman spectra. The *"ab initio"* simulations generally yield qualitatively IR and Raman spectra well comparable to experiments. The simulations of amorphous structures featuring high degree of disorder are time-consuming, requiring large unit cell of a system to be simulated. However, the simulations performed on related crystalline materials, whose structure is known, can already provide precious insight into the materials structure. Indeed, IR and Raman spectra simulations of ideal crystalline structures of GeN, SbN and TeN compounds allow to identify IR- and Raman-active modes assigned to N bonding with Ge, Sb or Te. These simulated spectra can further determine the possible N bonding contributions in the studied as-deposited N-doped Ge, Sb and Te compounds.

The simulations were performed using Vienna *Ab initio* Simulation Package (VASP) code [295,296] and Phonopy-Spectroscopy package [297]. The ideal crystal structures of Ge, Sb Te, as well as those of GeN, SbN, and TeN nitrides were obtained from Materials Project [298,299]. Structural relaxation was performed using Density Functional Theory (DFT) with Monkhorst-Pack (MP) mesh. Phonon modes were obtained using density functional perturbation theory. The Projector Augmented Wave (PAW) method with Perdew-Burke-Ernzerhof (PBE) functional [300] and 400 eV cut-off energy were used for the calculations. For the qualitative comparison of simulated and experimental data, the obtained spectra were normalized with respect to the most intense peak of the spectra.

First, simulated IR and Raman spectra of undoped Ge, Sb and Te structures are compared with the experimental results (Fig. 3.10), showing good agreement for IR spectra. Experimental IR spectra of Ge and Sb do not feature any active vibrational modes in the studied range, confirmed by the simulated spectra. The simulated IR spectrum of Te confirms the presence of Te vibrational mode at 90 cm^{-1} (A_2/E_1 modes of c-Te), while no contribution is observed at higher wavenumbers. The broad band observed in experimental spectra was assigned to the vibration Te-O modes, as discussed in the section 3.3.3. The simulated Raman spectra of undoped Ge, Sb and Te structures correspond with the experimental data concerning the number of peaks present in the spectra, which allows to assign the nature of these vibrations. The peak positions are, however, shifted to lower wavenumbers likely due to the choice of functional and exclusion of finite-temperature effects during the performed simulations. The difference in peaks intensity ratio observed between the experimental and the simulated Raman spectra of Sb and Te can be related to the fact that simulated spectra refer to the unit cell of ideal crystalline structures, while the samples are polycrystalline.

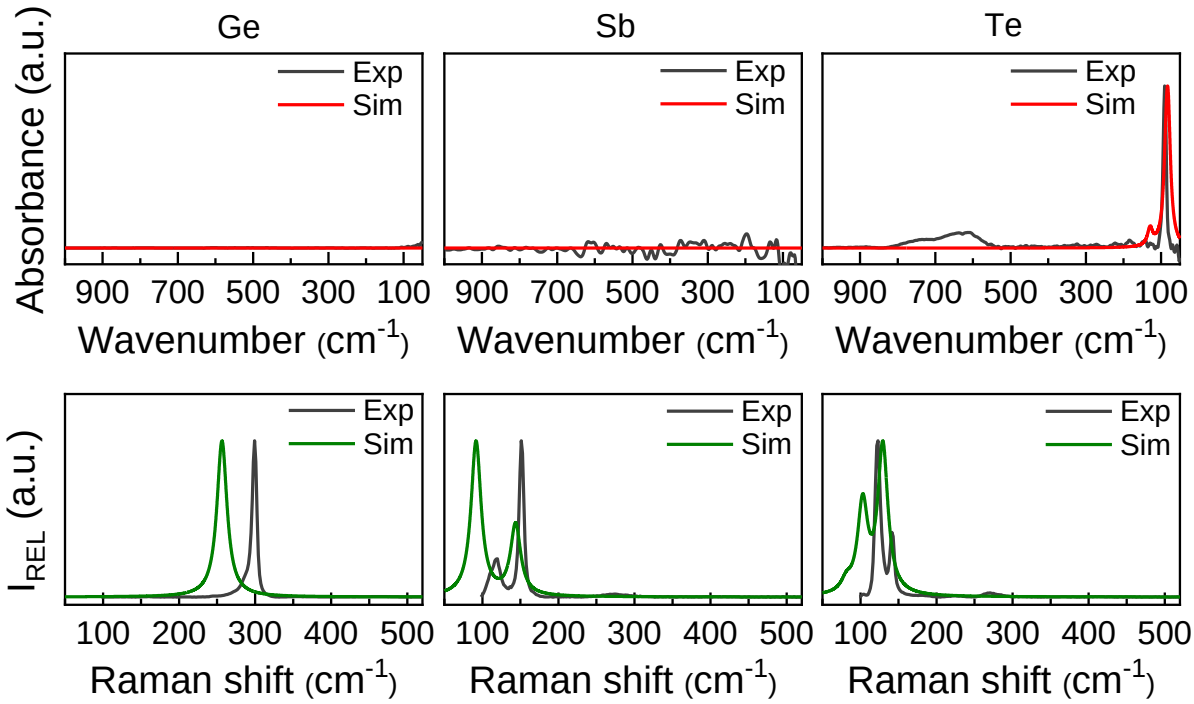

Fig. 3.10: Experimental (Exp) and simulated (Sim) IR spectra (upper panel) and Raman spectra (lower panel) of undoped Ge, Sb and Te compounds. The position in Raman peaks at lower wavenumbers in simulated spectra compared to experimental spectra is likely due to the choice of parameters during the simulations.

Second, IR and Raman spectra simulations were performed for different GeN, SbN and TeN ideal nitride structures. Particularly, hexagonal Ge_3N_4, for example, is the most referred germanium nitride structure; however, orthorhombic Ge_3N_4 and Ge_3N_2 structures were also reported [188,301,302]. Simulations of different nitride structures allow searching for the most coherent vibrational modes analysis with regard to the obtained experimental data and can reveal spectral similarities and differences, contributing to better identification of the N bonding contributions. The simulated IR and Raman spectra for different GeN, SbN and TeN structures compared in this work are shown in Appendix 4. A good agreement between the simulated and experimental spectra was found for the following structures (Fig. 3.11):

- hexagonal Ge_3N_4 in case of GeN alloys;
- orthorhombic SbN in case of SbN alloys;
- monoclinic TeN_2 in case of TeN alloys.

The simulated IR spectrum of hexagonal Ge_3N_4 shows two main contributions in the region from 700 cm^{-1} to 800 cm^{-1} and additional contributions at about 300 cm^{-1}, both regions corresponding well to the broad band assigned to Ge_3N vibrational modes observed in the experimental GeN spectrum. The simulated Raman spectrum demonstrates strong Ge-N mode contributions at about 700 cm^{-1}, consistent with the broad band appearing at this location in the experimental GeN spectra. Moreover, several contributions can also be found at about 300 cm^{-1}. The contributions at 300 cm^{-1} could likely contribute to the broadening of the a-Ge bands due to increasing N content in the GeN alloys, observed in the experimental GeN spectra in the section 3.3.1 (Fig. 3.3).
The simulated IR spectrum of orthorhombic SbN structure shows two contributions in the main band at about 600 cm^{-1} and several contributions in the region around 300 cm^{-1}, corresponding to the broad bands observed in the experimental spectrum. Moreover, the contributions in both spectral regions correspond also in terms of intensity ratio. These results confirm that both vibrational regions in the experimental spectra can be therefore attributed to

Sb-N vibration. The simulated Raman spectrum shows a strong band at low wavenumbers at about 150 cm^{-1} and weaker bands at about 600 cm^{-1}. The presence of the low wavenumber band indicates a possible Sb-N contribution to the broad band assigned to a-Sb modes in the experimental spectrum (section 3.3.2), which can be likely responsible for the band shift with increasing N content (Fig. 3.5). Weaker Sb-N mode contributions at 600 cm^{-1} present in the simulated spectrum were not observed in our experimental spectra with lower N content. However, a corresponding low intense broad band was found for the SbN layer with the highest N content, i.e., SbN 20 sccm (Fig. 3.5).

The simulated IR spectrum of monoclinic TeN_2 shows a good match between the simulated and experimental results, presenting three main contributions in the band at 250 - 850 cm^{-1}. On the contrary, the Raman spectrum of as-deposited TeN layer does not match with the simulated Raman spectra of TeN_2 structure. The vibrational modes of Te-N bonds in the simulated TeN_2 structure (at about 230 cm^{-1}, 560 cm^{-1} and 630 cm^{-1}) are not observed, likely due to very weak intensity of Te-N vibrations with regard to the Te-Te vibrational modes in our experimental spectra. Indeed, the IR intensity of the broad Te-N band (250 cm^{-1} - 850 cm^{-1}) in the TeN spectra reaches the maximum absorbance value of less than 0.03 for the highest doping level used (Fig. 3.6), which is more than twice lower than in SbN and GeN layers for the same doping level. Moreover, the overall incorporated N content is much lower than in the case of SbN or GeN as shown in Fig. 3.1.

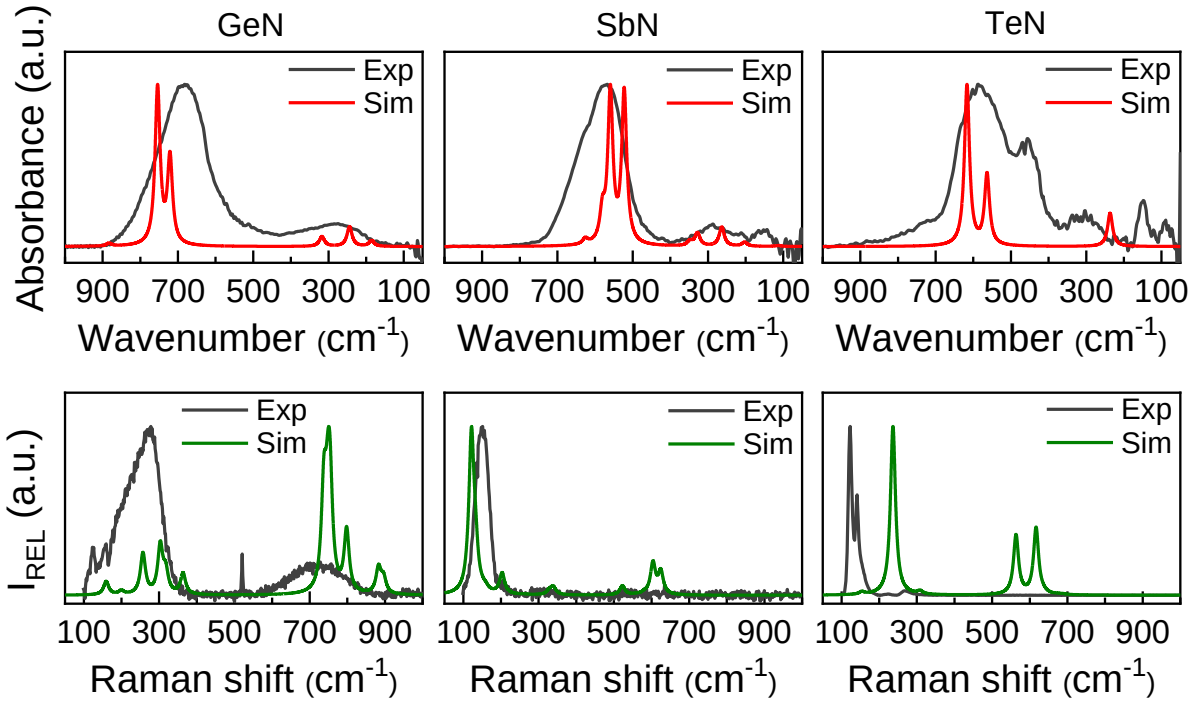

Fig. 3.11: Experimental (Exp) and simulated (Sim) IR and Raman spectra of GeN, SbN and TeN compounds. Experimental data are taken for N-doped alloys deposited with the N_2 flow of 10 sccm. The simulated spectra result from crystalline hexagonal Ge_3N_4, orthorhombic SbN and monoclinic TeN_2 structures.

3.6 Identification of nitrogen bonding in N-doped GeSbTe alloy

Based on the results presented in the previous sections, further investigation of N-doped more complex chalcogenide alloys can be performed. The alloys of two different material families of ternary GeSbTe system were chosen, namely Ge-rich and Sb-rich GeSbTe, as these alloys have been highly considered for effective PCRAM device integration [148,303]. N-doped Ge-rich and Sb-rich GeSbTe layers (GGSTN and SGSTN, respectively) were deposited by co-sputtering of $Ge_2Sb_2Te_5$ and Ge or Sb targets, using the N_2 flow of 2 sccm. Based on the

above-described results on N-doped Ge, Sb and Te layers, IR spectra are compared, as FTIR spectroscopy demonstrated to be the most suitable among the used techniques for the analysis of N bonding in such alloys.
The direct comparison of the IR spectra of the N-doped compounds (Fig. 3.12) highlights the significant position and intensity differences of the bands assigned to the Ge-N, Sb-N and Te-N bonds of the related N-doped single-element layers. For the GGSTN, the best match is found with GeN alloy, in terms of position and shape of the observed features, thus confirming the strong preference of the Ge-N bonds formation in GGSTN alloys. The IR spectrum of SGSTN features two contributions correlated with GeN and SbN, hence indicating the formation of both Ge-N and Sb-N bonds in the system. Despite the high Sb content in SGSTN, the intensity ratio between the contributions highlights the preferential formation of Ge-N bonds over Sb-N bonds in the system.

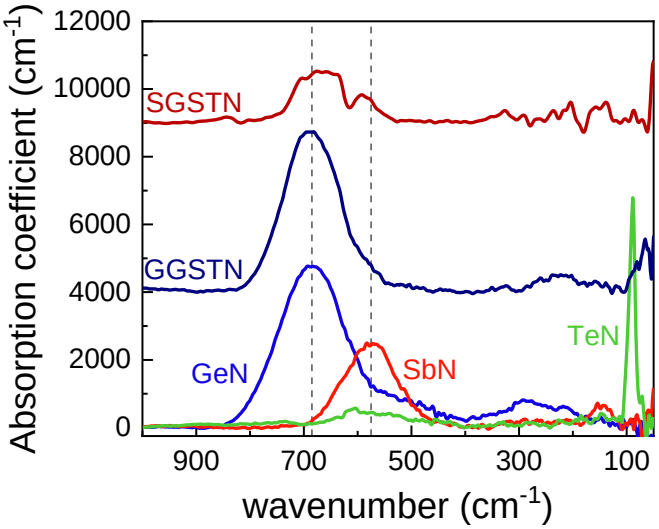

Fig. 3.12: The comparison of IR spectra of N-doped Ge, Sb, Te and Ge-rich and Sb-rich GST alloys (N_2 flow of 2 sccm was considered for all the compared layers in our experiment). Dashed lines indicate the position of Ge-N bonds contribution in GGSTN and Ge-N and Sb-N bonds contributions in SGSTN.

3.7 Structural evolution of the single-element layers

Further studies were performed on both undoped and N-doped Ge, Sb and Te layers in order to investigate the structural stability or evolution a) in time; b) as a function of temperature.

3.7.1 Structural evolution as a function of time

The IR and Raman spectra of undoped and N-doped layers discussed above were acquired just after the deposition process. The layers were further kept in the cleanroom environment and remeasured after 18 months of ageing. It is important to note that the layers were protected by an in-situ deposited carbon capping layer (~3.5 nm).
Both IR and Raman spectra show no changes of the present absorption features in the case of undoped layers (spectra not shown). Concerning the N-doped layers, all the prepared layers were remeasured after ageing. Only IR spectra for the layers with the highest N content (N_2 flow of 20 sccm) are presented here, as the structural changes induced by doping would be likely more visible at higher dopant contents. Indeed, no changes in absorption features are observed for lower N doping content. The IR spectra of N-doped Ge and Sb do not demonstrate any changes in the position or shape of the absorption bands (i.e., Ge-N and Sb-N band, respectively) even for the highest used N content (Fig. 3.13). This indicates the high stability of as-deposited undoped layers and N-doped Ge and Sb layers in time.

TeN layers with low N doping, also, do not demonstrate any significant changes. On the contrary, the IR spectrum of TeN 20 sccm layer features great changes in the broad absorption band in the range from 800 cm^{-1} to 400 cm^{-1}, indicating the reduction of contributions assigned to Te-N bonds and the increase of contributions related to Te-O bonds. This can be clearly seen from the comparison with the undoped as-deposited Te layer spectrum (inset in TeN spectrum in Fig. 3.13), where the Te-O absorption band was identified. Moreover, several contributions assigned to N-O and N-H absorption bands are observed at higher wavenumbers (3500 - 2500 cm^{-1} and 1800 – 1300 cm^{-1}) in the IR spectrum of the aged TeN layer. These results confirm the instability of Te-N bonding, as expected from its high value of the formation enthalpy (reported in the section 3.1), likely followed by layer oxidation despite of the deposited protective carbon capping layer. Indeed, the Te-N bond breaking leaves both Te and N atoms unbonded. The atmospheric oxygen can be then easily incorporated as the Te structure remains disordered due to N in interstitial positions, leading to the formation of stable bonds with both involved elements, i. e., Te-O and N-O.

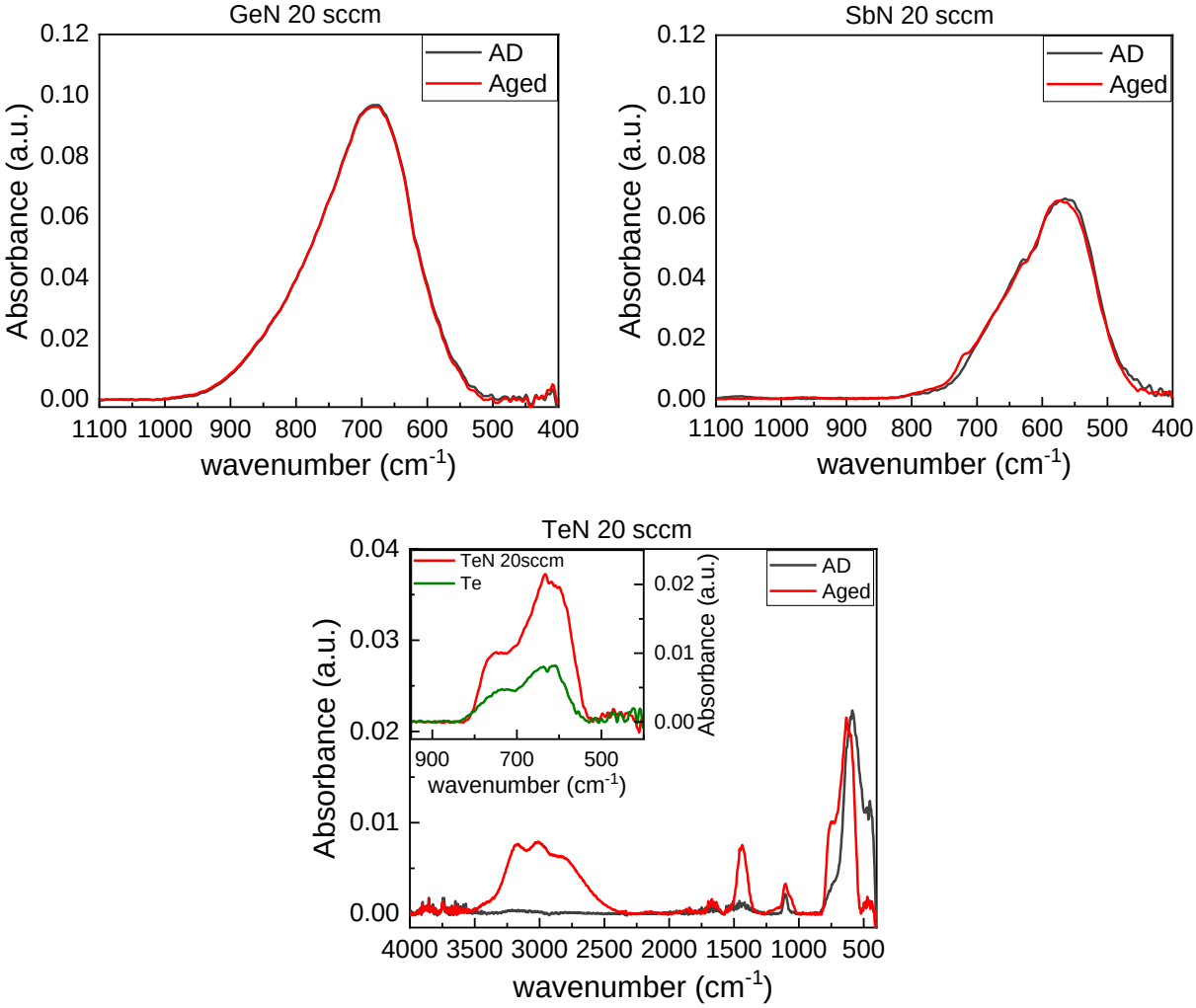

Fig. 3.13: Comparison of as-deposited and aged IR spectra for GeN, SbN and TeN layers with the N_2 flow of 20 sccm. The IR spectra of GeN and SbN layers do not show any changes after 18 months of ageing. Aged TeN spectrum shows new broad absorption bands at 3500 - 2500 cm^{-1} and 1800 – 1300 cm^{-1} corresponding to N-H and N-O vibrational modes, indicating the layer degradation. The inset in TeN graph shows the comparison between aged TeN 20 sccm layer and as-deposited Te layer highlighting the similarities in the shape of Te-O absorption bands.

3.7.2 Structural evolution as a function of temperature

Both undoped and N-doped layers (N_2 flow of 2 sccm) were studied after employing the thermal budget of 400 °C for all three systems (i.e., thermal budget of BEOL integration of PCRAM device, section 1.2.3). The comparison between as-deposited layers and annealed layers is presented in Fig. 3.14.

Undoped Ge layers show no changes in both IR and Raman spectra indicating no impact of the performed annealing at 400 °C. These results are in good agreement with literature, as the temperature of crystallization of Ge is reported to be 480 – 500 °C [304–307]. The undoped as-deposited Sb layer demonstrated to be crystalline, as evidenced by two sharp peaks in the Raman spectrum and discussed in section 3.3.2. These peaks do not show significant changes upon layer annealing, thus confirming that both as-deposited and annealed Sb layers are crystalline. On the contrary, the IR spectrum of annealed Sb layer shows a sharp peak at 720 cm^{-1}, which can be assigned to Sb-O vibrational modes [308,309], thus suggesting the layer oxidation at this annealing temperature. Both IR and Raman spectra of Te layers show significant changes upon annealing. The IR spectrum of annealed Te features a large band of several overlapping contributions in the range from 800 cm^{-1} to 400 cm^{-1}, assigned to Te-O vibrational modes. The two sharp peaks of crystalline Te present in the Raman spectrum are completely reduced, while intense contributions of the Si modes from substrate can be seen (521 cm^{-1} and 950 cm^{-1}) along with several peaks over the whole range from 100 cm^{-1} to 1000 cm^{-1}, assigned also to Te-O vibrational modes. This suggests the complete oxidation of undoped Te layer upon annealing at 400 °C. Indeed, this temperature is already relatively close to the Te melting point (T_m ~450 °C) [310,311].

The IR and Raman spectra of annealed (400 °C) N-doped Ge, Sb and Te layers highlight significant changes for SbN and TeN layers, while only slight changes can be observed in case of GeN layer. Indeed, only a slight shift in position of Ge-N peak maximum (<10 cm^{-1}) in IR spectra and a reduction of the shoulder in a-Ge modes in Raman spectra are observed. These changes are likely due to minor structural relaxation upon annealing, thus suggesting the high stability of formed Ge-N bonding in N-doped Ge layers. On the contrary, the annealing at 400 °C of N-doped Sb layer likely affects the Sb-N bonding causing their breaking, as the Sb-N band (590 cm^{-1}) in IR spectra is completely reduced. Upon this annealing temperature, the N atoms are likely released from the structure in the form of molecular N_2, while Sb layer crystallizes, as evidenced by two sharp Sb peaks in the Raman spectrum. Moreover, Sb oxidation is evidenced by a sharp Sb-O peak (720 cm^{-1}) in the IR spectrum, similar to that observed in the annealed undoped Sb layer. Annealing of N-doped Te layers at 400 °C shows layer degradation, comparable to previously observed in undoped Te, i.e., complete disappearance of Te crystalline structure (including the breaking of Te-N bonds) and layer oxidation.

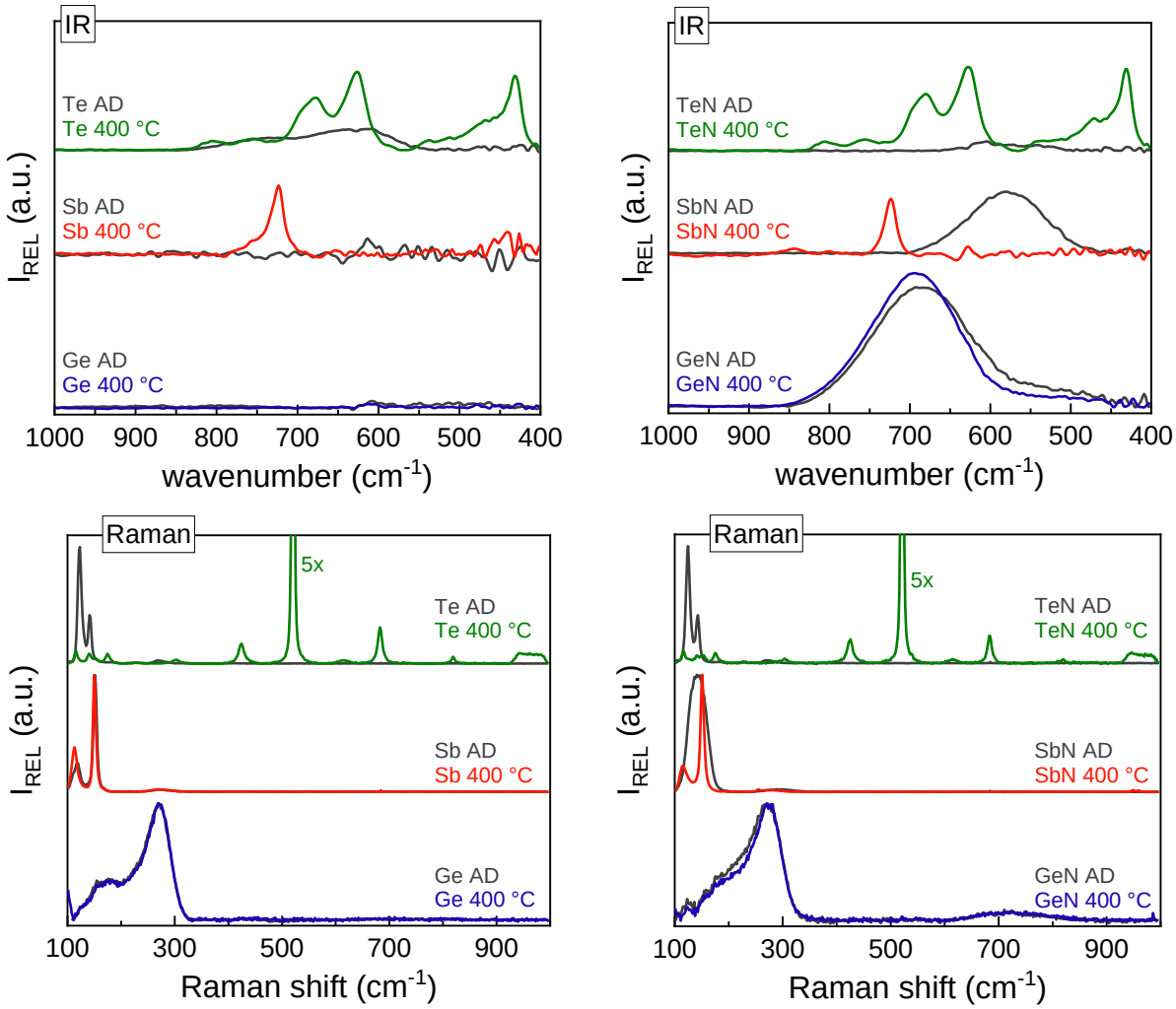

Fig. 3.14: IR and Raman spectra of (left column) as-deposited and annealed (400 °C) undoped layers and (right column) N-doped (N_2 flow 2 sccm) layers, highlighting high stability of GeN alloys, crystallization and partial oxidation of SbN and oxidation of Te and TeN layers upon annealing at 400 °C.

Observing the stability of GeN alloys at the annealing temperature of 400 °C, the undoped and N-doped layers were further annealed at higher temperatures. GeN layers with the lowest and the highest N content (2 sccm and 40 sccm) are presented (Fig. 3.15). The undoped Ge layer is observed to crystallize at temperatures higher than 500 °C, as evidenced by a sharp peak of crystalline Ge (c-Ge) at 300 cm^{-1} in the Raman spectrum. This temperature is slightly higher than that reported in literature (480 – 500 °C) [304–307]. On the contrary, higher annealing temperatures do not significantly affect the N-doped layers. The slight shift of the Ge-N band in IR spectra and changes in Raman spectra already observed at 400 °C are maintained up to 550 °C without no further evolution in case of both GeN layers. Indeed, the formation of Ge-N bonds, which are stronger with regard to Ge-Ge bonds ($E_{Ge–N}$ ~ 2.65 eV and $E_{Ge–Ge}$ ~ 1.94 eV [188]), results in reinforcing the GeN structure and thus in enhanced stability of the GeN system. This stability-enhancing effect of N doping on the structure of a Ge layer is effective already for low N doping contents, as shown in our GeN 2 sccm layer.

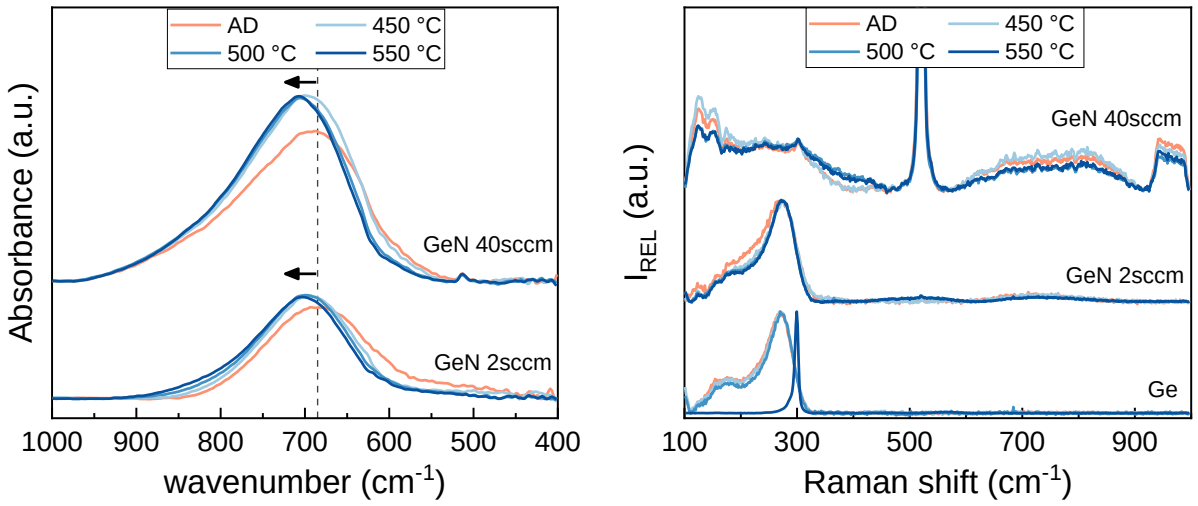

Fig. 3.15: IR and Raman spectra of Ge, GeN 2 sccm and GeN 40 sccm layers annealed at 450 °C, 500 °C and 550 °C demonstrating the crystallization of Ge layer between 500 °C and 550 °C, and the stability of N-doped layers up to higher temperatures.

3.8 Chapter summary

In this chapter, we presented the structural investigation of undoped and N-doped as-deposited Ge, Sb and Te layers performed in order to understand the layer structure and the effect of N doping. The structural studies of the layers were based on results obtained by IR and Raman spectroscopy, which were further supported by EXAFS and XANES analyses and *"ab initio"* simulations.

The incorporation of N into Ge leads to the formation of Ge-N bonds, which further dominate the layer structure owing to their higher stability over Ge-Ge bonds. Indeed, EXAFS results confirm lower contribution of Ge-Ge bonds in the local structure as the N content in the layer increases. N doping in Sb layers leads also to relatively high N incorporation into Sb structure and to the formation of Sb-N bonds. N atoms likely substitute Sb atoms in its crystalline structure, owing to same valence electrons number and atom coordination. Smaller atomic radius causes the shift of the atoms from their ideal position, resulting in an amorphous/disordered character of SbN layers. In case of Te layers, N atoms show to be less prone to incorporate into Te structure, occupying likely the interstitial positions between the Te chains of the crystalline lattice. The N atoms in interstitial positions likely break the weaker secondary bonding between the Te chains of the lattice unit, forming weak Te-N bonds and slightly changing the chain orientation owing to stereochemical effects of Te and N lone pairs. This results in disorder increase in the layer structure, demonstrated as an amorphous Te contribution in the Raman spectrum, while Te chains are still maintained.

The absorption bands in IR and Raman spectra related to the formation of Ge-N, Sb-N and Te-N bonds and their vibrational modes were identified owing to the comparison of the experimental spectra with simulated spectra of ideal crystalline structures of related nitrides. Several nitride structures were used for the spectra simulations for each system, searching for the best match in absorption features.

The investigation of as-deposited layers was further followed by the studies of stability and structural evolution of the layers as function of time and temperature. The as-deposited layers were studied after 18 months of ageing in cleanroom conditions. No structural changes were observed for all the undoped layers as well as for the N-doped Ge and Sb layers, thus demonstrating to be stable in such time period. On the contrary, TeN spectra show the reduction of bands related to Te-N bonds, while the Te-O bands simultaneously appeared. This indicates the low stability of formed Te-N bonds in the structure and significant layer oxidation likely due to disordered Te structure which enables easier O incorporation. Furthermore, the stability of the layers as a function of temperature was investigated, starting from annealing at 400 °C. GeN layers show high stability at this temperature while SbN and TeN layers demonstrate N bonds breaking and layer oxidation. This effect is particularly enhanced in TeN layers at this annealing temperature. GeN layers were further investigated at higher annealing temperatures, showing high stability and no crystallization up to 550 °C.

These results increase the understanding of the structure of undoped Ge, Sb and Te elemental compounds and the effect of N doping and formation of N bonding in such systems. This insight provides useful information, in particular on element-N bonding, and can be applied for the investigation of more complex systems, in particular N-doped GeSbTe alloys, as it is presented in the next chapter.

Chapter 4

Ge-Sb-Te alloys

Material engineering of GST alloys results in significant improvements of their thermal stability, necessary to ensure the data retention of PCRAM device over extended temperature range. In particular, Ge enrichment and N doping of stoichiometric $Ge_2Sb_2Te_5$ alloy showed to be suitable solutions, as presented in the chapter 1. Indeed, owing to Ge enrichment in GST alloys, PCRAM device demonstrated high thermal stability, fulfilling the strict requirements of embedded automotive applications. Moreover, N doping in such alloys could potentially even more stabilize the amorphous phase, resulting from formation of Ge-N bonds in the alloy structure. Another benefit of N doping would result from GeN precipitation at grain boundaries upon alloy crystallization, reducing the grain size of crystalline phases, thus improving the cyclability and reducing the programming current of PCRAM device.
Despite the proven benefits of Ge enrichment and N doping of these alloys on PCRAM device performances, the effect of Ge and N incorporation and their content on the alloy structure remains unclear, as well as structural evolution of such alloys as a function of annealing temperature. In this chapter, we present the structural investigation of undoped and N-doped Ge-rich GST alloys, using the combination of Raman and FTIR spectroscopy with XRD analyses, accompanied by other characterization techniques, such as TEM-EDX and ellipsometry. In the first part, we compare the structure of the reference $Ge_2Sb_2Te_5$ and one Ge-rich GST composition, identifying the main structural units of the alloy. We highlight the structural evolutions as a function of temperature, outlining the crystallization mechanism of such alloys. Further, we study the effect of Ge enrichment, and we demonstrate the contribution of different phenomena occurring during the crystallization mechanism. In the second part, N doping in Ge-rich GST alloys are studied. We show the impact of nitrogen on the structural evolution and crystallization mechanisms described for undoped alloys and we demonstrate the effect of different N content.

4.1 Ge-rich GST: Structural Evolution

Investigation of the structure of Ge-rich GST alloy and its evolution as a function of temperature is presented in this part. Ge-rich GST with Ge content of 45 at.% (GGST) was chosen for this structural investigation, owing to its promising properties, such as high crystallization temperature and thus high data retention of amorphous phase, presented in the chapter 1. The structural investigation of GGST is compared to $Ge_2Sb_2Te_5$ (GST225) alloy, considered as a reference compound. The alloys are studied by Raman spectroscopy and XRD, accompanied by R vs T measurements and TEM-EDX analysis.

R vs T measurements performed on GST225 and GGST (Fig. 4.1) highlight the main resistivity drops of the layers with increasing temperature, as the as-deposited layers undergo amorphous-to-crystalline phase transition. Two transitions at 160 °C and 330 °C can be observed for GST225 layer, related to the cubic (fcc) and hexagonal (hex) phase transitions, respectively. The amorphous-to-crystalline transition of GGST layer is significantly shifted to higher temperatures, featuring a double step transition with the first drop at 300 °C and the second one slightly below 350 °C. This highlights the enhanced stability of amorphous phase of Ge-enriched alloys, as observed in [24,143] and discussed in the section 1.3.3. While both layers demonstrate the same resistivity values for amorphous phase, GGST features higher resistivity in crystalline phase with respect to GST225.

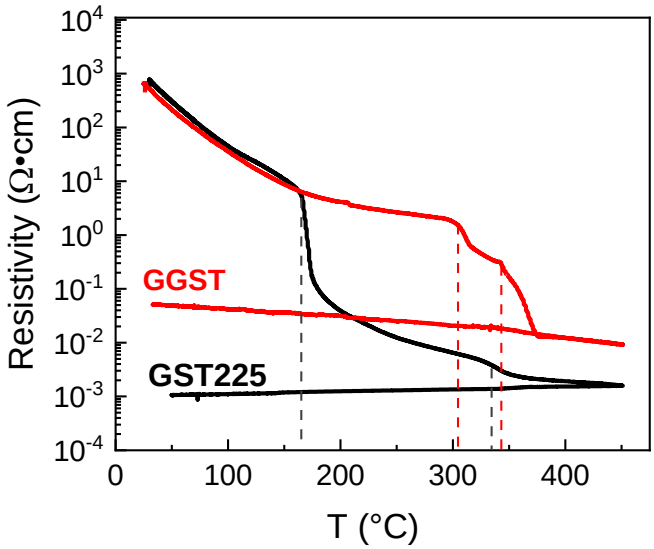

Fig. 4.1: Resistivity as a function of temperature for $Ge_2Sb_2Te_5$ (GST225) and Ge_{45}GST (GGST) alloys. GST225 features two resistivity drops at 160 °C and 340 °C corresponding to amorphous-to-fcc and fcc-to-hex phase transitions, respectively. GGST shows one double step amorphous-to-fcc transition at 300 - 350 °C, shifted to higher temperatures compared to GST225.

4.1.1 $Ge_2Sb_2Te_5$

Raman spectrum of amorphous as-deposited (AD) GST225 is dominated by a broad band covering the frequency region between 100 cm^{-1} and 190 cm^{-1}, formed by overlapping contributions at 124 cm^{-1} and 154 cm^{-1} (Fig. 4.2). The broad band is further accompanied by low intense band at ~220 cm^{-1}. The main contribution at 154 cm^{-1} can result from the vibrational modes assigned to different structural units, as described in the section 2.2.3. The stretching vibrational modes of Sb-Te in $SbTe_3$ pyramidal units [212,312] appears to be the most accurate assignment of this contribution.

The contributions at 124 cm^{-1} and 220 cm^{-1} can be assigned to the different vibrational modes of Ge-Te bonds present in tetrahedral and defective octahedral structures as observed in amorphous GeTe [96,123,221]. In general, the vibrational modes of defective octahedra are

mostly described to be observed below 190 cm^{-1}, whilst weaker features at high wavenumbers above 190 cm^{-1} can be assigned to vibrations of Ge in tetrahedral sites [221]. Taking into account the analysis performed on GeTe [179], the peak at ~ 124 cm^{-1} is assigned to the A_1 vibration mode of corner-sharing tetrahedra $GeTe_{4-n}Ge_n$ (n = 1, 2) and the peak at ~220 cm^{-1} is assigned to the vibrational mode of $GeTe_4$ tetrahedral units [179,212].
Significant changes in Raman spectra can be observed for GST225 upon annealing. The broad band still demonstrates its maximum at 154 cm^{-1} (Sb-Te modes) also for layer annealed at 250 °C, thus demonstrating the dominance of these structural units even for the cubic crystalline phase (GST225-fcc) of the alloy [136,221,312] (this annealing temperature is well above the first transition as observed in RvsT curve, Fig. 4.1). A new band contribution appears at 174 cm^{-1}, while the intensity of the contributions in the range of 100 - 140 cm^{-1} (Ge-Te modes) slightly decreases. Raman spectra of GST225 annealed at higher temperatures demonstrate further intensity increase of the peak at 174 cm^{-1} at the expense of the peak at 154 cm^{-1}. The latter one gradually disappears, while the former one becomes dominant in the spectra. This new dominant peak at 174 cm^{-1} is also assigned to the Sb-Te vibrational modes, however, in structural arrangement characteristic for GST225 hexagonal crystalline phase (GST225-hex). Indeed, the alloy passed the second transition, which is observed by R vs T measurements (Fig. 4.1). The Raman spectra annealed at 350 °C and higher temperatures do not significantly change as the hexagonal crystalline phase is already well formed. The observed progressive development between the contributions assigned to different Sb-Te vibrational modes with increasing annealing temperature is the evidence of the ongoing structural rearrangement in GST225 from fcc to hex crystalline phase [313]. The Raman spectra decomposition for both as-deposited and annealed (400 °C) GST225 are presented in Appendix 5.

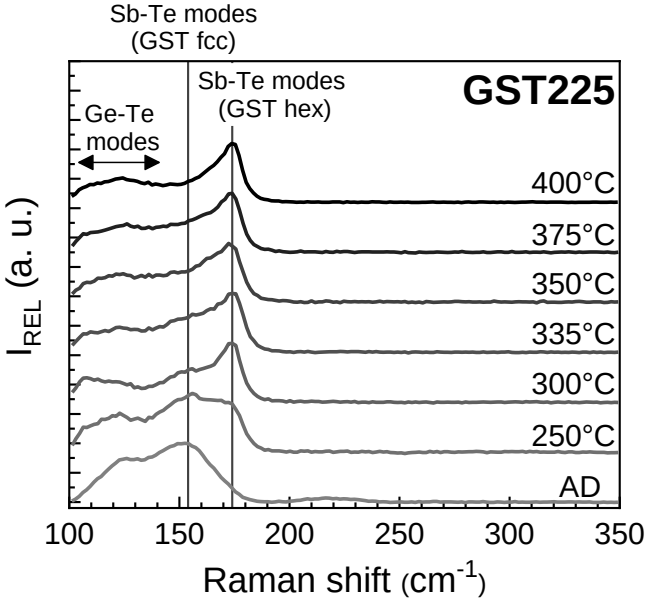

Fig. 4.2: Raman spectra of amorphous as-deposited (AD) and annealed GST225 (from 250 °C up to 400 °C). Vertical lines at 154 cm^{-1} and 174 cm^{-1} highlight main vibrational modes of SbTe structural units.

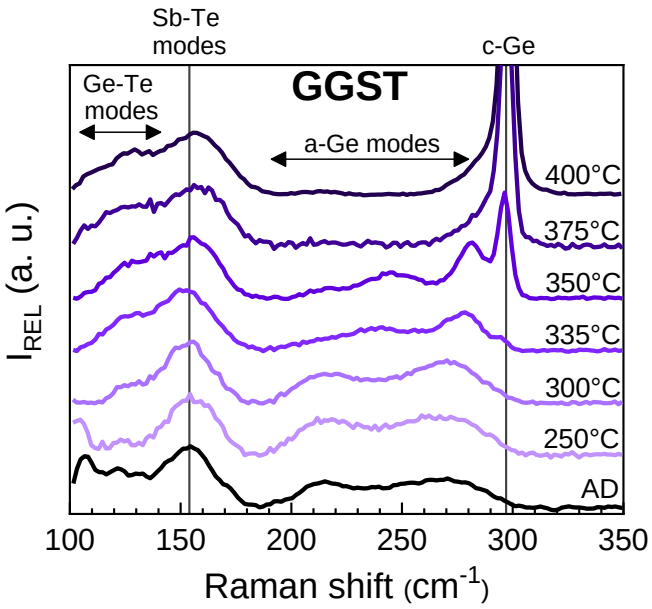

Fig. 4.3: Raman spectra of amorphous as-deposited (AD) and annealed GGST. Vertical lines show the position of the Sb-Te vibrational modes (154 cm^{-1}) and crystalline Ge modes (297 cm^{-1}) [313].

4.1.2 Ge-rich GST

The Raman spectrum of as-deposited GGST (Fig. 4.3) can be divided into three main parts [313]:

- main contribution at 154 cm^{-1} assigned to the Sb-Te stretching mode of $SbTe_3$ pyramidal units, already evidenced in GST225;
- contributions at low wavenumbers (below ~150 cm^{-1}) corresponding to vibrational modes of GeTe structural units;
- broad band at higher wavenumbers in the range of 190 – 300 cm^{-1} formed by two overlapping contributions at ~272 cm^{-1} and ~230 cm^{-1}. These contributions correspond respectively to the TO-like and LO-like vibrational modes of amorphous Ge (a-Ge) [187,188,314,315].

The contribution at 154 cm^{-1} (SbTe units) does not significantly change either in position nor FWHM up to the annealing temperature of 400 °C, contrary to what was observed in GST225. The low wavenumber part of the spectra (GeTe units) evidences an evolution up to 335 °C, after which the band shape corresponds to that of amorphous as-deposited and crystalline GST225-fcc (Fig. 4.2). These findings already suggest the stability of SbTe structural units and the absence of the cubic-to-hexagonal transition even at high temperature [316]. In the a-Ge part of the spectra, gradual development of TO-like and LO-like modes is observed with increasing annealing temperature. New sharp peak at 297 cm^{-1}, assigned to Ge crystalline phase (c-Ge), appears in the spectrum at 335 °C, suggesting the Ge crystallization. Such temperature is particularly low for Ge crystallization when compared with that of an elemental a-Ge layer (crystallization at 500 – 550 °C; Chapter 3, Fig. 3.15).
Further analysis of the Raman bands was performed in order to follow the evolution trends of the different structural units of GGST alloy as a function of temperature. The sum of the peaks integrated intensities was computed, considering: peaks at 110 cm^{-1} and 124 cm^{-1} for Ge-Te vibrational modes; peaks at 220 cm^{-1} and 270 cm^{-1} for a-Ge vibrational modes and peak at 297 cm^{-1} for c-Ge. The sum of peak integrated intensity for each type of structural units was normalized relative to the integrated intensity of Sb-Te modes (main peak at

154 cm^{-1}), which remains stable for the layers at the studied temperatures. The results are presented as a function of annealing temperature (Fig. 4.4) and highlight the following evolutions:

- The intensity of Ge-Te modes present in the amorphous as-deposited layer initially decrease with the annealing temperature, reaching the minimum value at 300 °C. At the same time, the intensity of a-Ge modes slightly increase, reaching the maximum value at 250 °C;
- The intensity of Ge-Te modes involved in the ordering process of the layer begin to increase after 300 °C, reaching an almost stable intensity after 375 °C;
- Simultaneously with the intensity increase of Ge-Te modes, the a-Ge modes gradually disappear, turning into the sharp peak of crystalline Ge. The c-Ge peak first appears at 335 °C and increases in intensity up to maximum annealing temperature.

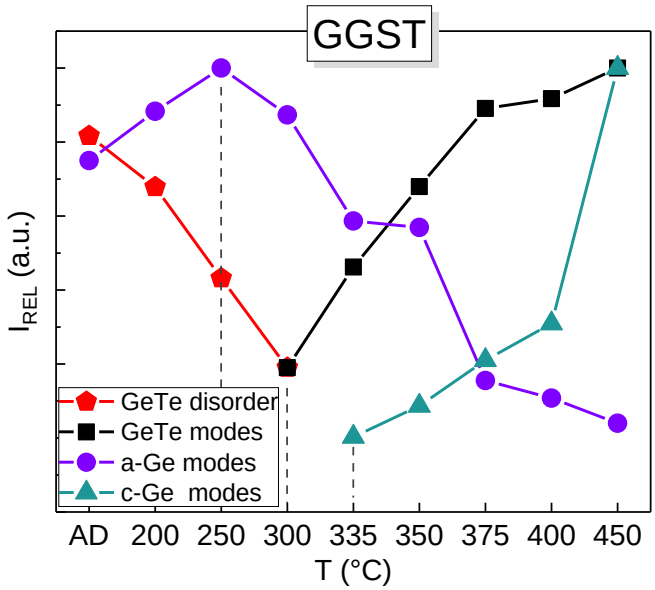

Fig. 4.4: Intensity evolution of Ge-Te, a-Ge and c-Ge modes from the Raman spectra of GGST as a function of annealing temperature. The integrated intensities were computed and normalized relative to the integrated intensity of stable contribution assigned to Sb-Te modes [313]. Dashed lines indicate the maximum intensity for a-Ge modes (at 250 °C), minimum intensity for Ge-Te modes (300 °C) and the appearance of c-Ge modes (335 °C).

The Raman spectra analyses demonstrate that initial temperature increase up to 300 °C results in a first reorganization step, characterized by the decrease of Ge-Te modes and simultaneous enhancement of a-Ge modes. Indeed, the breaking of unfavorable bonding in mixed GeSbTe units (e.g., $GeSbTe_3$, Ge_2SbTe_2 or $GeSb_2Te_2$ [134,135]) and the rearrangement of $GeTe_{4-n}Ge_n$ (n = 0, 1, 2, 3, 4) tetrahedral units likely occur in originally amorphous disordered system, both resulting in reduction of the Ge-Te modes. As a consequence, the Ge atoms in mixed units are liberated, slightly increasing the intensity of a-Ge modes. This is in agreement with previous investigations on amorphous GeTe alloys [179], based on the random bonding model [317], in which the combination of the different tetrahedra complex units depends also on the layer stoichiometry.

The structural evolution becomes more significant at higher annealing temperatures. The relative intensity of Ge-Te modes reaches the minimum value at the temperature of 300 °C, which is likely related to the end of the first reorganization step and liberation of Ge atoms. Progressive increase of Ge-Te modes relative intensity at higher temperatures indicates the gradual rearrangement of Ge-Te bonds around Sb-Te structural units upon GeSbTe phase

crystallization. The crystalline GeSbTe phase then further nucleates and grows. Disappearance of a-Ge modes at temperatures above 300 °C is associated with the progressive reorganization of Ge structure, i.e., ordering of Ge atoms in amorphous phase (a-Ge) leading towards the nucleation and growth of the Ge cubic crystalline phase.
XRD analysis was performed to further investigate the development of the crystalline phases in GGST (Fig. 4.5). The as-deposited layer and the layers annealed up to 300 °C do not shown any diffraction peaks, thus confirming the amorphous nature of the layers. Well-defined diffraction peaks are observed starting from the XRD pattern at 350 °C. The characteristic peaks of the GST225-fcc crystalline phase coexist with the peaks of the Ge cubic phase, whose intensity further increases with the annealing temperature up to 450 °C. The crystallites sizes were calculated by Scherrer's law for [220] Bragg peak of GST225-fcc phase and for [111] Bragg peak of Ge cubic phase (Table 4-I). GST225-fcc phase shows an almost stable grain size at all the temperatures, whereas the Ge grains approximately double in size from 350 °C to 450 °C [313].

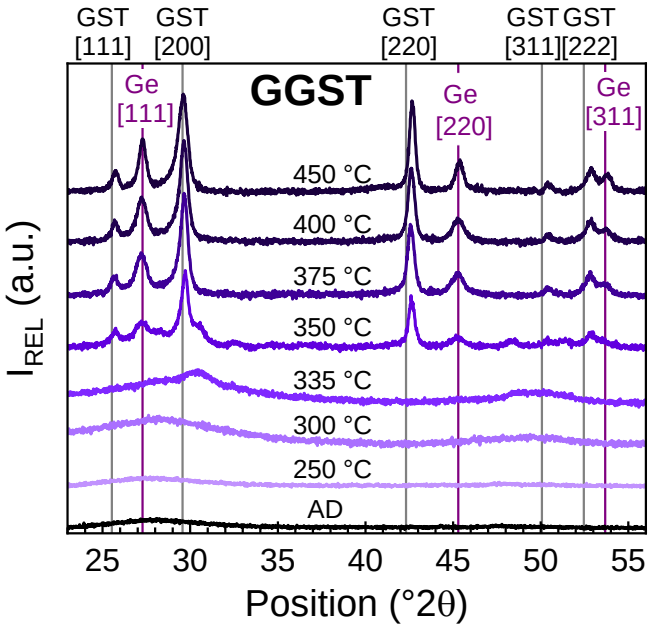

Fig. 4.5: XRD patterns of amorphous as-deposited (AD) and annealed GGST up to 450 °C. Indexation is performed from database data (ICDD PDF No. 00-054-0484 and 00-004-0545) [313].

Table 4-I: Crystallites sizes calculated by Scherrer's law for GST225-fcc and Ge phases from the XRD patterns of annealed GGST [313].

T (°C)	Crystallites size (nm)	
	GST225 [220]	Ge [111]
350 °C	26 nm	9 nm
375 °C	22 nm	11 nm
400 °C	24 nm	18 nm
450 °C	28 nm	19 nm

The XRD pattern at 335 °C features a broad band reaching the maximum at ~30.5° (2θ), which can be further recognized in the XRD pattern at 350 °C as a broad shoulder of the GST[200] main peak. Moreover, several other small peaks can be observed in the XRD

pattern at 350 °C, but they disappear at higher annealing temperatures together with the above-mentioned broad band at ~30.5°. The presence of these features highlights the appearance of an intermediate structural evolution step, which the system passes before the appearance of GST225-fcc and Ge crystalline phases. The formation of a transient phase (G^+GST) can be suggested, featuring higher Ge content with respect to standard GST225 alloy. The evidence of such a "double step" crystallization mechanism can be already found in R vs T measurement of GGST in Fig. 4.1.

To confirm the hypothesis of transient G^+GST phase, isothermal XRD measurements were performed for the duration of 70 hours (Fig. 4.6). The temperature of the isothermal annealing was kept at ~300 °C, i.e., the temperature, at which the first changes in XRD spectra are observed. The aim was to sufficiently slow down the mechanisms and therefore to achieve the clear sequence of the different phases appearing in the spectra. The G^+GST broad band appears in the XRD pattern after about one hour of annealing. Only few hours later, the main peak of GST225-fcc phase (GST[200]) starts to increase. The intensity of G^+GST peak then decreases progressively as the intensity of the GST[200] peak increases, suggesting the gradual expulsion of Ge from G^+GST in favor of the crystallization of more stable GST225-fcc phase. This is rather in agreement with previous observations on a crystallization-induced segregation in Te-rich GeSbTe materials [144]. More than 30 hours of annealing are required to initiate the growth of Ge crystals, when liberated Ge atoms are finally accumulated on the grain boundaries outside of GeSbTe crystalline regions. The presence of GeSbTe crystalline interfaces likely induces the heterogeneous nucleation of Ge, followed by the rapid growth of Ge crystallites. The rapid growth of Ge crystalline phase overtakes the crystallization dynamics of the system and limits the further development of GeSbTe crystals (i.e., crystallites size of GST225-fcc remains constant with temperature, as shown in Table 4-I). Heterogeneous nucleation of Ge from the neighbor seed crystal allows Ge to crystallize at temperatures lower than in elemental a-Ge layers, as observed in Fig. 4.3 and Fig. 4.5.

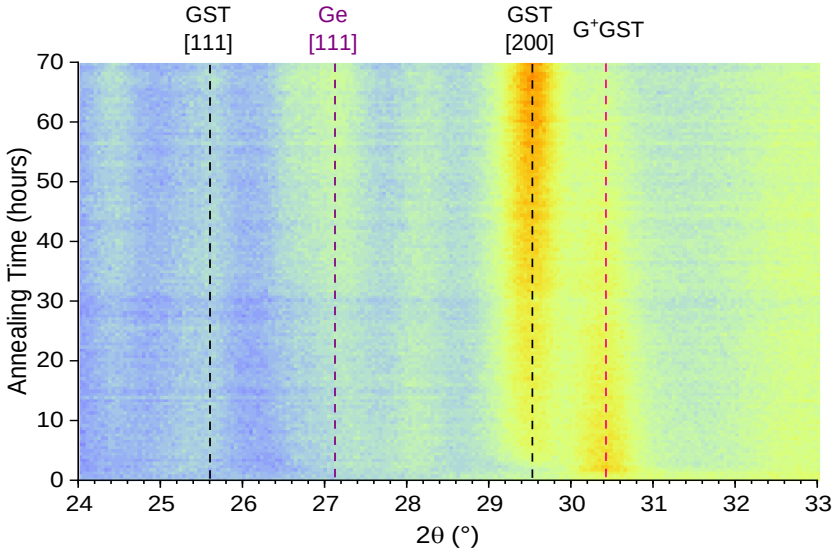

Fig. 4.6: Isothermal XRD measurements at ~300 °C on GGST showing the development of GST225-fcc and Ge crystalline phases (black and violet dashed lines, respectively). A transient G^+GST phase (red dashed line) is detected before the appearance of GST225-fcc phase [313].

In order to further support the Raman and XRD results, the combination of TEM images with EDX analyses (TEM-EDX) was performed in order to provide the elemental mapping of the layer after annealing. This allows to visualize and to follow the demixing process in the alloy (Fig. 4.7).

The image of the layer annealed at 300 °C indicates the perfect homogeneity of the as-deposited amorphous alloy up to this temperature. An elemental migration starts to be visible at 335 °C, which corresponds well with the beginning of the resistivity decrease (Fig. 4.1), the progressive rearrangement of the Ge-Te bonds around stable Sb-Te structural units observed by Raman spectroscopy (Fig. 4.3 and Fig. 4.4) and the appearance of the transient G^+GST phase in XRD pattern (Fig. 4.6). The migration becomes more evident at 380 °C, where the Ge-rich and Sb-/Te-rich regions are already clearly separated. Formation of such regions evidences the demixing process of Ge and GeSbTe phases described above. The separated Ge-rich regions confirm the obtained XRD results (Fig. 4.5) showing the already developed Ge crystalline phase around this temperature. At 450 °C, the phase separation is fully completed as the perfectly formed Ge and GeSbTe crystalline phases can be distinguished. Hence, the crystallization growth of separated Ge and GeSbTe phases dominates the system at this temperature [313].

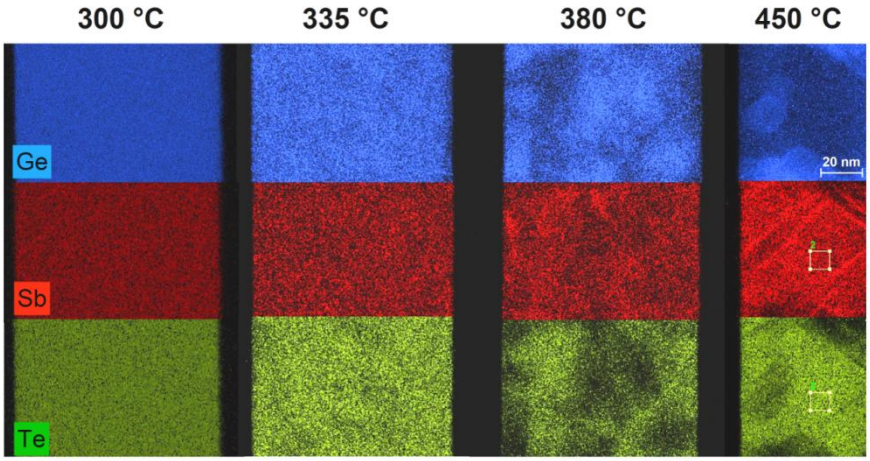

Fig. 4.7: TEM-EDX analyses of GGST alloy annealed at 300 °C, 335 °C, 380 °C and 450 °C. Ge, Sb and Te cartographies highlight the elemental migration and the formation of Ge- and Sb-/Te-enriched zones, evidencing the ongoing demixing process. Yellow squares in cartographies at 450 °C highlight the region with GeSbTe grains [313].

4.1.3 Summary of the section

To resume this section, the combination of the results obtained from Raman spectroscopy and XRD analysis allows to highlight the main structural evolution in Ge-rich GST alloys as a function of annealing temperature. XRD analysis confirms the amorphous character of the as-deposited $Ge_{45}GST$ layer. Simultaneously, Raman spectroscopy identifies main structural units forming the basis of the structure of as-deposited Ge-rich GeSbTe alloys, i.e., vibrational modes of Sb-Te and Ge-Te bonds along with a-Ge vibrational modes from Ge excess in the layer. Sb-Te modes showed to remain stable up to high annealing temperature, indicating that these bonds form the dominant component of the structure.

The local reorganization of the structure is achieved with increasing annealing temperature, ordering the Ge-Te bonds around the stable SbTe units. These rearrangements along with increased mobility of Ge atoms drive the system locally towards a gradual expulsion of Ge from mixed GeSbTe and Ge-rich GeTe units, giving rise to a G^+GST transient phase. Moreover, the nucleation and growth of this G^+GST transient phase then continues to feed the demixing process. The red circle in Fig. 4.8 highlights the region around $Ge_3Sb_2Te_6$, in which possible transient phases can be found, based on the comparison of the experimental XRD pattern with various PDF cards from the database (ICDD PDF No. 04-019-5066; 01-084-5074; 01-085-2822; 01-084-5063). At higher annealing temperatures, the progressive

Ge expulsion further leads to the complete disappearance of the G^{+}GST transient phase, driving the system towards the stable GST225-fcc crystalline phase along with segregated Ge crystalline phase. Owing to the rapid Ge crystal growth, the crystallization dynamics of the system is overtaken by Ge phase, thus limiting further development of GeSbTe crystals. The schematic overview of the described evolution steps as a function of temperature is presented in Fig. 4.9.

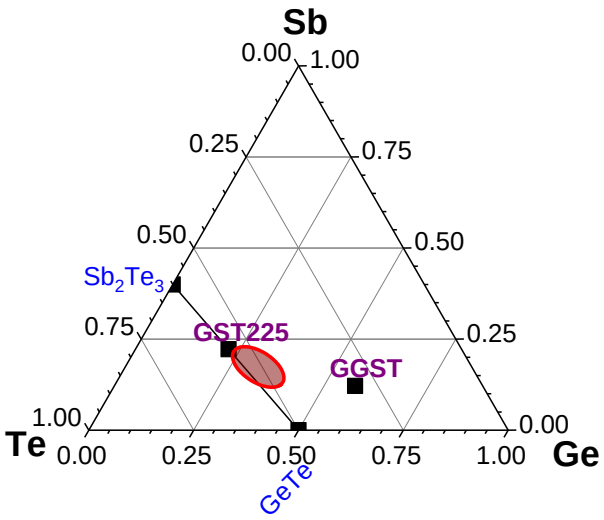

Fig. 4.8: Ge-Sb-Te ternary diagram highlighting GST225 and GGST compositions. Red circle indicates the region (around $Ge_3Sb_2Te_6$) of the transient G^{+}GST phase, which give rise to the partial crystallization in GGST, as observed by XRD [313].

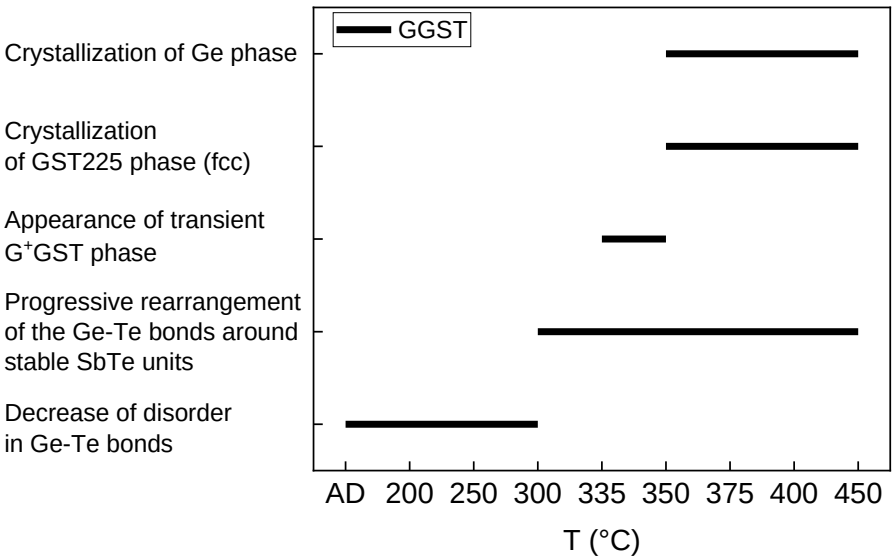

Fig. 4.9: Diagram summarizing the main steps of structural evolution of GGST alloy as a function of annealing temperature.

4.2 Ge-rich GST: Effect of Ge content

The investigation performed on $Ge_{45}GST$ alloy were further extended to Ge-rich GST compositions varying the Ge content from 15 at.% to 55 at.% (Fig. 4.10; hereafter referred as Ge_xGST, where x represents the Ge enrichment). These studies allow to demonstrate several competing phenomena in the system, such as Ge diffusion and segregation as well as nucleation and growth of both GST and Ge phases, as a function of Ge content and increasing temperature. The obtained results allow to describe the overall crystallization mechanisms and their dynamics in Ge-rich GST alloys.

First, the as-deposited samples were studied by WDXRF, Ellipsometry and Raman spectroscopy. Next, the structural evolution of Ge-rich GST compositions as a function of annealing temperature is presented, using the results based on Raman Spectroscopy, XRD and TEM-EDX analyses.

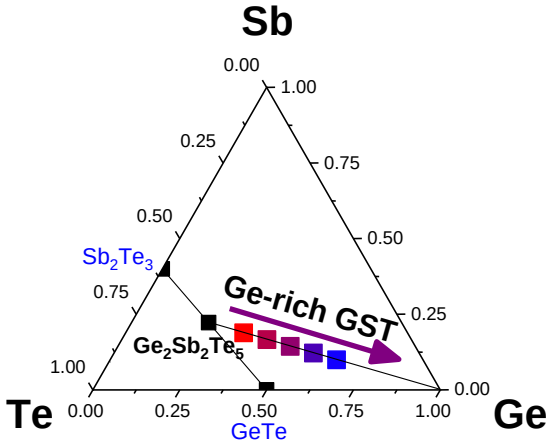

Fig. 4.10: Ge-Sb-Te ternary diagram showing the studied Ge-rich GST compositions [318].

4.2.1 As-deposited Ge-rich GST layers

WDXRF quantification of the Ge, Sb and Te content in the studied Ge-rich GST layers (Fig. 4.11) shows good agreement of the measured values with the nominal ones, keeping the Sb over Te ratio of 0.4, as expected from the $Ge_2Sb_2Te_5$ target used for the deposition. The global Ge content in the studied alloys increases from about 20 at.% up to more than 60 at.% [318].

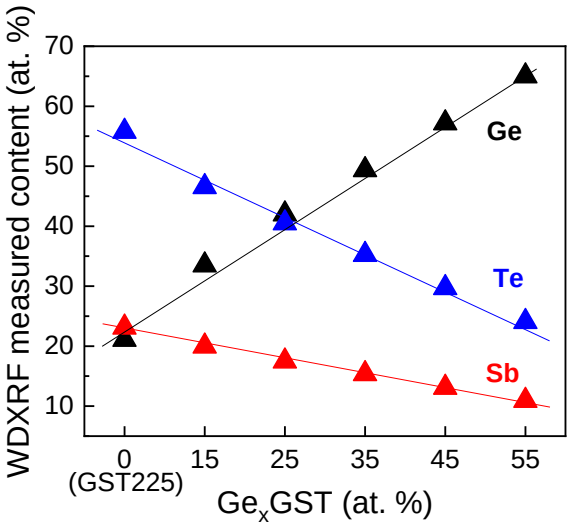

Fig. 4.11: Ge, Sb and Te content in studied Ge-rich GST alloys measured by WDXRF. Ge content in the alloys increases un to more than 60 at.% for $Ge_{55}GST$ [318].

In-situ ellipsometry was performed in order to observe changes in the optical behavior of Ge-rich GST samples with increasing temperature. Fig. 4.12 shows the angle psi (ψ), related to the ratio between reflection coefficient for p- and s- polarization, as a function of the annealing temperature. The GST225 (presented as reference alloy) shows two sharp increases of ψ at around ~165 °C and ~350 °C, which correspond to amorphous-to-fcc and fcc-to-hex transitions, respectively. Increasing the Ge content in the layers leads to the delay of the first transition to higher temperatures, whereas the fcc-to-hex transition is not observed anymore, at least up to 400 °C. Moreover, the global difference in ψ is reduced as the Ge content increases. In Ge_{35}GST and Ge_{45}GST, the first transition is separated into two steps, evidencing the growth of an intermediary phase, presented already in the section 4.1.2. Similar double step transition was already observed in R vs T measurements of Ge_{45}GST (Fig. 4.1), well demonstrating the complementarity of ellipsometry and R vs T measurements, presented already in the section 2.2.2. A second sharp increase of ψ observed in Ge-rich GST at higher temperatures may be likely attributed to the growth of the GST phase once Ge phase is completely segregated [318].

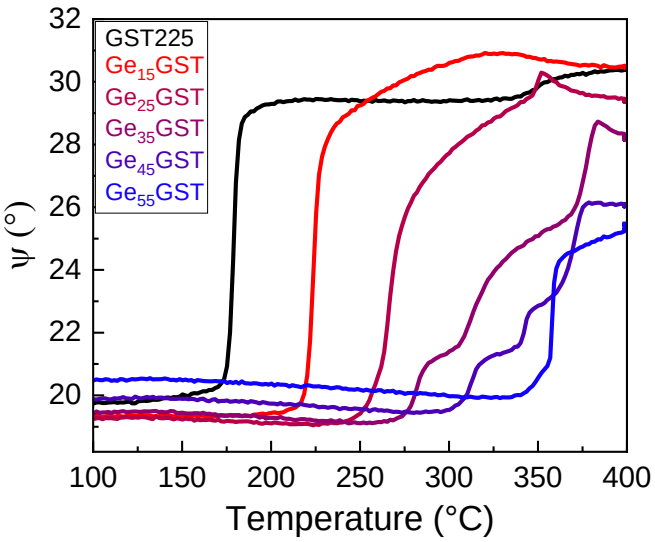

Fig. 4.12: In-situ ellipsometry measurements showing the delay of the amorphous-to-fcc transition of GST phase and Ge phase crystallization for studied Ge-rich GST alloys with increasing Ge content [318].

Raman spectra of amorphous as-deposited (AD) Ge-rich GST layers are reported in Fig. 4.13. The spectra were normalized with regard to the intensity of the peak at 154 cm^{-1} and can be divided into two main frequency regions [318]:

- From 100 cm^{-1} to 190 cm^{-1}, overlapping bands at 110 cm^{-1}, 124 cm^{-1} and 154 cm^{-1} are present, corresponding to the vibrational modes of the GST phase, already described in the section 4.1. In particular, the band at 154 cm^{-1} is assigned to the Sb-Te vibrational modes of $SbTe_3$ structural units, the band at 124 cm^{-1} is assigned to the Ge-Te vibrational modes of $GeTe_{4-n}Ge_n$ (n = 1, 2) mixed units. The identification of the band at 110 cm^{-1} required more investigation, employing lower wavenumber region of Raman shift, as several contributions to this peak are possible. The band identification is described in detail in Appendix 5. Based to the performed analysis, the band at ~110 cm^{-1} likely corresponds to E_g^2 vibrational mode of Sb-Te bonds.
- From 190 cm^{-1} to 300 cm^{-1}, two overlapping bands can be distinguished at about 270 cm^{-1} and 220 cm^{-1}, assigned to the TO-like and LO-like vibrational modes of a-Ge, respectively (reported in the section 4.1.).

The described bands can be distinguished in the spectra of all Ge-rich GST samples. It can be noted that the band at 154 cm^{-1} (Sb-Te) is stable in position and width and represents the dominant peak in the spectra independently from the Ge content in the layer. On the contrary, the decrease in intensity of Ge-Te modes at 124 cm^{-1} and the clearer separation of the peak at 110 cm^{-1} can be observed in the alloys with higher Ge content. The intensity of the a-Ge modes increases respectively with the Ge content in the layer.

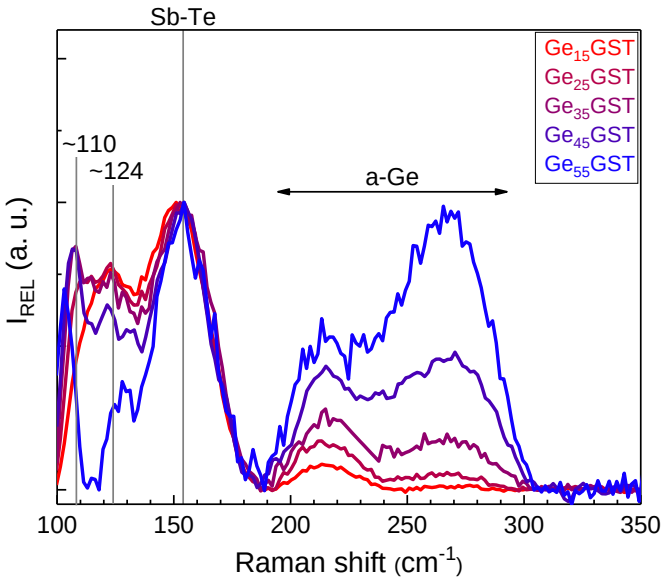

Fig. 4.13: Raman spectra of as-deposited Ge_xGST layers highlighting the changes in the Ge-Te modes (100 - 130 cm^{-1}) and the intensity of amorphous Ge (a-Ge) modes as a function of increasing Ge content [318].

4.2.2 Structural evolution of the Ge-rich GST layers as a function of temperature

Ge_xGST layers were annealed under inert N_2 atmosphere to temperatures in the range from 300 °C to 450 °C. The results are shown for all the alloys in the Ge enrichment range from 15 at.% to 55 at.%, i.e., including the $Ge_{45}GST$ alloy, which was investigated and described in the section 4.1.

Fig. 4.14 shows the Raman spectra of the annealed Ge_xGST layers. The intensity of measured spectra was normalized with regard to the intensity of the peak at 154 cm^{-1}. Indeed, this well-defined peak assigned to the Sb-Te vibrational mode is present in all the spectra at all different annealing temperatures. In the spectra of $Ge_{15}GST$, $Ge_{25}GST$ and $Ge_{35}GST$ at 300 °C, the broad band below 190 cm^{-1} (Sb-Te and Ge-Te vibrational modes of GST phase) already corresponds to that of crystalline GST225-fcc. This likely indicates that the Ge-Te bond rearrangement around Sb-Te units in the layer structure is highly advanced or even completed. On the contrary, the intensity of Ge-Te modes in $Ge_{45}GST$ and $Ge_{55}GST$ is significantly lower, indicating that the stucture is still disordered. The a-Ge modes (190 - 300 cm^{-1}) present in all compositions indicate that the Ge in the layer still remains amorphous.

At the annealing temperature of 350 °C, the reorganization of Ge-Te modes can be already observed in all the compositions. Moreover, the peak at 110 cm^{-1}, observed at lower temperatures, completely disappears. The most significant changes occur in the region of a-Ge modes, where the c-Ge mode appears in all the spectra except for $Ge_{35}GST$. The intensity of c-Ge mode varies correspondingly with the Ge content in the layer. In $Ge_{35}GST$, however, clear shift of a-Ge modes towards the position of c-Ge can be observed (note an intermediary peak at 280 cm^{-1}), highlighting the ongoing Ge structural reorganization. Layers

annealed at 400 °C and 450 °C show a good match between the spectra of all compositions, indicating already well formed GST and Ge crystalline phases. The intensity of the c-Ge peak increases with the Ge content. Slight asymmetry and hence the position shift of the GST phase band (100-190 cm^{-1}) in the spectra at 450 °C is due to the presence of an additional low intense contribution at ~170 cm^{-1}. This contribution is assigned to vibrational modes of Sb-Te bonds observed mainly in GST225-hex phase, as described earlier in the section 4.1. The presence of this contribution is therefore likely related to the eventual reordering of SbTe units between the GeSbTe cubic and hexagonal phases, giving rise to the fcc-hex phase transition at higher temperatures (showed for GST225 in the section 4.1.1) [318].

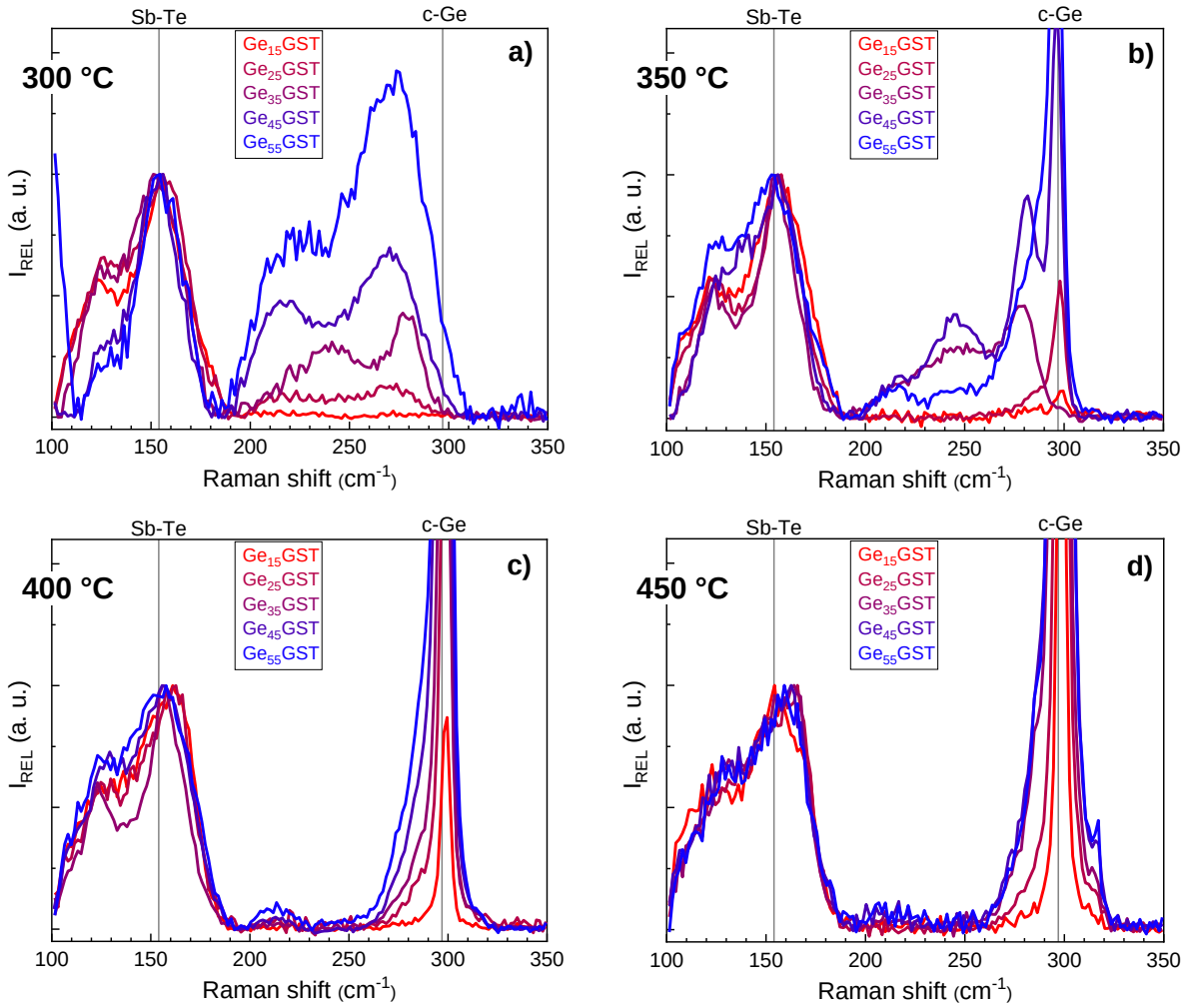

Fig. 4.14: Raman spectra of Ge_xGST layers annealed at (a) 300 °C, (b) 350 °C, (c) 400 °C and (d) 450 °C. The spectra demonstrate the stability of Sb-Te modes (154 cm^{-1}) and changes in GeTe and a-Ge modes (100 - 130 cm^{-1} and 190 – 300 cm^{-1}, respectively). The c-Ge modes are observed from the annealing temperature of 350 °C [318].

The XRD patterns of the studied layers are presented in Fig. 4.15. The peak intensity in all patterns was normalized with regard to the dominant peak of the GST225-fcc phase (i.e., GST[200] peak). The XRD patterns of the layers annealed at 300 °C (Fig. 4.15a) show the presence only of the GST225-fcc crystalline phase for $Ge_{15}GST$, $Ge_{25}GST$ and $Ge_{35}GST$, while the XRD patterns of $Ge_{45}GST$ and $Ge_{55}GST$ show only a broad feature indicating still a disordered amorphous structure. No XRD peaks corresponding to Ge crystalline phase are observed at this temperature. The XRD patterns at 350 °C (Fig. 4.15b) evidence the already developed GST225-fcc phase in all the studied compositions. The second set of peaks can be

observed, assigned to the Ge cubic crystalline phase. The set of Ge peaks appears in all the patterns except for the $Ge_{35}GST$. These observations are in good agreement with the Raman analyses [318].

Furthermore, the broad band at ~30.5°, alongside the dominant GST[200] peak, is observed in the pattern of $Ge_{35}GST$ at 300 °C, later disappearing at higher temperatures. This band can be assigned to the $G^{+}GST$ transient phase, similar to that previously observed in $Ge_{45}GST$ at 350 °C discussed in the section 4.1.2. These findings are also supported by the ellipsometry results, evidencing an intermediary transition along the increasing ψ values (Fig. 4.12) [318].

High annealing temperatures of 400 °C and 450 °C result in continuous intensity increase and narrowing of the GST225-fcc and Ge cubic peaks in the related XRD patterns, demonstrating the crystal growth of the separated GST225-fcc and Ge phases. In $Ge_{15}GST$ and $Ge_{25}GST$, these annealing temperature further induces the intensity increase of the peaks corresponding to the GST[111] and GST[222] planes, which indicates the preferential crystallization of the GST225-fcc phase along these planes. Moreover, XRD pattern of $Ge_{15}GST$ at 450 °C also evidences the significant position shift of the GST[200] and GST[220] peaks and the appearance of several new broad bands. These changes suggest the advancing fcc-to-hex phase transition of GST225 (GST225-hex: ICDD PDF No. 04-008-1147), or much more likely the vacancies reordering in the cubic phase, which occurs well before the fcc-to-hex transition [319].

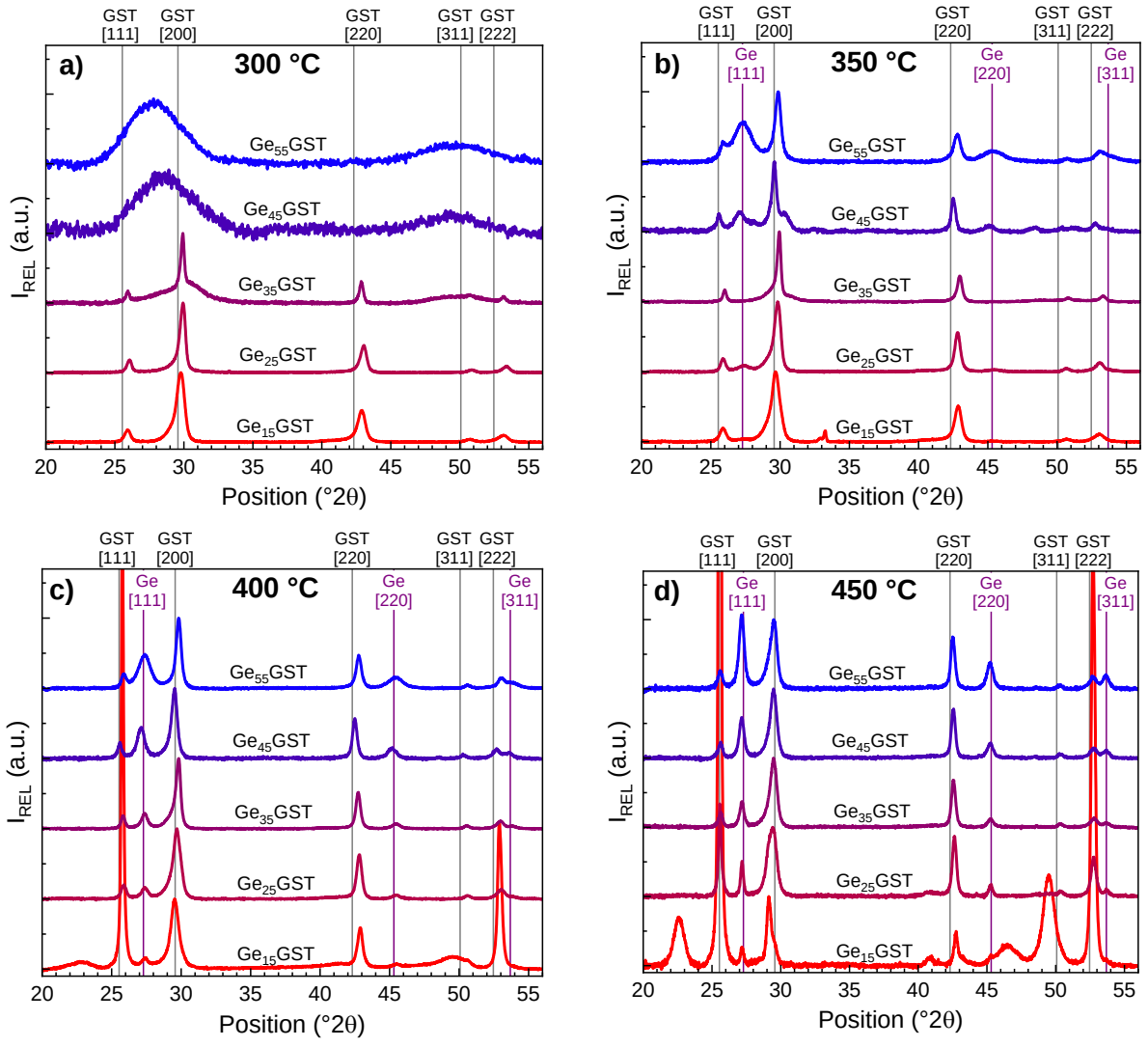

Fig. 4.15: XRD patterns of Ge_xGST layers annealed at (a) 300 °C, (b) 350 °C, (c) 400 °C and (d) 450 °C [318].

In general, slight position shifts can be observed for the peaks in XRD patterns compared to the position of reference data (ICDD PDF No. 00-054-0484 and 00-004-0545). This position shift might be likely related to the stress introduced in the layer owing to Ge enrichment. However, the stress is not taken into account in our analysis as only Bragg-Brentano configuration was used for XRD patterns acquisition. In order to perform further stress analysis, different XRD measurement configurations would be necessary.
The combination of Raman spectroscopy and XRD analysis highlights the main structural evolutions common to all studied Ge-rich GST layers, independently of Ge content [318]. The stability of SbTe structural units characteristic for GST225-fcc phase is maintained up to high annealing temperatures in all the studied compositions, as observed by Raman spectroscopy, thus confirming these units to be the dominant component of GST structure. The changes in Ge-Te modes intensity with temperature observed in all the studied layers indicate the ongoing Ge-Te bonds rearrangement around SbTe units, which was already described more in detail for $Ge_{45}GST$ in the section 4.1. In $Ge_{15}GST$, $Ge_{25}GST$ and $Ge_{35}GST$, such rearrangement leads to the formation of the crystalline GST225-fcc phase at 300 °C confirmed by XRD (Fig. 4.15). In $Ge_{45}GST$ and $Ge_{55}GST$, however, the formation of the crystalline GST225-fcc phase is delayed to 350 °C. The coexistence of both GST225-fcc and Ge crystalline phases is observed from 350 °C, which demonstrates that the Ge phase segregation already started. $Ge_{35}GST$ is the only sample not showing the Ge crystalline phase at 350 °C, however, the already advanced evolution of Raman a-Ge modes (i.e., ordering) through the gradual shift of a-Ge band towards c-Ge indicates that the process is also ongoing for this alloy (an intermediary Raman peak at 280 cm^{-1} can be observed in Fig. 4.14).
These observations highlight the existing competition/concurrence of the following phenomena, which depend on Ge content in the layer and on temperature [318]:

- nucleation and growth of a GST phase (i.e., GST225-fcc);
- Ge segregation out of the formed GST phase, which is delayed by increasing Ge content (i.e., lower diffusivity), but favored by increasing temperature (i.e., higher diffusivity of Ge);
- backward chemical diffusion of Ge (hinders the GST phase formation), which increases with Ge content;
- nucleation and growth of Ge crystalline phase (favors the Ge segregation).

Such a sequence of several competing phenomena shows that the final segregation of the different phases is actually initiated by the reorganization driven by the stable SbTe units in GST phase and by the consequent nucleation of a GST phase. In $Ge_{35}GST$, the balance between Ge (~50 at.%) and Sb/Te content likely delays the formation of the Ge crystalline phase due to the competition between delayed Ge segregation and enhanced Ge backward diffusion. The Ge segregation is then greatly disfavored in $Ge_{45}GST$ and $Ge_{55}GST$ by high Ge content, which can explain the observed delay of the GST phase crystallization to 350 °C.
Fig. 4.16 shows the values of peak broadening at FWHM for GST[220] and Ge[111] peaks and the calculated crystallites sizes of each phase by Scherrer's law. The FWHM parameter represents the line broadening of the peak after subtracting the instrumental contribution. For both GST225-fcc and Ge phases we can observe the decrease of FWHM, i.e., increase of crystallites size with temperature, indicating a strong correlation between the crystalline growth of both phases. It is interesting to notice that the GST225-fcc crystallites size is larger than the equivalent Ge crystal size at all compositions. On the contrary, there is no evident dependence on Ge content.The crystallites size of both phases reaches similar values for the annealing temperature of 450 °C, independently of the Ge content in the layer. This result supports the primary nucleation and crystalline growth of GST phase and consequent

crystalline growth of the Ge phase. Fig. 4.16 also highlights the crystallization temperature of Ge reduced below 350 °C in all the studied layers, as already mentioned for $Ge_{45}GST$ (section 4.1.2), resulting likely from heterogeneous nucleation of Ge induced at the interfaces of the already existing GST crystalline seeds [320–322].

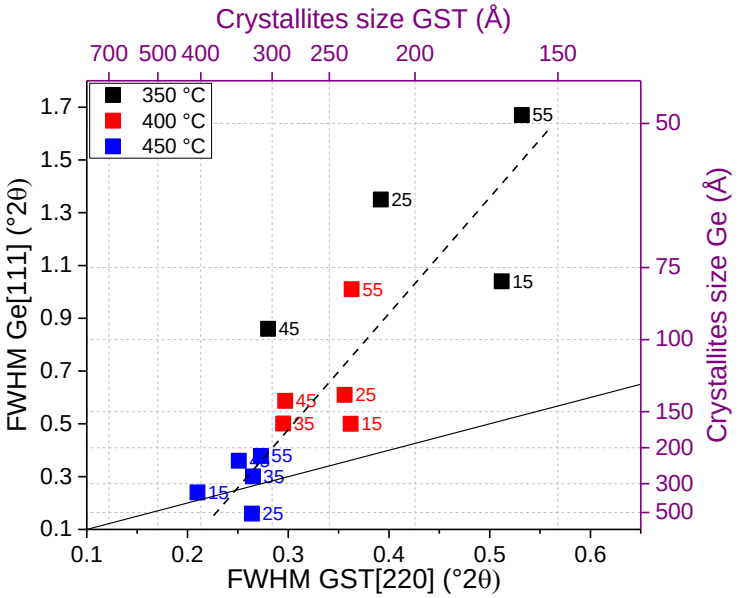

Fig. 4.16: Correlation of the FWHM and crystallites sizes for the GST225-fcc phase and Ge crystalline phases (dashed line). The values were taken from the GST[220] and Ge[111] peaks. The solid line represents the 1:1 ratio between the crystallites size of both phases [318].

The progression of GST crystallization followed by Ge crystallization is well observable in particular in the Ge_xGST layers with low Ge enrichment, in which the two phases appear at different annealing temperatures. On the contrary, the GST and Ge crystalline phases appear at the same annealing temperature in the Ge-rich GST layers with higher Ge enrichment, which results from two concurrent phenomena: delayed GST phase crystallization and high crystalline growth speed of Ge phase.

The progression of the GST crystallization and Ge segregation processes can be therefore well observed in $Ge_{35}GST$. XRD patterns of $Ge_{35}GST$ at 300 °C, 350 °C and 400 °C without normalization are shown in Fig. 4.17. The measurement parameters were kept the same during the acquisition, which allows comparing the peak intensity of the emerging GST225-fcc phase. The XRD pattern at 300 °C shows the peak GST[200] together with the broad band of the transient phase G^+GST at~30.5°. The low intense but narrow peak of GST[200] indicates the formation of high quality grains though present in small quantity, which are enclosed in a disordered Ge-enriched G^+GST phase. High Ge content and relatively low temperature do not yet allow the system to expulse abundant Ge and therefore completely separate the Ge and GST225-fcc phases. Increasing the annealing temperature up to 350 °C, the Ge diffusivity and hence the Ge expulsion from G^+GST are enhanced. This process leads to the gradual disappearance of the transient G^+GST phase and to the progressive definition of GST polycrystalline and Ge crystalline regions. This is evidenced in the XRD pattern at 350 °C as the intensity of the GST[200] peak increases and the peak becomes slightly broader than at 300 °C. The broad feature assigned to G^+GST is then reduced in intensity. XRD pattern at 400 °C further confirms the complete disappearance of G^+GST phase, whilst the separated Ge phase appears (Ge[111] peak), enhanced by the heterogeneous nucleation and high growth speed at the interface with the already formed GST225-fcc phase. The model is represented schematically in Fig. 4.18.

The difficulty to observe such transient phenomena in Ge_xGST layers with lower Ge contents is likely related to the reduced formation of the region enriched in Ge, which surrounds the GST225-fcc nuclei. Lowering the Ge content likely reduces the time scale for observing the broad band as well as its intensity [318].

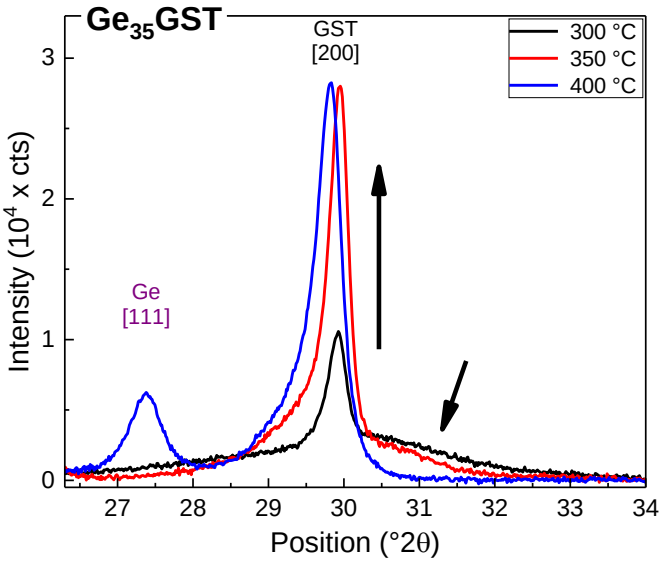

Fig. 4.17: XRD patterns (range 26°-34°) for Ge_{35}GST alloy at 300 °C, 350 °C and 400 °C highlighting the intensity increase of the GST[200] peak related to the GST225-fcc phase and the reduction of the broad band assigned to transient G^+GST phase [318].

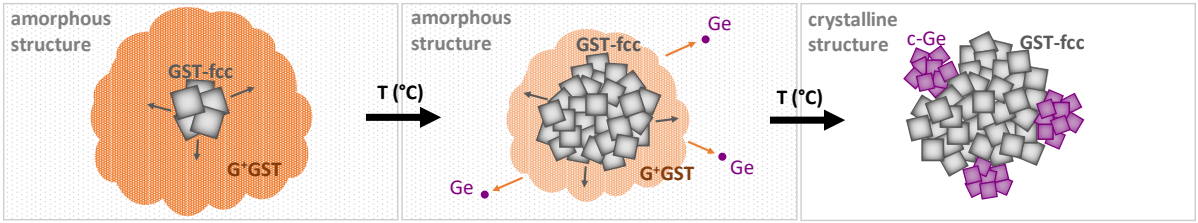

Fig. 4.18: Scheme representing the progress of GST225-fcc phase crystallization, disappearance of transient G^+GST phase with the expulsion of Ge atoms and following Ge phase crystallization with increasing annealing temperature [318].

In order to follow the progress of the demixing process in the alloy, TEM images with EDX analyses were performed on Ge_xGST layers annealed at 400 °C. The Ge and Te cartographies in Fig. 4.19a show the formation of Ge-rich and Te-rich regions, which indicates complete segregation of GST and Ge phases. These findings confirm the XRD results (Fig. 4.15), where the already developed GST225-fcc and Ge cubic crystalline phase are observed. The cartographies show the dominance of the Ge phase with increasing Ge content, as expected. Based on the data extracted from EDX analyses, we reconstructed the compositional distribution of phases present along the tie line between GST225 phase and pure Ge phase. The cartographies (Fig. 4.19b) demonstrate the distribution from highly to less occurred phases (i.e., transition from dark to light zones, respectively) for the studied alloys. The gradual transition of the distribution towards the pure Ge phase can be observed as the Ge content in the layers increases. This transition suggests the progressive tendency of the pure Ge phase to dominate the system dynamics, which is in good agreement with the XRD results [318].

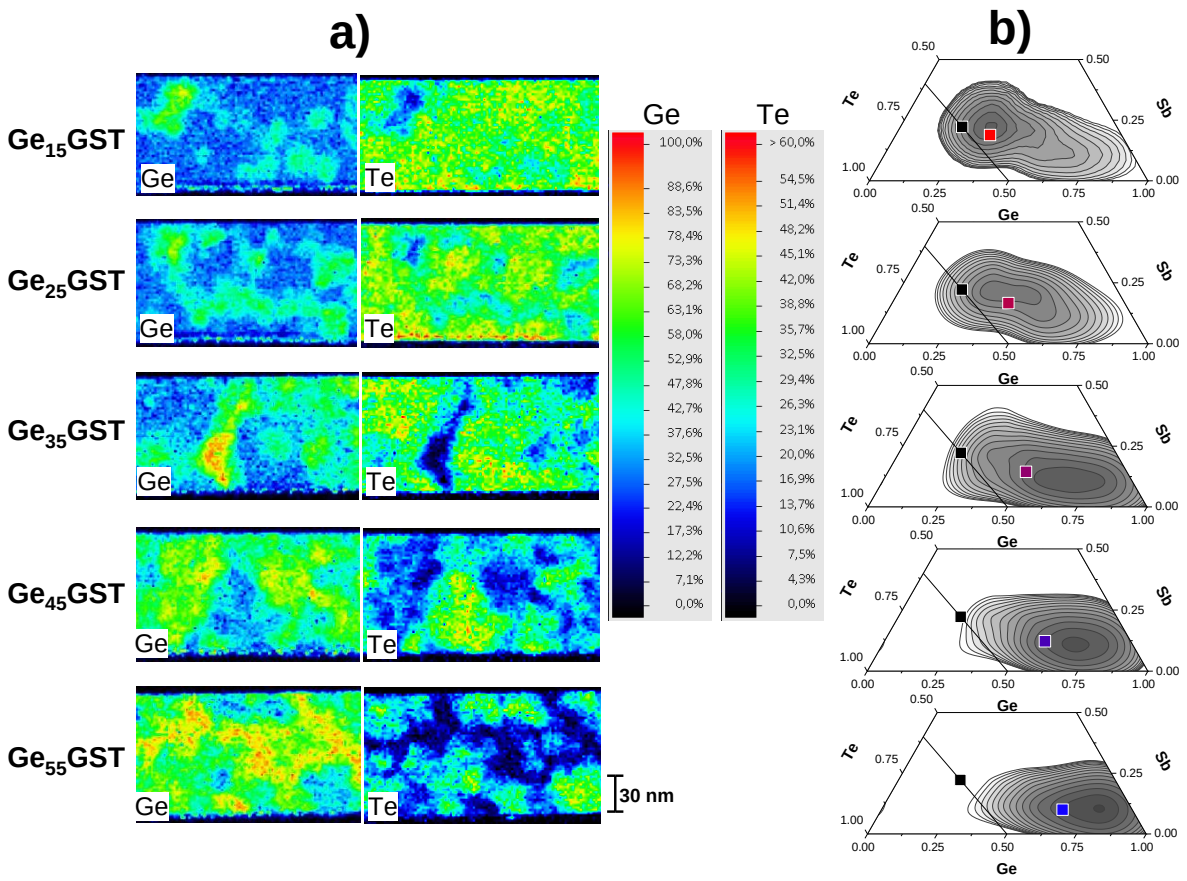

Fig. 4.19: TEM-EDX analyses on Ge_xGST layers annealed at 400 °C: a) Ge an Te cartographies highlighting the elemental migration; b) Ge-Sb-Te ternary diagram showing the compositional distribution along the tie-line between GST225 (black square) and pure Ge phase (right bottom corner of the ternary diagram). The colored squares represent the position of corresponding Ge_xGST [318].

4.2.3 Summary of the section

In summary of this part, the SbTe structural units demonstrated to be stable and characteristic of the GST phase independently from Ge content in the alloy. We decribe the structural evolution in the Ge-rich GST alloys, starting with Ge-Te bond rearrangement around these stable SbTe units forming the GeSbTe phase. Indeed, the primary crystallization of GST225-fcc phase was observed in the alloys, followed by the heterogeneous crystallization of Ge crystalline phase. This crystallization sequence is particularly well seen for the Ge-rich GST alloys with low Ge content since the crystalline phases appear at different temperatures. On the contrary, these two crystallization processes appear simultaneously at high temperature in the alloys with high Ge content, resulting from delayed GST phase crystallization and fast Ge crystal growth, owing to the competition between delayed Ge segregation and enhanced Ge backward diffusion. Moreover, the transient G^+GST phase, presented in the section 4.1.2, is observed for $Ge_{35}GST$ and $Ge_{45}GST$ alloys, demonstrating the gradual expulsion of Ge atoms from Ge-enriched GST zones. The crystallites sizes of the segregated GST225-fcc and Ge phases are strongly correlated and increase with annealing temperature, independently of Ge content in the alloy.

4.3 N-doped Ge-rich GST: Structural evolution

The choice of N doping as a suitable way for the enhancement of thermal-retention properties of the GeSbTe alloy has been presented in the chapter 1. As already mentioned, the combination of both material optimizations, i.e., Ge enrichment and N doping, has shown first promising achievements concerning the alloy properties. In this part, the impact of nitrogen doping on the structure of Ge-rich GST alloys is deeply investigated, taking into account the findings from N-doped single element layers, presented in the chapter 3, and undoped Ge-rich GST alloys, presented in the first part of this chapter.

First, two N-doped Ge-rich GST alloys are studied, considering the nominal Ge-rich GST composition of 45 at.% Ge and 55 at.% GST225 (i.e., $Ge_{45}GST$) and N_2 flow of 2 sccm and 10 sccm during the deposition process (hereafter referred as GGSTN and GGSTN$^+$, respectively). The used N_2 flow of 2 sccm and 10 sccm correspond to N content in the alloys of about 8 at.% and 20 at.%, respectively, quantified by WDXRF. R vs T measurements as well as Raman and FTIR spectroscopy and XRD analysis are performed to study the structure of N-doped Ge-rich GST and its evolution as a function of temperature. The obtained results are compared with GST225 and undoped $Ge_{45}GST$ (GGST).

R vs T measurements (Fig. 4.20) highlight the main resistivity drops for GST225, GGST and GGSTN alloys with increasing temperature. The two resistivity decreases observed in GST225 and one double step transition observed in GGST are described in detail in the section 4.1. GGSTN layer shows a single transition at about 390 °C, confirming higher temperature stability of the amorphous phase reported in previous works [24,141]. Higher resistivity of the crystalline state of the annealed GGSTN compared to the GGST highlights that N doping hinders the crystallization mechanism and the phases segregation in such alloys [313].

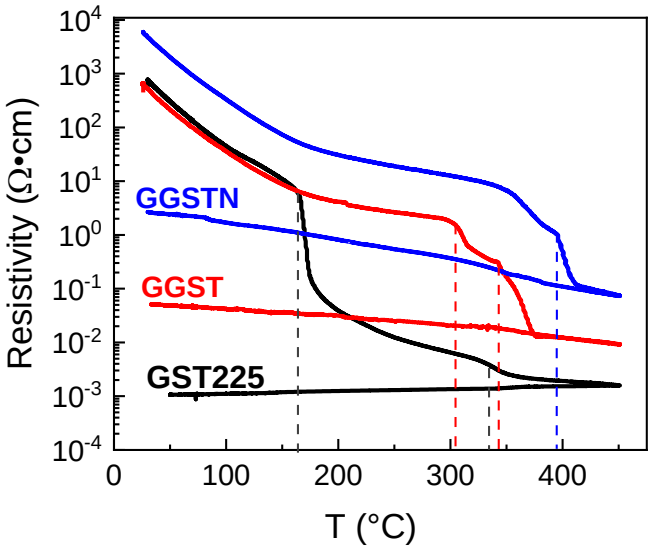

Fig. 4.20: R vs T measurements for GST225, GGST and GGSTN thin layers. Dashed lines indicate the main resistivity transitions observed in the different alloys [313].

4.3.1 Structural evolution of N-doped Ge-rich GST as a function of temperature

Raman spectra of as-deposited and annealed GGSTN layers (Fig. 4.21) feature the same vibrational modes recognized in GGST (Fig. 4.3 and Fig. 4.14). However, the previously observed structural evolutions are shifted towards higher temperatures. The well-established band of GST phase (100 – 190 cm^{-1}) can be observed from 375 °C and the c-Ge peak (297 cm^{-1}) does not appear until 450 °C (both observed from 335 °C for annealed GGST).

GGSTN^{+} layers resulted in more noisy Raman spectra due to higher N incorporation and thus higher structure disorder. However, similar structural evolution trends were observed and the computed data of peak integrated intensities are discussed later in this section.

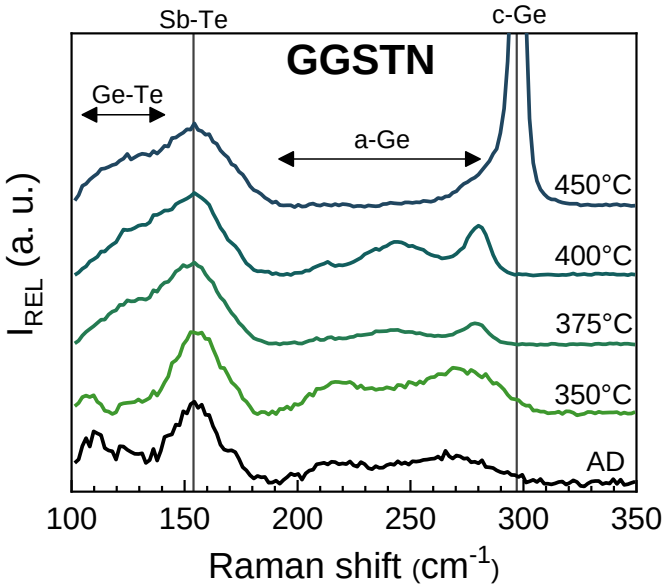

Fig. 4.21: Raman spectra of amorphous as-deposited (AD) and annealed GGSTN. Vertical lines show the position of Sb-Te modes (154 cm^{-1}) and crystalline Ge modes (297 cm^{-1}) [313].

The Raman spectra analysis of N-doped GGST alloys was performed in the same way as for GGST (Fig. 4.4), i.e., the integrated intensities of contributions related to Ge-Te and a-Ge modes were obtained from spectra deconvolution and normalized with respect to the integrated intensity of the contribution related to Sb-Te modes. This analysis highlights the temperature-dependent evolution trends of the different structural units of the alloys.
The evolution of Ge-Te and a-Ge modes in the three layers is compared in Fig. 4.22. Ge-Te modes reach minimum intensity at temperature that increases with the N content, namely at about 300 °C, 350 °C and 400 °C for GGST, GGSTN and GGSTN^{+}, respectively. For the sake of clarity, no distinction is done for Ge-Te modes before and after the detected minimum intensity, as in case of GGST (section 4.1.2). However, this detected minimum intensity is still attributed to the end of reordering of amorphous layer and the beginning of GST phase crystallization. For a-Ge modes, a similar trend is observed for the temperature, at which the maximum intensity is reached (at about 250 °C, 350 °C and 375 °C for GGST, GGSTN and GGSTN^{+}, respectively). The reached maximum intensity of a-Ge modes is followed by abrupt intensity decrease, which is more pronounced in the case of both N-doped GGST layers compared to GGST [313].

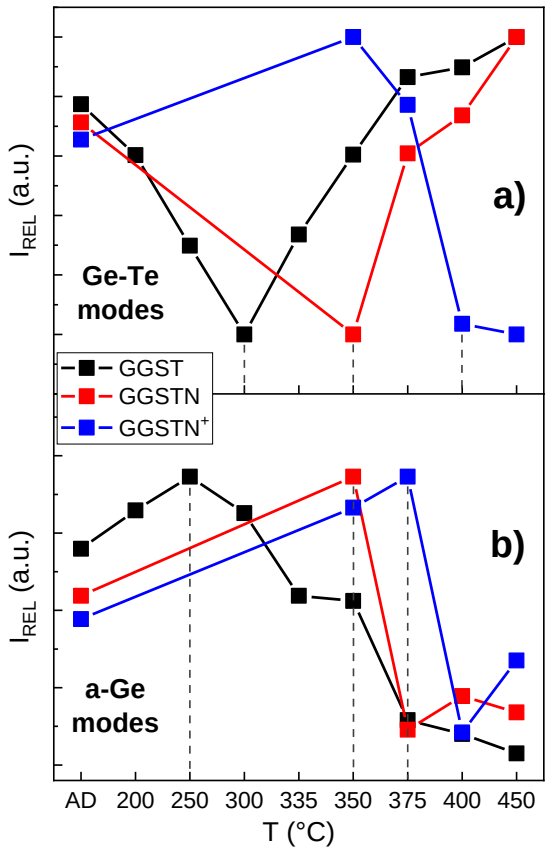

Fig. 4.22: Comparison of the evolution in temperature of (a) Ge-Te and (b) a-Ge modes obtained from Raman spectra in GGST, GGSTN and GGSTN$^+$. Dashed vertical lines highlight the inversion trends for both types of modes, showing that structural transitions are delayed to higher temperatures, the higher the nitrogen content [313].

XRD measurements on GGSTN layers Fig. 4.23 show the first diffraction peaks at 375 °C. The acquired diffraction pattern might correspond to the GST225-fcc phase. However, the diffraction peaks positions are significantly shifted with respect to database data (ICDD PDF No. 00-054-0484). The Ge enrichment, the presence of nitrogen and the effect of annealing may all induce stress and changes in the lattice parameters resulting in the shift of the peak positions. However, it was previously observed that N-doping slightly increases the lattice parameter of GST225-fcc phase with an expected shift of the peaks to lower 2θ angles [203], which is contrary to our observations. The origin of such a shift may be attributed to the crystallization of a transitional G$^+$GST phase with Ge content higher than in GST225, as already observed in undoped Ge-rich GST alloys (sections 4.1and 4.2). Indeed, the 375 °C XRD pattern can be assigned to several phases with stoichiometry close to $Ge_3Sb_2Te_6$ (ICDD PDF No. 04-019-5066; 01-084-5074; 01-085-2822; 01-084-5063), as previously showed for undoped Ge_xGST alloys (Ge-Sb-Te ternary diagram in Fig. 4.8). N doping likely reduces the mobility of Ge in the alloy, leading to the delay of the demixing process of Ge and GST phases to higher temperatures. As a result, the nucleation and growth of the transitional G$^+$GST phase might be enhanced, making the transition step more evident in N-doped samples. In the XRD pattern at 400 °C, the GST225-fcc peaks are already well identified, with the presence of the broad band at ~30.5°, previously highlighted in case of undoped GGST [313].

The diffraction peaks of Ge crystalline phase appear only at 450 °C. The crystallites sizes were calculated by Scherrer's law for [220] Bragg peak of GST225-fcc phase and for [111] Bragg peak of Ge crystalline phase (Table 4-II), confirming the delayed nucleation and growth of both identified phases.

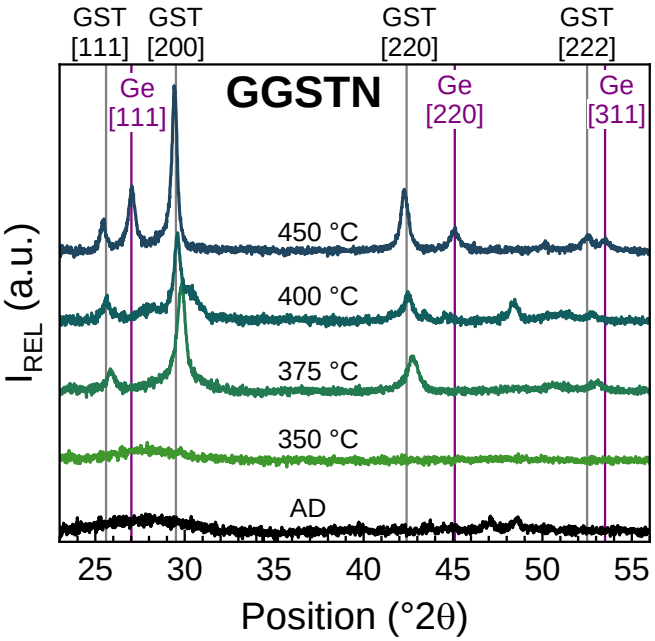

Fig. 4.23: XRD pattern of amorphous as-deposited (AD) and annealed GGSTN up to 450 °C. Indexation is performed from the database (ICDD PDF No. 00-054-0484 and 00-004-0545). The diffraction peaks assigned to GeSbTe phase are observed from 375 °C, while Ge diffraction peaks appear in the XRD pattern of 450 °C [313].

*Table 4-II: Crystallites sizes calculated by Scherrer's law for GST225-fcc and Ge phases from the XRD pattern of annealed GGSTN. *Crystallites size (~12 nm) calculated from XRD pattern at 375 °C, which is assigned to the transient G^+GST phase (i.e., different from GST225 phase) [313].*

T (°C)	Crystallites size (nm)	
	GST225 [220]	Ge [111]
350 °C	/	/
375 °C	*	/
400 °C	16 nm	/
450 °C	21 nm	19 nm

4.3.2 Formation of Ge-N bonds in the structure

The N bonding in N-doped layers based on Ge, Sb and Te elemental systems is well observed by FTIR spectroscopy, as already presented in the chapter 3. Therefore, the N-doped GGST layers were further investigated by this technique to support the results of Raman and XRD analysis presented above. As reported in the chapter 2 and shown in the chapter 3, nitrogen tends to principally bond with Ge, forming the Ge-N bonds. A considerable charge transfer from Ge to N produces strong IR absorption bands related to the Ge-N bond structure. IR spectra of as-deposited and annealed GGSTN and $GGSTN^+$ were compared with N-doped elemental Ge thin layers (hereafter referred as GeN and GeN^+, respectively) with the same thickness and with N incorporation close to N-doped GGST compositions (Fig. 4.24). The band intensities in the spectra were normalized with respect to their maximum values. The IR absorption band centered at ~700 cm^{-1} (vibrational modes of Ge_3N group), is observed in both as-deposited N-doped Ge and GGST layers. The asymmetric form of the band, particularly well observed in GeN^+ and $GGSTN^+$ spectra, suggests a second band contribution at higher wavenumbers (750 - 830 cm^{-1}), described more in detail in the section 3.3.1. As explained

earlier, this second contribution is also ascribed to Ge-N vibrations and the position shift results from enhanced inductive effect due to changed local environment, as more nitrogen atoms surround Ge atoms. The increasing temperature does not affect N-doped Ge layers and the absorption band remains stable in position and FWHM (section 3.7.2). On the contrary, a significant band shift of up to ~40 cm^{-1} (at 450 °C) to higher wavenumbers is observed for GGSTN with the annealing temperature. This progressive band shift to higher wavenumbers likely suggests the increasing dominance of the second contribution described above. Indeed, Ge-N bonds (E_{Ge-N} ~2.65 eV) are stronger than Ge-Ge bonds (E_{Ge-Ge} ~1.94 eV) [188] and require higher annealing temperature for breaking. The gradual change of the Ge and N atoms arrangement correlates with the impoverishment in Ge around the main Ge-N vibration, as the Ge-Ge bonds more likely break, liberating the Ge atoms. The liberated Ge is then progressively involved in Ge phase crystallization, enhancing the Ge phase segregation out of primary formed GST, as described for undoped Ge-rich GST alloys (section 4.2.2). The trend is particularly evident in GGSTN, where the crystallization of the layer is more advanced with respect to $GGSTN^+$ for the applied thermal budget (IR absorption band shift of ~10 cm^{-1} and ~40 cm^{-1}at 450 °C in $GGSTN^+$ and GGSTN, respectively). The comparison of N-doped GGST spectra with almost unchanged N-doped Ge spectra clearly reveals the effect of ongoing crystallization of the GST phase on the Ge phase nucleation and consequently on the close environment rearrangement of the Ge-N bonds [313].

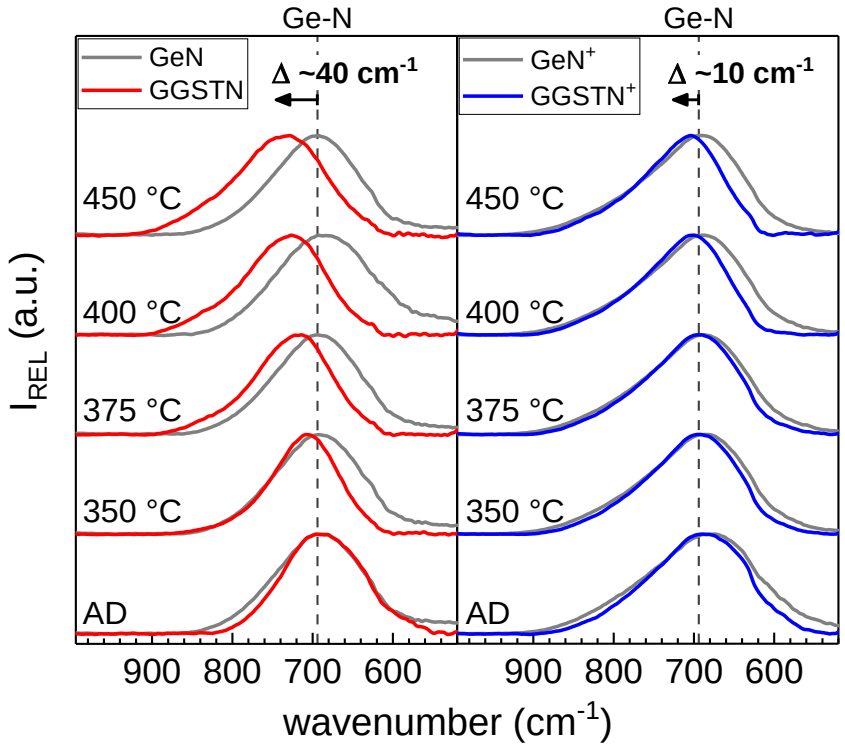

Fig. 4.24: FTIR spectra of amorphous as-deposited (AD) and annealed N-doped Ge and GGST, highlighting the position shift of the main GeN band with annealing temperature [313].

4.3.3 Summary of the section

To resume this section, nitrogen in the as-deposited N-doped GGST layers leads to the formation of Ge-N bonds, which are stable up to high annealing temperatures. The N incorporation and the formation of Ge-N bonds delay the entire process of structural rearrangement, starting from Ge-Te bonds reorganization around stable SbTe structural units. Upon the increasing annealing temperature, Ge atoms are progressively liberated from the close environment around the Ge-N units and can be further involved in Ge phase segregation and crystallization. Although the Ge segregation is favored by increasing temperatures, the Ge mobility is reduced due to higher thermal stability of Ge-N bonds. As a result, the nucleation and growth of the transitional $G^{+}GST$ phase, already observed in undoped Ge-rich GST alloys, is likely enhanced, making this transition step more evident in N-doped GGST alloys. Finally, the complete segregation of crystalline Ge and GST225-fcc phase is delayed to higher temperatures, thus demonstrating the enhanced stability of the amorphous phase of these alloys. The overall review of the structural evolution steps in GGSTN as a function of annealing temperatures and their delay with respect to the undoped GGST is shown in Fig. 4.25.

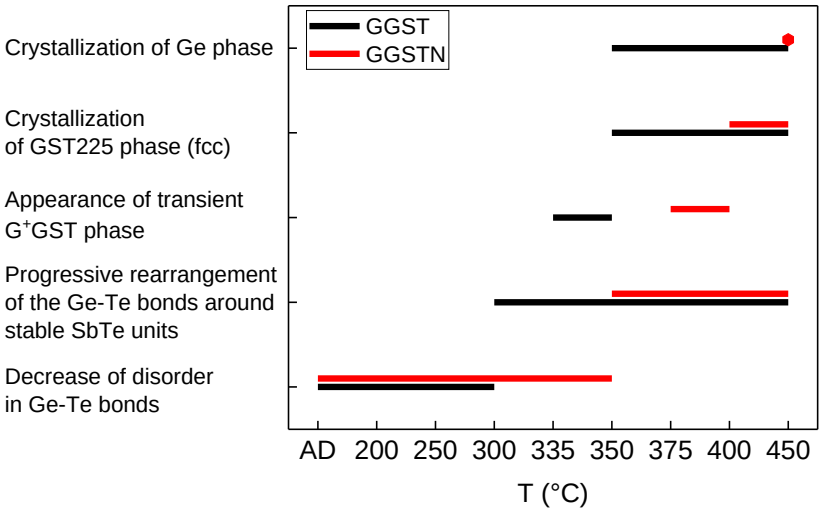

Fig. 4.25: Diagram summarizing the main features related to the structural evolution of GGST (black, bottom bars) and GGSTN (red, top bars) with annealing temperature [313].

4.4 N-doped Ge-rich GST: Effect of N content

N-doped GGST layers were further investigated in order to reveal the impact of different N content on the structure and the structural evolution in the alloys. A set of N-doped GGST layers with a nominal thickness of 100 nm were deposited on 300 mm Si wafers. The deposition was performed by reactive co-sputtering from Ge and $Ge_2Sb_2Te_5$ targets (Applied Materials Endura300) in Ar/N_2 gas mixture in the deposition chamber. The deposition temperature was kept at ~60 °C. The N incorporation in the as-deposited layers was regulated by varying the N_2 flow during the deposition from 0 to 12 sccm resulting in N content from 0 to about 15 at.%. The quantification of the prepared layers was performed by WDXRF measurements and the corresponding atomic concentrations for Ge, Sb, Te and N are presented in Table 4-III. The Sb over Te ratio of 0.4 is maintained in the as-deposited layers, as expected from the $Ge_2Sb_2Te_5$ target used for the deposition. Raman and FTIR spectroscopy along with XRD analysis were employed to study these alloys.

Table 4-III: WDXRF measured composition of studied N-doped Ge-rich GST alloys.

Composition	Content (at.%)			
	Ge	**Sb**	**Te**	**N**
GGST	68.6	9.4	22.0	0
GGSTN	65.4	8.9	20.9	4.8
	62.8	8.5	20.1	8.6
	60.9	8.2	19.5	11.4
	58.3	7.8	18.6	15.3

4.4.1 As-deposited N-doped GGST

Raman spectra of as-deposited N-doped GGST alloys (Fig. 4.26) show the stable contribution of Sb-Te modes of GeSbTe phase (154 cm^{-1}) and the contributions of a-Ge modes (190 - 300 cm^{-1}), described in the section 4.1.2. The Ge-Te vibrational modes of GeSbTe phase (100 - 140 cm^{-1}) are highly reduced due to the large excess of Ge in the alloys, which was already observed in section 4.2.2. Moreover, a broad band assigned to Ge-N vibrational modes can be observed at 720 cm^{-1}. The spectra were normalized with respect to the intensity of the peak at 154 cm^{-1} (Sb-Te modes), as in the previous analyses. The integrated intensities of contributions assigned to different vibrational modes (i.e., a-Ge, Ge-N) were also normalized with respect to the integral intensity of this peak. Increasing N content in the layer clearly changes the relative intensities of a-Ge and Ge-N bands (Fig. 4.27), resulting in decrease (resp. increase) of the relative intensity of a-Ge modes (resp. Ge-N modes). This correlation is in good agreement with our findings on GeN layers in the section 3.3.1. Indeed, the decrease in a-Ge modes is related with reduced contribution of Ge-Ge bonds, as more stable Ge-N bonds are formed in the alloy. The increasing formation of Ge-N bonds is also evidenced by IR spectra, where the main band at ~700 cm^{-1} vibrational modes of Ge_3N group), increases with N content (Fig. 4.26).

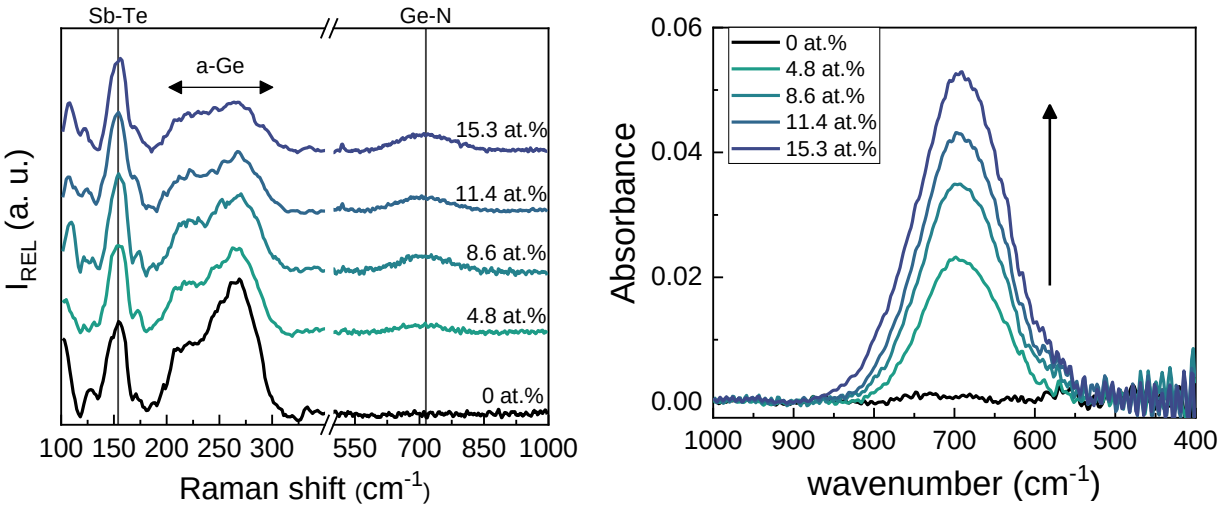

Fig. 4.26: Raman spectra (left) and IR spectra (right) of as-deposited N-doped Ge-rich GST alloys with different N content. Raman spectra demonstrate the reduction of a-Ge modes (200-300 cm^{-1}) and increasing band of Ge-N modes with N content. IR spectra highlight the increasing intensity of Ge-N band with N content.

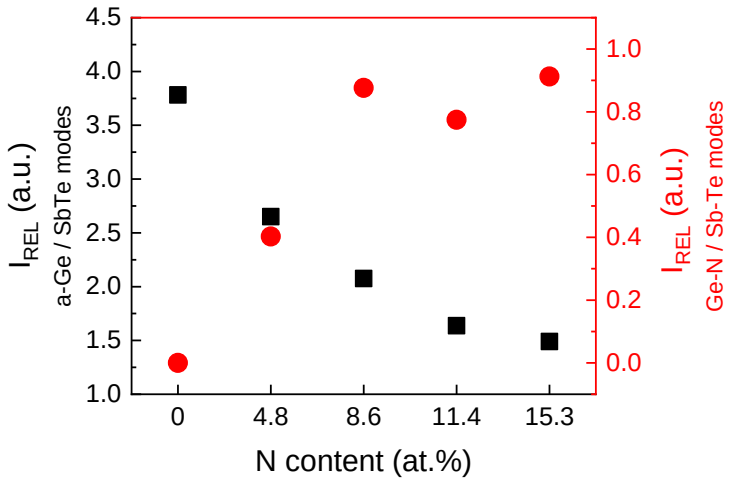

Fig. 4.27: Relative intensity of a-Ge (black squares) and Ge-N (red circles) vibrational modes with regard to the stable SbTe vibrational modes. The relative intensities are plotted as a function of N content, showing the gradual decrease of a-Ge modes intensity and increase of Ge-N modes intensity.

4.4.2 Annealed N-doped GGST

The studied N-doped GGST layers were annealed at temperatures from 375 °C to 500 °C. Raman spectra of the alloys annealed at 400 °C (Fig. 4.28) show, that undoped GGST and N-doped GGST layers with lower N content are already crystalline. Indeed, well-established GeSbTe phase (both Sb-Te and Ge-Te vibrational modes contributions can be distinguished in the broad band at 100 – 190 cm^{-1}) and segregated crystalline Ge phase (sharp c-Ge peak at 300 cm^{-1}) can be observed. On the contrary, layers with higher N content still demonstrate an amorphous character, featuring reduced Ge-Te modes contribution and a-Ge modes broad band. These observations are confirmed by XRD analysis (Fig. 4.29). Increasing the temperature up to 450 °C results in crystallization and GST225-fcc and Ge phase segregation in all studied alloys.

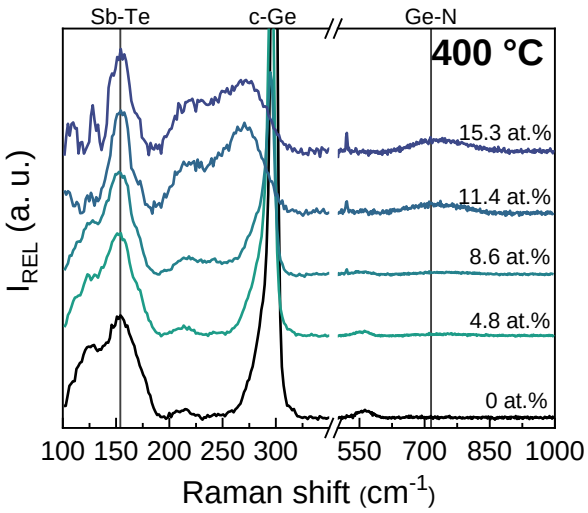

Fig. 4.28: Raman spectra of the N-doped Ge-rich GST alloys with different N content, annealed at 400 °C. The spectra show the organized broad band of GST phase (100 - 190 cm^{-1}) and the c-Ge peak (300 cm^{-1}) for lower N content (up to 8.6 at.% of N) while the spectra of the layers with higher N content still feature the broad band of a-Ge (190 – 300 cm^{-1}).

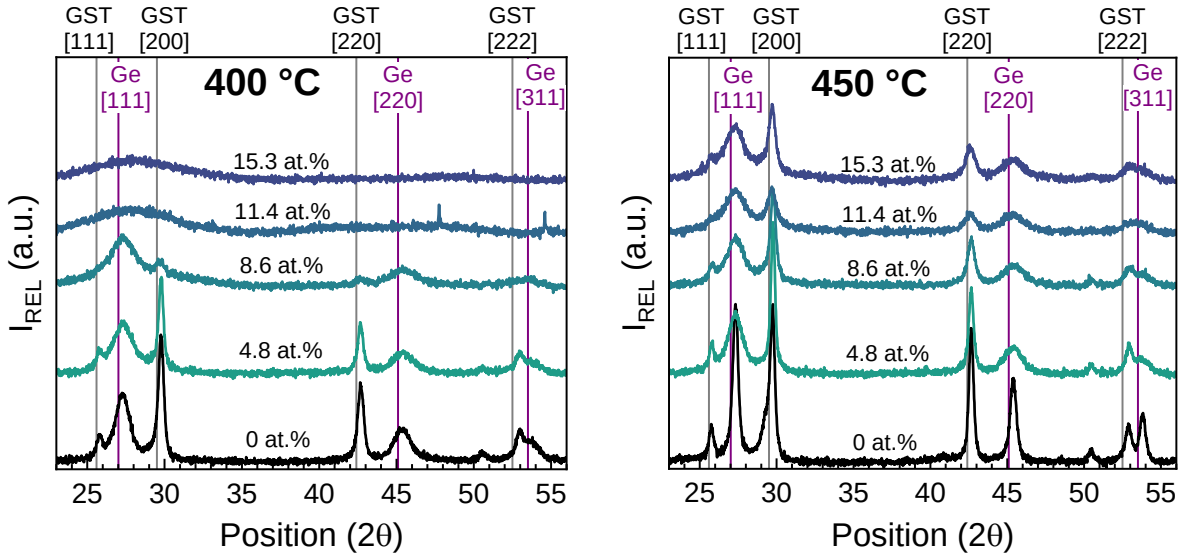

Fig. 4.29: XRD patterns of N-doped Ge-rich GST alloys with different N contents at annealing temperatures of (left) 400 °C and (right) 450 °C.

Fig. 4.30 shows the values of peak broadening FWHM for GST[200] and Ge[111] peaks and the crystallites sizes of each phase calculated by Scherrer's law as for undoped Ge-rich GST alloys in section 4.2.2. The FWHM parameter represents the line broadening of the peak after subtracting the instrumental contribution. For both GST225-fcc and Ge phases, the decrease of FWHM (i.e., increase of crystallites size) as function of temperature is observed, demonstrating a strong correlation between the phases' crystalline growth. The GST225-fcc crystallites size is larger than the equivalent Ge crystal size at all N-doped GGST compositions, which corresponds to the previous result observed in undoped alloys (Fig. 4.16). The crystallites sizes of the two phases reach similar values for the annealing temperature of 500 °C, independently of the N content in the layer. These results confirm the presence of the same crystallization mechanism, which was already described for undoped GGST alloys: the primary nucleation and crystalline growth of GST phase and the consequent

crystalline growth of the Ge phase (section 4.2). Owing to the formation of Ge-N bonds in the system, this mechanism is, however, delayed to higher annealing temperatures.
Although the transitional G^+GST phase was observed in undoped GGST alloys ($Ge_{35}GST$ and $Ge_{45}GST$, in particular) and N-doped GGST alloys described previously in the sections 4.2.2 and 4.3.1, we did not observe any gradual transition of Raman a-Ge modes or XRD peaks corresponding to such transitional phase in these N-doped GGST alloys. This is likely due to higher Ge content in the alloys with regard to the layers investigated in the section 4.3.1. Higher Ge content together with the formation of Ge-N bonds delays the crystallization to higher temperatures. As a results, Ge diffusivity and already rapid Ge crystal gowth are even more enhanced, highly reducing the time scale, in which the phase segregation occurs, thus making the monitoring of the intermediate G^+GST difficult. *In-situ* Raman or XRD characterization techniques may highlight such phase formation in these alloys, provided that the measurement time is short enough to evidence such a fast transition in Ge-rich GST alloys.

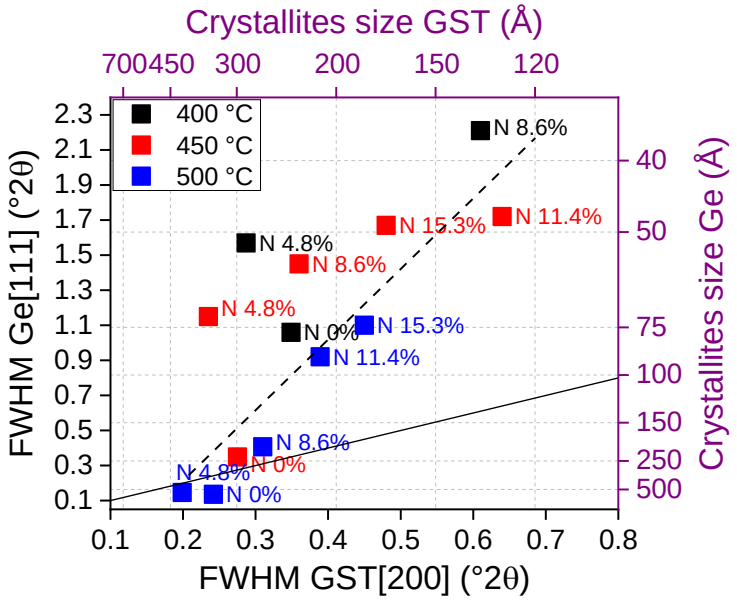

Fig. 4.30: Correlation of the FWHM and crystallites sizes for the GST225-fcc phase and Ge crystalline phases (dashed line). The values were taken from the GST[200] and Ge[111] peaks. The solid line represents the 1:1 ratio between the crystallites size of both phases.

Moreover, the position of IR band assigned to Ge-N vibrations (~700 cm^{-1}) was followed as a function of temperature (Fig. 4.31). The results correspond to the observations in the section 4.3.2, i.e., the IR band shifts in position to higher wavenumbers with annealing temperature (the shift of about 65 cm^{-1} for the layers annealed at 500 °C comapred to as-deposited layers). As already discussed, this shift can be attributed to the changed local environment of Ge_3N structural units, resulting from the liberation of Ge atoms surrounding the Ge_3N units with increasing temperature and involved in the Ge phase segregation and crystallization. The close environment around Ge_3N thus becomes richer in N atoms, forming more Ge-N bonds and thus modifying the original vibrational mode of the Ge_3N group. This can be demonstrated as the increasing additional contribution to the main band at higher wavenumbers (described in GeN layers in the section 3.3.1), which overtakes the dominance with increasing temperature.

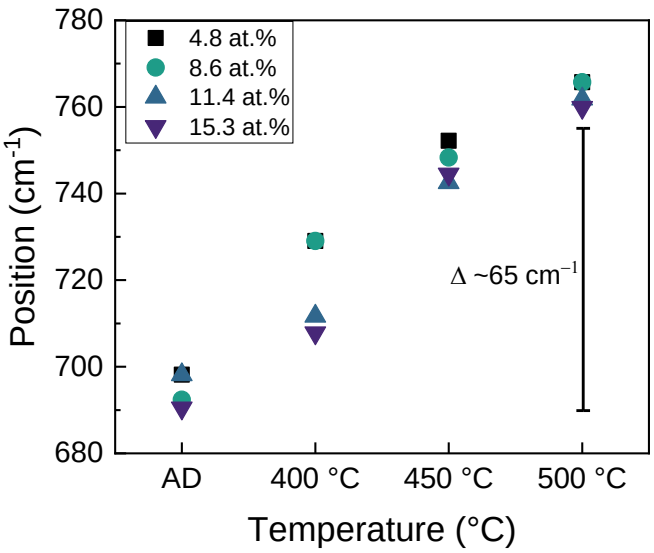

Fig. 4.31: Position shift of the main absorption band in IR spectra assigned to Ge-N vibrational modes, plotted as a function of annealing temperature. The position shift of about 65 cm^{-1} is highlighted between as deposited and annealed (500 °C) layers.

4.4.3 Summary of the section

As-deposited and annealed N-doped GGST alloys were studied as a function of N content. Increasing N content in the alloys leads to the increased formation of Ge-N bonds at expense of Ge-Ge bonds, as observed by FTIR and Raman spectroscopy. Upon annealing, the system features a similar evolution as observed in undoped GGST alloys, resulting in segregation of crystalline GST225-fcc and Ge phases. However, increasing N content delays the crystallization mechanism and phase segregation in the alloys. Indeed, upon annealing to 400 °C, the alloys with lower N doping feature the crystallization and segregation to GST225-fcc and Ge phases, while the alloys with higher N doping remain amorphous. The temperature increase up to 450 °C results in the crystallization of both phases in all the studied alloys. The comparison of FWHM and crystallite sizes of GST225-fcc and Ge phases demonstrates a similar correlation as observed for undoped GGST in the previous section. This further supports the idea that the crystallization mechanism and phase segregation in the N-doped GGST alloys remained unchanged, while delayed at higher temperatures. Such a delay is likely due to the formation of Ge-N bonds, which reduces the Ge mobility (i.e., Ge diffusivity in the system) and therefore the Ge phase crystallization. No transitent $G^{+}GST$ phase was observed in these alloys, which is likely due to higher Ge content compared to the N-doped Ge-rich GST alloys studied in the previous section. Indeed, higher Ge content delays the Ge nucleation to higher temperatures, resulting also in faster Ge crystal growth and ongoing phase segregation once initialized. The systematic studies of N content effect on GGST alloys with lower Ge content would be an asset, further contributing to our investigation.

4.5 Chapter summary

In this chapter, we investigated the structure and crystallization mechanism of undoped and N-doped Ge-rich GST alloys. Raman spectroscopy and XRD confirmed the amorphous character of all the as-deposited alloys. Raman spectroscopy further allowed to identify the main structural units that form the basis of the structure of undoped Ge-rich GST alloys, i.e., Sb-Te and Ge-Te units along with amorphous Ge from Ge excess in the alloys. The structural evolution as a function of temperature was studied, taking $Ge_2Sb_2Te_5$ as a reference alloy. We demonstrated that the Sb-Te structural units in Ge-rich GST alloys remain stable up to high annealing temperatures, indicating that these bonds form the dominant component of the structure. We described the structural evolution in the Ge-rich GST alloys and we highlight the existing competition of the following phenomena: nucleation and growth of GST225-fcc phase, starting with Ge-Te bonds rearrangement around the stable Sb-Te units; Ge segregation out of the formed GST phase and heterogeneous nucleation and growth of Ge crystalline phase. This sequence was observed in both undoped and N-doped Ge-rich GST alloys. Moreover, the formation of a transient G^+GST phase is highlighted, resulting from Ge-Te bonds rearrangement and gradual expulsion from mixed GeSbTe and Ge-rich GeTe units in the first part of structural evolution before reaching the stable and well formed GST225-fcc phase.

Varying the Ge enrichment demonstrated to either enhance or hinder different steps of structural evolution of the studied alloys. The structural evolution is particularly well evidenced in the Ge-rich GST alloys with low Ge content since the crystalline phases appear at different temperatures. On the contrary, the competition between delayed Ge segregation and enhanced Ge backward diffusion occurs in the alloys with high Ge content, which results in delayed GST phase crystallization and the rapid Ge crystal growth. Therefore, both processes become faster and the segregated GST and Ge phases appear almost simultaneously at higher temperatures.

The transient G^+GST phase, mentioned above, is therefore well observed only in Ge_{35}GST and Ge_{45}GST alloys. The crystallites sizes of the developed GST225-fcc and Ge phases are strongly correlated and increase with annealing temperature, independently from Ge content in the alloy.

Nitrogen doping in as-deposited Ge-rich GST alloys leads to the formation of Ge-N bonds, confirmed by Raman and FTIR spectroscopy. The formation of Ge-N bonds affects the entire process of structural rearrangement described above, starting from Ge-Te bonds reorganization around stable SbTe structural units. Thus the entire mechanism of structural evolution is delayed to higher temperatures, enhancing the stability of the amorphous phase of these alloys. Indeed, Ge-N bonds are stable up to high annealing temperatures and although the Ge segregation is favored by increased temperature, the Ge mobility is reduced by Ge-N bonds. Varying the N content in the alloys further confirms the presented mechanism of structural evolution, demonstrating the correlation between the crystallites sizes of the GST225-fcc and Ge phases similar to the one found in undoped Ge-rich GST.

Conclusion and perspectives

Material engineering plays an irreplaceable role in the current development of PCRAM device technology. The integrated phase-change materials based on GST stoichiometric alloys demonstrated to be suitable for optical data storage and stand-alone memories. However, they do not dispose of sufficient properties for the requirements of embedded PCRAM device applications. Promising results were achieved by two ways of material optimization, i.e., Ge enrichment and Nitrogen (N) doping. The PCRAM device with such integrated non-stoichiometric or doped alloys demonstrated great performances, such as high data retention, high cyclability and reduced power consumption, while still maintaining good switching speed. The optimized materials allowed the PCRAM device to fulfill the embedded application requirements, in particular the challenging requirements of automotive applications, as presented in the chapter 1. However, the material structure, the mechanisms of crystallization and the phenomena occurring during the crystallization are still not fully understood and rise a lot of questions. The understanding the material structure provides the important information about the origin of material properties, which are responsible for final PCRAM device performances. Moreover, material limits can be identified, leading for further material optimization in order to meet the requirements of PCRAM device applications. The thorough structural analysis can also provide the clues for the identification of other suitable phase-change materials for different PCRAM device applications.

This work focuses on the investigation of structural arrangement and crystallization of GST-based phase-change materials. The material investigation was carried out in two directions: a) Ge, Sb and Te elemental systems and b) Ge-rich GST alloys. For both groups of materials, the structure of undoped and N-doped as-deposited layers with the thickness of 100 nm were investigated as well as their structural evolution as a function of temperature. A wide set of complementary characterization techniques was employed: Raman and FTIR spectroscopy, XRD and TEM-EDX analysis, supported in some cases by XAS measurements and *"ab initio"*simulations (Table 5-I). The contribution of the employed techniques in structural analyses, along with possible challenges concerning the material, instrumentation and data analysis is descried in the chapter 2. The section 2.2 then demonstrates the practical examples of application of these characterization techniques for structural information of elemental systems and GeSbTe alloys at nanoscale and microscale level, reported in literature. These examples further provided the base of information for the investigation perfomed in the chapters 3 and 4.

Table 5-I: Summary of studied materials and characterization techniques for structural investigation, employed in this work.

Studied materials	Employed characterization techniques
Ge, Sb, Te elementary systems	Raman and FTIR spectroscopy, WDXRF, XAS, *"ab initio"* simulations
Ge-rich GST alloys	RvsT, Raman and FTIR spectroscopy, ellipsometry, WDXRF, XRD / isothermal XRD, TEM-EDX

The structural investigation of Ge, Sb and Te elemental systems (chapter 3) allows to identify the characteristic structural motives of each of studied system. The as-deposited Ge layers showed the amorphous character (Fig. 3.3), while the as-deposited Sb and Te layers feature

the crystalline structure (Fig. 3.5 and Fig. 3.6). N doping in all systems lead to the formation of X-N bonds (X = Ge, Sb, Te), increasing the disorder in the layers. The highest level of N incorporation was achieved for Ge layers, while the lowest N content at the same N_2 flow during the deposition was reached for Te layers (Fig. 3.1). The structural rearrangement due to N incorporation differs depending on the elemental system (section 3.3). The N atoms incorporated in Ge layers well form the Ge-N bonds, replacing less stable Ge-Ge bonds in the system and making the alloy structure more rigid. This consequently results in high stability of N-doped Ge systems in temperature. The N atoms in Sb layers likely substitute the Sb atoms in the crystalline structure, owing to the same electrons number and atom coordination of both elements. On the contrary, N atoms are the least prone to be incorporated in Te layers, likely occupying the interstitial positions between the Te chains of the crystalline lattice. The identification of X-N bonds in elemental systems can be well applied for the identification of such bonds in more complex N-doped GST alloys, as demonstrated in the section 3.6. It was shown, that Ge-N bonds are preferentially formed even in Sb-rich GST alloys. Indeed, the stability of Ge-N bonds were observed both in time and at high annealing temperatures, as the GeN system remains stable at least up to 550 °C (Fig. 3.15), already for the lowest level of studied N content.

The investigation of as-deposited amorphous Ge-rich GST alloys (chapter 4) showed the presence of three different kinds of structural units, as expected: Sb-Te, Ge-Te and Ge. The Sb-Te structural units demonstrated the outstanding stability as a function of temperature, thus suggesting that Sb-Te units form the main part of these alloys, while the GeTe structural units rearrange along these Sb-Te. The structural evolution of Ge-rich GST alloys as a function of temperature can be then summarized in the sequence of following steps (section 4.2.2):

- Progressive rearrangement of GeTe around stable SbTe, resulting in primary nucleation and growth of GST crystalline phase;
- Ge segregation out of the formed GST phase;
- Rapid nucleation and growth of Ge crystalline phase.

The suggested sequence of several steps is dependent on Ge content and/or N content in the GST alloys. In particular, the Ge segregation is affected by Ge content, Ge backward chemical diffusion and annealing temperature. Increasing Ge content lowers the Ge diffusivity in the system, hindering even the formation of GST crystalline phase and thus improving the thermal stability of amorphous phase of the alloy. On the contrary, Ge segregation is favored by increasing temperature enhancing the Ge diffusivity and the rapid nucleation and growth of Ge crystalline phase once the GST phase has crystallized. The N incorporation in Ge-rich GST alloys (sections 4.3 and 4.4) leads to the formation of Ge-N bonds, affecting the diffusivity of Ge atoms. The number of formed Ge-N bonds in the alloy increases with N doping content at expense of Ge-Ge bonds, making the structure more rigid, i.e. increasing the thermal stability of amorphous phase. Moreover, as the Ge atoms are forming not only Ge-Ge bonds, but also Ge-Te bonds in the alloys, the formation of Ge-N also affects GeTe structural units, thus delaying the rearrangement of GeTe around stable SbTe and the nucleation of GST phase to higher temperatures. However, since the GST phase starts to nucleate, the entire crystallization mechanism is overtaken by Ge segregation and Ge heterogeneous nucleation and growth, as the speed of these processes is largely enhanced by the temperature. This also results in the reduced crystallites size of GST phase.

In this work, the effect of increasing N content was studied in highly Ge-enriched GST alloys (Ge ~58-68 at.%), which provides high thermal stability of amorphous phase and therefore the suitable solution for embedded PCRAM applications, notably for automotive requirements. However, additional studies performed on Ge-rich GST alloys with lower Ge enrichment are

suggested in order to follow the structural rearrangement and the individual steps of the crystallization mechanism upon the N doping content. The crystallization temperature of such alloys is reduced, slowing down the speed of different phenomena, described in the section 4.3, and also likely enhancing their intensity. Therefore, the observation of these phenomena would be more easily achievable, applying the appropriate characterization techniques. The application of *in-situ* or isothermal measurements would be beneficial in such case.

As mentioned above, the investigation of Ge-rich GST alloys demonstrated the outstanding stability of SbTe structural units of the GST as a function of temperature, i.e., in both amorphous and fcc crystalline phase. It is important to note, that our studied systems are based on Ge-enriched stoichiometric $Ge_2Sb_2Te_5$ alloy. Further studies on the stability of such structural units or their evolution as a function of temperature can be suggested considering the use of other stoichiometric GST alloys such as $Ge_1Sb_2Te_4$ or $Ge_1Sb_4Te_7$ instead of $Ge_2Sb_2Te_5$, or simply by the variation of Sb/Te ratio, such as in Sb-rich GST. Such alloys, called as δ-GST, were recently investigated in [148], potentially targeting high speed performance applications, owing to the growth-dominated type of crystallization. Such investigation can bring more information about the crucial role of Sb-Te structural units in GST alloys.

The N doping effect on GST alloys was in our work investigated in deposited layers with nominal thickness of 100 nm. For the purpose of this work, we assume the in-depth homogeneity of N distribution in the as-deposited layers. Further investigations can be considered targeting the precise quantification of the N content and its role in layer structure as a function of layer thickness. The deposition of the layers with reduced thickness could favor different quantity of incorporated Nitrogen, forming different number of Ge-N bonds in GST structure and therefore to affect the crystallization temperature of deposited alloys. This could lead to reduced thermal stability of amorphous phase of the GST alloy and therefore to modified PCRAM device performances. Moreover, the surface and possible interface effects are enhanced, taking into account the reduced volume of the deposited layer. Considering the device point of view, the thickness of integrated phase-change material would also affect the overall device architecture and the choice of material and parameters of employed electrodes, targeting the high scalability of PCRAM. Currently, the metrological studies on the N quantification as a function of deposited N-doped GST layer thickness carry on in CEA Leti, using primary the inline characterization by WDXRF as a process control technique. The N content is further determined by IBA techniques in the collaboration with CEA IRAMIS, providing the independent method to certify the Nitrogen standards for GST alloys and allowing to establish the reliable metrological protocols for quantification by WDXRF.

Concerning further material engineering, the superlattice-like (SLL) structures can be suggested, combining the properties of different phase-change alloys. The thin layers of two materials are alternated in the stack, where the number and thickness of the alternating layers determine the total thickness of the material. As the first attempts, $GeTe/Sb_2Te_3$ SLL structures were suggested contrary to $Ge_2Sb_2Te_5$ monolayers [323–328]. Recently, new SLL systems based on $Ge_2Sb_2Te_5$/Sb or $Ge_2Sb_2Te_5/Sb_2Te_3$ have been demonstrated, combining the phase transition of $Ge_2Sb_2Te_5$ with attractive fast crystallization speed of Sb or Sb-based alloys [329–331]. In the context of our work, new SLL structures based on $Ge_2Sb_2Te_5$/GeN stack could be suggested instead of N-doped Ge-rich GST monolayered alloys, employing the high thermal stability of GeN alloys, while possibly avoiding the issues related to the GST and Ge phase segregation, both presented in this work.

This thesis demonstrates the benefits of application several characterization techniques in the investigation of phase change materials structure and the complementary effect of the

obtained results. Indeed, the combination of Raman spectroscopy and XRD analysis allows to outline the structure in both amorphous and crystalline phases of the studied alloys, i.e., across the crystallization transition. In general, Raman spectra and XRD patterns are acquired at discrete temperatures, giving the overall idea about the system evolution. Application of *in-situ* or isothermal measurements could provide more detailed data about the structural evolution in a real time and allow to determine the system dynamics. Indeed, *in-situ* ellipsometry and isothermal XRD measurements (Fig. 4.12 and Fig. 4.6, respectively), provided such kind of information. *In-situ* and isothermal Raman spectroscopy and XRD with fast enough acquisition would be suitable methods how to further study the effects of N-doping in Ge-rich GST alloys, in which, especially, the different phenomena occurs rapidly, once the system reaches high crystallization temperatures. *In-situ* Raman spectroscopy coupled with resistivity measurements could be also suggested for more detailed study of structural rearrangement in amorphous phase, when the alloy resistivity slightly decreases before reaching the sudden drop related to the system crystallization.

Raman spectroscopy, in particular, provides the deep insight in the structure of the amorphous phase by identifying the vibrational modes of different structural units. Most of the works, including this thesis, employ the unpolarized Raman measurements. However, the polarization dependence of the Raman signal was observed in reference binary Sb_2Te_3 and GeTe alloys [123,179,210,332–334]. Considering the analogy with these binary systems, the application of polarized Raman measurements on (Ge-rich) GST alloys can enhance or reduce the intensity of different vibration modes of GeTe and SbTe structural units and therefore bring the additional information concerning the structural evolution of such alloys. Polarized Raman measurement could be also beneficial in deeper investigation of the role of Sb-Te bonds in other non-stoichiometric GST systems (e.g., Sb-rich GST), mentioned above. Moreover, a resonance effect of such bonds was observed in binary Sb-based alloys [335,336], enhancing the Raman signal intensity in a dependence on selected laser excitation wavelength. Taking advantage of this phenomenon, Resonance Raman spectroscopy could be also applied in further investigation.

XRD analysis in Bragg-Brentano configuration allows to identify the structural arrangement of the crystalline phase and can provide further information about its development as a function of temperature by following the crystallite sizes of the formed phases in the studied alloys. In order to calculate the approximated values of crystallites size, the contribution of internal stress to the FWHM of the XRD peaks is omitted. However, the presence of such stress in undoped and N-doped Ge-rich GST alloys during the crystallization is highly probable, owing to both Ge enrichment and N doping. The detailed stress analysis by adopting the different XRD techniques, as reported in [203,222,337], would support the investigations of crystalline phases microstructure.

Last but not least, other characterization techniques not used in this work can be employed in order to study the structure of GST phase-change materials. Nuclear Magnetic Resonance (NMR) can be named as an example of such characterization. In particular, NMR analysis has been largely used for spectroscopic studies of Te-based organometallic and other telluride compounds [197,256,258]. This characterization technique can provide significant information on local coordination environment of studied atom in both amorphous and crystalline phase, such as the identification of the nearest and the next-nearest neighbor atoms, coordination numbers, local site symmetry and degree of covalency. Considering the investigation of undoped and N-doped GST alloys, all elements, i.e. Ge, Sb, Te and N provide NMR-active nuclei, which could be used for structural investigation of both N-doped elemental systems presented in chapter 3 and undoped/N-doped GST alloys presented in chapter 4. Only a limited number of NMR studies were designed for GST

phase-change alloys so far [338–340], which could possibly open a new field of investigation, where the NMR could play a role as a structural technique complementary to XRD and XAS.

The focus of this work is paid primarily on the GST phase-change materials achieving high temperature stability of the amorphous phase enabling to fulfill the requirements of embedded PCRAM applications in automotive industry. However, the structural investigation performed in this work contributes to the understanding of elementary Ge, Sb and Te systems and GST alloys, their structure, bonding arrangements and mechanisms of structural evolutions along with the effect of nitrogen incorporation. Besides the PCRAM applications and neuromorphic computing mentioned in the section 1.2.5, GST alloys and other chalcogenide phase-change materials attract the attention in particular in the field of photonic devices, exploiting the optical contrast upon material phase transition. In this field, GST alloys have found the promising applications in waveguides, metasurfaces, modulators, absorptive color filters or tunable metalenses [13,80,81,341]. Therefore, the results of this thesis can allow further material engineering of alloys based on Ge, Sb and Te elements also for the other applications than which are offered by PCRAM devices.

References

[1] IDC White Paper Doc# US44413318: The Digitization of the World - From Edge to Core, (2018). https://www.seagate.com/files/www-content/our-story/trends/files/idc-seagate-dataage-whitepaper.pdf.

[2] S.M.S. Privitera, V. Sousa, C. Bongiorno, G. Navarro, C. Sabbione, E. Carria, E. Rimini, Atomic diffusion in laser irradiated Ge rich GeSbTe thin films for phase change memory applications, J. Phys. Appl. Phys. 51 (2018) 145103. https://doi.org/10.1088/1361-6463/aab1d0.

[3] M. Agati, M. Vallet, S. Joulié, D. Benoit, A. Claverie, Chemical phase segregation during the crystallization of Ge-rich GeSbTe alloys, J. Mater. Chem. C. 7 (2019) 8720–8729. https://doi.org/10.1039/C9TC02302J.

[4] M. Agati, F. Renaud, D. Benoit, A. Claverie, In-situ transmission electron microscopy studies of the crystallization of N-doped Ge-rich GeSbTe materials, MRS Commun. 8 (2018) 1145–1152. https://doi.org/10.1557/mrc.2018.168.

[5] A. Redaelli, ed., Phase Change Memory, Springer International Publishing, Cham, 2018. https://doi.org/10.1007/978-3-319-69053-7.

[6] S. Raoux, F. Xiong, M. Wuttig, E. Pop, Phase change materials and phase change memory, MRS Bull. 39 (2014) 703–710. https://doi.org/10.1557/mrs.2014.139.

[7] A. Chen, A review of emerging non-volatile memory (NVM) technologies and applications, Solid-State Electron. 125 (2016) 25–38. https://doi.org/10.1016/j.sse.2016.07.006.

[8] J.S. Meena, S.M. Sze, U. Chand, T.-Y. Tseng, Overview of emerging nonvolatile memory technologies, Nanoscale Res. Lett. 9 (2014) 526. https://doi.org/10.1186/1556-276X-9-526.

[9] M. Le Gallo, A. Sebastian, An overview of phase-change memory device physics, J. Phys. Appl. Phys. 53 (2020) 213002. https://doi.org/10.1088/1361-6463/ab7794.

[10] P. Cappelletti, R. Annunziata, F. Arnaud, F. Disegni, A. Maurelli, P. Zuliani, Phase change memory for automotive grade embedded NVM applications, J. Phys. Appl. Phys. 53 (2020) 193002. https://doi.org/10.1088/1361-6463/ab71aa.

[11] F.-M. Lee, Embedded Memory: The Future of Emerging Memories, in: 2019 Int. Symp. VLSI Technol. Syst. Appl. VLSI-TSA, IEEE, Hsinchu, Taiwan, 2019: pp. 1–1. https://doi.org/10.1109/VLSI-TSA.2019.8804627.

[12] G.W. Burr, R.M. Shelby, A. Sebastian, S. Kim, S. Kim, S. Sidler, K. Virwani, M. Ishii, P. Narayanan, A. Fumarola, L.L. Sanches, I. Boybat, M. Le Gallo, K. Moon, J. Woo, H. Hwang, Y. Leblebici, Neuromorphic computingusingnon-volatile memory, Adv. Phys. X. 2 (2017) 89–124. https://doi.org/10.1080/23746149.2016.1259585.

[13] Z. Gong, F. Yang, L. Wang, R. Chen, J. Wu, C.P. Grigoropoulos, J. Yao, Phase change materials in photonic devices, J. Appl. Phys. 129 (2021) 030902. https://doi.org/10.1063/5.0027868.

[14] L. Wang, S.-R. Lu, J. Wen, Recent Advances on Neuromorphic Systems Using Phase-Change Materials, Nanoscale Res. Lett. 12 (2017) 347. https://doi.org/10.1186/s11671-017-2114-9.

[15] S.R. Ovshinsky, Reversible Electrical Switching Phenomena in Disordered Structures, Phys. Rev. Lett. 21 (1968) 1450–1453. https://doi.org/10.1103/PhysRevLett.21.1450.

[16] S. Raoux, M. Wuttig, eds., Phase Change Materials - Science and Applications, Springer US, Boston, MA, 2009. https://doi.org/10.1007/978-0-387-84874-7.

[17] S. Raoux, W. Wełnic, D. Ielmini, Phase Change Materials and Their Application to Nonvolatile Memories, Chem. Rev. 110 (2010) 240–267. https://doi.org/10.1021/cr900040x.
[18] Z. Song, S. Song, M. Zhu, L. Wu, K. Ren, W. Song, S. Feng, From octahedral structure motif to sub-nanosecond phase transitions in phase change materials for data storage, Sci. China Inf. Sci. 61 (2018). https://doi.org/10.1007/s11432-018-9404-2.
[19] G.W. Burr, M.J. Breitwisch, M. Franceschini, D. Garetto, K. Gopalakrishnan, B. Jackson, B. Kurdi, C. Lam, L.A. Lastras, A. Padilla, B. Rajendran, S. Raoux, R.S. Shenoy, Phase change memory technology, J. Vac. Sci. Technol. B Nanotechnol. Microelectron. Mater. Process. Meas. Phenom. 28 (2010) 223–262. https://doi.org/10.1116/1.3301579.
[20] M. Wuttig, N. Yamada, Phase-change materials for rewriteable data storage, Nat. Mater. 6 (2007) 824–832. https://doi.org/10.1038/nmat2009.
[21] S. Gabardi, S. Caravati, G.C. Sosso, J. Behler, M. Bernasconi, Microscopic origin of resistance drift in the amorphous state of the phase-change compound GeTe, Phys. Rev. B. 92 (2015) 054201. https://doi.org/10.1103/PhysRevB.92.054201.
[22] F.G. Volpe, A. Cabrini, M. Pasotti, G. Torelli, Drift induced rigid current shift in Ge-Rich GST Phase Change Memories in Low Resistance State, in: 2019 26th IEEE Int. Conf. Electron. Circuits Syst. ICECS, IEEE, Genoa, Italy, 2019: pp. 418–421. https://doi.org/10.1109/ICECS46596.2019.8964986.
[23] D. Ielmini, A.L. Lacaita, Phase change materials in non-volatile storage, Mater. Today. 14 (2011) 600–607. https://doi.org/10.1016/S1369-7021(11)70301-7.
[24] P. Zuliani, E. Palumbo, M. Borghi, G. Dalla Libera, R. Annunziata, Engineering of chalcogenide materials for embedded applications of Phase Change Memory, Solid-State Electron. 111 (2015) 27–31. https://doi.org/10.1016/j.sse.2015.04.009.
[25] Global standards for the microelectronics industry, (n.d.). www.jedec.org.
[26] H.-S.P. Wong, S. Raoux, S. Kim, J. Liang, J.P. Reifenberg, B. Rajendran, M. Asheghi, K.E. Goodson, Phase Change Memory, Proc. IEEE. 98 (2010) 2201–2227. https://doi.org/10.1109/JPROC.2010.2070050.
[27] P. Noé, C. Vallée, F. Hippert, F. Fillot, J.-Y. Raty, Phase-change materials for non-volatile memory devices: from technological challenges to materials science issues, Semicond. Sci. Technol. 33 (2018) 013002. https://doi.org/10.1088/1361-6641/aa7c25.
[28] J.S. Bae, K.M. Hwang, K.H. Park, S.B. Jeon, J. Choi, J.H. Ahn, S.S. Kim, D.-H. Ahn, H.S. Jeong, S.W. Nam, G.T. Jeong, H.K. Cho, D.H. Jang, C.-G. Park, Investigation on physical origins of endurance failures in PRAM, in: 2012 IEEE Int. Reliab. Phys. Symp. IRPS, IEEE, Anaheim, CA, USA, 2012: p. EM.7.1-EM.7.4. https://doi.org/10.1109/IRPS.2012.6241900.
[29] A. Pirovano, F. Pellizzer, A. Redaelli, I. Tortorelli, E. Varesi, F. Ottogalli, M. Tosi, P. Besana, R. Cecchini, R. Piva, M. Magistretti, M. Scaravaggi, G. Mazzone, P. Petruzza, F. Bedeschi, T. Marangon, A. Modelli, D. Ielmini, A.L. Lacaita, R. Bez, μTrench phase-change memory cell engineering and optimization, in: Proc. 35th Eur. Solid-State Device Res. Conf. 2005 ESSDERC 2005, IEEE, Grenoble, France, 2005: pp. 313–316. https://doi.org/10.1109/ESSDER.2005.1546648.
[30] A. Pirovano, F. Pellizzer, I. Tortorelli, A. Riganó, R. Harrigan, M. Magistretti, P. Petruzza, E. Varesi, A. Redaelli, D. Erbetta, T. Marangon, F. Bedeschi, R. Fackenthal, G. Atwood, R. Bez, Phase-change memory technology with self-aligned μTrench cell architecture for 90nm node and beyond, Solid-State Electron. 52 (2008) 1467–1472. https://doi.org/10.1016/j.sse.2008.04.031.

[31] R. Bez, Chalcogenide PCM: a memory technology for next decade, in: 2009 IEEE Int. Electron Devices Meet. IEDM, IEEE, Baltimore, MD, USA, 2009: pp. 1–4. https://doi.org/10.1109/IEDM.2009.5424415.
[32] M. Boniardi, A. Redaelli, C. Cupeta, F. Pellizzer, L. Crespi, G. D'Arrigo, A.L. Lacaita, G. Servalli, Optimization metrics for Phase Change Memory (PCM) cell architectures, in: 2014 IEEE Int. Electron Devices Meet., IEEE, San Francisco, CA, USA, 2014: p. 29.1.1-29.1.4. https://doi.org/10.1109/IEDM.2014.7047131.
[33] Y.C. Chen, C.T. Rettner, S. Raoux, G.W. Burr, S.H. Chen, R.M. Shelby, M. Salinga, W.P. Risk, T.D. Happ, G.M. McClelland, M. Breitwisch, A. Schrott, J.B. Philipp, M.H. Lee, R. Cheek, T. Nirschl, M. Lamorey, C.F. Chen, E. Joseph, S. Zaidi, B. Yee, H.L. Lung, R. Bergmann, C. Lam, Ultra-Thin Phase-Change Bridge Memory Device Using GeSb, in: 2006 Int. Electron Devices Meet., IEEE, San Francisco, CA, 2006: pp. 1–4. https://doi.org/10.1109/IEDM.2006.346910.
[34] D.H. Im, J.I. Lee, S.L. Cho, H.G. An, D.H. Kim, I.S. Kim, H. Park, D.H. Ahn, H. Horii, S.O. Park, U.-I. Chung, J.T. Moon, A unified 7.5nm dash-type confined cell for high performance PRAM device, in: 2008 IEEE Int. Electron Devices Meet., IEEE, San Francisco, CA, USA, 2008: pp. 1–4. https://doi.org/10.1109/IEDM.2008.4796654.
[35] G. Navarro, G. Bourgeois, J. Kluge, A.L. Serra, A. Verdy, J. Garrione, M.-C. Cyrille, N. Bernier, A. Jannaud, C. Sabbione, M. Bernard, E. Nolot, F. Fillot, P. Noe, L. Fellouh, G. Rodriguez, V. Beugin, O. Cueto, N. Castellani, J. Coignus, V. Delaye, C. Socquet-Clerc, T. Magis, C. Boixaderas, S. Barnola, E. Nowak, Phase-Change Memory: Performance, Roles and Challenges, in: 2018 IEEE Int. Mem. Workshop IMW, IEEE, Kyoto, 2018: pp. 1–4. https://doi.org/10.1109/IMW.2018.8388845.
[36] DerChang Kau, S. Tang, I.V. Karpov, R. Dodge, B. Klehn, J.A. Kalb, J. Strand, A. Diaz, N. Leung, J. Wu, Sean Lee, T. Langtry, Kuo-wei Chang, C. Papagianni, Jinwook Lee, J. Hirst, S. Erra, E. Flores, N. Righos, H. Castro, G. Spadini, A stackable cross point Phase Change Memory, in: 2009 IEEE Int. Electron Devices Meet. IEDM, IEEE, Baltimore, MD, USA, 2009: pp. 1–4. https://doi.org/10.1109/IEDM.2009.5424263.
[37] G. Molas, D.A. Robayo, J. Minguet Lopez, L. Grenouillet, C. Carabasse, G. Navarro, C. Sabbione, M. Bernard, C. Cagli, N. Castellani, D. Deleruyelle, M. Bocquet, J.M. Portal, E. Nowak, Crosspoint Memory Arrays: Principle, Strengths and Challenges, in: 2020 IEEE Int. Mem. Workshop IMW, IEEE, Dresden, Germany, 2020: pp. 1–4. https://doi.org/10.1109/IMW48823.2020.9108143.
[38] D.H. Yoon, J. Chang, R.S. Schreiber, N.P. Jouppi, Practical nonvolatile multilevel-cell phase change memory, in: Proc. Int. Conf. High Perform. Comput. Netw. Storage Anal., ACM, Denver Colorado, 2013: pp. 1–12. https://doi.org/10.1145/2503210.2503221.
[39] A. Athmanathan, M. Stanisavljevic, N. Papandreou, H. Pozidis, E. Eleftheriou, Multilevel-Cell Phase-Change Memory: A Viable Technology, IEEE J. Emerg. Sel. Top. Circuits Syst. 6 (2016) 87–100. https://doi.org/10.1109/JETCAS.2016.2528598.
[40] https://www.intel.co.uk/content/www/uk/en/architecture-and-technology/optane-memory.html, Intel® Optane™ Memory, Intel. (n.d.). https://www.intel.co.uk/content/www/uk/en/architecture-and-technology/optane-memory.html.
[41] H.-Y. Cheng, F. Carta, W.-C. Chien, H.-L. Lung, M.J. BrightSky, 3D cross-point phase-change memory for storage-class memory, J. Phys. Appl. Phys. 52 (2019) 473002. https://doi.org/10.1088/1361-6463/ab39a0.
[42] J. Choe, Intel's 2nd Generation XPoint Memory, TechInsights. (2021). https://www.techinsights.com/blog/memory/intels-2nd-generation-xpoint-memory (accessed February 5, 2022).

[43] A. Lotnyk, M. Behrens, B. Rauschenbach, Phase change thin films for non-volatile memory applications, Nanoscale Adv. 1 (2019) 3836–3857. https://doi.org/10.1039/C9NA00366E.

[44] F. Arnaud, P. Zuliani, J.P. Reynard, A. Gandolfo, F. Disegni, P. Mattavelli, E. Gomiero, G. Samanni, C. Jahan, R. Berthelon, O. Weber, E. Richard, V. Barral, A. Villaret, S. Kohler, J.C. Grenier, R. Ranica, C. Gallon, A. Souhaite, D. Ristoiu, L. Favennec, V. Caubet, S. Delmedico, N. Cherault, R. Beneyton, S. Chouteau, P.O. Sassoulas, A. Vernhet, Y. Le Friec, F. Domengie, L. Scotti, D. Pacelli, J.L. Ogier, F. Boucard, S. Lagrasta, D. Benoit, L. Clement, P. Boivin, P. Ferreira, R. Annunziata, P. Cappelletti, Truly Innovative 28nm FDSOI Technology for Automotive Micro-Controller Applications embedding 16MB Phase Change Memory, in: 2018 IEEE Int. Electron Devices Meet. IEDM, IEEE, San Francisco, CA, 2018: p. 18.4.1-18.4.4. https://doi.org/10.1109/IEDM.2018.8614595.

[45] F. Disegni, R. Annunziata, A. Molgora, G. Campardo, P. Cappelletti, P. Zuliani, P. Ferreira, A. Ventre, G. Castagna, A. Cathelin, A. Gandolfo, F. Goller, S. Malhi, D. Manfre, A. Maurelli, C. Torti, F. Arnaud, M. Carfi, M. Perroni, M. Caruso, S. Pezzini, G. Piazza, O. Weber, M. Peri, Embedded PCM macro for automotive-grade microcontroller in 28nm FD-SOI, in: 2019 Symp. VLSI Circuits, IEEE, Kyoto, Japan, 2019: pp. C204–C205. https://doi.org/10.23919/VLSIC.2019.8778129.

[46] I. Boybat, C. di Nolfo, S. Ambrogio, M. Bodini, N.C.P. Farinha, R.M. Shelby, P. Narayanan, S. Sidler, H. Tsai, Y. Leblebici, G.W. Burr, Improved Deep Neural Network Hardware-Accelerators Based on Non-Volatile-Memory: The Local Gains Technique, in: 2017 IEEE Int. Conf. Rebooting Comput. ICRC, IEEE, Washington, DC, 2017: pp. 1–8. https://doi.org/10.1109/ICRC.2017.8123642.

[47] A. Sebastian, M. Le Gallo, G.W. Burr, S. Kim, M. BrightSky, E. Eleftheriou, Tutorial: Brain-inspired computing using phase-change memory devices, J. Appl. Phys. 124 (2018) 111101. https://doi.org/10.1063/1.5042413.

[48] H. Iwasaki, Y. Ide, M. Harigaya, Y. Kageyama, I. Fujimura, Completely Erasable Phase Change Optical Disk, Jpn. J. Appl. Phys. 31 (1992) 461–465. https://doi.org/10.1143/JJAP.31.461.

[49] M.L. Lee, L.P. Shi, Y.T. Tian, C.L. Gan, X.S. Miao, Crystallization behavior of $Sb_{70}Te_{30}$ and $Ag_3In_5Sb_{60}Te_{32}$ chalcogenide materials for optical media applications, Phys. Status Solidi A. 205 (2008) 340–344. https://doi.org/10.1002/pssa.200723398.

[50] J. Orava, D.W. Hewak, A.L. Greer, Fragile-to-Strong Crossover in Supercooled Liquid Ag-In-Sb-Te Studied by Ultrafast Calorimetry, Adv. Funct. Mater. 25 (2015) 4851–4858. https://doi.org/10.1002/adfm.201501607.

[51] T. Matsunaga, Y. Umetani, N. Yamada, Structural study of a $Ag_{3.4}In_{3.7}$ $Sb_{76.4}Te_{16.5}$ quadruple compound utilized for phase-change optical disks, Phys. Rev. B. 64 (2001) 184116. https://doi.org/10.1103/PhysRevB.64.184116.

[52] J. Akola, R.O. Jones, Phase change materials: Density functional / molecular dynamics simulations of Ag/In-doped Sb_4Te alloy, in: 2012 12th IEEE Int. Conf. Nanotechnol. IEEE-NANO, IEEE, Birmingham, United Kingdom, 2012: pp. 1–6. https://doi.org/10.1109/NANO.2012.6321950.

[53] J.H. Kim, D.-S. Byeon, D.-H. Ko, J.H. Park, Physical and electrical characteristics of Ge_xSb_{100-x} films for use as phase-change materials, Thin Solid Films. 659 (2018) 1–6. https://doi.org/10.1016/j.tsf.2018.05.034.

[54] S. Raoux, C. Cabral, L. Krusin-Elbaum, J.L. Jordan-Sweet, K. Virwani, M. Hitzbleck, M. Salinga, A. Madan, T.L. Pinto, Phase transitions in Ge–Sb phase change materials, J. Appl. Phys. 105 (2009) 064918. https://doi.org/10.1063/1.3091271.

[55] C.-C. Chang, C.-T. Chao, J.-C. Wu, T.-R. Yew, M.-J. Tsai, T.-S. Chin, The use of $Ga_{16}Sb_{84}$alloy for electronic phase-change memory, Scr. Mater. 64 (2011) 801–804. https://doi.org/10.1016/j.scriptamat.2010.12.046.
[56] P.-C. Chang, H.-W. Huang, C.-C. Chang, S.-C. Chang, M.-J. Tsai, T.-S. Chin, $Ga_{19}Sb_{81}$ film for multi-level phase-change memory, Thin Solid Films. 544 (2013) 107–111. https://doi.org/10.1016/j.tsf.2013.04.101.
[57] H.Y. Cheng, W.C. Chien, M. BrightSky, Y.H. Ho, Y. Zhu, A. Ray, R. Bruce, W. Kim, C.W. Yeh, H.L. Lung, C. Lam, Novel fast-switching and high-data retention phase-change memory based on new Ga-Sb-Ge material, in: 2015 IEEE Int. Electron Devices Meet. IEDM, IEEE, Washington, DC, USA, 2015: p. 3.5.1-3.5.4. https://doi.org/10.1109/IEDM.2015.7409620.
[58] J. Feng, Z.F. Zhang, Y. Zhang, B.C. Cai, Y.Y. Lin, T.A. Tang, B. Chen, Crystallization process and amorphous state stability of Si-Sb-Te films for phase change memory, J. Appl. Phys. 101 (2007) 074502. https://doi.org/10.1063/1.2717562.
[59] K.-H. Kim, J.-C. Park, J.-H. Lee, J.-G. Chung, S. Heo, S.-J. Choi, Nitrogen-Doping Effect on $Ge_2Sb_2Te_5$ Chalcogenide Alloy Films during Annealing, Jpn. J. Appl. Phys. 49 (2010) 101201. https://doi.org/10.1143/JJAP.49.101201.
[60] S. Kozyukhin, V. Kudoyarova, H.P. Nguyen, A. Smirnov, V. Lebedev, Influence of doping on the structure and optical characteristics of $Ge_2Sb_2Te_5$ amorphous films, Phys. Status Solidi C. 8 (2011) 2688–2691. https://doi.org/10.1002/pssc.201084060.
[61] S. Kozyukhin, M. Veres, H.P. Nguyen, A. Ingram, V. Kudoyarova, Structural Changes in Doped $Ge_2Sb_2Te_5$ Thin Films Studied by Raman Spectroscopy, Phys. Procedia. 44 (2013) 82–90. https://doi.org/10.1016/j.phpro.2013.04.011.
[62] A. Sherchenkov, P. Lazarenko, T. Terekhov, S. Kozyukhin, Electrical properties of Ge-Sb-Te-Bi Thin Films for Phase Change Memory Application, in: Proc. 2016 Int. Conf. Mech. Mater. Struct. Eng., Atlantis Press, Jeju Island,South-Korea, 2016. https://doi.org/10.2991/icmmse-16.2016.61.
[63] C. Koch, T. Dankwort, A.-L. Hansen, M. Esters, D. Häußler, H. Volker, A. von Hoegen, M. Wuttig, D.C. Johnson, W. Bensch, L. Kienle, Investigation of the phase change mechanism of $Ge_6Sn_2Sb_2Te_{11}$, Acta Mater. 152 (2018) 278–287. https://doi.org/10.1016/j.actamat.2018.04.029.
[64] E. Cho, Y. Youn, S. Han, Enhanced amorphous stability of carbon-doped $Ge_2Sb_2Te_5$: *Ab Initio* investigation, Appl. Phys. Lett. 99 (2011) 183501. https://doi.org/10.1063/1.3657139.
[65] T. Li, L. Wu, X. Ji, Y. Zheng, G. Liu, Z. Song, J. Shi, M. Zhu, S. Song, S. Feng, Carbon doping induced Ge local structure change in as-deposited $Ge_2Sb_2Te_5$ film by EXAFS and Raman spectrum, AIP Adv. 8 (2018) 025201. https://doi.org/10.1063/1.5020614.
[66] S. Privitera, E. Rimini, R. Zonca, Amorphous-to-crystal transition of nitrogen- and oxygen-doped $Ge_2Sb_2Te_5$ films studied by *in situ* resistance measurements, Appl. Phys. Lett. 85 (2004) 3044–3046. https://doi.org/10.1063/1.1805200.
[67] S. Privitera, E. Rimini, C. Bongiorno, A. Pirovano, R. Bez, Effects of dopants on the amorphous-to-fcc transition in $Ge_2Sb_2Te_5$ thin films, Nucl. Instrum. Methods Phys. Res. Sect. B Beam Interact. Mater. At. 257 (2007) 352–354. https://doi.org/10.1016/j.nimb.2007.01.265.
[68] J.M. Skelton, T.H. Lee, S.R. Elliott, Structural, dynamical, and electronic properties of transition metal-doped $Ge_2Sb_2Te_5$ phase-change materials simulated by *ab initio* molecular dynamics, Appl. Phys. Lett. 101 (2012) 024106. https://doi.org/10.1063/1.4736577.

[69] A. Ghosh, J. Sinha, S. Chattopadhyay, A comparative study on the performance of RESET based electro-thermal process in ring shaped confined $Ge_2Sb_2Te_5$ and $Ge_1Cu_2Te_3$ chalcogenide memory structures, Mater. Today Commun. 13 (2017) 325–331. https://doi.org/10.1016/j.mtcomm.2017.10.017.

[70] L. Men, J. Tominaga, H. Fuji, T. Kikukawa, N. Atoda, The Effects of Metal-Doped GeSbTe Films on Light Scattering-Mode Super-Resolution Near-Field Structure (Super-RENS), Jpn. J. Appl. Phys. 40 (2001) 1629–1633. https://doi.org/10.1143/JJAP.40.1629.

[71] W.-D. Song, L.-P. Shi, X.-S. Miao, C.-T. Chong, Synthesis and Characteristics of a Phase-Change Magnetic Material, Adv. Mater. 20 (2008) 2394–2397. https://doi.org/10.1002/adma.200702282.

[72] Y.-J. Huang, Y.-C. Chen, T.-E. Hsieh, Phase transition behaviors of Mo- and nitrogen-doped $Ge_2Sb_2Te_5$ thin films investigated by *in situ* electrical measurements, J. Appl. Phys. 106 (2009) 034916. https://doi.org/10.1063/1.3194787.

[73] C.-T. Lie, P.-C. Kuo, W.-C. Hsu, T.-H. Wu, P.-W. Chen, S.-C. Chen, $Ge_2Sb_2Te_5$ Thin Film Doped with Silver, Jpn. J. Appl. Phys. 42 (2003) 1026–1028. https://doi.org/10.1143/JJAP.42.1026.

[74] J.-H. Seo, K.-H. Song, H.-Y. Lee, Crystallization behavior of amorphous $Al_x(Ge_2Sb_2Te_5)_{1-x}$ thin films, J. Appl. Phys. 108 (2010) 064515. https://doi.org/10.1063/1.3471799.

[75] S. Raoux, M. Salinga, J.L. Jordan-Sweet, A. Kellock, Effect of Al and Cu doping on the crystallization properties of the phase change materials SbTe and GeSb, J. Appl. Phys. 101 (2007) 044909. https://doi.org/10.1063/1.2654556.

[76] S. Hatayama, Y. Sutou, S. Shindo, Y. Saito, Y.-H. Song, D. Ando, J. Koike, Inverse Resistance Change $Cr_2Ge_2Te_6$-Based PCRAM Enabling Ultralow-Energy Amorphization, ACS Appl. Mater. Interfaces. 10 (2018) 2725–2734. https://doi.org/10.1021/acsami.7b16755.

[77] M. Xu, Y. Guo, Z. Yu, K. Xu, C. Chen, H. Tong, X. Cheng, M. Xu, S. Wang, C.Z. Wang, K.-M. Ho, X. Miao, Understanding $CrGeTe_3$: an abnormal phase change material with inverse resistance and density contrast, J. Mater. Chem. C. 7 (2019) 9025–9030. https://doi.org/10.1039/C9TC02963J.

[78] N. Raeis-Hosseini, J. Rho, Metasurfaces Based on Phase-Change Material as a Reconfigurable Platform for Multifunctional Devices, Materials. 10 (2017) 1046. https://doi.org/10.3390/ma10091046.

[79] A.V. Pogrebnyakov, J.A. Bossard, J.P. Turpin, J.D. Musgraves, H.J. Shin, C. Rivero-Baleine, N. Podraza, K.A. Richardson, D.H. Werner, T.S. Mayer, Reconfigurable near-IR metasurface based on $Ge_2Sb_2Te_5$ phase-change material, Opt. Mater. Express. 8 (2018) 2264. https://doi.org/10.1364/OME.8.002264.

[80] P. Guo, A. Sarangan, I. Agha, A Review of Germanium-Antimony-Telluride Phase Change Materials for Non-Volatile Memories and Optical Modulators, Appl. Sci. 9 (2019) 530. https://doi.org/10.3390/app9030530.

[81] M.N. Julian, C. Williams, S. Borg, S. Bartram, H.J. Kim, Reversible optical tuning of GeSbTe phase-change metasurface spectral filters for mid-wave infrared imaging, Optica. 7 (2020) 746. https://doi.org/10.1364/OPTICA.392878.

[82] Y. Meng, T. Cao, Y. Long, Progress in metasurfaces based on Ge–Sb–Te phase-change materials, J. Appl. Phys. 128 (2020) 140904. https://doi.org/10.1063/5.0023925.

[83] C.A. Angell, K.L. Ngai, G.B. McKenna, P.F. McMillan, S.W. Martin, Relaxation in glassforming liquids and amorphous solids, J. Appl. Phys. 88 (2000) 3113–3157. https://doi.org/10.1063/1.1286035.

[84] S. Hong, O. Auciello, D. Wouters, eds., Emerging Non-Volatile Memories, Springer US, Boston, MA, 2014. https://doi.org/10.1007/978-1-4899-7537-9.
[85] J.W.P. Schmelzer, V.M. Fokin, A.S. Abyzov, Crystallization of Glass: What We Know, What We Need to Know, Int. J. Appl. Glass Sci. 7 (2016) 253–261. https://doi.org/10.1111/ijag.12212.
[86] N.A. Mauro, M. Blodgett, M.L. Johnson, A.J. Vogt, K.F. Kelton, A structural signature of liquid fragility, Nat. Commun. 5 (2014) 4616. https://doi.org/10.1038/ncomms5616.
[87] I.M. Kalogeras, H.E. Lobland, The nature of the glassy state: structure and glass transitions, J. Mater. Educ. 34 (2012) 69–94.
[88] J.C. Phillips, Topology of covalent non-crystalline solids I: Short-range order in chalcogenide alloys, J. Non-Cryst. Solids. 34 (1979) 153–181. https://doi.org/10.1016/0022-3093(79)90033-4.
[89] M. Micoulaut, Linking rigidity transitions with enthalpic changes at the glass transition and fragility: insight from a simple oscillator model, J. Phys. Condens. Matter. 22 (2010) 285101. https://doi.org/10.1088/0953-8984/22/28/285101.
[90] M.A. Paesler, D.A. Baker, G. Lucovsky, A.E. Edwards, P.C. Taylor, EXAFS study of local order in the amorphous chalcogenide semiconductor $Ge_2Sb_2Te_2$, J. Phys. Chem. Solids. 68 (2007) 873–877. https://doi.org/10.1016/j.jpcs.2007.03.041.
[91] M.A. Paesler, D.A. Baker, G. Lucovsky, Bond constraint theory studies of chalcogenide phase change memories, J. Non-Cryst. Solids. 354 (2008) 2706–2710. https://doi.org/10.1016/j.jnoncrysol.2007.09.045.
[92] M. Micoulaut, J.-Y. Raty, C. Otjacques, C. Bichara, Understanding amorphous phase-change materials from the viewpoint of Maxwell rigidity, Phys. Rev. B. 81 (2010) 174206. https://doi.org/10.1103/PhysRevB.81.174206.
[93] A.V. Kolobov, P. Fons, J. Tominaga, A.L. Ankudinov, S.N. Yannopoulos, K.S. Andrikopoulos, Crystallization-induced short-range order changes in amorphous GeTe, J. Phys. Condens. Matter. 16 (2004) S5103–S5108. https://doi.org/10.1088/0953-8984/16/44/008.
[94] M. Krbal, A.V. Kolobov, P. Fons, J. Tominaga, S.R. Elliott, J. Hegedus, A. Giussani, K. Perumal, R. Calarco, T. Matsunaga, N. Yamada, K. Nitta, T. Uruga, Crystalline GeTe-based phase-change alloys: Disorder in order, Phys. Rev. B. 86 (2012) 045212. https://doi.org/10.1103/PhysRevB.86.045212.
[95] J. Akola, R.O. Jones, Structural phase transitions on the nanoscale: The crucial pattern in the phase-change materials $Ge_2Sb_2Te_5$ and GeTe, Phys. Rev. B. 76 (2007) 235201. https://doi.org/10.1103/PhysRevB.76.235201.
[96] S. Caravati, M. Bernasconi, T.D. Kühne, M. Krack, M. Parrinello, Coexistence of tetrahedral- and octahedral-like sites in amorphous phase change materials, Appl. Phys. Lett. 91 (2007) 171906. https://doi.org/10.1063/1.2801626.
[97] M.H.R. Lankhorst, Modelling glass transition temperatures of chalcogenide glasses. Applied to phase-change optical recording materials, J. Non-Cryst. Solids. 297 (2002) 210–219. https://doi.org/10.1016/S0022-3093(01)01034-1.
[98] W.H. Zachariasen, THE ATOMIC ARRANGEMENT IN GLASS, J. Am. Chem. Soc. 54 (1932) 3841–3851. https://doi.org/10.1021/ja01349a006.
[99] P. Tronc, M. Bensoussan, A. Brenac, C. Sebenne, Optical-Absorption Edge and Raman Scattering in Ge_xSe_{1-x} Glasses, Phys. Rev. B. 8 (1973) 5947–5956. https://doi.org/10.1103/PhysRevB.8.5947.
[100] G. Lucovsky, F.L. Galeener, R.C. Keezer, R.H. Geils, H.A. Six, Structural interpretation of the infrared and Raman spectra of glasses in the alloy system $Ge_{1-x}S_x$, Phys. Rev. B. 10 (1974) 5134–5146. https://doi.org/10.1103/PhysRevB.10.5134.

[101] J. Bicerano, S.R. Ovshinsky, Chemical bond approach to the structures of chalcogenide glasses with reversible switching properties, J. Non-Cryst. Solids. 74 (1985) 75–84. https://doi.org/10.1016/0022-3093(85)90402-8.
[102] J. Akola, R.O. Jones, Density functional study of amorphous, liquid and crystalline $Ge_2Sb_2Te_5$: homopolar bonds and/or AB alternation?, J. Phys. Condens. Matter. 20 (2008) 465103. https://doi.org/10.1088/0953-8984/20/46/465103.
[103] S. Caravati, M. Bernasconi, T.D. Kühne, M. Krack, M. Parrinello, First-principles study of crystalline and amorphous $Ge_2Sb_2Te_5$ and the effects of stoichiometric defects, J. Phys. Condens. Matter. 21 (2009) 255501. https://doi.org/10.1088/0953-8984/21/25/255501.
[104] K. Shportko, S. Kremers, M. Woda, D. Lencer, J. Robertson, M. Wuttig, Resonant bonding in crystalline phase-change materials, Nat. Mater. 7 (2008) 653–658. https://doi.org/10.1038/nmat2226.
[105] M. Wuttig, V.L. Deringer, X. Gonze, C. Bichara, J.-Y. Raty, Incipient Metals: Functional Materials with a Unique Bonding Mechanism, Adv. Mater. 30 (2018) 1803777. https://doi.org/10.1002/adma.201803777.
[106] D. Lencer, M. Salinga, B. Grabowski, T. Hickel, J. Neugebauer, M. Wuttig, A map for phase-change materials, Nat. Mater. 7 (2008) 972–977. https://doi.org/10.1038/nmat2330.
[107] J. Raty, M. Schumacher, P. Golub, V.L. Deringer, C. Gatti, M. Wuttig, A Quantum-Mechanical Map for Bonding and Properties in Solids, Adv. Mater. 31 (2019) 1806280. https://doi.org/10.1002/adma.201806280.
[108] Y.-J. Huang, T.-C. Chung, C.-H. Wang, T.-E. Hsieh, Characterizations of AgInSbTe and Its Nanocomposite Thin Films for Phase-Change Memory Applications, J. Electrochem. Soc. 157 (2010) P113. https://doi.org/10.1149/1.3502531.
[109] J.A. Kalb, C.Y. Wen, F. Spaepen, H. Dieker, M. Wuttig, Crystal morphology and nucleation in thin films of amorphous Te alloys used for phase change recording, J. Appl. Phys. 98 (2005) 054902. https://doi.org/10.1063/1.2034655.
[110] J.J. Gervacio Arciniega, E. Prokhorov, F.J. Espinoza Beltran, G. Trapaga, Crystallization of Ge:Sb:Te Thin Films for Phase Change Memory Application, in: M. Andreeta (Ed.), Cryst. - Sci. Technol., InTech, 2012. https://doi.org/10.5772/35577.
[111] J.L.F. Da Silva, A. Walsh, H. Lee, Insights into the structure of the stable and metastable $(GeTe)_m(Sb_2Te_3)_n$ compounds, Phys. Rev. B. 78 (2008) 224111. https://doi.org/10.1103/PhysRevB.78.224111.
[112] N. Yamada, Origin, secret, and application of the ideal phase-change material GeSbTe, Phys. Status Solidi B. 249 (2012) 1837–1842. https://doi.org/10.1002/pssb.201200618.
[113] T. Matsunaga, R. Kojima, N. Yamada, K. Kifune, Y. Kubota, Y. Tabata, M. Takata, Single Structure Widely Distributed in a $GeTe{-}Sb_2Te_3$ Pseudobinary System: A Rock Salt Structure is Retained by Intrinsically Containing an Enormous Number of Vacancies within its Crystal, Inorg. Chem. 45 (2006) 2235–2241. https://doi.org/10.1021/ic051677w.
[114] T. Matsunaga, H. Morita, R. Kojima, N. Yamada, K. Kifune, Y. Kubota, Y. Tabata, J.-J. Kim, M. Kobata, E. Ikenaga, K. Kobayashi, Structural characteristics of GeTe-rich $GeTe–Sb_2Te_3$ pseudobinary metastable crystals, J. Appl. Phys. 103 (2008) 093511. https://doi.org/10.1063/1.2901187.
[115] L.E. Shelimova, O.G. Karpinskii, M.A. Kretova, V.I. Kosyakov, V.A. Shestakov, V.S. Zemskov, F.A. Kuznetsov, Homologous series of layered tetradymite-like compounds in the Sb-Te and $GeTe\text{-}Sb_2Te_3$ systems, Inorg. Mater. 36 (2000) 768–775. https://doi.org/10.1007/BF02758595.

[116] P.I. Lazarenko, S.A. Kozyukhin, A.A. Sherchenkov, A.V. Babich, S.P. Timoshenkov, D.G. Gromov, A.V. Zabolotskaya, V.V. Kozik, Electrophysical Properties of Ge–Sb–Te Thin Films for Phase Change Memory Devices, Russ. Phys. J. 59 (2017) 1417–1424. https://doi.org/10.1007/s11182-017-0925-x.
[117] A.V. Kolobov, J. Tominaga, Chalcogenides: Metastability and Phase Change Phenomena, Springer Berlin Heidelberg, Berlin, Heidelberg, 2012. https://doi.org/10.1007/978-3-642-28705-3.
[118] G. Bruns, P. Merkelbach, C. Schlockermann, M. Salinga, M. Wuttig, T.D. Happ, J.B. Philipp, M. Kund, Nanosecond switching in GeTe phase change memory cells, Appl. Phys. Lett. 95 (2009) 043108. https://doi.org/10.1063/1.3191670.
[119] L. Perniola, V. Sousa, A. Fantini, E. Arbaoui, A. Bastard, M. Armand, A. Fargeix, C. Jahan, J.-F. Nodin, A. Persico, D. Blachier, A. Toffoli, S. Loubriat, E. Gourvest, G. Betti Beneventi, H. Feldis, S. Maitrejean, S. Lhostis, A. Roule, O. Cueto, G. Reimbold, L. Poupinet, T. Billon, B. De Salvo, D. Bensahel, P. Mazoyer, R. Annunziata, P. Zuliani, F. Boulanger, Electrical Behavior of Phase-Change Memory Cells Based on GeTe, IEEE Electron Device Lett. 31 (2010) 488–490. https://doi.org/10.1109/LED.2010.2044136.
[120] G. Lama, G. Bourgeois, M. Bernard, N. Castellani, J. Sandrini, E. Nolot, J. Garrione, M.C. Cyrille, G. Navarro, E. Nowak, Reliability analysis in GeTe and GeSbTe based phase-change memory 4kb arrays targeting storage class memory applications, Microelectron. Reliab. 114 (2020) 113823. https://doi.org/10.1016/j.microrel.2020.113823.
[121] J.E. Boschker, R. Wang, R. Calarco, GeTe: a simple compound blessed with a plethora of properties, CrystEngComm. 19 (2017) 5324–5335. https://doi.org/10.1039/C7CE01040K.
[122] A.V. Kolobov, J. Tominaga, P. Fons, T. Uruga, Local structure of crystallized GeTe films, Appl. Phys. Lett. 82 (2003) 382–384. https://doi.org/10.1063/1.1539926.
[123] R. Mazzarello, S. Caravati, S. Angioletti-Uberti, M. Bernasconi, M. Parrinello, Signature of Tetrahedral Ge in the Raman Spectrum of Amorphous Phase-Change Materials, Phys. Rev. Lett. 104 (2010) 085503. https://doi.org/10.1103/PhysRevLett.104.085503.
[124] D.A. Baker, M.A. Paesler, G. Lucovsky, S.C. Agarwal, P.C. Taylor, Application of Bond Constraint Theory to the Switchable Optical Memory Material $Ge_2Sb_2Te_5$, Phys. Rev. Lett. 96 (2006) 255501. https://doi.org/10.1103/PhysRevLett.96.255501.
[125] S. Kohara, K. Kato, S. Kimura, H. Tanaka, T. Usuki, K. Suzuya, H. Tanaka, Y. Moritomo, T. Matsunaga, N. Yamada, Y. Tanaka, H. Suematsu, M. Takata, Structural basis for the fast phase change of $Ge_2Sb_2Te_5$: Ring statistics analogy between the crystal and amorphous states, Appl. Phys. Lett. 89 (2006) 201910. https://doi.org/10.1063/1.2387870.
[126] B. Fang, Z. Zeng, X. Yan, Z. Hu, Effects of annealing on thermoelectric properties of Sb_2Te_3 thin films prepared by radio frequency magnetron sputtering, J. Mater. Sci. Mater. Electron. 24 (2013) 1105–1111. https://doi.org/10.1007/s10854-012-0888-1.
[127] K.A. Kokh, V.V. Atuchin, T.A. Gavrilova, N.V. Kuratieva, N.V. Pervukhina, N.V. Surovtsev, Microstructural and vibrational properties of PVT grown Sb_2Te_3 crystals, Solid State Commun. 177 (2014) 16–19. https://doi.org/10.1016/j.ssc.2013.09.016.
[128] H. Plank, S.D. Ganichev, A review on terahertz photogalvanic spectroscopy of Bi_2Te_3- and Sb_2Te_3-based three dimensional topological insulators, Solid-State Electron. 147 (2018) 44–50. https://doi.org/10.1016/j.sse.2018.06.002.

[129] N. Yamada, E. Ohno, K. Nishiuchi, N. Akahira, M. Takao, Rapid-phase transitions of GeTe-Sb_2Te_3 pseudobinary amorphous thin films for an optical disk memory, J. Appl. Phys. 69 (1991) 2849–2856. https://doi.org/10.1063/1.348620.
[130] I.I. Petrov, R.M. Imamov, Z.G. Pinsker, Electron-diffraction determination of the structures of $Ge_2Sb_2Te_5$ and $GeSb_4Te_7$., Sov Phys Crystallogr 133. (1968) 339–342.
[131] B.J. Kooi, J.Th.M. De Hosson, Electron diffraction and high-resolution transmission electron microscopy of the high temperature crystal structures of $Ge_xSb_2Te_{3+x}$ (x=1,2,3) phase change material, J. Appl. Phys. 92 (2002) 3584–3590. https://doi.org/10.1063/1.1502915.
[132] T. Matsunaga, N. Yamada, Y. Kubota, Structures of stable and metastable $Ge_2Sb_2Te_5$, an intermetallic compound in GeTe–Sb_2Te_3 pseudobinary systems, Acta Crystallogr. B. 60 (2004) 685–691. https://doi.org/10.1107/S0108768104022906.
[133] A.V. Kolobov, P. Fons, A.I. Frenkel, A.L. Ankudinov, J. Tominaga, T. Uruga, Understanding the phase-change mechanism of rewritable optical media, Nat. Mater. 3 (2004) 703–708. https://doi.org/10.1038/nmat1215.
[134] P. Jóvári, I. Kaban, J. Steiner, B. Beuneu, A. Schöps, A. Webb, 'Wrong bonds' in sputtered amorphous $Ge_2Sb_2Te_5$, J. Phys. Condens. Matter. 19 (2007) 335212. https://doi.org/10.1088/0953-8984/19/33/335212.
[135] P. Jóvári, I. Kaban, J. Steiner, B. Beuneu, A. Schöps, M.A. Webb, Local order in amorphous $Ge_2Sb_2Te_5$ and $Ge_1Sb_2Te_4$, Phys. Rev. B. 77 (2008) 035202. https://doi.org/10.1103/PhysRevB.77.035202.
[136] Z. Xu, C. Chen, Z. Wang, K. Wu, H. Chong, H. Ye, Optical constants acquisition and phase change properties of $Ge_2Sb_2Te_5$ thin films based on spectroscopy, RSC Adv. 8 (2018) 21040–21046. https://doi.org/10.1039/C8RA01382A.
[137] A.V. Kolobov, P. Fons, J. Tominaga, T. Uruga, Why DVDs work the way they do: The nanometer-scale mechanism of phase change in Ge–Sb–Te alloys, J. Non-Cryst. Solids. 352 (2006) 1612–1615. https://doi.org/10.1016/j.jnoncrysol.2005.09.050.
[138] M. Boniardi, A. Redaelli, I. Tortorelli, S. Lavizzari, A. Pirovano, F. Pellizzer, E. Varesi, D. Erbetta, C. Bresolin, A. Modelli, R. Bez, Electrical and Thermal Behavior of Tellurium Poor GeSbTe Compounds for Phase Change Memory, in: 2012 4th IEEE Int. Mem. Workshop, IEEE, Milan, Italy, 2012: pp. 1–3. https://doi.org/10.1109/IMW.2012.6213679.
[139] M. Boniardi, A. Redaelli, Phase Change Memory: Device scaling and challenges for material engineering in the GeSbTe compound system, Microelectron. Eng. 137 (2015) 1–4. https://doi.org/10.1016/j.mee.2014.09.021.
[140] H.Y. Cheng, T.H. Hsu, S. Raoux, J.Y. Wu, P.Y. Du, M. Breitwisch, Y. Zhu, E.K. Lai, E. Joseph, S. Mittal, R. Cheek, A. Schrott, S.C. Lai, H.L. Lung, C. Lam, A high performance phase change memory with fast switching speed and high temperature retention by engineering the $Ge_xSb_yTe_z$ phase change material, in: 2011 Int. Electron Devices Meet., IEEE, Washington, DC, USA, 2011: p. 3.4.1-3.4.4. https://doi.org/10.1109/IEDM.2011.6131481.
[141] V. Sousa, G. Navarro, N. Castellani, M. Coue, O. Cueto, C. Sabbione, P. Noe, L. Perniola, S. Blonkowski, P. Zuliani, R. Annunziata, Operation fundamentals in 12Mb Phase Change Memory based on innovative Ge-rich GST materials featuring high reliability performance, in: 2015 Symp. VLSI Technol. VLSI Technol., IEEE, Kyoto, Japan, 2015: pp. T98–T99. https://doi.org/10.1109/VLSIT.2015.7223708.
[142] N. Ciocchini, E. Palumbo, M. Borghi, P. Zuliani, R. Annunziata, D. Ielmini, Modeling Resistance Instabilities of Set and Reset States in Phase Change Memory With Ge-Rich GeSbTe, IEEE Trans. Electron Devices. 61 (2014) 2136–2144. https://doi.org/10.1109/TED.2014.2313889.

[143] P. Zuliani, E. Varesi, E. Palumbo, M. Borghi, I. Tortorelli, D. Erbetta, G.D. Libera, N. Pessina, A. Gandolfo, C. Prelini, L. Ravazzi, R. Annunziata, Overcoming Temperature Limitations in Phase Change Memories With Optimized $Ge_xSb_yTe_z$, IEEE Trans. Electron Devices. 60 (2013) 4020–4026. https://doi.org/10.1109/TED.2013.2285403.
[144] A. Debunne, K. Virwani, A. Padilla, G.W. Burr, A.J. Kellock, V.R. Deline, R.M. Shelby, B. Jackson, Evidence of Crystallization–Induced Segregation in the Phase Change Material Te-Rich GST, J. Electrochem. Soc. 158 (2011) H965. https://doi.org/10.1149/1.3614508.
[145] E. Palumbo, P. Zuliani, M. Borghi, R. Annunziata, Forming operation in Ge-rich $Ge_xSb_yTe_z$ phase change memories, Solid-State Electron. 133 (2017) 38–44. https://doi.org/10.1016/j.sse.2017.03.016.
[146] H.-Y. Cheng, S. Raoux, J.L. Jordan-Sweet, Crystallization properties of materials along the pseudo-binary line between GeTe and Sb, J. Appl. Phys. 115 (2014) 093101. https://doi.org/10.1063/1.4867045.
[147] S. Raoux, H.-Y. Cheng, J. Sandrini, J. Li, J. Jordan-Sweet, Materials engineering for Phase Change Random Access Memory, in: 2011 11th Annu. Non-Volatile Mem. Technol. Symp. Proceeding, IEEE, Shanghai, China, 2011: pp. 1–5. https://doi.org/10.1109/NVMTS.2011.6137090.
[148] G. Navarro, C. Sabbione, M. Bernard, G. Bourgeois, J. Sandrini, N. Castellani, O. Cueto, J. Garrione, M.C. Cyrille, M. Frei, L. Nistor, N. Bernier, F. Fillot, E. Nolot, C. Socquet-Clerc, T. Magis, F. Laulagnet, M. Pakala, E. Nowak, Highly Sb-Rich Ge-Sb-Te Engineering in 4Kb Phase-Change Memory for High Speed and High Material Stability Under Cycling, in: 2019 IEEE 11th Int. Mem. Workshop IMW, IEEE, Monterey, CA, USA, 2019: pp. 1–4. https://doi.org/10.1109/IMW.2019.8739656.
[149] G. D'Arrigo, A.M. Mio, M. Boniardi, A. Redaelli, E. Varesi, S. Privitera, G. Pellegrino, C. Spinella, E. Rimini, Crystallization properties of Sb-rich GeSbTe alloys by in-situ morphological and electrical analysis, Mater. Sci. Semicond. Process. 65 (2017) 100–107. https://doi.org/10.1016/j.mssp.2016.07.014.
[150] I.S. Kim, S.L. Cho, D.H. Im, E.H. Cho, D.H. Kim, G.H. Oh, D.H. Ahn, S.O. Park, S.W. Nam, J.T. Moon, C.H. Chung, High performance PRAM cell scalable to sub-20nm technology with below 4F2 cell size, extendable to DRAM applications, in: 2010 Symp. VLSI Technol., IEEE, Honolulu, HI, USA, 2010: pp. 203–204. https://doi.org/10.1109/VLSIT.2010.5556228.
[151] R. Kojima, S. Okabayashi, T. Kashihara, K. Horai, T. Matsunaga, E. Ohno, N. Yamada, T. Ohta, Nitrogen Doping Effect on Phase Change Optical Disks, Jpn. J. Appl. Phys. 37 (1998) 2098–2103. https://doi.org/10.1143/JJAP.37.2098.
[152] T.H. Jeong, M.R. Kim, H. Seo, J.W. Park, C. Yeon, Crystal Structure and Microstructure of Nitrogen-Doped $Ge_2Sb_2Te_5$ Thin Film, Jpn. J. Appl. Phys. 39 (2000) 2775–2779. https://doi.org/10.1143/JJAP.39.2775.
[153] H.Y. Cheng, J.Y. Wu, R. Cheek, S. Raoux, M. BrightSky, D. Garbin, S. Kim, T.H. Hsu, Y. Zhu, E.K. Lai, E. Joseph, A. Schrott, S.C. Lai, A. Ray, H.L. Lung, C. Lam, A thermally robust phase change memory by engineering the Ge/N concentration in (Ge, N)$_x$Sb$_y$Te $_z$ phase change material, in: 2012 Int. Electron Devices Meet., IEEE, San Francisco, CA, USA, 2012: p. 31.1.1-31.1.4. https://doi.org/10.1109/IEDM.2012.6479141.
[154] Z. Xu, B. Liu, Y. Chen, Z. Zhang, D. Gao, H. Wang, Z. Song, C. Wang, J. Ren, N. Zhu, Y. Xiang, Y. Zhan, S. Feng, The improvement of nitrogen doped $Ge_2Sb_2Te_5$ on the phase change memory resistance distributions, Solid-State Electron. 116 (2016) 119–123. https://doi.org/10.1016/j.sse.2015.11.001.

[155] D. Yao, X. Zhou, L. Wu, Z. Song, L. Cheng, F. Rao, B. Liu, S. Feng, Investigation on nitrogen-doped $Ge_2Sb_2Te_5$ material for phase-change memory application, Solid-State Electron. 79 (2013) 138–141. https://doi.org/10.1016/j.sse.2012.07.020.
[156] J.-Y. Cho, D. Kim, Y.-J. Park, T.-Y. Yang, Y.-Y. Lee, Y.-C. Joo, The phase-change kinetics of amorphous $Ge_2Sb_2Te_5$ and device characteristics investigated by thin-film mechanics, Acta Mater. 94 (2015) 143–151. https://doi.org/10.1016/j.actamat.2015.04.058.
[157] N. Matsuzaki, K. Kurotsuchi, Y. Matsui, O. Tonomura, N. Yamamoto, Y. Fujisaki, N. Kitai, R. Takemura, K. Osada, S. Hanzawa, H. Moriya, T. Iwasaki, T. Kawahara, N. Takaura, M. Terao, M. Matsuoka, M. Moniwa, Oxygen-doped GeSbTe phase-change memory cells featuring 1.5 V/100-μA Standard 0.13-μm CMOS operations, in: IEEE Int. Devices Meet. 2005 IEDM Tech. Dig., IEEE, Tempe, Arizon, USA, 2005: pp. 738–741. https://doi.org/10.1109/IEDM.2005.1609459.
[158] M.H. Jang, S.J. Park, D.H. Lim, M.-H. Cho, K.H. Do, D.-H. Ko, H.C. Sohn, Phase change behavior in oxygen-incorporated $Ge_2Sb_2Te_5$ films, Appl. Phys. Lett. 95 (2009) 012102. https://doi.org/10.1063/1.3168551.
[159] R. Golovchak, Y.G. Choi, S. Kozyukhin, Yu. Chigirinsky, A. Kovalskiy, P. Xiong-Skiba, J. Trimble, R. Pafchek, H. Jain, Oxygen incorporation into GST phase-change memory matrix, Appl. Surf. Sci. 332 (2015) 533–541. https://doi.org/10.1016/j.apsusc.2015.01.203.
[160] S. Tripathi, P. Kotula, M.K. Singh, C. Ghosh, G. Bakan, H. Silva, C.B. Carter, Role of Oxygen on Chemical Segregation in Uncapped $Ge_2Sb_2Te_5$ Thin Films on Silicon Nitride, ECS J. Solid State Sci. Technol. 9 (2020) 054007. https://doi.org/10.1149/2162-8777/ab9a19.
[161] B.J. Kooi, W.M.G. Groot, J.Th.M. De Hosson, *In situ* transmission electron microscopy study of the crystallization of $Ge_2Sb_2Te_5$, J. Appl. Phys. 95 (2004) 924–932. https://doi.org/10.1063/1.1636259.
[162] T. Li, J. Shen, L. Wu, Z. Song, S. Lv, D. Cai, S. Zhang, T. Guo, S. Song, M. Zhu, Atomic-Scale Observation of Carbon Distribution in High-Performance Carbon-Doped $Ge_2Sb_2Te_5$ and Its Influence on Crystallization Behavior, J. Phys. Chem. C. 123 (2019) 13377–13384. https://doi.org/10.1021/acs.jpcc.9b02098.
[163] Q. Hubert, C. Jahan, A. Toffoli, G. Navarro, S. Chandrashekar, P. Noé, V. Sousa, L. Perniola, J.- Nodin, A. Persico, S. Maitrejean, A. Roule, E. Henaff, M. Tessaire, P. Zuliani, R. Annunziata, G. Reimbold, G. Pananakakis, B.D. Salvo, Carbon-doped Ge2Sb2Te5phase-change memory devices featuring reduced RESET current and power consumption, in: 2012 Proc. Eur. Solid-State Device Res. Conf. ESSDERC, 2012: pp. 286–289. https://doi.org/10.1109/ESSDERC.2012.6343389.
[164] Z. Song, D. Cai, Y. Cheng, L. Wang, S. Lv, T. Xin, G. Feng, 12-state multi-level cell storage implemented in a 128 Mb phase change memory chip, Nanoscale. 13 (2021) 10455–10461. https://doi.org/10.1039/D1NR00100K.
[165] X. Zhou, L. Wu, Z. Song, F. Rao, M. Zhu, C. Peng, D. Yao, S. Song, B. Liu, S. Feng, Carbon-doped $Ge_2Sb_2Te_5$ phase change material: A candidate for high-density phase change memory application, Appl. Phys. Lett. 101 (2012) 142104. https://doi.org/10.1063/1.4757137.
[166] S. Souiki, Q. Hubert, G. Navarro, A. Persico, C. Jahan, E. Henaff, V. Delaye, D. Blachier, V. Sousa, L. Perniola, E. Vianello, B. De Salvo, Reliability study of carbon-doped GST stack robust against Pb-free soldering reflow, in: 2013 IEEE Int. Reliab. Phys. Symp. IRPS, IEEE, Anaheim, CA, 2013: p. MY.8.1-MY.8.5. https://doi.org/10.1109/IRPS.2013.6532099.

[167] Z.T. Song, D.L. Cai, X. Li, L. Wang, Y.F. Chen, H.P. Chen, Q. Wang, Y.P. Zhan, M.H. Ji, High Endurance Phase Change Memory Chip Implemented based on Carbon-doped $Ge_2Sb_2Te_5$ in 40 nm Node for Embedded Application, in: 2018 IEEE Int. Electron Devices Meet. IEDM, IEEE, San Francisco, CA, 2018: p. 27.5.1-27.5.4. https://doi.org/10.1109/IEDM.2018.8614538.
[168] M.-C. Jung, Y.M. Lee, H.-D. Kim, M.G. Kim, H.J. Shin, K.H. Kim, S.A. Song, H.S. Jeong, C.H. Ko, M. Han, Ge nitride formation in N-doped amorphous $Ge_2Sb_2Te_5$, Appl. Phys. Lett. 91 (2007) 083514. https://doi.org/10.1063/1.2773959.
[169] K. Kim, J.-C. Park, J.-G. Chung, S.A. Song, M.-C. Jung, Y.M. Lee, H.-J. Shin, B. Kuh, Y. Ha, J.-S. Noh, Observation of molecular nitrogen in N-doped $Ge_2Sb_2Te_5$, Appl. Phys. Lett. 89 (2006) 243520. https://doi.org/10.1063/1.2408660.
[170] L.W.-W. Fang, R. Zhao, M. Li, K.-G. Lim, L. Shi, T.-C. Chong, Y.-C. Yeo, Dependence of the properties of phase change random access memory on nitrogen doping concentration in $Ge_2Sb_2Te_5$, J. Appl. Phys. 107 (2010) 104506. https://doi.org/10.1063/1.3383042.
[171] G. Navarro, V. Sousa, P. Noe, N. Castellani, M. Coue, J. Kluge, A. Kiouseloglou, C. Sabbione, A. Persico, A. Roule, O. Cueto, S. Blonkowski, F. Fillot, N. Bernier, R. Annunziata, M. Borghi, E. Palumbo, P. Zuliani, L. Perniola, N-Doping Impact in Optimized Ge-Rich Materials Based Phase-Change Memory, in: IEEE, 2016: pp. 1–4. https://doi.org/10.1109/IMW.2016.7495284.
[172] G. Navarro, M. Coue, A. Kiouseloglou, P. Noe, F. Fillot, V. Delaye, A. Persico, A. Roule, M. Bernard, C. Sabbione, D. Blachier, V. Sousa, L. Perniola, S. Maitrejean, A. Cabrini, G. Torelli, P. Zuliani, R. Annunziata, E. Palumbo, M. Borghi, G. Reimbold, B. De Salvo, Trade-off between SET and data retention performance thanks to innovative materials for phase-change memory, in: 2013 IEEE Int. Electron Devices Meet., IEEE, Washington, DC, USA, 2013: p. 21.5.1-21.5.4. https://doi.org/10.1109/IEDM.2013.6724678.
[173] M. Sardela, ed., Practical Materials Characterization, Springer New York, New York, NY, 2014. https://doi.org/10.1007/978-1-4614-9281-8.
[174] H. Seo, T.-H. Jeong, J.-W. Park, C. Yeon, S.-J. Kim, S.-Y. Kim, Investigation of Crystallization Behavior of Sputter-Deposited Nitrogen-Doped Amorphous $Ge_2Sb_2Te_5$ Thin Films, Jpn. J. Appl. Phys. 39 (2000) 745–751. https://doi.org/10.1143/JJAP.39.745.
[175] Y. Choi, M. Jung, Y.-K. Lee, Effect of Heating Rate on the Activation Energy for Crystallization of Amorphous $Ge_2Sb_2Te_5$ Thin Film, Electrochem. Solid-State Lett. 12 (2009) F17. https://doi.org/10.1149/1.3129137.
[176] P. Larkin, Infrared and raman spectroscopy: principles and spectral interpretation, Elsevier, Amsterdam ; Boston, 2011.
[177] B.C. Smith, Fundamentals of Fourier transform infrared spectroscopy, CRC Press, Boca Raton, Fla., 2011. https://public.ebookcentral.proquest.com/choice/publicfullrecord.aspx?p=681305 (accessed January 3, 2022).
[178] R.S. Mulliken, Report on Notation for the Spectra of Polyatomic Molecules, J. Chem. Phys. 23 (1955) 1997–2011. https://doi.org/10.1063/1.1740655.
[179] K.S. Andrikopoulos, S.N. Yannopoulos, G.A. Voyiatzis, A.V. Kolobov, M. Ribes, J. Tominaga, Raman scattering study of the a-GeTe structure and possible mechanism for the amorphous to crystal transition, J. Phys. Condens. Matter. 18 (2006) 965–979. https://doi.org/10.1088/0953-8984/18/3/014.
[180] A.R. Zanatta, I. Chambouleyron, Nitrogen in the amorphous-germanium network: From high dilution to the alloy phase, Phys. Rev. B. 48 (1993) 4560–4570. https://doi.org/10.1103/PhysRevB.48.4560.

[181] C. Guanghua, Z. Fangqing, Infrared and Raman spectra of reactively sputtered amorphous GeN_x:H film, Thin Solid Films. 185 (1990) 231–234. https://doi.org/10.1016/0040-6090(90)90087-T.
[182] F.C. Marques, I. Chambouleyron, F. Evangelisti, Infrared analysis of a-$Ge_{1-x}N_x$:H, J. Non-Cryst. Solids. 114 (1989) 561–563. https://doi.org/10.1016/0022-3093(89)90650-9.
[183] J. Song, C. Yang, H. Hu, X. Dai, C. Wang, H. Zhang, Penetration depth at various Raman excitation wavelengths and stress model for Raman spectrum in biaxially-strained Si, Sci. China Phys. Mech. Astron. 56 (2013) 2065–2070. https://doi.org/10.1007/s11433-013-5205-3.
[184] P. Vandenabeele, Practical Raman spectroscopy: an introduction, Wiley, Chichester, West Sussex, United Kingdom, 2013.
[185] D.L. Weaire, The Vibrational Density of States of Amorphous Semiconductors, in: W.A. Phillips (Ed.), Amorph. Solids, Springer Berlin Heidelberg, Berlin, Heidelberg, 1981: pp. 13–26. https://doi.org/10.1007/978-3-642-81534-8_2.
[186] R. Alben, D. Weaire, J.E. Smith, M.H. Brodsky, Vibrational properties of amorphous Si and Ge, Phys. Rev. B. 11 (1975) 2271–2296. https://doi.org/10.1103/PhysRevB.11.2271.
[187] P. Kazimierski, J. Tyczkowski, M. Kozanecki, Y. Hatanaka, T. Aoki, Transition from Amorphous Semiconductor to Amorphous Insulator in Hydrogenated Carbon−Germanium Films Investigated by Raman Spectroscopy, Chem. Mater. 14 (2002) 4694–4701. https://doi.org/10.1021/cm020428s.
[188] I. Chambouleyron, A.R. Zanatta, Nitrogen in germanium, J. Appl. Phys. 84 (1998) 1–30. https://doi.org/10.1063/1.368612.
[189] J.S. Lannin, J.M. Calleja, M. Cardona, Second-order Raman scattering in the group- V b semimetals: Bi, Sb, and As, Phys. Rev. B. 12 (1975) 585–593. https://doi.org/10.1103/PhysRevB.12.585.
[190] M. Zhao, J. Wu, Y. Wei, J. Chen, Preparation of antimonene by laser irradiation in different solvents for optical limiting, Opt. Mater. 109 (2020) 110132. https://doi.org/10.1016/j.optmat.2020.110132.
[191] C. Gibaja, D. Rodriguez-San-Miguel, P. Ares, J. Gómez-Herrero, M. Varela, R. Gillen, J. Maultzsch, F. Hauke, A. Hirsch, G. Abellán, F. Zamora, Few-Layer Antimonene by Liquid-Phase Exfoliation, Angew. Chem. Int. Ed. 55 (2016) 14345–14349. https://doi.org/10.1002/anie.201605298.
[192] J.S. Lannin, Raman scattering properties of amorphous As and Sb, Phys. Rev. B. 15 (1977) 3863–3871. https://doi.org/10.1103/PhysRevB.15.3863.
[193] D. Dragoni, J. Behler, M. Bernasconi, Mechanism of amorphous phase stabilization in ultrathin films of monoatomic phase change material, Nanoscale. 13 (2021) 16146–16155. https://doi.org/10.1039/D1NR03432D.
[194] G. Lucovsky, A comparison of the long wave optical phonons in trigonal Se and trigonal Te, Phys. Status Solidi B. 49 (1972) 633–641. https://doi.org/10.1002/pssb.2220490226.
[195] J.J. Loferski, Infrared Optical Properties of Single Crystals of Tellurium, Phys. Rev. 93 (1954) 707–716. https://doi.org/10.1103/PhysRev.93.707.
[196] B.H. Torrie, Raman spectrum of tellurium, Solid State Commun. 8 (1970) 1899–1901. https://doi.org/10.1016/0038-1098(70)90343-1.
[197] T. Chivers, R.S. Laitinen, Tellurium: a maverick among the chalcogens, Chem. Soc. Rev. 44 (2015) 1725–1739. https://doi.org/10.1039/C4CS00434E.

[198] G. Lucovsky, R.C. Keezer, E. Burstein, Infra-red lattice bands of trigonal tellurium and selenium, Solid State Commun. 5 (1967) 439–445. https://doi.org/10.1016/0038-1098(67)90589-3.
[199] M.H. Brodsky, R.J. Gambino, J.E. Smith, Y. Yacoby, The Raman Spectrum of Amorphous Tellurium, Phys. Status Solidi B. 52 (1972) 609–614. https://doi.org/10.1002/pssb.2220520229.
[200] H. Pattyn, S. Bukshpan, A study of amorphous tellurium, Hyperfine Interact. 27 (1986) 441–444. https://doi.org/10.1007/BF02354800.
[201] T. Ichikawa, Electron Diffraction Study of the Local Atomic Arrangement in Amorphous Tellurium Films: Electron Diffraction Study of the Local Atomic Arrangement in Te, Phys. Status Solidi B. 56 (1973) 707–715. https://doi.org/10.1002/pssb.2220560235.
[202] J. Akola, R.O. Jones, Structure and dynamics in amorphous tellurium and Te n clusters: A density functional study, Phys. Rev. B. 85 (2012) 134103. https://doi.org/10.1103/PhysRevB.85.134103.
[203] F. Fillot, C. Sabbione, F. Pierre, F. Hippert, P. Noé, Crystallization of $Ge_2Sb_2Te_5$ and nitrogren-doped $Ge_2Sb_2Te_5$ phase-change-materials thin films studied by *in situ* combined X-ray scattering techniques, J. Appl. Crystallogr. 51 (2018) 1691–1705. https://doi.org/10.1107/S1600576718015315.
[204] H.-Y. Cheng, S. Raoux, Y.-C. Chen, The impact of film thickness and melt-quenched phase on the phase transition characteristics of $Ge_2Sb_2Te_5$, J. Appl. Phys. 107 (2010) 074308. https://doi.org/10.1063/1.3357379.
[205] X. Wei, textscShi Luping, textscChong T. Chong, textscZhao Rong, textscLee H. Koon, Thickness Dependent Nano-Crystallization in $Ge_2Sb_2Te_5$ Films and Its Effect on Devices, Jpn. J. Appl. Phys. 46 (2007) 2211–2214. https://doi.org/10.1143/JJAP.46.2211.
[206] K. Jeong, S. Park, D. Park, M. Ahn, J. Han, W. Yang, H.-S. Jeong, M.-H. Cho, Evolution of crystal structures in GeTe during phase transition, Sci. Rep. 7 (2017) 955. https://doi.org/10.1038/s41598-017-01154-z.
[207] E. Carria, A.M. Mio, S. Gibilisco, M. Miritello, C. Bongiorno, M.G. Grimaldi, E. Rimini, Amorphous-Crystal Phase Transitions in Ge_xTe_{1-x} Alloys, J. Electrochem. Soc. 159 (2011) H130–H139. https://doi.org/10.1149/2.048202jes.
[208] W. Richter, C.R. Becker, A Raman and far-infrared investigation of phonons in the rhombohedral V2–VI3 compounds Bi_2Te_3, Bi_2Se_3, Sb_2Te_3 and $Bi_2(Te_{1-x}Se_x)_3$ ($0 < x < 1$), $(Bi_{1-y}Sb_y)_2Te_3$ ($0 < y < 1$), Phys. Status Solidi B. 84 (1977) 619–628. https://doi.org/10.1002/pssb.2220840226.
[209] L.M. Goncalves, P. Alpuim, A.G. Rolo, J.H. Correia, Thermal co-evaporation of Sb_2Te_3 thin-films optimized for thermoelectric applications, Thin Solid Films. 519 (2011) 4152–4157. https://doi.org/10.1016/j.tsf.2011.01.395.
[210] G.C. Sosso, S. Caravati, M. Bernasconi, Vibrational properties of crystalline Sb_2Te_3 from first principles, J. Phys. Condens. Matter. 21 (2009) 095410. https://doi.org/10.1088/0953-8984/21/9/095410.
[211] P. Němec, V. Nazabal, A. Moreac, J. Gutwirth, L. Beneš, M. Frumar, Amorphous and crystallized Ge–Sb–Te thin films deposited by pulsed laser: Local structure using Raman scattering spectroscopy, Mater. Chem. Phys. 136 (2012) 935–941. https://doi.org/10.1016/j.matchemphys.2012.08.024.
[212] K.S. Andrikopoulos, S.N. Yannopoulos, A.V. Kolobov, P. Fons, J. Tominaga, Raman scattering study of GeTe and $Ge_2Sb_2Te_5$ phase-change materials, J. Phys. Chem. Solids. 68 (2007) 1074–1078. https://doi.org/10.1016/j.jpcs.2007.02.027.

[213] I. Friedrich, V. Weidenhof, W. Njoroge, P. Franz, M. Wuttig, Structural transformations of $Ge_2Sb_2Te_5$ films studied by electrical resistance measurements, J. Appl. Phys. 87 (2000) 4130–4134. https://doi.org/10.1063/1.373041.
[214] J. Xu, C. Qi, L. Chen, L. Zheng, Q. Xie, The microstructural changes of $Ge_2Sb_2Te_5$ thin film during crystallization process, AIP Adv. 8 (2018) 055006. https://doi.org/10.1063/1.5025204.
[215] K. Shportko, L. Revutska, O. Paiuk, J. Baran, A. Stronski, A. Gubanova, E. Venger, Compositional dependencies in the vibrational properties of amorphous Ge-As-Se and Ge-Sb-Te chalcogenide alloys studied by Raman spectroscopy, Opt. Mater. 73 (2017) 489–496. https://doi.org/10.1016/j.optmat.2017.08.042.
[216] M.J. Shin, D.J. Choi, M. Kang, S. Choi, I.W. Jang, K.N. Lee, Y. Park, Chemical bonding characteristics of $Ge_2Sb_2Te_5$ for thin films., J. Korean Phys. Soc. 44 (2004) 10–13.
[217] M.-C. Jung, H.J. Shin, K. Kim, J.S. Noh, J. Chung, High-resolution x-ray photoelectron spectroscopy on oxygen-free amorphous $Ge_2Sb_2Te_5$, Appl. Phys. Lett. 89 (2006) 043503. https://doi.org/10.1063/1.2236216.
[218] E. Nolot, C. Sabbione, W. Pessoa, L. Prazakova, G. Navarro, Germanium, antimony, tellurium, their binary and ternary alloys and the impact of nitrogen: An X-ray photoelectron study, Appl. Surf. Sci. 536 (2021) 147703. https://doi.org/10.1016/j.apsusc.2020.147703.
[219] B. Casarin, A. Caretta, J. Momand, B.J. Kooi, M.A. Verheijen, V. Bragaglia, R. Calarco, M. Chukalina, X. Yu, J. Robertson, F.R.L. Lange, M. Wuttig, A. Redaelli, E. Varesi, F. Parmigiani, M. Malvestuto, Revisiting the Local Structure in Ge-Sb-Te based Chalcogenide Superlattices, Sci. Rep. 6 (2016) 22353. https://doi.org/10.1038/srep22353.
[220] M. Krbal, A.V. Kolobov, P. Fons, J. Tominaga, S.R. Elliott, J. Hegedus, T. Uruga, Intrinsic complexity of the melt-quenched amorphous $Ge_2Sb_2Te_5$ memory alloy, Phys. Rev. B. 83 (2011) 054203. https://doi.org/10.1103/PhysRevB.83.054203.
[221] G.C. Sosso, S. Caravati, R. Mazzarello, M. Bernasconi, Raman spectra of cubic and amorphous $Ge_2Sb_2Te_5$ from first principles, Phys. Rev. B. 83 (2011) 134201. https://doi.org/10.1103/PhysRevB.83.134201.
[222] F. Fillot, C. Sabbione, Nanoscale mechanics of thermally crystallized GST thin film by *in situ* x-ray diffraction, J. Appl. Phys. 128 (2020) 235107. https://doi.org/10.1063/5.0023653.
[223] M. Agati, C. Gay, D. Benoit, A. Claverie, Effects of surface oxidation on the crystallization characteristics of Ge-rich Ge-Sb-Te alloys thin films, Appl. Surf. Sci. 518 (2020) 146227. https://doi.org/10.1016/j.apsusc.2020.146227.
[224] Y. Zheng, Y. Cheng, R. Huang, R. Qi, F. Rao, K. Ding, W. Yin, S. Song, W. Liu, Z. Song, S. Feng, Surface Energy Driven Cubic-to-Hexagonal Grain Growth of $Ge_2Sb_2Te_5$ Thin Film, Sci. Rep. 7 (2017) 5915. https://doi.org/10.1038/s41598-017-06426-2.
[225] C. Jeynes, E. Nolot, C. Costa, C. Sabbione, W. Pessoa, F. Pierre, A. Roule, G. Navarro, M. Mantler, Quantifying nitrogen in GeSbTe:N alloys, J. Anal. At. Spectrom. 35 (2020) 701–712. https://doi.org/10.1039/C9JA00382G.
[226] A.L. Ankudinov, B. Ravel, J.J. Rehr, S.D. Conradson, Real-space multiple-scattering calculation and interpretation of x-ray-absorption near-edge structure, Phys. Rev. B. 58 (1998) 7565–7576. https://doi.org/10.1103/PhysRevB.58.7565.
[227] A. Cobelo-García, M. Filella, P. Croot, C. Frazzoli, G. Du Laing, N. Ospina-Alvarez, S. Rauch, P. Salaun, J. Schäfer, S. Zimmermann, COST action TD1407: network on technology-critical elements (NOTICE)—from environmental processes to human

health threats, Environ. Sci. Pollut. Res. 22 (2015) 15188–15194. https://doi.org/10.1007/s11356-015-5221-0.
[228] P. Nuss, G.A. Blengini, Towards better monitoring of technology critical elements in Europe: Coupling of natural and anthropogenic cycles, Sci. Total Environ. 613–614 (2018) 569–578. https://doi.org/10.1016/j.scitotenv.2017.09.117.
[229] S. Das, K.R. Khiangte, R.S. Fandan, J.S. Rathore, R.S. Pokharia, S. Mahapatra, A. Laha, On the correlation of growth, structural and electrical properties of epitaxial Ge grown on Si by solid source molecular beam epitaxy, Curr. Appl. Phys. 17 (2017) 327–332. https://doi.org/10.1016/j.cap.2016.12.020.
[230] Y. Kamata, High-k/Ge MOSFETs for future nanoelectronics, Mater. Today. 11 (2008) 30–38. https://doi.org/10.1016/S1369-7021(07)70350-4.
[231] J. Liu, R. Camacho-Aguilera, J.T. Bessette, X. Sun, X. Wang, Y. Cai, L.C. Kimerling, J. Michel, Ge-on-Si optoelectronics, Thin Solid Films. 520 (2012) 3354–3360. https://doi.org/10.1016/j.tsf.2011.10.121.
[232] Y. Wang, Z. Ren, M. Thway, K. Lee, S.F. Yoon, I.M. Peters, T. Buonassisi, E.A. Fizgerald, C.S. Tan, K.H. Lee, Fabrication and characterization of single junction GaAs solar cells on Si with As-doped Ge buffer, Sol. Energy Mater. Sol. Cells. 172 (2017) 140–144. https://doi.org/10.1016/j.solmat.2017.07.028.
[233] X. Yu, J. Kang, R. Zhang, M. Takenaka, S. Takagi, Characterization of ultrathin-body Germanium-on-insulator (GeOI) structures and MOSFETs on flipped Smart-Cut^{TM} GeOI substrates, Solid-State Electron. 115 (2016) 120–125. https://doi.org/10.1016/j.sse.2015.08.021.
[234] B. Fang, Z. Zeng, X. Yan, Z. Hu, Effects of annealing on thermoelectric properties of Sb2Te3 thin films prepared by radio frequency magnetron sputtering, J. Mater. Sci. Mater. Electron. 24 (2013) 1105–1111. https://doi.org/10.1007/s10854-012-0888-1.
[235] K.A. Kokh, V.V. Atuchin, T.A. Gavrilova, N.V. Kuratieva, N.V. Pervukhina, N.V. Surovtsev, Microstructural and vibrational properties of PVT grown Sb2Te3 crystals, Solid State Commun. 177 (2014) 16–19. https://doi.org/10.1016/j.ssc.2013.09.016.
[236] J.E. Boschker, R. Wang, R. Calarco, GeTe: a simple compound blessed with a plethora of properties, CrystEngComm. 19 (2017) 5324–5335. https://doi.org/10.1039/C7CE01040K.
[237] W.C. Johnson, NITROGEN COMPOUNDS OF GERMANIUM. I. THE PREPARATION AND PROPERTIES OF GERMANIC NITRIDE, J. Am. Chem. Soc. 52 (1930) 5160–5165. https://doi.org/10.1021/ja01375a078.
[238] P.V. Pavlov, E.I. Zorin, D.I. Tetelbaum, A.F. Khokhlov, Nitrogen as dopant in silicon and germanium, Phys. Status Solidi A. 35 (1976) 11–36. https://doi.org/10.1002/pssa.2210350102.
[239] M.I. Baraton, R. Marchand, P. Quintard, Comparative infrared study of silicon and germanium nitrides, J. Mol. Struct. 143 (1986) 9–12. https://doi.org/10.1016/0022-2860(86)85192-4.
[240] F. Boscherini, A. Filipponi, S. Pascarelli, F. Evangelisti, S. Mobilio, F.C. Marques, I. Chambouleyron, Short-range order in amorphous germanium-nitrogen alloys studied by extended x-ray-absorption fine-structure spectroscopy, Phys. Rev. B. 39 (1989) 8364–8370. https://doi.org/10.1103/PhysRevB.39.8364.
[241] S.S. Makler, G. Martins da Rocha, E.V. Anda, Electronic structure of *a* - Si 1 − x N x :H and *a* - Ge 1 − x N x :H, Phys. Rev. B. 41 (1990) 5857–5870. https://doi.org/10.1103/PhysRevB.41.5857.
[242] I. Chambouleyron, A.R. Zanatta, Nitrogen in germanium, J. Appl. Phys. 84 (1998) 1–30. https://doi.org/10.1063/1.368612.

[243] M. Yang, S.J. Wang, Y.P. Feng, G.W. Peng, Y.Y. Sun, Electronic structure of germanium nitride considered for gate dielectrics, J. Appl. Phys. 102 (2007) 013507. https://doi.org/10.1063/1.2747214.
[244] R.R. Lieten, S. Degroote, M. Kuijk, G. Borghs, Crystalline Ge_3N_4 on Ge(111), Appl. Phys. Lett. 91 (2007) 222110. https://doi.org/10.1063/1.2818679.
[245] G. Maggioni, S. Carturan, L. Fiorese, N. Pinto, F. Caproli, D.R. Napoli, M. Giarola, G. Mariotto, Germanium nitride and oxynitride films for surface passivation of Ge radiation detectors, Appl. Surf. Sci. 393 (2017) 119–126. https://doi.org/10.1016/j.apsusc.2016.10.006.
[246] K. Sardashti, K.-T. Hu, K. Tang, S. Madisetti, P. McIntyre, S. Oktyabrsky, S. Siddiqui, B. Sahu, N. Yoshida, J. Kachian, L. Dong, B. Fruhberger, A.C. Kummel, Nitride passivation of the interface between high-k dielectrics and SiGe, Appl. Phys. Lett. 108 (2016) 011604. https://doi.org/10.1063/1.4939460.
[247] L. Lian, Y. Liu, D. Li, S. Wei, High-pressure formation of antimony nitrides: a first-principles study, RSC Adv. 10 (2020) 2448–2452. https://doi.org/10.1039/C9RA09438E.
[248] B. Lyhs, D. Bläser, C. Wölper, S. Schulz, Syntheses and X-ray Crystal Structures of Organoantimony Diazides, Chem. - Eur. J. 17 (2011) 4914–4920. https://doi.org/10.1002/chem.201002730.
[249] R. Haiges, A. Vij, J.A. Boatz, S. Schneider, T. Schroer, M. Gerken, K.O. Christe, First Structural Characterization of Binary AsIII and SbIII Azides, Chem. - Eur. J. 10 (2004) 508–517. https://doi.org/10.1002/chem.200305482.
[250] A. Sharan, S. Lany, Computational discovery of stable and metastable ternary oxynitrides, J. Chem. Phys. 154 (2021) 234706. https://doi.org/10.1063/5.0050356.
[251] Q. Sun, W.-J. Li, Z.-W. Fu, A novel anode material of antimony nitride for rechargeable lithium batteries, Solid State Sci. 12 (2010) 397–403. https://doi.org/10.1016/j.solidstatesciences.2009.12.003.
[252] N. Pereira, M. Balasubramanian, L. Dupont, J. McBreen, L.C. Klein, G.G. Amatucci, The Electrochemistry of Germanium Nitride with Lithium, J. Electrochem. Soc. 150 (2003) A1118. https://doi.org/10.1149/1.1587724.
[253] N.S. Shaikh, S.B. Ubale, V.J. Mane, Jasmin.S. Shaikh, Vaibhav.C. Lokhande, S. Praserthdam, C.D. Lokhande, P. Kanjanaboos, Novel electrodes for supercapacitor: Conducting polymers, metal oxides, chalcogenides, carbides, nitrides, MXenes, and their composites with graphene, J. Alloys Compd. 893 (2022) 161998. https://doi.org/10.1016/j.jallcom.2021.161998.
[254] H.W. Roesky, J. Münzenberg, M. Noltemeyer, Synthesis and Structure of the Stable Tellurium Nitride$(ClTeNSN)_3N$, Angew. Chem. Int. Ed. Engl. 29 (1990) 61–63. https://doi.org/10.1002/anie.199000611.
[255] M. Bjorgvinsson, H.W. Roesky, The structures of compounds containing selenium-nitrogen and tellurium-nitrogen bonds, Polyhedron. 10 (1991) 2353–2370. https://doi.org/10.1016/S0277-5387(00)86196-3.
[256] H. Hartl, P. Huppmann, D. Lentz, K. Seppelt, Tellurium-nitrogen compounds, Inorg. Chem. 22 (1983) 2183–2187. https://doi.org/10.1021/ic00157a017.
[257] A. Haas, J. Kasprowski, M. Pryka, Tellurium— and selenium—nitrogen compounds: preparation, characterization and properties, Coord. Chem. Rev. 130 (1994) 301–353. https://doi.org/10.1016/0010-8545(94)80008-1.
[258] R. Haiges, J.A. Boatz, A. Vij, M. Gerken, S. Schneider, T. Schroer, K.O. Christe, Polyazide Chemistry: Preparation and Characterization of $Te(N_3)_4$ and$[P(C_6H_5)_4]_2[Te(N_3)_6]$ and Evidence for$[N(CH_3)_4][Te(N_3)_5]$, Angew. Chem. Int. Ed. 42 (2003) 5847–5851. https://doi.org/10.1002/anie.200352680.

[259] Z. Liu, D. Li, Q. Zhuang, F. Tian, D. Duan, F. Li, T. Cui, Formation mechanism of insensitive tellurium hexanitride with armchair-like cyclo-N_6 anions, Commun. Chem. 3 (2020) 42. https://doi.org/10.1038/s42004-020-0286-1.
[260] T.M. Klapötke, B. Krumm, P. Mayer, I. Schwab, Binary Tellurium(IV) Azides: $Te(N_3)_4$ and$[Te(N_3)_5]$-, Angew. Chem. Int. Ed. 42 (2003) 5843–5846. https://doi.org/10.1002/anie.200352656.
[261] T. Chivers, R.S. Laitinen, Neutral binary chalcogen–nitrogen and ternary S,N,P molecules: new structures, bonding insights and potential applications, Dalton Trans. 49 (2020) 6532–6547. https://doi.org/10.1039/D0DT00807A.
[262] J.-H. Lin, H. Zhang, X.-L. Cheng, Y. Miyamoto, Two-dimensional wide-band-gap nitride semiconductors: Single-layer $1T{-}XN_2$ (X = S , Se , and Te), Phys. Rev. B. 94 (2016) 195404. https://doi.org/10.1103/PhysRevB.94.195404.
[263] W. Sun, C.J. Bartel, E. Arca, S.R. Bauers, B. Matthews, B. Orvañanos, B.-R. Chen, M.F. Toney, L.T. Schelhas, W. Tumas, J. Tate, A. Zakutayev, S. Lany, A.M. Holder, G. Ceder, A map of the inorganic ternary metal nitrides, Nat. Mater. 18 (2019) 732–739. https://doi.org/10.1038/s41563-019-0396-2.
[264] The Materials Project, Materials Data on TeN2 by Materials Project, (2020). https://doi.org/10.17188/1318971.
[265] E. Nolot, C. Sabbione, W. Pessoa, L. Prazakova, G. Navarro, Germanium, antimony, tellurium, their binary and ternary alloys and the impact of nitrogen: An X-ray photoelectron study, Appl. Surf. Sci. 536 (2021) 147703. https://doi.org/10.1016/j.apsusc.2020.147703.
[266] D. Dimitrov, H.-P.D. Shieh, The influence of oxygen and nitrogen doping on GeSbTe phase-change optical recording media properties, Mater. Sci. Eng. B. 107 (2004) 107–112. https://doi.org/10.1016/j.mseb.2003.10.110.
[267] L. Cheng, L. Wu, Z. Song, F. Rao, C. Peng, D. Yao, B. Liu, L. Xu, Effects of germanium and nitrogen incorporation on crystallization of N-doped $Ge_{2+x}Sb_2Te_5$ (x = 0,1) thin films for phase-change memory, J. Appl. Phys. 113 (2013) 044514. https://doi.org/10.1063/1.4789388.
[268] S. Niu, Z. Wei, X. Fang, D. Wang, X. Wang, X. Gao, R. Chen, Brief Review of Epitaxy and Emission Properties of GaSb and Related Semiconductors, Crystals. 7 (2017) 337. https://doi.org/10.3390/cryst7110337.
[269] J. Buckeridge, D.O. Scanlon, T.D. Veal, M.J. Ashwin, A. Walsh, C.R.A. Catlow, N incorporation and associated localized vibrational modes in GaSb, Phys. Rev. B. 89 (2014) 014107. https://doi.org/10.1103/PhysRevB.89.014107.
[270] P. Jadaun, H.P. Nair, V. Lordi, S.R. Bank, S.K. Banerjee, Electronic and optical properties of GaSb:N from first principles, ArXiv13080363 Cond-Mat. (2014). http://arxiv.org/abs/1308.0363 (accessed January 31, 2022).
[271] R. Kudrawiec, D. Hommel, Bandgap engineering in III-nitrides with boron and group V elements: Toward applications in ultraviolet emitters, Appl. Phys. Rev. 7 (2020) 041314. https://doi.org/10.1063/5.0025371.
[272] F.A. Chowdhury, M.L. Trudeau, R. Wang, H. Guo, Z. Mi, Dilute-antimonide GaSbN/GaN dots-in-wire heterostructures grown by molecular beam epitaxy: Structural and optical properties, Appl. Phys. Lett. 118 (2021) 012101. https://doi.org/10.1063/5.0029761.
[273] J.S. Lannin, N. Maley, S.T. Kshirsagar, Raman scattering and short range order in amorphous germanium, Solid State Commun. 53 (1985) 939–942. https://doi.org/10.1016/0038-1098(85)90464-8.
[274] P.A. Temple, C.E. Hathaway, Multiphonon Raman Spectrum of Silicon, Phys. Rev. B. 7 (1973) 3685–3697. https://doi.org/10.1103/PhysRevB.7.3685.

[275] A. Zwick, R. Carles, Multiple-order Raman scattering in crystalline and amorphous silicon, Phys. Rev. B. 48 (1993) 6024–6032. https://doi.org/10.1103/PhysRevB.48.6024.
[276] J.B. Renucci, W. Richter, M. Cardona, E. SchÖstherr, Resonance raman scattering in group Vb semimetals: As, Sb, and Bi, Phys. Status Solidi B. 60 (1973) 299–308. https://doi.org/10.1002/pssb.2220600133.
[277] W. Leng, Y. Chen, Q. Zhang, L. Sun, X. Shen, R. Wang, G. Wang, J.-Q. Wang, T. Xu, Crystallization kinetics of monatomic antimony, Appl. Phys. Lett. 119 (2021) 171908. https://doi.org/10.1063/5.0064662.
[278] R. Hunger, N. Blick, N. Esser, M. Arens, W. Richter, V. Wagner, J. Geurts, Growth of Sb on Si(111) studied by Raman scattering, Surf. Sci. 307–309 (1994) 1061–1065. https://doi.org/10.1016/0039-6028(94)91540-7.
[279] Y. Hu, X. Zhu, H. Zou, J. Zhang, L. Yuan, J. Xue, Y. Sui, W. Wu, S. Song, Z. Song, Improved thermal stability of N-doped Sb materials for high-speed phase change memory application, Appl. Phys. Lett. 108 (2016) 223103. https://doi.org/10.1063/1.4953194.
[280] Y. Huang, W. Wu, S. Xu, X. Zhu, S. Song, Z. Song, Thickness effect on the crystallization characteristic of RF sputtered Sb thin films, J. Mater. Sci. Mater. Electron. 32 (2021) 24240–24247. https://doi.org/10.1007/s10854-021-06889-0.
[281] M. Mayo, E. Yahel, Y. Greenberg, G. Makov, Short range order in liquid pnictides, J. Phys. Condens. Matter. 25 (2013) 505102. https://doi.org/10.1088/0953-8984/25/50/505102.
[282] J. Buckeridge, D.O. Scanlon, T.D. Veal, M.J. Ashwin, A. Walsh, C.R.A. Catlow, N incorporation and associated localized vibrational modes in GaSb, Phys. Rev. B. 89 (2014) 014107. https://doi.org/10.1103/PhysRevB.89.014107.
[283] T. Shiraishi, Y. Arai, S. Yamazaki, Optical and electrical properties on transparency a-SbN films, J. Non-Cryst. Solids. 77–78 (1985) 1313–1316. https://doi.org/10.1016/0022-3093(85)90900-7.
[284] G. Lucovsky, R.C. Keezer, E. Burstein, Infra-red lattice bands of trigonal tellurium and selenium, Solid State Commun. 5 (1967) 439–445. https://doi.org/10.1016/0038-1098(67)90589-3.
[285] G. Lucovsky, A comparison of the long wave optical phonons in trigonal Se and trigonal Te, Phys. Status Solidi B. 49 (1972) 633–641. https://doi.org/10.1002/pssb.2220490226.
[286] Y. Dimitriev, V. Dimitrov, M. Arnaudov, IR spectra and structures of tellurite glasses, J. Mater. Sci. 18 (1983) 1353–1358. https://doi.org/10.1007/BF01111954.
[287] R.A. El-Mallawany, Theoretical and experimental IR spectra of binary rare earth tellurite glasses—1, Infrared Phys. 29 (1989) 781–785. https://doi.org/10.1016/0020-0891(89)90125-5.
[288] A.S. Pine, G. Dresselhaus, Raman Spectra and Lattice Dynamics of Tellurium, Phys. Rev. B. 4 (1971) 356–371. https://doi.org/10.1103/PhysRevB.4.356.
[289] M.H. Brodsky, R.J. Gambino, J.E. Smith, Y. Yacoby, The Raman Spectrum of Amorphous Tellurium, Phys. Status Solidi B. 52 (1972) 609–614. https://doi.org/10.1002/pssb.2220520229.
[290] Larkin, Peter, Infrared and Raman Spectroscopy, Elsevier, 2011. https://doi.org/10.1016/C2010-0-68479-3.
[291] H. Ikemoto, T. Miyanaga, Local structure of amorphous tellurium studied by EXAFS, J. Synchrotron Radiat. 21 (2014) 409–412. https://doi.org/10.1107/S1600577513032748.

[292] O. Peña, Chevrel phases: Past, present and future, Phys. C Supercond. Its Appl. 514 (2015) 95–112. https://doi.org/10.1016/j.physc.2015.02.019.
[293] Y. Kim, M.H. Jang, K. Jeong, M.-H. Cho, K.H. Do, D.-H. Ko, H.C. Sohn, M.G. Kim, Investigation of phase transition of Ge2Sb2Te5 and N-incorporated Ge2Sb2Te5 films using x-ray absorption spectroscopy, Appl. Phys. Lett. 92 (2008) 061910. https://doi.org/10.1063/1.2844878.
[294] J.M. Charnock, K.E.R. England, C.M.B. Henderson, J.F.W. Mosselmans, R.A.D. Pattrick, An XAS Study of the Semi-Conducting Sulfides M_2S_3 (M = As, Sb, Bi), J. Phys. IV. 7 (1997) C2-1137-C2-1138. https://doi.org/10.1051/jp4:19972161.
[295] G. Kresse, J. Furthmüller, Efficient iterative schemes for *ab initio* total-energy calculations using a plane-wave basis set, Phys. Rev. B. 54 (1996) 11169–11186. https://doi.org/10.1103/PhysRevB.54.11169.
[296] G. Kresse, D. Joubert, From ultrasoft pseudopotentials to the projector augmented-wave method, Phys. Rev. B. 59 (1999) 1758–1775. https://doi.org/10.1103/PhysRevB.59.1758.
[297] J.M. Skelton, L.A. Burton, A.J. Jackson, F. Oba, S.C. Parker, A. Walsh, Lattice dynamics of the tin sulphides SnS_2, SnS and Sn_2S_3: vibrational spectra and thermal transport, Phys. Chem. Chem. Phys. 19 (2017) 12452–12465. https://doi.org/10.1039/C7CP01680H.
[298] Materials Data on Ge3N4 (mp-13852), SbN (mp-1271276) and TeN2 (mvc-13772) structures by Materials Project; https://materialsproject.org/, Materials Data on Ge3N4 (mp-13852), SbN (mp-1271276) and TeN2 (mvc-13772) structures by Materials Project, (2020). https://materialsproject.org/materials/mp-13852/; https://materialsproject.org/materials/mp-1271276/; https://materialsproject.org/materials/mvc-13772/.
[299] Materials Data on Ge (mp-32), Sb (mp-104) and Te (mp-19) structures by Materials Project, Materials Data on Ge (mp-32), Sb (mp-104) and Te (mp-19) structures by Materials Project, (2022). https://materialsproject.org/materials/mp-32/; https://materialsproject.org/materials/mp-104/; https://materialsproject.org/materials/mp-19/.
[300] J.P. Perdew, K. Burke, M. Ernzerhof, Generalized Gradient Approximation Made Simple, Phys. Rev. Lett. 77 (1996) 3865–3868. https://doi.org/10.1103/PhysRevLett.77.3865.
[301] P. Popper, S.N. Ruddlesden, Structure of the Nitrides of Silicon and Germanium, Nature. 179 (1957) 1129–1129. https://doi.org/10.1038/1791129b0.
[302] W.C. Johnson, G.H. Ridgely, Nitrogen Compounds of Germanium. V. Germanous Nitride, J. Am. Chem. Soc. 56 (1934) 2395–2397. https://doi.org/10.1021/ja01326a051.
[303] F. Arnaud, P. Zuliani, J.P. Reynard, A. Gandolfo, F. Disegni, P. Mattavelli, E. Gomiero, G. Samanni, C. Jahan, R. Berthelon, O. Weber, E. Richard, V. Barral, A. Villaret, S. Kohler, J.C. Grenier, R. Ranica, C. Gallon, A. Souhaite, D. Ristoiu, L. Favennec, V. Caubet, S. Delmedico, N. Cherault, R. Beneyton, S. Chouteau, P.O. Sassoulas, A. Vernhet, Y.L. Friec, F. Domengie, L. Scotti, D. Pacelli, J.L. Ogier, F. Boucard, S. Lagrasta, D. Benoit, L. Clement, P. Boivin, P. Ferreira, R. Annunziata, P. Cappelletti, Truly Innovative 28nm FDSOI Technology for Automotive Micro-Controller Applications embedding 16MB Phase Change Memory, in: 2018 IEEE Int. Electron Devices Meet. IEDM, 2018: p. 18.4.1-18.4.4. https://doi.org/10.1109/IEDM.2018.8614595.
[304] F. Katsuki, K. Hanafusa, M. Yonemura, T. Koyama, M. Doi, Crystallization of amorphous germanium in an Al/a-Ge bilayer film deposited on a SiO_2 substrate, J. Appl. Phys. 89 (2001) 4643–4647. https://doi.org/10.1063/1.1359149.

[305] A.F. Khan, M. Mehmood, A.M. Rana, T. Muhammad, Effect of annealing on structural, optical and electrical properties of nanostructured Ge thin films, Appl. Surf. Sci. 256 (2010) 2031–2037. https://doi.org/10.1016/j.apsusc.2009.09.043.
[306] Q. Tao, N. Chen, C. Wang, M. Dayan, Y. Bai, J. Chen, Characterization and mechanism of crystallization of Ge films on silicon substrate with graphite buffer layer, Mater. Sci. Semicond. Process. 84 (2018) 167–170. https://doi.org/10.1016/j.mssp.2018.05.011.
[307] C.-Y. Tsao, J.W. Weber, P. Campbell, P.I. Widenborg, D. Song, M.A. Green, Low-temperature growth of polycrystalline Ge thin film on glass by in situ deposition and ex situ solid-phase crystallization for photovoltaic applications, Appl. Surf. Sci. 255 (2009) 7028–7035. https://doi.org/10.1016/j.apsusc.2009.03.035.
[308] E.I. Voit, A.E. Panasenko, L.A. Zemnukhova, Vibrational spectroscopic and quantum chemical study of antimony(III) oxide, J. Struct. Chem. 50 (2009) 60–66. https://doi.org/10.1007/s10947-009-0008-0.
[309] K. Kaviyarasu, D. Sajan, P.A. Devarajan, A rapid and versatile method for solvothermal synthesis of Sb_2O_3 nanocrystals under mild conditions, Appl. Nanosci. 3 (2013) 529–533. https://doi.org/10.1007/s13204-012-0156-y.
[310] D.A. Young, Phase diagrams of the elements, 1975. https://doi.org/10.2172/4010212.
[311] J. Akola, R.O. Jones, S. Kohara, T. Usuki, E. Bychkov, Density variations in liquid tellurium: Roles of rings, chains, and cavities, Phys. Rev. B. 81 (2010) 094202. https://doi.org/10.1103/PhysRevB.81.094202.
[312] P. Němec, A. Moreac, V. Nazabal, M. Pavlišta, J. Přikryl, M. Frumar, Ge–Sb–Te thin films deposited by pulsed laser: An ellipsometry and Raman scattering spectroscopy study, J. Appl. Phys. 106 (2009) 103509. https://doi.org/10.1063/1.3259435.
[313] L. Prazakova, E. Nolot, E. Martinez, F. Fillot, D. Rouchon, N. Rochat, M. Bernard, C. Sabbione, D. Morel, N. Bernier, A. Grenier, A.-M. Papon, M.-C. Cyrille, G. Navarro, Temperature driven structural evolution of Ge-rich GeSbTe alloys and role of N-doping, J. Appl. Phys. 128 (2020) 215102. https://doi.org/10.1063/5.0027734.
[314] H. Jamali, R. Mozafarinia, A. Eshaghi, Evaluation of chemical and structural properties of germanium-carbon coatings deposited by plasma enhanced chemical vapor deposition, J. Alloys Compd. 646 (2015) 360–367. https://doi.org/10.1016/j.jallcom.2015.06.091.
[315] H. Jamali, R. Mozafarinia, A. Eshaghi, The effect of carbon content on the phase structure of amorphous/nanocrystalline $Ge_{1-x}C_x$ films prepared by PECVD, Surf. Coat. Technol. 310 (2017) 1–7. https://doi.org/10.1016/j.surfcoat.2016.12.043.
[316] B. Liu, S. Zhi-Tang, Z. Ting, F. Song-Lin, C. Bomy, Raman spectra and XPS studies of phase changes in $Ge_2Sb_2Te_5$ films, Chin. Phys. 13 (2004) 1947–1950. https://doi.org/10.1088/1009-1963/13/11/033.
[317] H.R. Philipp, Optical and bonding model for non-crystalline SiO_x and SiO_xN_y materials, J. Non-Cryst. Solids. 8–10 (1972) 627–632. https://doi.org/10.1016/0022-3093(72)90202-5.
[318] L. Prazakova, E. Nolot, E. Martinez, D. Rouchon, F. Fillot, N. Bernier, R. Elizalde, M. Bernard, G. Navarro, The Effect of Ge Content on Structural Evolution of Ge-rich GeSbTe Alloys at Increasing Temperature, Materialia. (2022) 101345. https://doi.org/10.1016/j.mtla.2022.101345.
[319] J.-J. Wang, Y.-Z. Xu, R. Mazzarello, M. Wuttig, W. Zhang, A Review on Disorder-Driven Metal–Insulator Transition in Crystalline Vacancy-Rich GeSbTe Phase-Change Materials, Materials. 10 (2017) 862. https://doi.org/10.3390/ma10080862.

[320] E. Carria, A.M. Mio, S. Gibilisco, M. Miritello, C. Bongiorno, M.G. Grimaldi, E. Rimini, Amorphous-Crystal Phase Transitions in $Ge_x Te_{1-x}$ Alloys, J. Electrochem. Soc. 159 (2011) H130–H139. https://doi.org/10.1149/2.048202jes.
[321] A. Debunne, K. Virwani, A. Padilla, G.W. Burr, A.J. Kellock, V.R. Deline, R.M. Shelby, B. Jackson, Evidence of Crystallization–Induced Segregation in the Phase Change Material Te-Rich GST, J. Electrochem. Soc. 158 (2011) H965. https://doi.org/10.1149/1.3614508.
[322] W. Knaepen, S. Gaudet, C. Detavernier, R.L. Van Meirhaeghe, J.J. Sweet, C. Lavoie, *In situ* x-ray diffraction study of metal induced crystallization of amorphous germanium, J. Appl. Phys. 105 (2009) 083532. https://doi.org/10.1063/1.3110722.
[323] T.C. Chong, L.P. Shi, R. Zhao, P.K. Tan, J.M. Li, H.K. Lee, X.S. Miao, A.Y. Du, C.H. Tung, Phase change random access memory cell with superlattice-like structure, Appl. Phys. Lett. 88 (2006) 122114. https://doi.org/10.1063/1.2181191.
[324] D. Loke, L. Shi, W. Wang, R. Zhao, H. Yang, L.-T. Ng, K.-G. Lim, T.-C. Chong, Y.-C. Yeo, Ultrafast switching in nanoscale phase-change random access memory with superlattice-like structures, Nanotechnology. 22 (2011) 254019. https://doi.org/10.1088/0957-4484/22/25/254019.
[325] R.E. Simpson, P. Fons, A.V. Kolobov, T. Fukaya, M. Krbal, T. Yagi, J. Tominaga, Interfacial phase-change memory, Nat. Nanotechnol. 6 (2011) 501–505. https://doi.org/10.1038/nnano.2011.96.
[326] J. Momand, R. Wang, J.E. Boschker, M.A. Verheijen, R. Calarco, B.J. Kooi, Interface formation of two- and three-dimensionally bonded materials in the case of GeTe–Sb_2Te_3 superlattices, Nanoscale. 7 (2015) 19136–19143. https://doi.org/10.1039/C5NR04530D.
[327] X.-B. Li, N.-K. Chen, X.-P. Wang, H.-B. Sun, Phase-Change Superlattice Materials toward Low Power Consumption and High Density Data Storage: Microscopic Picture, Working Principles, and Optimization, Adv. Funct. Mater. 28 (2018) 1803380. https://doi.org/10.1002/adfm.201803380.
[328] Y. Huang, F. Liu, Y. Zhang, W. Li, G. Han, N. Sun, F. Liu, Effects of biaxial strain on interfacial intermixing and local structures in strain engineered GeTe-Sb_2Te_3 superlattices, Appl. Surf. Sci. 493 (2019) 904–912. https://doi.org/10.1016/j.apsusc.2019.07.069.
[329] S. Cecchi, E. Zallo, J. Momand, R. Wang, B.J. Kooi, M.A. Verheijen, R. Calarco, Improved structural and electrical properties in native $Sb_2Te_3/Ge_x Sb_2Te_{3+x}$ van der Waals superlattices due to intermixing mitigation, APL Mater. 5 (2017) 026107. https://doi.org/10.1063/1.4976828.
[330] Y. Hu, H. Zou, J. Zhang, J. Xue, Y. Sui, W. Wu, L. Yuan, X. Zhu, S. Song, Z. Song, $Ge_2Sb_2Te_5$/Sb superlattice-like thin film for high speed phase change memory application, Appl. Phys. Lett. 107 (2015) 263105. https://doi.org/10.1063/1.4939149.
[331] L. Zheng, X. Zhu, L. Zhai, Y. Hu, H. Zou, B. Liu, M. Pei, Z. Song, Interface effect and stress effect on $Ge_2Sb_2Te_5$/Sb superlattice-like thin films, Eur. Phys. J. Appl. Phys. 77 (2017) 30102. https://doi.org/10.1051/epjap/2017160397.
[332] J. Secor, M.A. Harris, L. Zhao, H. Deng, S. Raoux, L. Krusin-Elbaum, Phonon renormalization and Raman spectral evolution through amorphous to crystalline transitions in Sb_2Te_3 thin films, Appl. Phys. Lett. 104 (2014) 221908. https://doi.org/10.1063/1.4881937.
[333] V. Chis, I.Yu. Sklyadneva, K.A. Kokh, V.A. Volodin, O.E. Tereshchenko, E.V. Chulkov, Vibrations in binary and ternary topological insulators: First-principles calculations and Raman spectroscopy measurements, Phys. Rev. B. 86 (2012) 174304. https://doi.org/10.1103/PhysRevB.86.174304.

[334] W.J. Yang, H. Park, D.S. Kim, T. Ha, S.J. Park, M. Ahn, J.H. Kim, Y.-K. Kwon, M.-H. Cho, Phase-change like process through bond switching in distorted and resonantly bonded crystal, Sci. Rep. 9 (2019) 12816. https://doi.org/10.1038/s41598-019-49270-2.
[335] J.B. Renucci, W. Richter, M. Cardona, E. SchÖstherr, Resonance raman scattering in group Vb semimetals: As, Sb, and Bi, Phys. Status Solidi B. 60 (1973) 299–308. https://doi.org/10.1002/pssb.2220600133.
[336] K.M.F. Shahil, M.Z. Hossain, V. Goyal, A.A. Balandin, Micro-Raman spectroscopy of mechanically exfoliated few-quintuple layers of Bi_2Te_3, Bi_2Se_3 , and Sb_2Te_3 materials, J. Appl. Phys. 111 (2012) 054305. https://doi.org/10.1063/1.3690913.
[337] P.S. Prevéy, X-ray Diffraction Residual Stress Techniques, Met. Handb. 10 Met. Park Am. Soc. Met. (1986) 380–392.
[338] P. Hoff, J.P. Omtvedt, B. Fogelberg, H. Mach, M. Hellström, The Z = 52 and N = 84 nucleus 136 Te: Low spin states observed in the decay of 136 Sb, Phys. Rev. C. 56 (1997) 2865–2868. https://doi.org/10.1103/PhysRevC.56.2865.
[339] D.C. Bobela, P.C. Taylor, Nuclear Magnetic Resonance Studies of Tellurium and Antimony Bonding in Crystal Sb_2Te_3, GeTe, and $Ge_2Sb_2Te_5$, Jpn. J. Appl. Phys. 47 (2008) 8162–8165. https://doi.org/10.1143/JJAP.47.8162.
[340] D.C. Bobela, P.C. Taylor, Tellurium bonding in amorphous $Ge_2Sb_2Te_4$, $Ge_2Sb_2Te_5$ and $Ge_2Sb_2Te_7$: A 125Te NMR investigation, J. Non-Cryst. Solids. 354 (2008) 2665–2668. https://doi.org/10.1016/j.jnoncrysol.2007.09.052.
[341] C. Hu, L. Ma, X. Li, Z. Liu, M. Cui, Y. Li, S. Li, X. Cao, Y. Zhang, J. Zhu, X. Wang, W. Zheng, Full-color, multi-level transmittance modulators: From reflectivity/gradient absorption coupling mechanism to materials map, Acta Mater. 216 (2021) 117132. https://doi.org/10.1016/j.actamat.2021.117132.
[342] J.R. Ferraro, K. Nakamoto, C.W. Brown, Introductory Raman spectroscopy, 2nd ed, Academic Press, Amsterdam ; Boston, 2003.
[343] J.M. Chalmers, P.R. Griffiths, eds., Handbook of Vibrational Spectroscopy: Chalmers Vibrat 5V Set, John Wiley & Sons, Ltd, Chichester, UK, 2001. https://doi.org/10.1002/0470027320.
[344] P.R. Griffiths, J.A. De Haseth, Fourier transform infrared spectrometry, 2nd ed, Wiley-Interscience, Hoboken, N.J, 2007.
[345] I.R. Lewis, H.G.M. Edwards, eds., Handbook of Raman spectroscopy: from the research laboratory to the process line, Marcel Dekker, New York, 2001.
[346] E. Smith, G. Dent, Modern Raman spectroscopy: a practical approach, Second edition, Wiley, Hoboken, NJ, 2019.
[347] K. Babooram, Brief overview of polymer science, in: Polym. Sci. Nanotechnol., Elsevier, 2020: pp. 3–12. https://doi.org/10.1016/B978-0-12-816806-6.00001-7.
[348] M. Grundmann, The Physics of Semiconductors: An Introduction Including Nanophysics and Applications, Springer International Publishing, Cham, 2016. https://doi.org/10.1007/978-3-319-23880-7.
[349] V.K. Pecharsky, P.Y. Zavalij, Fundamentals of powder diffraction and structural characterization of materials, Springer, New York, 2005.
[350] D. Kriegner, Z. Matěj, R. Kužel, V. Holý, Powder diffraction in Bragg–Brentano geometry with straight linear detectors, J. Appl. Crystallogr. 48 (2015) 613–618. https://doi.org/10.1107/S1600576715003465.
[351] The Materials Project, Materials Data by Materials Project, (2020). https://materialsproject.org/ (accessed August 17, 2021).
[352] A. Jain, S.P. Ong, G. Hautier, W. Chen, W.D. Richards, S. Dacek, S. Cholia, D. Gunter, D. Skinner, G. Ceder, K.A. Persson, Commentary: The Materials Project: A

materials genome approach to accelerating materials innovation, APL Mater. 1 (2013) 011002. https://doi.org/10.1063/1.4812323.
[353] S. Caravati, M. Bernasconi, M. Parrinello, First-principles study of liquid and amorphous Sb 2 Te 3, Phys. Rev. B. 81 (2010) 014201. https://doi.org/10.1103/PhysRevB.81.014201.
[354] W. Richter, C.R. Becker, A Raman and far-infrared investigation of phonons in the rhombohedral V2–VI3 compounds Bi2Te3, Bi2Se3, Sb2Te3 and Bi2(Te1−xSex)3 (0 <x < 1), (Bi1−ySby)2Te3 (0 <y < 1), Phys. Status Solidi B. 84 (1977) 619–628. https://doi.org/10.1002/pssb.2220840226.
[355] G.C. Sosso, S. Caravati, M. Bernasconi, Vibrational properties of crystalline Sb_2Te_3 from first principles, J. Phys. Condens. Matter. 21 (2009) 095410. https://doi.org/10.1088/0953-8984/21/9/095410.
[356] J. Secor, M.A. Harris, L. Zhao, H. Deng, S. Raoux, L. Krusin-Elbaum, Phonon renormalization and Raman spectral evolution through amorphous to crystalline transitions in Sb_2Te_3 thin films, Appl. Phys. Lett. 104 (2014) 221908. https://doi.org/10.1063/1.4881937.
[357] G. Wang, C. Li, D. Shi, Y. Zhang, X. Shen, Laser-induced metastable phase in crystalline phase-change films by confocal Raman spectrometer, Spectrochim. Acta. A. Mol. Biomol. Spectrosc. 205 (2018) 551–556. https://doi.org/10.1016/j.saa.2018.07.077.
[358] Y. Zheng, M. Xia, Y. Cheng, F. Rao, K. Ding, W. Liu, Y. Jia, Z. Song, S. Feng, Direct observation of metastable face-centered cubic Sb2Te3 crystal, Nano Res. 9 (2016) 3453–3462. https://doi.org/10.1007/s12274-016-1221-8.
[359] Z. Wu, X. Chen, E. Mu, Y. Liu, Z. Che, C. Dun, F. Sun, X. Wang, Y. Zhang, Z. Hu, Lattice Strain Enhances Thermoelectric Properties in Sb_2Te_3 /Te Heterostructure, Adv. Electron. Mater. 6 (2020) 1900735. https://doi.org/10.1002/aelm.201900735.
[360] P. Kazimierski, J. Tyczkowski, M. Kozanecki, Y. Hatanaka, T. Aoki, Transition from Amorphous Semiconductor to Amorphous Insulator in Hydrogenated Carbon−Germanium Films Investigated by Raman Spectroscopy, Chem. Mater. 14 (2002) 4694–4701. https://doi.org/10.1021/cm020428s.

List of publications

Conferences:

[1] **L. Prazakova** et al., Temperature-Driven Structural Evolution of Ge-rich GeSbTe Alloys and Role of N-doping, *European Phase-Change and Ovonic Symposium (E\PCOS)*, 2021.

[2] **L. Prazakova** et al., Ge-rich GeSbTe Phase-Change Alloys: Thorough Investigation of Temperature-Driven Structural Evolution, *Pacific Rim Meeting on Electrochemical and Solid State Science (PRiME)*, 2020

[3] **L. Prazakova** et al., Structural investigation of N-doping Effects in Ge-rich Ge-Sb-Te System for Phase-Change Memory, *European Materials Research Society (E-MRS)*, 2019.

[4] **L. Prazakova** et al., N-doped Ge and Ge-rich Ge-Sb-Te Systems: Structural Investigation by Infrared and Raman Spectroscopy, *European Phase-Change and Ovonic Symposium (E\PCOS)*, 2019.

Journal articles

[1] **L. Prazakova** et al., Understanding the N-doping Effect in Phase-Change Materials: Spectroscopic Study of N-doped Ge, Sb and Te *(submitted).*

[2] C. Laguna, ..., **L. Prazakova**,... et al., "Ge Content Impact in $Ge_x(SbSe)_{1-x}N$ for Improved Reliability in Ovonic Threshold Switching Devices" (*under redaction*).

[3] **L. Prazakova**, et al., The Effect of Ge Content on Structural Evolution of Ge-rich GeSbTe Alloys at Increasing Temperature, *Materialia.* (2022) 101345. https://doi.org/10.1016/j.mtla.2022.101345

[4] E. Nolot, ..., **L. Prazakova**, ..., et al., Germanium, Antimony, Tellurium, Their Binary and Ternary Alloys and the Impact of Nitrogen: X-ray Photoelectron Study, *Applied Surface Science*. 536 (2021) 147703. https://doi.org/10.1016/j.apsusc.2020.147703.

[5] **L. Prazakova** et al., Temperature Driven Structural Evolution of Ge-rich GeSbTe Alloys and Role of N-doping, *Journal of Applied Physics*. 128 (2020) 215102. https://doi.org/10.1063/5.0027734.

Résumé en français

Introduction

A l'époque digitale d'aujourd'hui, la quantité des données à stocker et à procéder augmente rapidement. Effectivement, il est estimé que la quantité des données procédées atteindra 175 zettabytes en 2025. La nécessité de stocker autant de données encourage le développement de nouvelles technologies innovantes dans le domaine des mémoires Non-Volatiles, dont l'intérêt est qu'elles permettent de conserver des données sans alimentation d'énergie constante. Parmi les technologies NVM innovantes, les Mémoires à Changement de Phase (PCRAM) sont considérées comme la solution la plus avantageuse pour la prochaine génération de NVM, grâce à leurs capacités uniques telles qu'une haute scalabitié, de grandes vitesses de lecture et d'écriture et une cyclabilité élevée. Cette technologie a fait son entrée sur le marché d'abord dans le domaine des mémoires autonomes ("stand-alone") comme Storage Class Memory (SCM), permettant de profiter de sa non-volatilité, faisant concurrence aux mémoires Flash et Hard-Disk Drives, et en même temps de la vitesse opérationnelle proche de celle des mémoires volatiles comme la Dynamic Random Access Memory (DRAM). Récemment, les PCRAM ont montré leur maturité dans le domaine des mémoires embarquées pour les applications dans l'industrie automobile ou dans les systèmes d'intelligence artificielle.

Le dispositif PCRAM est basé sur un matériau à changement de phase qui est intégré entre deux électrodes et qui subit une transition entre sa structure amorphe et cristalline induite par la chaleur créée entre les électrodes. Le choix du matériau intégré joue un rôle décisif concernant les capacités finales du dispositif. Les matériaux chalcogénures du système ternaire Ge-Sb-Te sont les plus investigués comme matériaux à changement de phase, mettant en évidence l'alliage stoéchiométrique de $Ge_2Sb_2Te_5$ comme une référence. Malheureusement, sa stabilité thermique n'est pas suffisante pour des applications embarquées, notamment dans l'industrie automobile. Plusieurs voies sont proposées pour optimiser la stabilité thermique, dont les deux qui ont attiré le plus d'intérêt sont l'enrichissement en Ge et le dopage par l'azote (N). Ces matériaux optimisés ont bien démontré des effets positifs sur les capacités du dispositif final. Par contre, la compréhension de la structure, son évolution en fonction de la température et le mécanisme de cristallisation de ce type d'alliages restent peu connus.

L'objectif de ce travail est de mener des investigations structurales et de mieux comprendre le mécanisme de cristallisation dans les alliages GeSbTe (GST), permettant les applications exigeant la haute stabilité thermique. Nous étudions deux groupes de matériaux : a) les systèmes élémentaires de Ge, Sb et Te et b) les alliages GST enrichis en Ge. Nous identifions les principales caractéristiques de leurs structures et nous étudions leurs évolutions sous l'effet de l'incorporation de N. Nous employons des techniques de caractérisation diverses, e.g., les spectroscopies infrarouge (FTIR) et Raman, la Diffraction des rayons X (XRD) et la Microscopie Electronique en Transmission associée à la Spectroscopie de rayons X à Dispersion d'Energie (TEM-EDX), permettant d'obtenir des informations complémentaires sur les deux phases des matériaux (les phases amorphe et cristalline). Ces investigations permettent de contribuer à la compréhension de l'arrangement structural et la formation des liaisons avec N ainsi que les évolutions structurales en fonction de la température. Elles mettent en évidence les caractéristiques structurales clés responsables de la haute stabilité thermique.

Chapitre 1 : Mémoires à Changement de Phase : les Principes et la Technologie

Le chapitre 1 introduit les principes généraux de la technologie des PCRAM. Nous présentons les caractéristiques technologiques d'un dispositif PCRAM et la liaison entre les capacités du dispositif et les propriétés du matériau intégré. Ensuite, le chapitre se focalise sur les matériaux à changement de phase, présentant des concepts théoriques de mécanismes de cristallisation ainsi que la description générique des phases amorphe et cristalline, qui sont la clef du principe de fonctionnement des mémoires à changement de phase. Nous introduisons le système ternaire de Ge-Sb-Te, dont les alliages sont les plus utilisés en tant que matériaux à changement de phase. Nous décrivons la structure et les propriétés des alliages de référence binaire (GeTe et Sb_2Te_3) et ternaire ($Ge_2Sb_2Te_5$). Deux voies sont proposées pour optimiser les matériaux GST: la modification de stoéchiométrie de l'alliage et le dopage par des éléments légers. Des alliages non-stoéchiométriques enrichis en Ge et en Sb sont présentés, mettant en évidence leurs avantages pour des applications potentielles demandant la haute stabilité thermique et la haute vitesse des opérations, respectivement. Quant au dopage par les éléments légers, les dopages par C, O et notamment N sont présentés comme des solutions pour l'augmentation de la stabilité thermique. Dans le cadre de cette thèse, les GST enrichis en Ge et dopés par N sont ciblés pour l'investigation structurale.

Chapitre 2: Caractérisation des Matériaux à Changement de Phase

Le chapitre 2 présente brièvement les techniques de caractérisation utilisées dans le cadre de ce travail pour investiguer la structure des matériaux GST. Les techniques de caractérisation électrique, optique, par rayons X et de microscopie sont employées (Tableau 6-I) pour obtenir des informations complémentaires sur les matériaux étudiés.

Tableau 6-I : Domaines de caractérisation diverses avec la liste des techniques de caractérisation utilisées dans ce travail.

Domaine de caractérisation	Techniques de caractérisation
Propriétés électriques	Mesures de résistivité
Caractérisation optique	Spectroscopie FTIR, spectroscopie Raman
Caractérisation par Rayons X	XRD, XPS, WDXRF, XAS
Microscopie	TEM-EDX

Cela permet d'investiguer les domaines suivants:

- Transition de phases et température de cristallisation ;
- Arrangement de la structure, identification des liaisons formées ;
- Structure locale ;
- Microstructure ;
- Métrologie, quantification des éléments de dopage (N).

En plus, les techniques de caractérisation expérimentales peuvent être accompagnées par des simulations *« ab initio »*. Nous présentons des exemples pratiques de caractérisation des matériaux GST par les techniques employées dans ce travail. Nous présentons la recherche bibliographique sur ces matériaux, soulignant les informations obtenues sur la structure. Nous démontrons la complémentarité des mesures de résistivité avec l'ellipsométrie *in-situ* afin de suivre la transition de phases. Nous présentons des études par spectroscopie Raman et FTIR sur les systèmes élémentaires, binaires et ternaires, qui pourrons servir pour identifier des

liaisons et unités structurales dans la suite de cette thèse. Nous illustrons l'étude de l'oxydation du GST et l'identification des liaisons avec N par XPS et FTIR. Nous discutons l'investigation de la structure locale par XAS, complétée par des simulations. Enfin, nous présentons l'étude du mécanisme de cristallisation et du suivi de la ségrégation de phases dans GST enrichi en Ge par des analyses XRD et TEM-EDX, qui proposent la cristallisation prioritaire de la phase Ge suivie par la cristallisation de la phase GST. En complément du Chapitre 1, ce chapitre présente une base d'informations théoriques et expérimentales disponibles dans la littérature pour guider les investigations structurales présentées dans cette thèse. Enfin, nous présentons les détails de la préparation des matériaux investigués dans ce travail (couches minces déposées par pulvérisation cathodique) ainsi que les paramètres de mesures pour les techniques employées.

Chapitre 3 : Les systèmes élémentaires Ge , Sb et Te dopés par N

Le chapitre 3 est dédié à l'investigation structurale des systèmes élémentaires de Ge, Sb et Te et leur évolution structurale sous l'effet de dopage par N. Nous étudions la structure de ces matériaux par spectroscopie FTIR et Raman, complétés par des analyses par spectroscopie d'absorption des rayons X (XAS). En plus, des simulations *« ab initio »* viennent conforter les résultats expérimentaux. Les résultats de quantification par spectroscopie de Fluorescence de rayons X (WDXRF) montrent que la quantité de N incorporée est la plus élevée dans les couches élémentaires de Ge et la plus faible dans les couches élémentaire de Te. L'investigation de la structure du Ge montre le remplacement des liaisons Ge-Ge par des liaisons Ge-N (Fig. 6.1a), qui sont plus fortes et plus stables ; cela est confirmé par des études de stabilité en température. La couche Ge déposée est amorphe et cristallise entre 500-550 °C. La cristallisation des couches dopées N n'est pas observée jusqu'à cette température, même pour la quantité de dopage la plus faible utilisée dans ce travail. La structure de la couche Sb sans dopage semble être cristalline après le dépôt, ce qui est indiqué par des pics identifiés dans le spectre Raman. Apparemment, les atomes de N incorporés dans la structure de Sb substituent aux atomes de Sb et forment des liaisons Sb-N, cela est confirmé par une bande d'absorption identifiée dans les spectres IR (Fig. 6.1b). La substitution des atomes Sb par N est facilitée par la même coordination de ces éléments et le même nombre d'électrons de valence, comme les deux éléments se trouvent dans la même colonne du tableau périodique. La substitution raccourcit les distances interatomiques dans la structure Sb cristalline, en créant du désordre, indiqué par une bande élargie au lieux des deux pics Sb dans les spectres Raman. La structure de Te montre la moindre affinité à incorporer N. La structure dela couche de Te déposée est identifiée comme cristalline, comme l'indiquent les pics dans le spectre Raman. Le dopage par N perturbe la structure cristalline, comme dans le cas de Sb. Par contre, les atomes N s'incorporent plutôt dans les positions interstitielles entre les chaines atomiques de Te dans les coins de la maille cristalline. Le N forme des liaisons Te-N faibles entre l'atome de N et des Te des trois chaines à proximité (Fig. 6.1c). Cela perturbe le système, changeant les distances entre les chaines et leur rotation due à la stéréochimie des paires d'électrons libres des deux éléments Te et N. Enfin, la structure de TeN maintient les chaines de Te, mais le désordre induit dans la structure fait monter une contribution amorphe observée par spectroscopie Raman. Les liaisons Te-N formées dans la structure sont faibles, ce que montrent les études de stabilité en temps. Les spectres IR des couches TeN viellies ont montré une réduction des bandes d'absorption assignées à Te-N et l'apparition de bandes liées à Te-O, indiquant l'oxydation des couches TeN, malgré la couche d'encapsulation déposée.
Ces études permettent de comprendre le mécanisme d'incorporation de N dans les systèmes élémentaires de Ge, Sb et Te et la formation des liaisons avec N. Des bandes d'absorption attribuées à la formation des liaisons X-N (X = Ge, Sb, Te) ont été identifiées dans les

spectres IR, ce qui n'était pas référencé dans la littérature auparavant. Les résultat obtenus de ces études peuvent être appliqués pour l'identification des liaisons X-N dans les systèmes plus complexes, notamment les alliages GST enrichis en Ge, qui améliorera la compréhension de l'arrangement structural et de l'effet du dopage N.

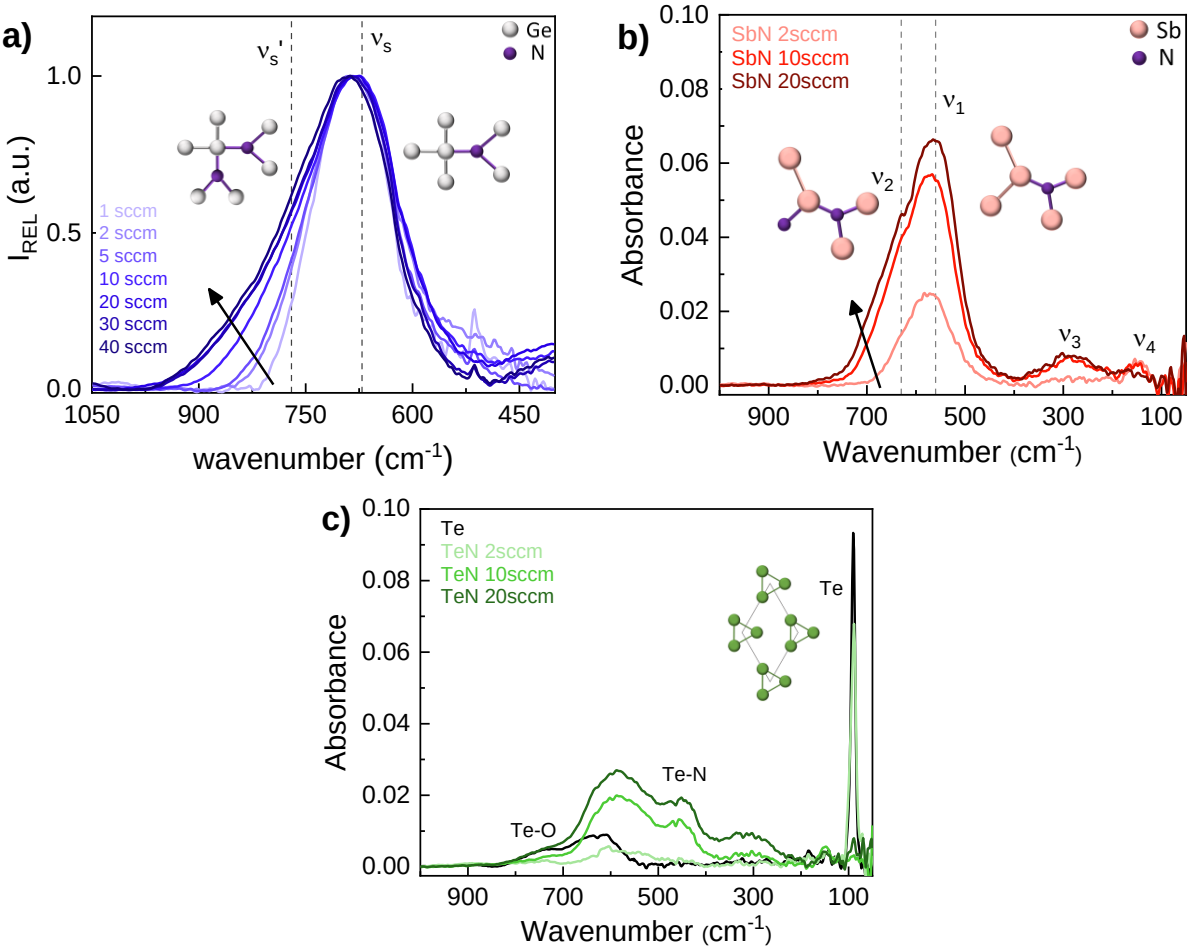

Fig. 6.1: spectres infrarouge de a) alliages GeN, b) alliages SbN, c) alliages TeN démontrant les bandes d'absorption assignées aux modes des vibrations des liaisons Ge-N, Sb-N, Te-N, respectivement. Les figures sont accompagnées par des illustration de la structures des éléments sous l'impact de l'incorporation de N.

Chapitre 4 : Les alliages GeSbTe

Le chapitre 4 est dédié à l'investigation des alliages GST enrichis en Ge. Dans la première partie du chapitre, les alliages sans dopage N sont étudiés, en variant la quantité d'enrichissement de Ge entre 15 et 55 at.% (Fig. 2). La structure des phases amorphe et cristalline et le mécanisme du cristallisation sont étudiés par spectroscopie Raman et XRD. Les résultats sont comparés par rapport à la composition de référence de $Ge_2Sb_2Te_5$, mettant en évidence la stabilité des unités structurales à la base des liaisons Sb-Te jusqu'aux hautes températures dans les alliages enrichis en Ge. L'évolution structurale en température observée peut être résumée par les étapes suivantes (Fig. 6.2):

- Réarrangement progressif des liaisons Ge-Te autour des unités SbTe, pour former la structure cristalline cubique de la phase GST ;
- Ségrégation du Ge de la phase GST formée ;
- Nucléation et croissance rapide d'une phase cristalline de Ge.

La cristallisation de la phase GST avant la cristallisation de la phase Ge est bien évidente dans les spectres XRD à 300 °C, confirmant la formation de la phase GST sans la présence de la phase Ge. Plusieurs phénomènes sont mis en évidence pendant l'évolution structurale des GST enrichis en Ge, en fonction de la quantité de Ge. En effet, la ségrégation de la phase Ge est bloquée en augmentant la quantité de Ge dans le système (diffusivité des atomes Ge ralentie), ce qui retarde la cristallisation de la phase GST. Au contraire, la diffusivité du Ge augmente avec la température ainsi que la vitesse de nucléation et croissance cristalline de Ge, une fois que la phase GST est établie.
D'ailleurs, nous avons observé la formation d'une phase de transition notée $G^{+}GST$, notamment pendant l'évolution structurale de $Ge_{35}GST$ et $Ge_{45}GST$. Cette phase, enrichie en Ge par rapport au $Ge_2Sb_2Te_5$ mais moins que les compositions d'origine, ajoute une étape intermédiaire. L'apparition de cette phase confirme le procédé de ségrégation du Ge en dehors de la phase GST formée (Fig. 6.3). La phase $G^{+}GST$ disparait à nouveau à des températures élevées, ce qui augmente la diffusivité du Ge et donc le progrès du système vers des phases cristallines stables, i.e., les phases $Ge_2Sb_2Te_5$ et Ge. La ségrégation de système est suivie et confirmée par des résultats TEM-EDX. En calculant la taille des cristallites, nous avons trouvé une bonne corrélation entre les deux phases ségrégées. La taille des cristallites augmente en température pour les deux phases, indépendamment de la quantité de Ge dans l'alliage, atteigant des valeurs similaires à haute température (~450 °C).
La deuxième partie du chapitre 4 étudie l'impact de dopage N et de sa quantité sur la structure du GST enrichi en Ge et son évolution en température. Nous démontrons la formation des liaisons Ge-N, stabilisant la phase amorphe du système vers des températures plus élevées. La formation du Ge-N impacte l'évolution structurale en température dès la première étape, c'est-à-dire dès le réarrangement des liaisons Ge-Te autour des unités structurales SbTe. Comme la température de cristallisation augmente, la dynamique de ségrégation et cristallisation des phases dans le système est plus rapide, dominée notamment par la vitesse de cristallisation de la phase Ge.
La quantité des liaisons Ge-N formées dans la structure augmente en correspondance avec la quantité de dopage par N, comme le montrent les spectres IR. Simultanément, la quantité des liaisons Ge-Ge diminue. Cela confirme les résultats obtenus lors de l'investigation des couches de Ge élémentaire dopées N dans le chapitre 3. La formation élevée du Ge-N augmente encore plus la stabilité de la phase amorphe du système en augmentant la température de cristallisation. Toutefois, les étapes du mécanisme d'évolution structurale proposées pour le GST enrichi en Ge et non dopé sont maintenues. Le calcul de la taille des cristallites des phases ségrégées démontre une corrélation similaire à ce qui était observé précédemment pour des alliages sans dopage, atteignant des valeurs similaires pour les deux phases ségrégées à la haute température (~500 °C).

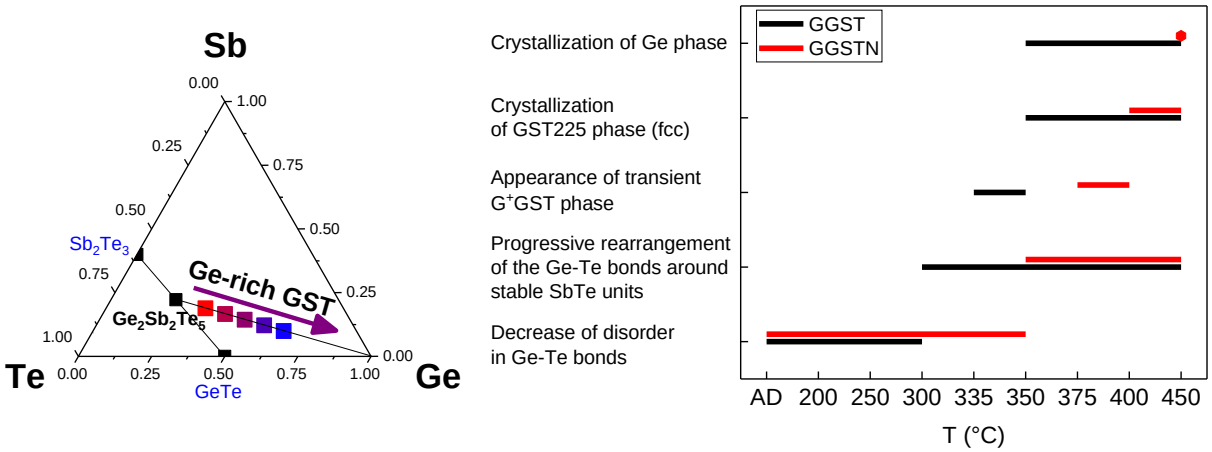

Fig. 6.2 : (gauche) Diagramme ternaire du système Ge-Sb-Te démontrant la composition de référence $Ge_2Sb_2Te_5$; (droite) représentation de l'évolution structurale en fonction de température des alliages GST enrichis en Ge et GST enrichis en Ge et dopé azote (N).

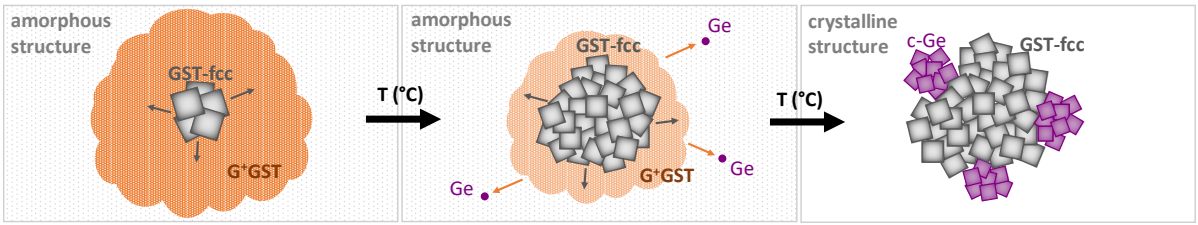

Fig. 6.3 : Illustration de la ségrégation et cristallisation progressive des phases GST et Ge dans les alliages GST enrichis en Ge en passant par l'étape intermédiaire de la phase G^+GST.

Conclusion et Perspectives

L'optimisation des matériaux à changement de phase joue un rôle fondamental pour le futur développement des PCRAM, notamment pour les applications embarquées employées dans l'industrie automobile. Pour cela, les matériaux intégrés dans les dispositifs doivent exceller par la haute stabilité thermique. L'enrichissement de la stoéchiométrie des alliages GST par Ge et le dopage par N sont proposés comme des solutions prometteuses. Cette thèse contribue à la compréhension de la structure de ce matériaux et de l'effet de l'enrichissement en Ge et du dopage N. D'abord, les structures des systèmes élémentaires Ge, Sb et Te sont investigués pour comprendre l'effet de l'incorporation de N et de la formation des liaisons de ces éléments avec N. Effectivement, les liaisons Ge-N sont démontrées être les plus favorables et les plus stables parmi les systèmes investigués. Les résultats de cette investigation sont appliqués plus tard pour l'identification des liaisons formées dans les systèmes complexes (GST enrichi en Ge et dopé N). L'investigation des structures amorphe et cristalline de GST enrichi en Ge permet de démontrer la stabilité et la prédominance des unités SbTe et le réarrangement progressif de la structure. L'évolution structurale démarre par ce réarrangement structural (GeTe autour des unités SbTe) en donnant lieu à la nucléation et la croissance primaire de la phase GST, suivie par la ségrégation et cristallisation rapide de la phase Ge. Le dopage de N dans le GST enrichi en Ge augmente la stabilité de la phase amorphe et augmente la température de cristallisation du système. En effet, les atomes N incorporés dans la structure forment des liaisons Ge-N stables, qui bloquent la diffusion des atomes Ge, ce qui reporte déjà la première étape de l'évolution structurale (i.e., réarrangement de Ge-Te autour de SbTe).

Plusieurs possibilités pour des futures investigations des matériaux GST sont proposées comme perspectives à ce travail. Des études d'alliages GST enrichis en Ge et dopés N avec un contenu de Ge réduit par rapport aux alliages étudiés dans ce travail (contenu global de Ge 58 – 68 at.%) sont proposés pour compléter les résultats sur l'évolution structurale établis dans ce travail. La réduction de l'enrichissement en Ge permettrait de ralentir le procédé de ségrégation afin de suivre des étapes séparées de ce procédé. En plus, l'application des techniques *in-situ* ou isotherme, notamment pour la spectroscopie Raman ou l'XRD, présenterait des avantages pour la caractérisation avancée de ces évolutions structurales. Pour mieux comprendre la stabilité et le rôle dominant des unités structurales SbTe, l'investigation d'autres alliages avec une variation du ratio Sb/Te est suggérée (les systèmes à base de $Ge_2Sb_2Te_5$ avec un ratio Sb/Te ~0.4 sont étudiés dans ce travail). Concernant le dopage par N, nous proposons des études avancées de l'incorporation de N en fonction de l'épaisseur de la couche. La scalabilité est une caractéristique importante des dispositifs PCRAM, mais qui apporte aussi de nouveaux défis. L'incorporation de N dans des couches plus minces (i.e., < 100 nm, qui est l'épaisseur des couches dans le cadre de cette thèse) pourrait être soit favorisée soit réduite et va impacter le nombre des liaisons Ge-N formées, donc la stabilité thermique du matériau. En plus, l'importance des effets des surfaces et interfaces augmente et leur compréhension est nécessaire. Pour ces raisons, un protocole métrologique de quantification de N devrait être établi, par exemple par WDXRF, la technique déjà bien employée pour le contrôle des procédés de dépôt. L'analyse de la structure globale d'un matériau intégré dans le dispositif PCRAM pourrait aussi apporter des suggestions intéressantes à appliquer. Par exemple, la structure notée comme superlattice-like (SLL) peut être proposée car combinant les propriétés des deux matériaux à changement de phase. Ce type de structure était déjà proposé pour $GeTe/Sb_2Te_3$ pour remplacer une monocouche de $Ge_2Sb_2Te_5$. De nouvelles structures SLL $Ge_2Sb_2Te_5/Sb$ et $Ge_2Sb_2Te_5/Sb_2Te_3$ ont été considérées récemment, combinant la transition de phases de $Ge_2Sb_2Te_5$ et la vitesse de cristallisation de Sb et ses alliages. Dans ce contexte, des nouvelles structures SLL à base d'empilements de $Ge_2Sb_2Te_5$/GeN peuvent être proposées au lieu d'une monocouche de GST enrichie en Ge et dopée N, toujours en profitant de la haute stabilité thermique apportée par le GeN.

A part l'optimisation des matériaux à changement de phase, cette thèse démontre la complémentarité des techniques de caractérisation utilisées et leurs avantages. La combinaison de la spectroscopie Raman et des analyses XRD permet d'étudier l'arrangement structural dans les phases amorphe et cristalline complétée par des informations concernant la ségrégation des phases et la taille des cristallites. Dans ce travail, des mesures ex-situ ont été principalement employées pour étudier les systèmes. Pour la suite, nous proposons l'application des techniques *in-situ* ou isotherme qui permettraient de suivre l'évolution structurale en temps réel et donc d'offrir plus de détails. Le couplage de ces techniques présente aussi un autre avantage de la caractérisation avancée. Dans ce cadre, des mesures de résistivité couplées avec de la spectroscopie Raman *in-situ* pourraient être proposées. La spectroscopie Raman, en particulier, propose d'autres possibilités pour les investigations structurales dans les alliages GST. Une source d'excitation non polarisée a été utilisée dans ce travail. Cependant, l'utilisation d'une source d'excitation polarisée pourrait apporter des information additionnelles, permettant d'augmenter ou réduire l'intensité des modes de vibrations des liaisons Ge-Te et Sb-Te et donc d'améliorer leur distinction. En plus, l'investigation avancée de la stabilité et prédominance des liaisons Sb-Te discutée auparavant pourrait être facilitée par la source polarisée, sachant qu'une dépendence en fonction de la polarisation a été observée dans les alliages binaires Sb_2Te_3. Concernant les analyses de la microstructure par XRD et TEM-EDX, la contribution du stress interne n'est pas évaluée dans ce travail. Néanmoins, sa présence est fortement probable comme le système possède

plusieurs phases différentes (i.e., GST, Ge, GeN). L'analyse du stress en adoptant des mesures XRD appropriées pourrait compléter les analyses présentées ici. Enfin, d'autres techniques de caractérisation pourraient être aussi proposées, apportant des informations complémentaires. La spectroscopie par Résonance Magnétique Nucléaire (NMR) est une technique utilisée notamment pour des composés organométalliques à base de Te. Très peu d'études NMR ont été publiées sur les matériaux GST jusqu'à ce jour, cela permettant d'ouvrir une nouvelle sphère d'investigation qui pourrait offrir des informations sur la structure locale de la phase amorphe ainsi que la phase cristalline, complétant les analyses XRD ou XAS.

Appendix 1
Theoretical background of characterization techniques

Optical characterization

The optical characterization uses the interaction of material with electromagnetic radiation in the range of energies between 1.2 meV and 124 eV. This covers the range from Infrared (IR), Visible (VIS) to Ultraviolet (UV) spectral region (Fig. A1-1). The electromagnetic radiation (light) can be described by the wave-particle duality concept originating from quantum mechanics. This concept says that the light can exhibit the behavior of both a particle and a wave. Its particle behavior is represented by a photon, a quantum particle with no mass and no charge. Light as a wave is described in terms of continuous sinusoidal motion of coupled oscillating electric and magnetic fields (Fig. A1-2). Typically for IR and Raman spectroscopy, only the electric field component is considered and the magnetic field is neglected.

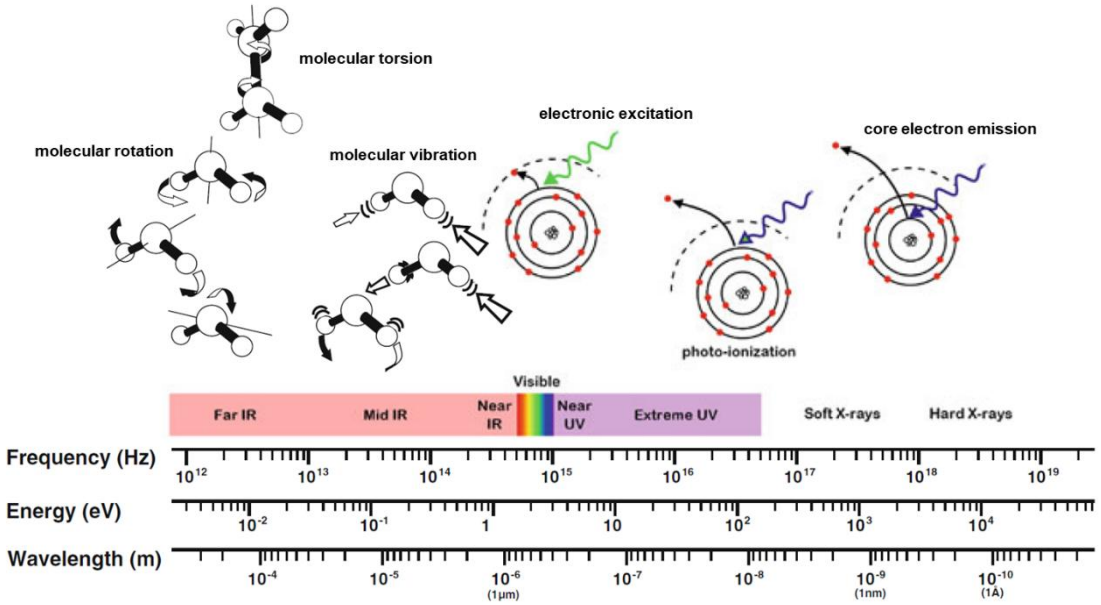

Fig. A1-1: Frequency, energy and wavelength range of electromagnetic radiation (light) and the schematic representation of possible interaction between the light and matter [173].

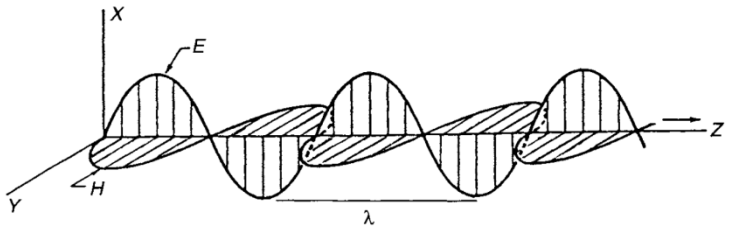

Fig. A1-2: The propagation of the electromagnetic radiation as a function of time (in z axis). The electric field component (E) is only taken into account in IR and Raman spectroscopy, while magnetic field component (H) is omitted [342].

Considering only the electric field component of the electromagnetic radiation, the energy of the electromagnetic radiation is closely linked with the frequency and the speed of light in vacuum though the formula:

$$E = h\nu = h\frac{c}{\lambda} \quad \text{(A1.1)}$$

Where h is Planck's constant, ν is frequency, c is speed of light in vacuum and λ is wavelength of the electromagnetic radiation. The energy is thus proportional to frequency and inversely proportional to wavelength. Another commonly used property is wavenumber $(\bar{\nu})$ representing the number of cycles an electromagnetic wave undergoes per unit of length. The wavenumber is the inverse of the wavelength:

$$\bar{\nu} = 1/\lambda \ (cm^{-1}) \quad \text{(A1.2)}$$

The interaction of light with matter results in light absorption, transmission or scattering (elastic or inelastic). The nature of the interaction depends on the physical, chemical and structural properties of the matter, as well as the intensity and energy of interacting light (photons). Upon the interaction and depending on the photon energy, different effects are generated in the matter causing energy changes (ΔE), related to the electronic (E_{el}), vibrational (E_{vib}) and/or rotational (E_{rot}) energies. In a first approximation, these energies are considered to be additive:

$$\Delta E = E_{el} + E_{vib} + E_{rot} \quad \text{(A1.3)}$$

Photons with higher energy and shorter wavelength (i.e., from UV and VIS region) are more likely to interact with electrons of the outer shells of the matter and to excite them to higher energetic levels, leading to electronic transitions (E_{el}). On the contrary, photons with lower energy and higher wavelength (i.e., from IR region), are more likely to interact with the material lattice, yielding to molecular rotations (E_{rot}) and vibrations (E_{vib}) states. In the vibrational spectroscopies, only the changes in E_{vib} are considered for the condensed states. IR and Raman spectroscopies are the most widely used techniques belonging to the group of vibrational spectroscopies, providing the specific information about a molecule, its structure and chemical environment

IR and Raman spectroscopies are complementary techniques, in which some types of vibrations can be observed only by IR spectroscopy whilst others by Raman spectroscopy, whereas some types of vibrations can be observed by both techniques. The observation of different vibrational modes arises from the specific selection rules based on the different principles of these techniques, explained in the following. In order to understand the vibrational modes, the normal vibrations need to be discussed at first.

Normal vibrations

A set of motions of a molecule can be described as a number of internal degrees of freedom. A molecule with N atoms can provide 3N degrees of freedom in X, Y and Z axes. Three of the degrees represent a translational motion and three represent a rotational motion. Reduced by the number of these motions, the remaining 3N-6 degrees of freedom describe the vibrational modes of a non-linear molecule (3N-5 in case of linear molecule). These vibrational modes are also called normal vibrations or normal modes and include the motions with changes in the distance between atoms (stretching vibrations) or the angle between the bonds (bending vibrations) (Fig. A1-3).

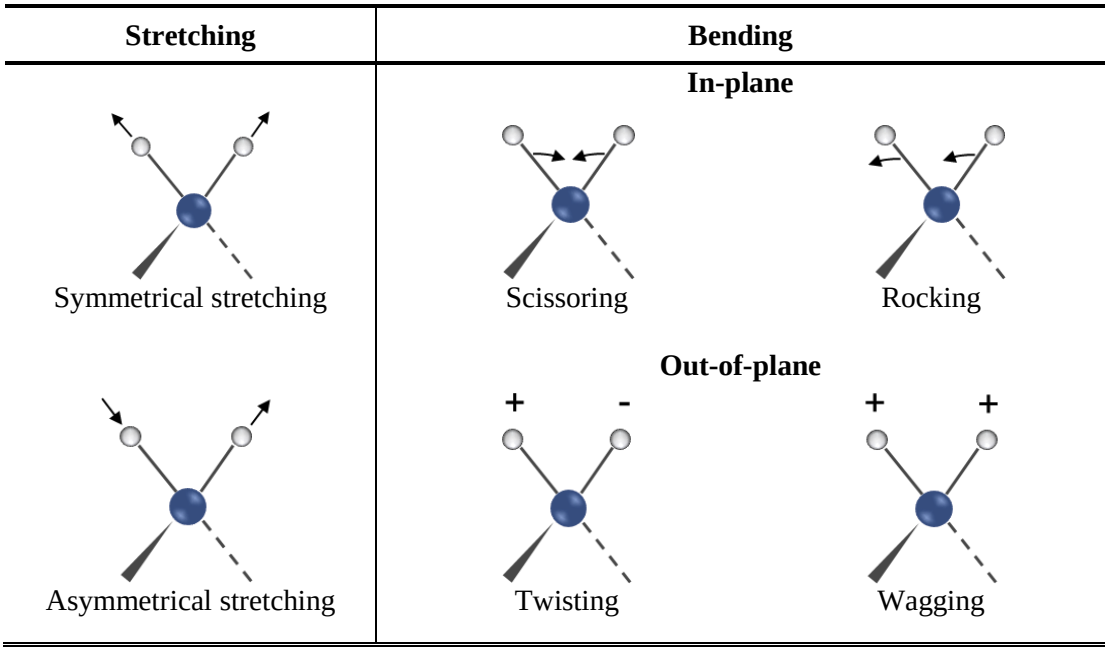

Fig. A1-3: Schematic representation of normal stretching (symmetrical / assymetrical) and bending (in-plane / out-of-plane) vibrational modes.

Although IR and Raman spectroscopies are based on different selection rules described below. The nature of the vibrational modes allows to define which vibrations are Raman or/and IR active. In general, symmetric and in-phase vibrations of non-polar bonds or groups are more easily studied by Raman spectroscopy, whilst asymmetric, out-of-plane and polar bonds or groups are better observed by IR spectroscopy. Moreover, Group Theory employing the symmetry elements (e.g., planes, axes) can help to determine IR-or Raman-active vibrational modes and approximate the idea of the vibrational spectra [177,342,343].

Infrared spectroscopy

The infrared spectroscopy technique is based on the absorption process of the IR radiation. The interaction of the IR radiation with the molecules can be described in terms of a resonance effect, where the specific IR radiation frequency matches the frequency of a normal vibrational mode of the molecule. The energy of the IR radiation is absorbed only under the condition that the molecular vibration changes the dipole moment of the molecule ($\vec{\mu}$), which indicates a charge separation in a molecule. It is a function of the magnitude of atomic charges (q_i) and their positions ($\vec{r_i}$):

$$\vec{\mu} = \sum q_i \vec{r_i} \tag{A1.4}$$

The final dipole moment acts in the direction of the vector quantity. The dipole moment is derived from partial charges on the atoms, determined by molecular orbital calculations. In first approximation, the partial charges can be estimated from the electronegativity values of the atoms. Homonuclear diatomic molecules, such as N_2 or O_2 have no dipole moment; therefore, they are IR inactive. On the contrary, heteronuclear molecules (NO, CO, H_2O) do have dipole moments and thus active IR vibrations (Fig. A1-4). In general, IR spectroscopy is suitable for the observation of polar groups and asymmetric vibrations of the molecules [173,176,177].

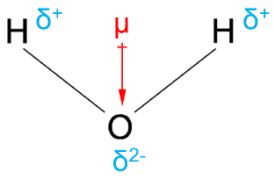

Fig. A1-4: Scheme of H_20 molecule with indicated dipole moment and partial charges on the atoms.

The IR range of the electromagnetic spectrum is divided into three regions:

- Near-IR (~14 000 – 4 000 cm^{-1})
- Mid-IR (~4 000 – 400 cm^{-1})
- Far-IR (~400 – 10 cm^{-1})

Absorption of the radiation from near-IR results in few broad spectral features, which are usually difficult to interpret. Moreover, these features often result from the overtones and the combinations of some fundamental vibrations of higher frequency modes from Mid-IR region. Near-IR region is used in UV-VIS-NIR spectroscopy for the measurements and calculations of optical parameters (e.g., optical bandgap) and for the determination of layer thickness. Mid-IR region is the most practically used in IR spectroscopy as it contains characteristic group frequencies, widely employed for compounds identification in organic chemistry. With increasing atomic weight of the atoms in the molecule, IR radiations with lower frequencies are absorbed. For such molecules, low wavenumber part of Mid-IR and Far-IR region are the most interesting.
A typical IR spectrum is plotted as the transmittance (*%T*) or absorbance (*A*) as a function of the wavenumber (Fig. A1-5). The transmittance represents the percentage of light transmitted by a sample:

$$\%T = 100 \cdot I / I_0 \tag{A1.5}$$

Where, *%T* is the transmittance in percent value, *I* is the intensity of sample spectrum and I_0 is the intensity of background spectrum. The absorbance is related to the transmittance by the following formula:

$$A = -log\ (T) \tag{A1.6}$$

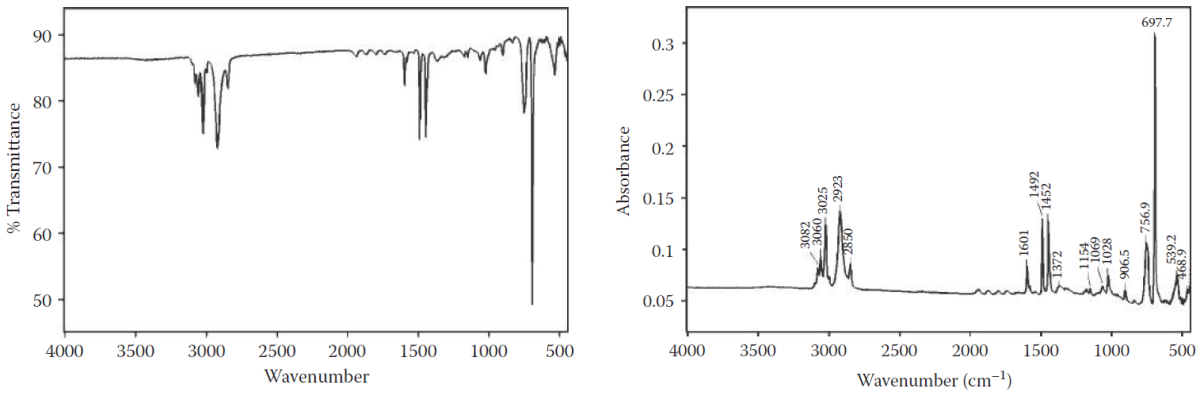

Fig. A1-5: An example of IR spectrum plotted in % transmittance (left) and absorbance (right) mode [177].

The interest in IR spectroscopy rapidly increased in 1960s, when the first commercially available instrumentation was developed by Perkin-Elmer. Further major breakthrough in the IR spectroscopy instrumentation was reached owing to considerable advancement in the

computing system, resulting in the construction of Fourier-Transform IR (FTIR) spectrometers. A Michelson interferometer is used in the FTIR spectrometers to modulate the incident IR light prior to passing through the sample and the detected raw data are processed using the Fourier Transform (FT) algorithm [344].
The FTIR spectrometer can be divided into three components (Fig. A1-6): IR source, interferometer and detector. The interferometer further includes a beamsplitter and two perpendicular planes of mirrors, from which one mirror is fixed and the other one is moving. The light from the IR source is collimated to the beamsplitter, where it is divided into two beams: 50 % of the light intensity is transmitted to the fixed mirror, whilst the other 50 % of the light intensity is reflected on the moving mirror. The reflected beams from both mirrors then return to the beamsplitter, where they interfere andpart of the light is sent towards the sample and the detector.

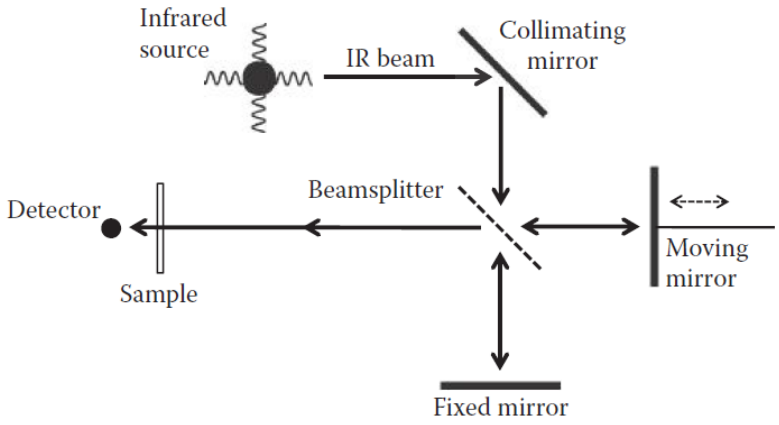

Fig. A1-6: Diagram of FTIR instrumentation with Michelson interferometer[177].

The two light beams divided on beamsplitter travel different path lengths due to the varying positions of the moving mirror, which is called mirror displacement (Δl). The difference in the distance between the beams reflected from fixed and moving mirrors is referred as optical path difference (δ). Mirror displacement Δl gives optical path difference $\delta = 2\Delta l$ as the light passes the displaced distance twice (on the way to and from the moving mirror). The two reflected beams recombine on the beamsplitter resulting in either constructive or destructive interferences for the beam further passing through a sample and the detector. Considering the IR source containing only single monochromatic wavelength λ, the two beams undergo the constructive interference, if δ equals an integral number of the wavelengths, i.e., $\delta = n\lambda$ (0, λ, 2λ, …), and the destructive interference for the values δ with intervals of $\lambda/2$, i.e., $\delta = (n+1/2)/\lambda$ (Fig. A1-7). If the distances travelled by the two light beams is identical (i.e., $\Delta l = 0$), then $\delta = 0$, which is called as zero path difference. The interferometer records the interferogram, i.e., the intensity of the phase-dependent interference as a function of optical path difference δ. Using a polychromatic IR source, the interferogram consists of a sum of the interferograms corresponding to each wavenumber of the IR source (Fig. A1-7). All the wavelengths will be in phase only at zero path difference, resulting in the interferogram containing a very strong center-burst (proportional to the total amount of IR light intensity from the source) and with the intensity falling rapidly on the interferogram sides (wings). In order to measure precisely the optical path difference, a He-Ne laser is used to follow the IR beam through the interferometer.

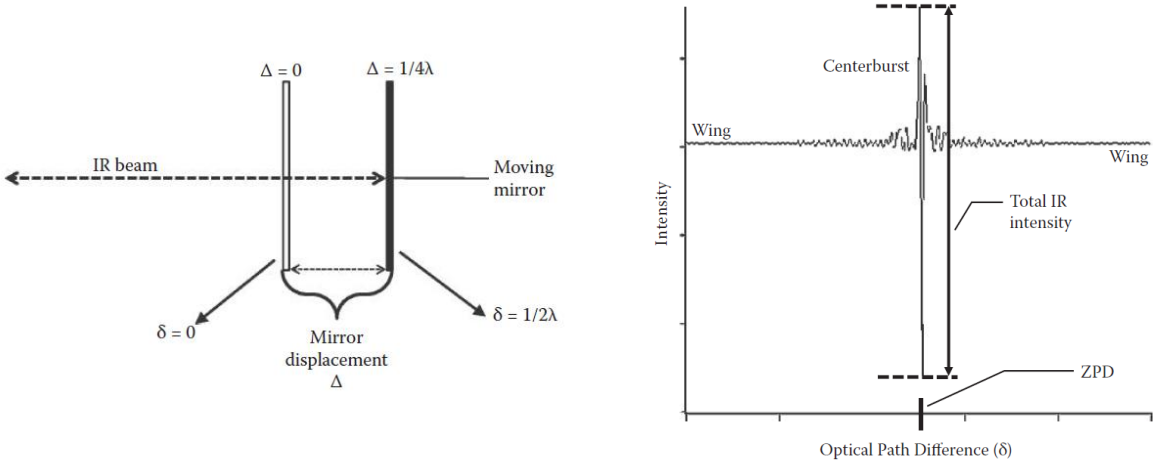

Fig. A1-7: (left) scheme of moving mirror displacement producing zero and non-zero optical path difference; (right) Interferogram of the polychromatic IR radiation showing high intensity center-burst and low intensity interferogram sides [177].

An IR source is based on the concept of black body radiation. Usually, an inert solid material is electrically heated to high temperature, when the heated material emits the IR radiation. The most common sources for Mid-IR region are resistively heated Globar (silicon carbide rod), Nernst glower (rare earth oxides) and nichrome or Kanthal wire coils. A high-pressure mercury lamp is a common source used for Far-IR region [177,344]. An ideal material for the beamsplitters should have a high refractive index. The principle is to cause a multiple internal reflection on parallel-sided thin layers of such material and thus to generate the interference fringes. Therefore, germanium or silicon are widely used elements. Ge thin layers are sandwiched between two IR transparent windows, usually made from KBr. A common type of detectors used in IR spectroscopy is based on deuterated triglycine sulfate (DTGS). This thermal detector works on the principle that its electrical polarization changes with temperature. The second type of the detectors is based on the interaction of the radiation with the electrons in a solid, exciting the atoms to higher energy states. Such detectors, usually called quantum detectors, are made with mercury cadmium telluride (MCT). Comparing to DTGS, the MCT detector is faster and less noisy, however, it suffers from lower spectral range and it must be cooled by liquid nitrogen (LN_2) in order to minimize the noise generated by randomly emitted photons [177,344].

Raman spectroscopy

In contrast to IR spectroscopy, Raman spectroscopy is based on the scattering mechanism. It is a two-photon inelastic event, in which the incident photon interacts with the molecule and loses part of its energy to enable the molecular vibration, yielding to a scattered photon with reduced frequency. The interaction between incident light and matter is not based on the principle of resonance as in IR spectroscopy, but involves the polarizability of the molecule and induces dipole moment (Fig. A1-8).

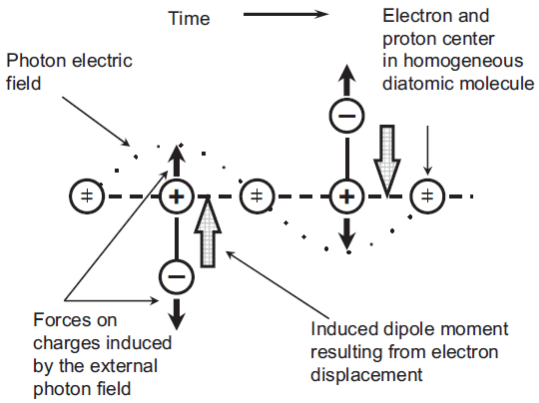

Fig. A1-8: Induced dipole moment originating from the oscillating electric field of the incident radiation [176].

In the classical approach, the light scattering mechanism in described in terms of the interaction of the molecule with an electromagnetic field of the incident radiation. The electric field vector (E) of the electromagnetic wave oscillates in time (t) with the frequency (ν_0):

$$\vec{E} = \vec{E}_0 \cos(2\pi\nu_0 t) \tag{A1.7}$$

The oscillating electric field ($\vec{E}$) can induce a dipole moment ($\vec{\mu}$) in the molecule, which is proportional to the electric field:

$$\vec{\mu} = \tilde{\alpha}(\nu) \cdot \vec{E} \tag{A1.8}$$

Where $\tilde{\alpha}(\nu)$ is the polarizability of the molecule describing the deformability of the electron cloud of the molecule by an external electric field (i.e., the response of electron distribution to the nuclei movement of the molecule). The polarizability is a linear function of the nuclear displacement (q), dependent on the molecule vibrating frequency ν_m:

$$\tilde{\alpha}(\nu) = \tilde{\alpha}_0(\nu_0) + \left(\frac{\delta\tilde{\alpha}}{\delta q}\right)_0 \cdot q \tag{A1.9}$$

$$q = q_0 \cos 2\pi\nu_m t \tag{A1.10}$$

Where α_0 is the polarizability in the equilibrium position and $(\delta\alpha/\delta q)_0$ is the rate of change of α with respect to the change of q. Combining the equations A1.7 – A1.10, the formula for induced dipole moment is obtained [176,184,345]:

$$\vec{\mu} = \tilde{\alpha}_0\vec{E}_0 \cos(2\pi\boldsymbol{\nu_0}t) + \frac{1}{2}\left(\frac{\delta\tilde{\alpha}}{\delta q}\right)_0 q_0\vec{E}_0[\cos\{2\pi t(\boldsymbol{\nu_0} + \boldsymbol{\nu_m})\} + \cos\{2\pi t(\boldsymbol{\nu_0} - \boldsymbol{\nu_m})\}] \tag{A1.11}$$

The right side of the equation A1.11 is composed by three terms corresponding to the polarizabilities that depend on different frequencies ν_0,$(\nu_0 + \nu_m)$ and $(\nu_0 - \nu_m)$. The first term represents the scattering at which the frequency of the incident light remains unchanged. This type of scattering is referred to as elastic or Rayleigh scattering.The second and third terms describe the scattering, in which the frequencies are shifted from ν_0 of the incident light by the frequency of the vibrating mode of the molecule ν_m. This type of scattering is called inelastic or Raman scattering. Only the molecular vibrations causing a change in polarizability are Raman-active. The Raman scattering is very weak process, far less probable compared to the Rayleigh scattering. Most of the photons of the incident light are scattered elastically, only 10^{-6} of the incident light is scattered inelastically [177].

The scattering processes along with the IR absorption are illustrated by the corresponding energy-level diagram (Fig. A1-9). In case of IR spectroscopy, the transition between the electronic ground state and excited states ($\nu = 0 \rightarrow \nu = 1$) is observed and the IR absorption achieves the state change in one step. On the contrary, the scattering is a two-photon process. The incident photon is temporarily absorbed by a transition from the ground state into so-called virtual states, which are well above the energy of the vibrational transition, but below the first electronic excited states. The transition back from the virtual states to the ground states results in scattered photons. In the case of elastic Rayleigh scattering, the frequency (hence the energy) of the incident light remains unchanged. For the Raman scattering, the frequency of the incident light is changed, giving rise to two possible energy shifts (Fig. A1-9). Molecules, which are initially at the lowest level on the ground state $\nu = 0$, gain energy and are promoted to an excited state $\nu = 1$, i.e., $(\nu_0 - \nu_m)$, which is called as Stokes scattering. However, some molecules may be initially present in excited states $\nu = 1$ (due to thermal energy) and lose energy while returning into the ground state $\nu = 0$, i.e., $(\nu_0 + \nu_m)$, which is called as anti-Stokes scattering. The intensity ratio between the Stokes and the anti-Stokes Raman bands is ruled by temperature and energy difference between the vibrational states. Considering Maxwell-Boltzmann distribution law, the population of molecules at vibrational states $\nu = 0$ is much larger that at $\nu = 1$ under normal conditions, hence Stokes lines are stronger than anti-Stokes. Since both Stokes and anti-Stokes give the same information, usually only the Stokes side of the spectrum is measured [177,184].

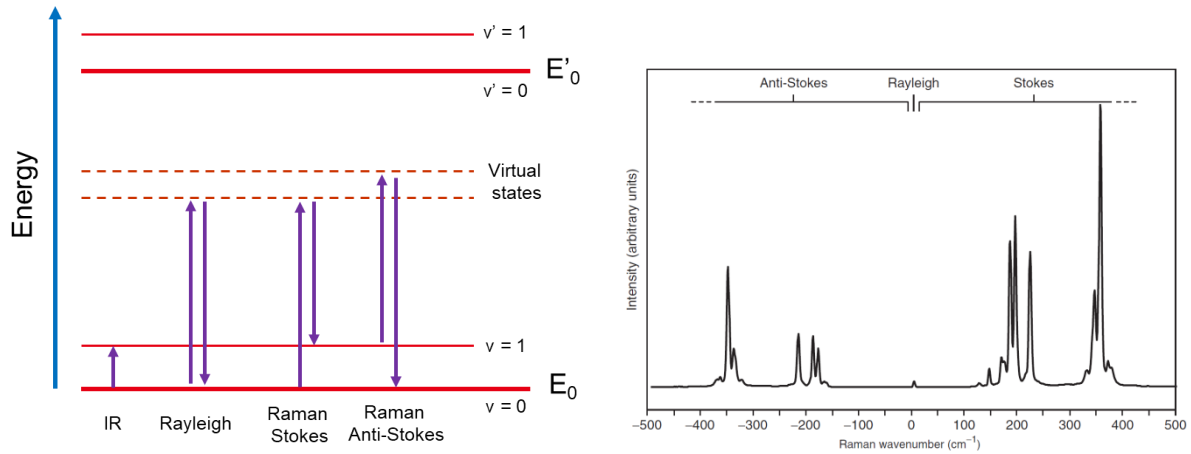

Fig. A1-9: (left) Schematic illustration of IR absorption, Rayleigh and Raman (Stokes and anti-Stokes) scattering processes; (right) Example of Raman spectrum showing both the Stokes and anti-Stokes region. The intensity of Rayleigh scattering is suppressed by a holographic notch filter [184].

The Raman instrumentation typically consists of laser excitation source, collection optics, spectral analyzer (monochromator or interferometer) and detector (Fig. A1-10). Since the Raman scattering is considerably weak, the laser beam must be properly focused and the scattered radiation efficiently collected. Two most common experimental configurations for collecting the Raman scattered radiations use 90° and 180° backscattering geometries. The collection systems are based on reflective and refractive optics [176]. In order to suppress the Rayleigh radiation, holographic notch filters are employed. A monochromator is used as the spectral analyzer in dispersive-based system. It consists of an entrance slit and the system of diffraction grating and focusing mirror, directing the dispersed radiation through the exit slit on a detector. Charge-Coupled Devices (CCD's) are commonly used as detectors. The choice of the collection optics and the detector type depends on the used laser excitation source and its wavelength.

Besides the dispersive system, Raman instrumentation using the Fourier Transform (FT) was developed. In such systems, the monochromator is replaced by an interferometer and InGaAs is usually employed as detector. The FT-Raman measurements typically use a Nd:YAG laser (i.e., Nd-doped yttrium aluminum garnet $Y_3Al_5O_{12}$), which is a near-IR excitation source with a wavelength of 1064 nm. Indeed, the choice of the laser excitation source and its parameters (e.g. wavelength, power, density and laser exposure time) is essential for Raman spectroscopy, as already discussed in the chapter 2 (section 2.1.2). The advantage of FT-Raman spectroscopy is that it provides spectra without resonant enhancement and can reduce or even avoid interference phenomena (e.g., fluorescence).

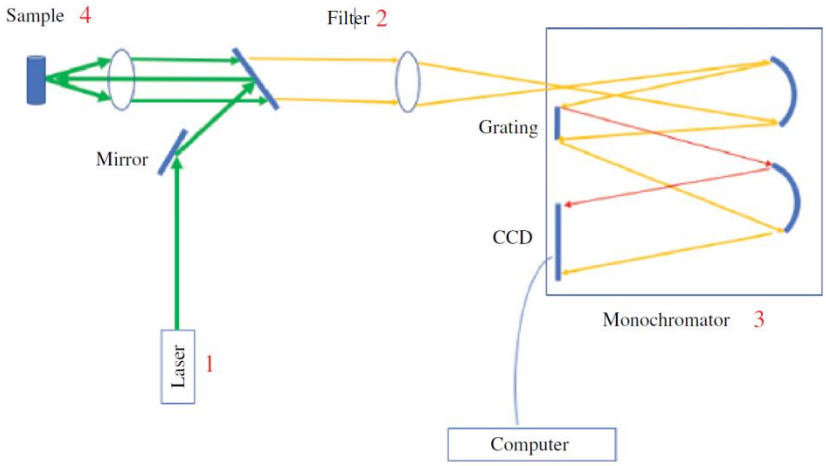

Fig. A1-10: Diagram of dispersive Raman instrumentation [346].

X-Ray diffraction

The diffraction phenomenon generally occurs when the electromagnetic radiation (wave) encounters an obstacle or an aperture comparable in size to its wavelength. The wavelength of X-rays is comparable to the interatomic spacing of crystalline solids, thus making X-ray Diffraction (XRD) suitable to study the crystalline structure of materials. In particular, XRD allows identification of the crystal structure, determination of preferred orientation of a single crystal or grains in polycrystalline materials and can provide the information on size, shape and internal stress of small crystalline regions.

Crystalline materials feature an ordered structure with a periodic lattice composed by the individual atoms, which can be imagined as the diffraction gratings. The incident X-ray waves are elastically scattered by the atoms of the periodic lattice, giving rise to constructive or destructive interferences and generating a diffraction pattern specific of the crystalline material (Fig. A1-11). The X-rays diffraction by a crystalline material is described by Bragg's law:

$$2\, d_{hkl}\, sin\theta = n\, \lambda \qquad \text{(A1.12)}$$

Where d_{hkl} is the interatomic spacing, θ is the angle of the incident X-ray beam, λ is the wavelength and n is an integer number, also called as the order of the diffracted beam. The n express the path difference in terms of wavelength between the waves scattered by two different atomic planes. The Bragg's law is satisfied only for wavelengths $\lambda \leq 2d$. In the XRD pattern of a crystalline phase, well-defined diffraction peaks are present at specific diffraction angles. On the contrary, the XRD pattern of an amorphous material shows a broad band extended over a large range of diffraction angles (Fig. A1-11). The orientation of the atomic planes in crystals is typically described by Miller indices (hkl), which may denote a single

plane or a set of parallel planes. When a plane does not intercept a vector, the Miller index is equal to zero.

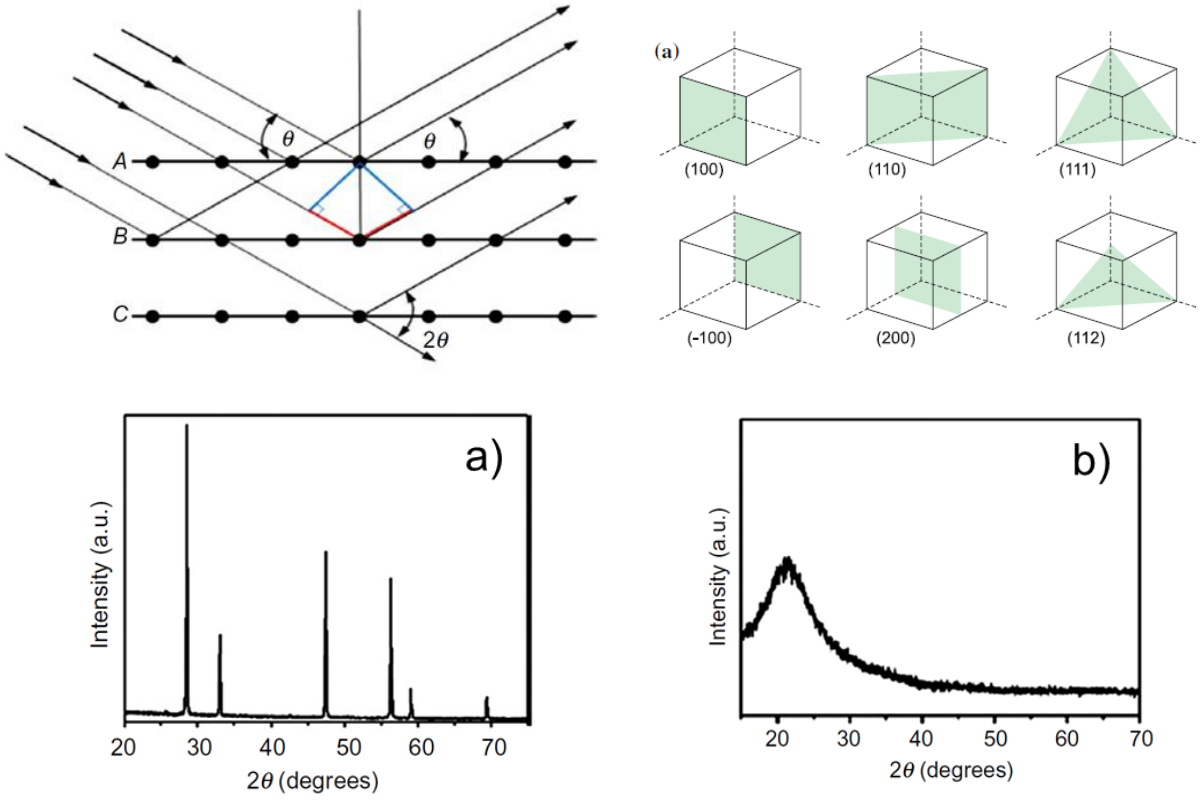

Fig. A1-11: (top) Schematic representation of (left) the Bragg's law by the reflection from adjacent planes in a crystal and (right) crystalline planes of simple cubic lattice with associated Miller indices; (bottom) XRD patterns of (a) crystalline and (b) amorphous materials [347,348].

The results of diffraction techniques consist of some form of representation in the reciprocal space. The concept of direct (real) and reciprocal spaces needs to be understood in order to analyze the acquired data and to describe the material properties. In general, features seen in reciprocal space result from Fourier Transformation of the features from direct space. Hence, the particular set of planes (hkl) in direct space corresponds to a particular point (hkl) in reciprocal space. Also, the d-spacing (d_{hkl}) in direct and reciprocal spaces has the inverse relationship [349]:

$$\vec{g}_{hkl} = \frac{2\pi}{d_{hkl}} \tag{A1.13}$$

where $\vec{g}_{hkl}$ is the reciprocal lattice vector. The reciprocal space is commonly described by using the concept of the Ewald's sphere [173,349]. The inverse relationship between both spaces is the crucial aspect of the diffraction techniques. Hence, broad diffraction peaks correspond to small coherent volumes (e.g. grain sizes) in the direct space and vice versa. Moreover, peaks observed at small diffraction angles correspond to large d-spacing in direct space.

XRD diffraction can provide a wide set of information about the crystalline phase of the material. The positions and the intensities of the diffraction peaks allow the identification of the crystalline phase by comparison with PDF cards in a database. Once the crystalline phase is identified, the diffraction angle and the calculated d-spacing are used to determine the

lattice constants, i.e, lengths a, b, c and angles α, β, γ of the unit cell. The peak FWHM can be used to calculate the average crystallites size by the Scherrer's equation (section 2.1.3).
X-ray diffractometers are most widely based on the Bragg-Brentano focusing geometry or its variations (Fig. A1-12). In this configuration, the X-ray source and the detector are located at the intersection points of the goniometer and the focusing circle, while the sample is placed in its center. The goniometer radius is fixed, whilst the radius of the focusing circle radius varies with the goniometer angle [350]. The incident X-ray beam passes through the Soller slits in order to reduce the angular beam divergence. The second set of Soller slits is placed between the sample and the detector in order to collimate the diffracted beam before reaching the detector. Moreover, an additional slit (also called β-filter) can be added to reduce the background scattering. A sealed vacuum tube with tungsten filament as a cathode is used for the X-ray source. The heated cathode emits electrons, which are accelerated towards the metallic anode, typically Cu, Al, Mo or Mg. The electrons deaccelerate when hitting the anode, generating the X-ray radiation. The X-ray radiation is composed by two types: Bremsstrahlung, which generates a continuous spectrum, and characteristic X-rays, resulting from electron recombination induced in the atoms of the metallic anode and providing an emission spectrum with discrete frequencies (particular for the element of the anode material). These characteristic X-rays are the one used to perform the XRD measurement.
The incident beam and the diffracted beam form the angle 2θ, whilst the incident beam and the sample form the angle ω. In a typical configuration, the angle ω is given to be ½ of the detector angle 2θ, i.e.ω = θ. The usually used setup then operates in the θ-2θ scan mode, in which the X-ray source is fixed whereas the sample and the detector rotate with a rate θ/min and 2θ/min, respectively. The θ-θ scan mode is also possible. In this case, the sample is fixed and both X-ray source and detector rotate with a rate θ/min. Depending on the goniometer construction, other rotation movements of the angles ω, ϕ and χ can be also provided. Whilst ω is associated with the angle between the incident beam and the sample, the angles ϕ and χ are associated with the sample rotation. Such sample rotations allow analyzing the texture or the microstrainin the material crystalline structure [173,203,222].

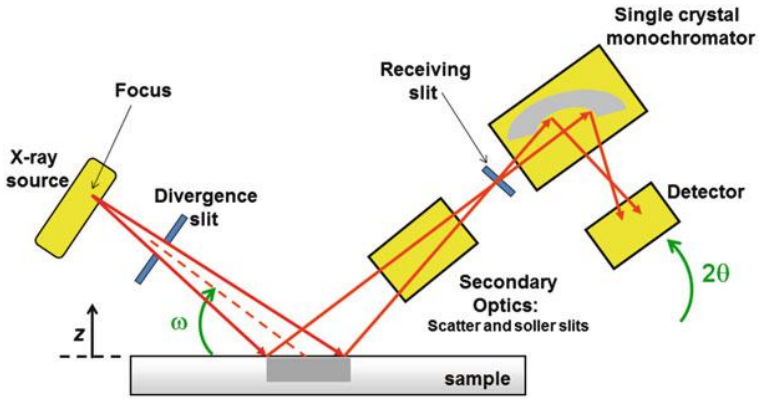

Fig. A1-12: Diagram of Bragg-Brentano configuration of XRD measurements.

Appendix 2
N content quantification in GeN alloys

Table A2-1: Comparison of N content quantification in GeN layers by WDXRF and IBA techniques.

Composition	Ge (at. %)		N (at. %)	
	WDXRF	**IBA**	**WDXRF**	**IBA**
Ge	99.2	100.0	0.8	0.0
GeN 10 sccm	73.9	71.2	26.1	28.8
GeN 25 sccm	56.1	51.3	43.9	48.7
GeN 30 sccm	53.6	48.6	46.5	51.4
GeN 40 sccm	50.8	43.6	49.3	56.4
GeN 50 sccm	49.7	44.5	50.1	55.5

Appendix 3
IR and Raman spectra deconvolution of elemental systems

N-doped Ge

The fitted IR spectrum of GeN 10 sccm layer is presented in Fig. A3-1. The spectrum features two main bands with maxima at 690 cm^{-1} and 300 cm^{-1}. The bands are assigned to the asymmetric stretching and disorder-induced breathing vibrational mode of Ge_3N structural unit, respectively. The bands contributions and their positions are listed in Table A3-I for all the investigated GeN layers.
While the GeN 1 sccm layer can be fitted only with one contribution for each band (ν_s and ν_b with maxima at ~680 cm^{-1} and 275 cm^{-1}, respectively), secondary contributions ν_s' and ν_b' are added to the both bands as the N content in the layer increases, reaching maxima at ν_s' ~750 cm^{-1} and ν_b' ~390 cm^{-1}. They are assigned to the disorder-induced modes of the Ge_3N group caused by the presence of more neighboring Ge-N bonds as the N content increases. These additional contributions shift in position to higher wavenumbers with the N content. Furthermore, the integrated area of the present bands contributions was calculated. For the most intense band in IR spectrum, the integrated area of the additional contribution (ν_s' ~750 cm^{-1}) increases with the N content with respect to the integrated area of the main contribution (ν_s ~680 cm^{-1}). In the case of the band at 300 cm^{-1}, the peak area ratio keeps in values from 0.7 to 0.96. The contribution at 520 cm^{-1} is added to ensure the proper fit of the IR spectrum.

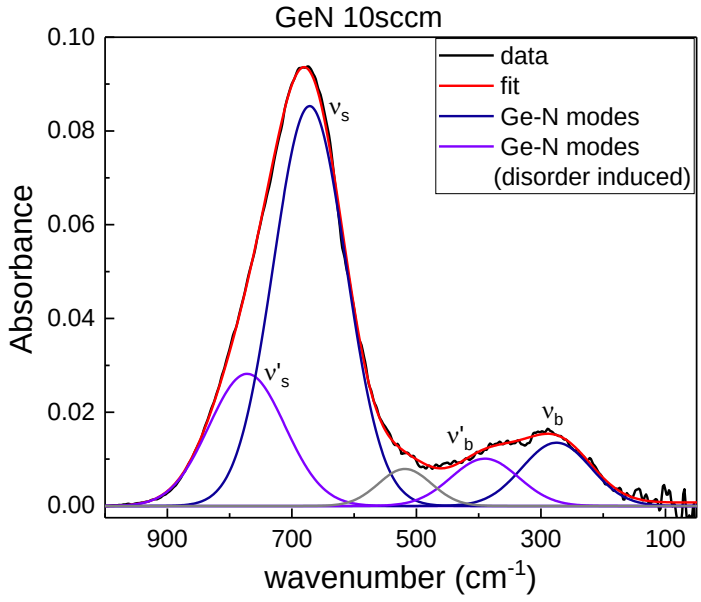

Fig. A3-1: Fit of the IR spectrum of GeN 10 sccm layer.

Table A3-I: Position and integrated area ratio of the contributions in the IR spectra of GeN layers.

IR spectroscopy						
GeN layer	**MIR**			**FIR**		
	Peak position (cm^{-1})		**Peak area ratio (ν_s' / ν_s)**	**Peak position (cm^{-1})**		**Peak area ratio (ν_b' / ν_b)**
	ν_s	**ν_s'**		**ν_b**	**ν_b'**	
GeN 1sccm	686	/	/	275	/	/
GeN 2sccm	681	748	0.058	275	/	/
GeN 5sccm	681	772	0.073	277	/	/
GeN 10sccm	671	772	0.346	275	390	0.761
GeN 20sccm	671	778	0.517	288	393	0.969
GeN 30sccm	676	776	0.568	290	390	0.837
GeN 40sccm	681	781	0.588	290	395	0.926

N-doped Sb

Fig. A3-2 and Fig. A3-3 show the fitted IR and Raman spectra of SbN 10 sccm layer. The IR spectrum features three main bands with maxima at ~600 cm^{-1}, ~275 cm^{-1} and ~150 cm^{-1}. The most intense band at 600 cm^{-1} is formed by two contributions ν_1 and ν_2. Considering the analogy with previously described GeN layers, the main contribution ν_1 at ~560 cm^{-1} can be likely assigned to the vibrations of the Sb-N structural unit and the additional contribution ν_2 at ~630 cm^{-1} to the disorder induced vibrational modes of the same unit. The ν_2 contribution shifts to higher wavenumbers and the integrated area ratio ν_2 / ν_1 of these contributions increases with N content in favor of this additional contribution ν_2. The positions of the band contributions and the integrated area ratio for all the investigated SbN layers are listed in Table A3-II.

The fit of the Raman spectrum highlights several contributions to the main band in the low wavenumber range (100-250 cm^{-1}). The position of the Raman band contributions are listed in Table A3-II. We can distinguish two main contributions related to the Sb: A_{1g} and E_g vibrations respectively at 150 cm^{-1} and 120 cm^{-1} (for a better fit, the E_g contribution is composed by two bands at 118 cm^{-1} and 109 cm^{-1}). These contributions are significantly broadened as a result of the lack of long range order in the layer due to N-doping. The contribution at ~130 cm^{-1}, likely related to the broadening of the Sb modes, needs to be added to achieve a good fit. For SbN 10 sccm and SbN 20 sccm, an additional contribution at ~170 cm^{-1} appears, which can be likely assigned to the vibrational mode of Sb-N bonds, as observed from the simulated Raman spectra (Fig. 3.11). This contribution shifts to higher wavenumbers and increases in intensity with the N content.

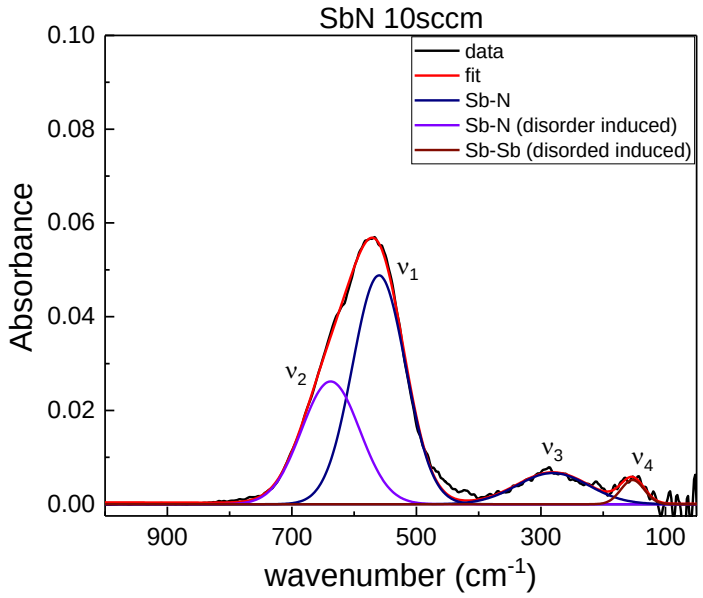

Fig. A3-2: Fit of the IR spectrum of SbN 10 sccm layer.

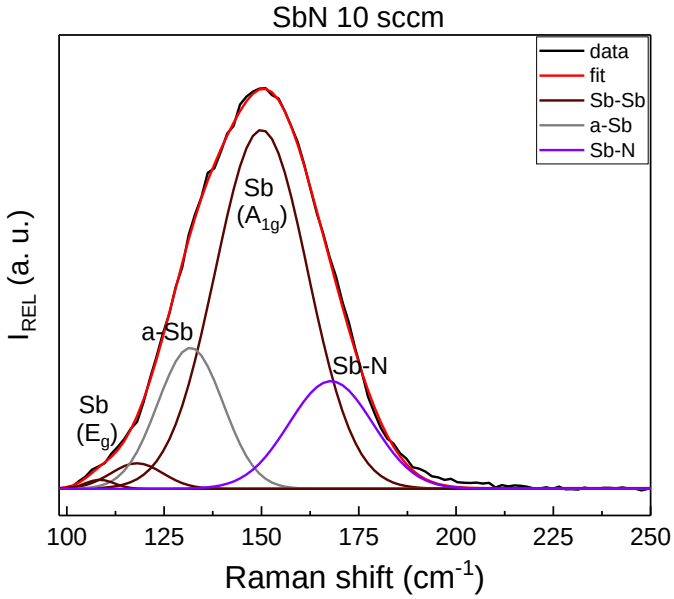

Fig. A3-3: Fit of the Raman spectrum of SbN 10 sccm layer.

Table A3-II: Position and integrated area ratio of the contributions in the IR spectra of SbN layers.

IR spectroscopy					
SbN layer	**Peak position (cm^{-1})**				**Peak area ratio (ν_2/ν_1)**
	ν_1	**ν_2**	**ν_3**	**ν_4**	
SbN 2sccm	566	625	275	150	0.239
SbN 10sccm	563	645	282	153	0.448
SbN 20sccm	558	647	283	156	0.578

Table A3-III: Position and integrated area ratio of the contributions in the Raman spectra of SbN layers.

Raman spectroscopy					
SbN layer	**Peak position (cm^{-1})**				**Peak area ratio (Sb-N / Sb(A_{1g}))**
	Sb (E_g)	**a-Sb**	**Sb (A_{1g})**	**Sb-N**	
SbN 2sccm	122	133	150	/	/
SbN 10sccm	118	132	150	168	0.272
SbN 20sccm	119	131	150	170	0.556

N-doped Te

The IR spectrum of TeN 10 sccm (Fig. A3-4) features several contributions in the range from 100 cm^{-1} up to 900 cm^{-1}. Two bands at ~90 cm^{-1} and ~150 cm^{-1} are assigned to the c-Te vibrations, whose intensity is highly reduced in N-doped Te. The broad band with the contributions at ~315 cm^{-1}, ~450 cm^{-1} and ~570 cm^{-1} are likely related to the vibration modes of Te-N. Low intense contributions can be added at higher wavenumbers, 635 cm^{-1} and 730 cm^{-1}, which can be assigned to the Te-O vibration modes. These vibrations were mainly observed in undoped Te layers, however, their contribution is evident also in TeN 10 sccm and TeN 20 sccm layers. The presence of Te-O contributions in N-doped Te, suggests that these layers may tend to oxidation despite the in-situ capping layer, or to absorb the residual oxygen in the deposition chamber before the capping. The IR data are listed in Table A3-IV.
Fig. A3-5 shows the fit of the Raman spectrum of TeN 10 sccm layer. The A_1 and E_2 vibrational modes of Te are present in all N-doped samples. The peaks are slightly broadening with increasing N content. An additional contribution at ~150 cm^{-1}, assigned to the vibrational modes of amorphous Te, appears in TeN 10 sccm and TeN 20 sccm layers. The integral area of this contribution increases in particular in TeN 20 sccm layer. In this layer, the ratio between the A_1 and E_2 modes significantly decreases (see inset of Fig. A3-5), indicating the impact of N-doping on the intensity of E_2 mode, which is related to the inter-chain bonding of the crystalline Te structure.

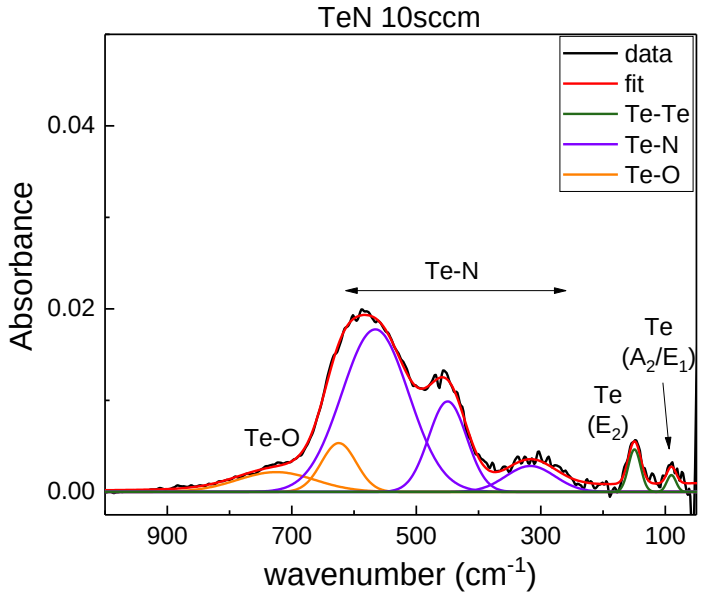

Fig. A3-4: Fit of the IR spectrum of TeN 10 sccm layer.

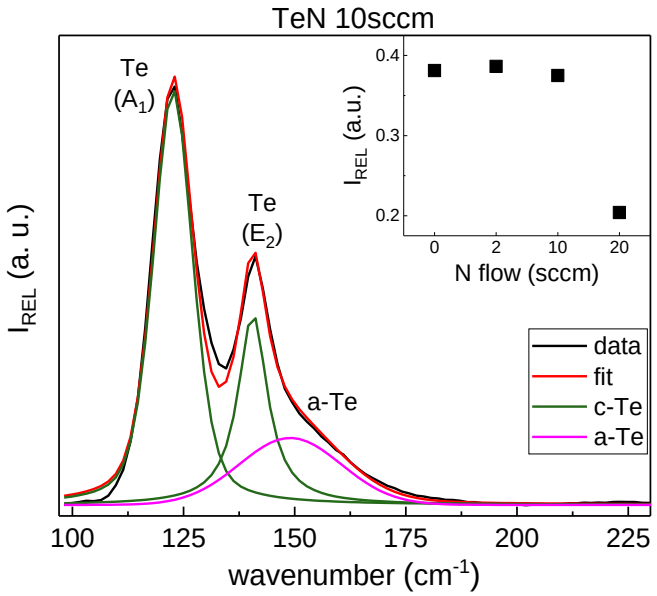

Fig. A3-5: Fit of the Raman spectrum of TeN 10 sccm layer. Inset: relative intensity ratio between the E_2 and A_1 modes with increasing N_2 flow.

Table A3-IV: Position of the band contributions in the IR spectra of TeN layers.

IR spectroscopy							
TeN layer	**Peak position (cm^{-1})**						
	Te		**Te-N**			**Te-O**	
	A_2 / E_1	**E_2**	**ν_1**	**ν_2**	**ν_3**	**ν_4**	**ν_5**
Te	90	149	/	/	/	635	728
TeN 2sccm	89	149	568	/	/	/	/
TeN 10sccm	90	149	568	451	315	632	730
TeN 20sccm	/	150	567	450	319	633	729

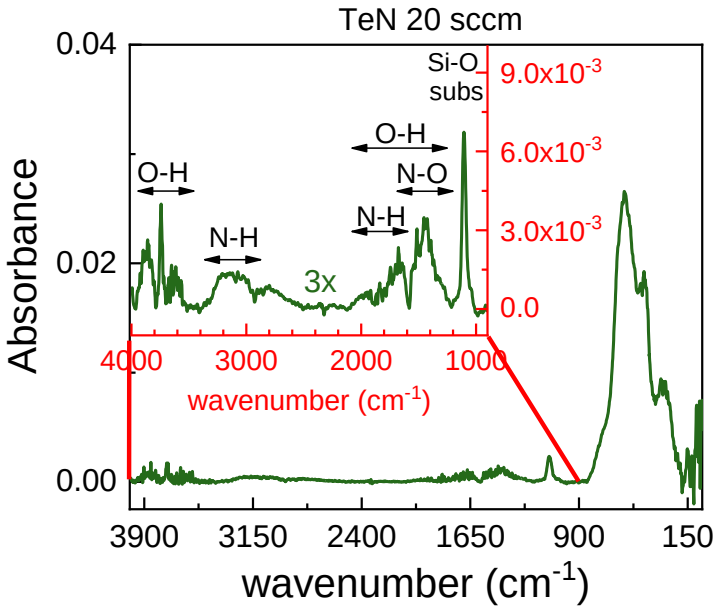

Fig. A3-6: IR spectrum (4000 – 100 cm^{-1}) of TeN 20 sccm layer, highlighting the IR bands assigned to O-H, N-H and N-O vibrations in the region from 4000 to 1000 cm^{-1} (closer view presented in the inset) , demonstrating the oxidations effect (i.e., layer degradation).

Appendix 4
"Ab initio" simulations of elemental nitrides

The *"ab-initio"* simulations of different nitrides structures of Ge, Sb and Te systems are shown in this section. The ideal nitride structures of each system were taken from Materials Project [351,352]. Both IR and Raman spectra of simulated nitride structures are compared with those of as-deposited N-doped Ge, Sb and Te layers (gray line in the graphs) deposited with the N_2 flow of 10 sccm. The name of the nitride structure showing the most suitable match between the simulated and experimental spectra and presented in the section 3.5 of the chapter 3 is highlighted by box frame.

IR and Raman spectra simulations of Germanium nitrides structures

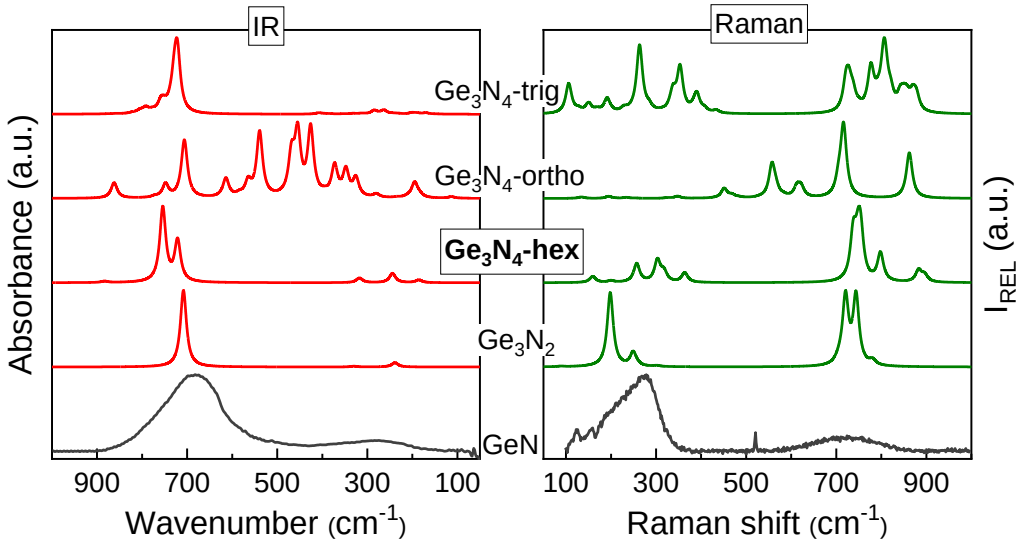

Fig. A4-1: IR and Raman spectra simulations of Germanium nitrides structures.

IR and Raman spectra simulations of Antimony nitrides structures

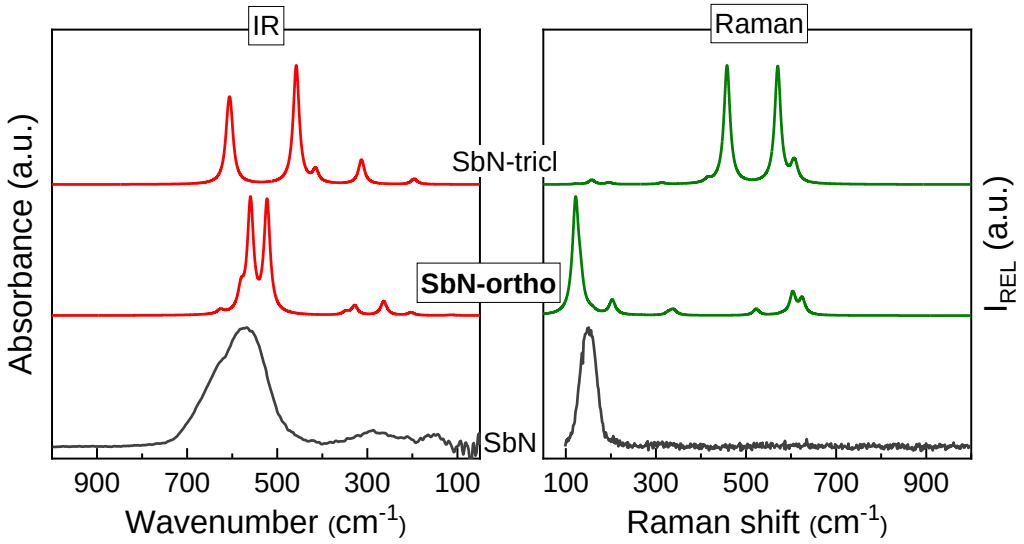

Fig. A4-2: IR and Raman spectra simulations of Antimony nitrides structures.

IR and Raman spectra simulations of Tellurium nitrides structures

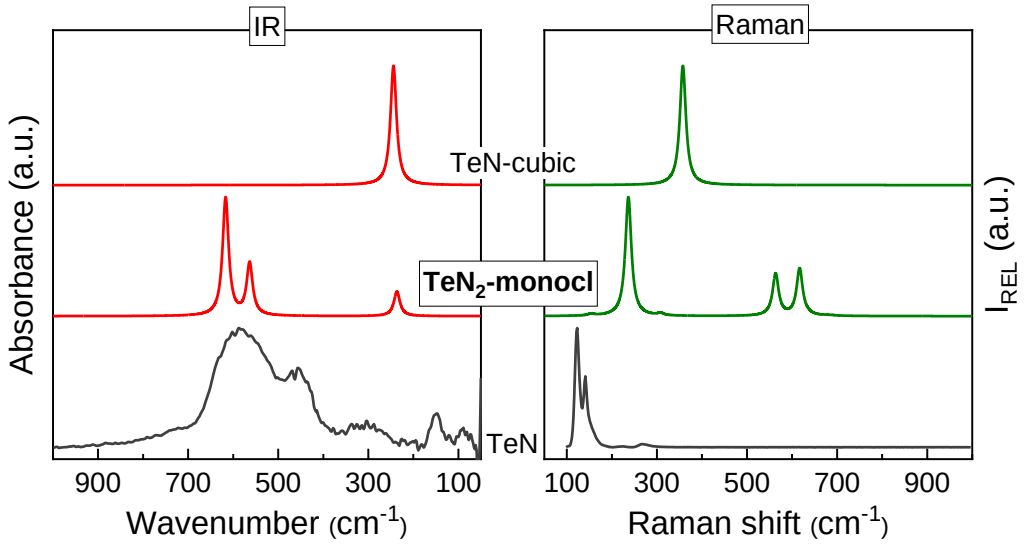

Fig. A4-3: IR and Raman spectra simulations of Tellurium nitrides structures.

Appendix 5
Raman spectra deconvolutions of GST alloys

Raman spectra fit of $Ge_2Sb_2Te_5$

The fit of Raman spectrum of as-deposited GST225 (Fig. A5-1) highlights the presence of the dominant contribution at 154 cm^{-1} assigned to A_{1g}^2 vibrational mode of Sb-Te bonds in $SbTe_3$ pyramidal units, accompanied by contributions at 124 cm^{-1} and 220 cm^{-1}. These two contributions are assigned to the Ge-Te vibrational modes, in particular to the A_1 vibration mode of corner-sharing tetrahedra $GeTe_{4-n}Ge_n$ (n = 1, 2) and the vibrational mode of $GeTe_4$ tetrahedral units, respectively [179,212]. In as-deposited GST225, a low intense contribution at 110 cm^{-1} is added for the better fit of the spectra, contributing to the intensity of the band at 124 cm^{-1}. Therefore, this contribution is also assigned to Ge-Te vibrational modes.
The fit of Raman spectrum of GST225 layer annealed at 400 °C (Fig. A5-1) features the two contributions at 124 cm^{-1} (Ge-Te modes) and 154 cm^{-1} (Sb-Te modes), however, the dominant contribution appears at 174 cm^{-1} and it is assigned to the vibrational modes of Sb-Te bond in structural arrangement characteristic for GST225 hexagonal phase. The intensity of Sb-Te modes at 154 cm^{-1} is significantly reduced, giving rise to the additional contribution at 160 cm^{-1}. Considering the analyses of GeTe films, this contribution can be likely assigned to an additional A_1 mode of $GeTe_{4-n}Ge_n$ (n = 0, 1, 2) edge-sharing tetrahedra. A considerable separation is achieved for the contribution at 110 cm^{-1}, previously ascribed as the additional contribution to Ge-Te modes at 124 cm^{-1}. In annealed GST225, this contribution could, however, also results from E_g^2 vibrational mode of Sb-Te bonds, as the structure is crystallized and Sb-Te vibrational modes are enhanced, forming the dominant structural units in the alloy.

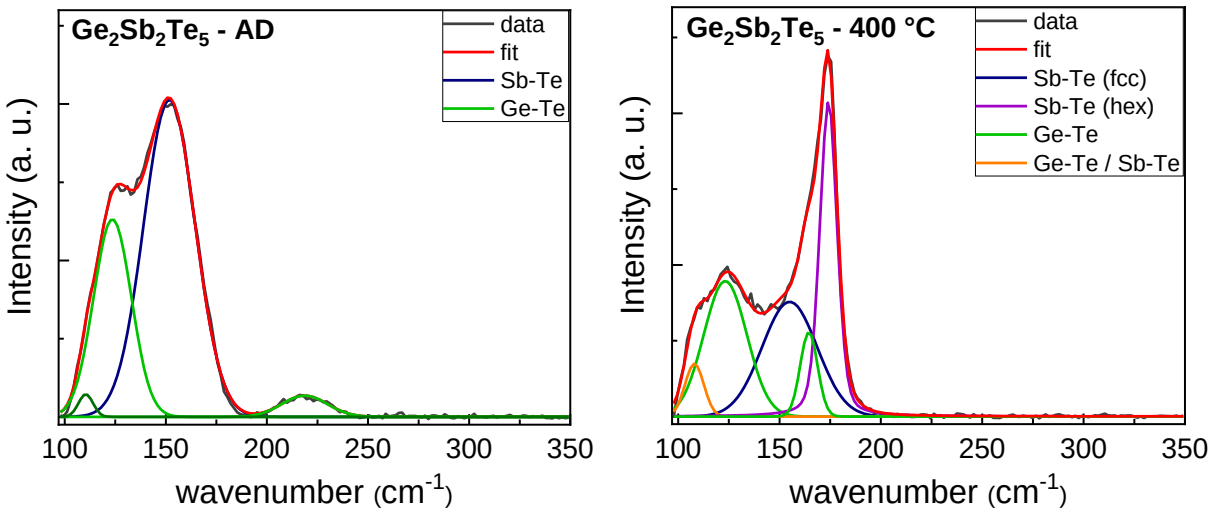

Fig. A5-1: Raman spectra fit of as-deposited (AD; left) and annealed (400 °C, right) $Ge_2Sb_2Te_5$ alloy, showing the contributions of main vibrational modes assigned to Sb-Te and Ge-Te bonds.

Raman spectra fit of Ge_xGST alloys

Raman spectroscopy analyses at low wavenumbers were performed on as-deposited and annealed (350 °C) layers of Ge_{15}GST, Ge_{35}GST and Ge_{55}GST in order to investigate the origin of the peak observed at ~110 cm^{-1}. The laser excitation source with the wavelength of 514 nm was used.

The narrow peak at ~110 cm^{-1} was observed in the Ge-rich GST layers highly enriched in Ge content. As can be observed from the spectra of as-deposited and annealed layers of Ge_{15}GST (Fig. A5-2a and Fig. A5-2b), which is the closest composition to the stoichiometric GST225 among the studied layers, there is no evidence of such a peak. On the contrary, the spectra of as-deposited layers of Ge_{35}GST and Ge_{55}GST (Fig. A5-2c and Fig. A5-2e) feature a narrow and very intense contribution at this wavenumber. Moreover, the relative intensity of this contribution compared to the main peak of the spectra at ~150 cm^{-1} (Sb-Te modes), increases with Ge content in the layer, whilst the vibrational modes of Ge-Te bonds are significantly reduced.

Owing to the comparison with the Raman spectrum of Sb_2Te_3 binary alloy [353–359], the contribution at ~110 cm^{-1} can be most likely attributed to the E_g^2 vibrational mode of Sb-Te bond. The appearance of this mode is probably related to the increasing Ge content in the layer. Ge-rich GST alloys with lower Ge enrichment (e.g., Ge_{15}GST) are close in composition to the stoichiometric GST225, in which the formed structural units correspond to those of later GST225-fcc crystalline structure. On the contrary, the increase of Ge content introduces more disorder in the amorphous as-deposited layers. Note that for Ge_{55}GST, the global Ge content reaches more than 60 at.% of layer composition. Although the as-deposited layer is homogeneous, large regions of Ge atoms enclose the SbTe structural units, which become more separated. Therefore, other vibrational modes of SbTe units, similar to those in Sb_2Te_3 alloys, can be likely enhanced.

While increasing the annealing temperature, the reorganization of the Ge-Te bonds around stable SbTe units leads to the formation of the GST crystalline phase and hence to the reduction of the described E_g^2 mode. This phenomenon can be observed in Fig. A5-2d and Fig. A5-2f, where the intensity reduction and complete disappearance of the peak at 110 cm^{-1} can be observed as the broad band 50 – 190 cm^{-1} reaches the form corresponding to that of GST225-fcc crystalline phase.

The broad band with the maxima at ~79 cm^{-1} in the Raman spectra of Ge_{35}GST and Ge_{55}GST as-deposited layers is assigned to TA-like mode of a-Ge [360]. This mode later disappears as the Ge phase crystallizes, as observed in Fig. A5-2f.

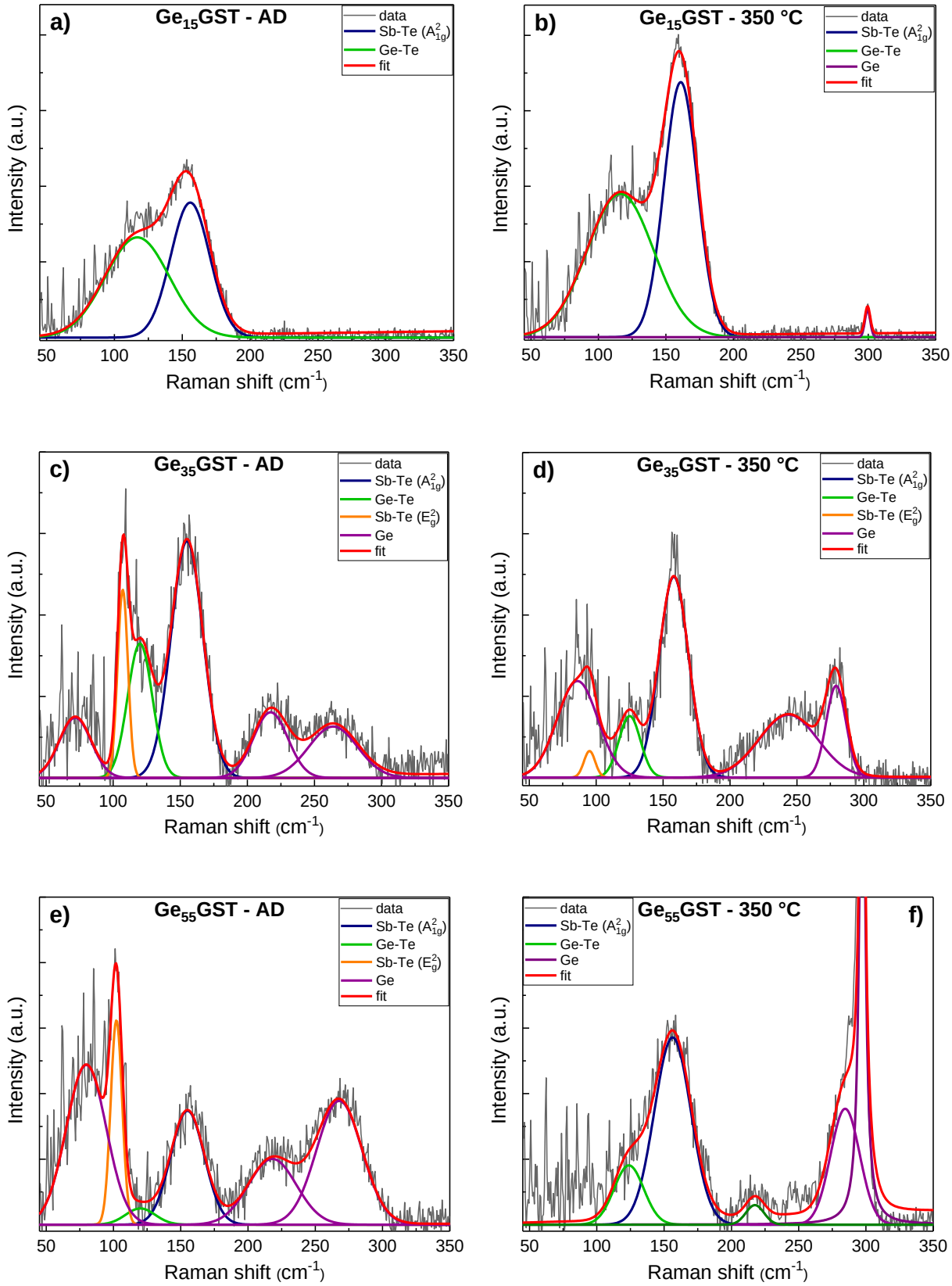

Fig. A5-2: Low wavenumber region Raman spectra of Ge_xGST layers: a) as-deposited Ge_{15}GST, b) Ge_{15}GST annealed at 350 °C, c) as-deposited Ge_{35}GST, d) Ge_{35}GST annealed at 350 °C, e) as-deposited Ge_{55}GST, f) Ge_{55}GST annealed at 350 °C.